

Cover Page



Universiteit Leiden



The handle <http://hdl.handle.net/1887/20578> holds various files of this Leiden University dissertation.

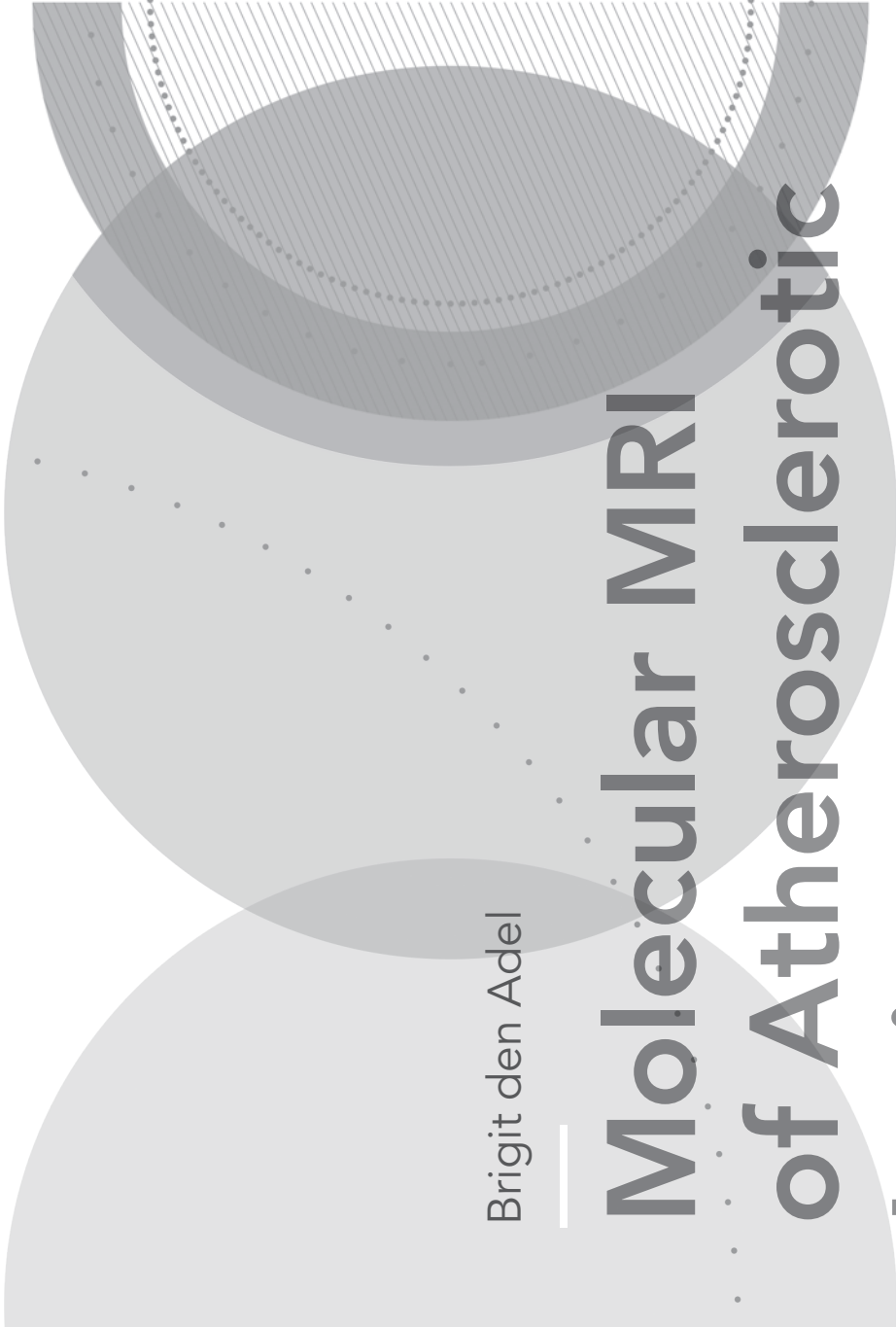
Author: Adel, Brigit den

Title: Molecular MRI of Atherosclerotic lesions

Issue Date: 2013-02-28

Brigit den Adel

Molecular MRI of Atherosclerotic Lesions





Colophon

Molecular MRI of Atherosclerotic Lesions

Brigit den Adel

Thesis Leiden University Medical Center

Cover illustration: Jort Braam | www.studiokern.nl

Lay-out: www.wenzid.nl | Wendy Schoneveld

Printed by: Off Page

ISBN 978-90-9027303-7

© Brigit den Adel 2013

All rights reserved. No part of this book may be reproduced or transmitted, in any form or by any means, without written permission of the author.



Molecular MRI of Atherosclerotic Lesions

proefschrift

ter verkrijging van de graad van

Doctor aan de Universiteit Leiden,

op gezag van Rector Magnificus prof.mr. C.J.J.M. Stolker

volgens besluit van het College voor Promoties

te verdedigen op donderdag 28 Februari 2013

klokke 13.45 uur

door

Brigit den Adel

geboren te Rotterdam

in 1981

Promotiecommissie

promotor Prof. Dr. R.E. Poelmann

co-promotor Dr. L. van der Weerd

overige leden Prof. Dr. J.W. Jukema

Prof. Dr. K. Nicolay (TUE Eindhoven)

Prof. Dr. G. Pasterkamp (UMC Utrecht)

The work presented in this thesis was carried out at the department of Anatomy & Embryology and Radiology in the Leiden University Medical Center.

Financial support by the Dutch Heart Foundation for the publication of this thesis is gratefully acknowledged. The research described in this thesis was supported by a grant of the Dutch Heart Foundation (DHF-2006T06).



Financial support by Guerbet Nederland for the publication of this thesis is gratefully acknowledged.

Contents

Chapter 1	
General Introduction	7
Chapter 2	
Molecular MRI of the vulnerable plaque – is it possible?	19
Chapter 3	
Self-gated CINE MRI for combined contrast-enhanced imaging and wall-stiffness measurements of murine aortic atherosclerotic lesions	41
Chapter 4	
Contrast enhancement by lipid-based MRI contrast agents in mouse atherosclerotic plaques; a longitudinal study	63
Chapter 5	
Scavenger receptor-AI targeted iron oxide nanoparticles for in vivo MRI detection of atherosclerotic lesions	81
Chapter 6	
Vascular cell adhesion molecule-1 targeted nanoparticles discriminate between atherosclerotic plaque stages in disease progression and therapy	99
Chapter 7	
E-selectin targeted MRI visualizes progression of atherosclerotic plaques	119
Chapter 8	
Micelle-mediated rosiglitazone treatment of atherosclerosis	139
Chapter 9	
Histological validation of iron-oxide and gadolinium based MRI contrast agents in experimental atherosclerosis: the do's and don't's	155
Chapter 10	
General discussion	169
Appendix	
Summary	180
Samenvatting	182
Curriculum Vitae	184
Publications	185
Dankwoord	187





Chapter 1

Introduction

INTRODUCTION

Cardiovascular disease (CVD), particularly atherosclerosis, is the leading cause of morbidity and mortality in the Western world, despite increasing awareness of a healthy lifestyle and wide prescription of cholesterol-lowering drugs¹. In developing countries, the disease is quickly becoming the leading cause of mortality, and therefore now accounting for a fifth of all deaths worldwide^{2,3}. Disease progression is usually slow and remains asymptomatic until either arterial blood flow becomes obstructed or a plaque rupture occurs precipitating clinical events^{4,5}. Clinical manifestations include angina pectoris, myocardial infarction stroke, aneurism and transient ischemic attacks (TIA)⁶.

The development of atherosclerosis is a complex multifactorial process. Two major factors contributing to the pathophysiology of atherosclerosis are hyperlipidemia and inflammation⁷. Many other risk factors have been identified, including both genetic (hypertension, dysglycemia) and environmental factors (smoking, high intake of saturated fats).

BIOLOGY OF ATHEROSCLEROSIS

Atherosclerosis is a progressive inflammatory auto-immune-like disease of the large and medium sized arteries characterized by the accumulation of lipids, fibrous components and debris in the vessel wall^{1,2}. Already in 1977, Ross et al., launched his "response to injury" concept in which atherosclerotic lesion development is viewed as a pathogenic response to endothelial injury⁸.

Endothelial injury changes the permeability of the arterial wall, leading to an influx of low density lipoproteins (LDL), which elicits in turn an inflammatory response in the vascular wall. Subsequent binding of monocytes and T-cells to the endothelium results in increased migration of cells into the intimal layer of the arterial wall, where monocytes differentiate into macrophages. Macrophages ingest modified lipoproteins, which transforms them into foam cells. As a result, other macrophages produce several cytokines and proteases that further damage the vessel wall. This vicious circle of lipid-driven inflammation can lead to narrowing of the vessel lumen.

Atherosclerotic lesions develop at sites of low and disturbed shear stress close to arterial bifurcations and branching points⁹ where enhanced expression of inflammatory markers and increased leukocyte adherence can be observed. Lesions may already start developing in these areas from the second decade of life onwards. Early lesions and fatty streaks, which consist of the above described foam cells and T lymphocytes in the intima, are already common in infants and young children. Further development of an atherosclerotic lesion to a more intermediate lesion is characterized by accumulation of more macrophages and smooth muscle cells. In more advanced stages, the plaque has a large lipid core covered by a fibrous cap. Advanced lesions are predominantly found in people at the age of 30 years and older, and are characterized by extra-cellular deposition of amorphous lipids, preceding the influx of macrophages and T lymphocytes¹⁰. The advanced plaque may be at risk to rupture (so-called vulnerable plaque)¹¹, which may trigger acute clinical complications such as stroke, peripheral vascular disease and myocardial infarction, depending on the anatomical location of the plaque.

In the cascade of events from an early fatty streak to a vulnerable plaque, inflammatory cells are continuously recruited. The classical vulnerable plaque that is prone to rupture is characterized by a thin fibrous cap (<70 μm), a large lipid-rich necrotic core (>40% of the plaque area) and many inflammatory cells in the shoulder regions of the cap¹². The degree of inflammation is not only

determined by the number of macrophages, but also by the activity of these macrophages. Expression of molecular markers like matrix metalloproteinases and scavenger receptors are thus also indices of the vulnerability of the plaque.

Figure 1 shows an illustration of the different processes and molecules involved in atherosclerosis over time. Increased expression of leukocyte adhesion markers is one of the earliest hallmarks of atherosclerosis. Molecules like P-selectin, E-selectin, VCAM-1 and ICAM-1 may serve as biomarkers for vascular inflammation. In later plaque stages monocyte and macrophage accumulation can be important markers to detect.

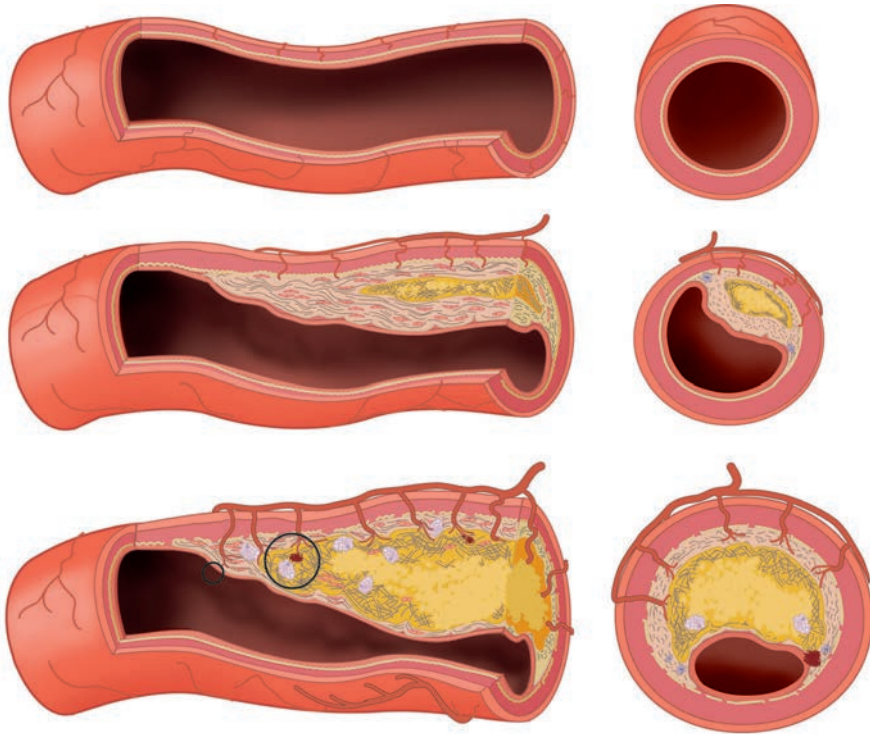


Figure 1 | Atherosclerotic plaque development. Atherosclerotic plaques develop as a chronic inflammatory healing response, secondary to endothelial damage. The top panels show a cross section of a normal muscular artery without atherosclerosis. The vessel lumen is covered by endothelial cells that rest upon a basement membrane. The vessel wall consists of 3 layers, the tunica intima, separated from the tunica media by the lamina elastica interna, and the tunica adventitia. The human intima generally consists of a layer of endothelial cells and smooth muscle cells scattered within the intimal extracellular matrix. The media consists of multiple layers of smooth muscle cells, embedded in an elastin as well as collagen-rich matrix. The adventitia, the outer layer of arteries, contains mast cells, nerve endings and microvessels. Endothelial dysfunction leads to fatty streak formation and thickening of the intima and the accumulation of lipids as visualized in the middle panels. The initial steps of atherosclerosis include leukocyte adhesion to the endothelium, migration of the leukocytes into the intima, maturation of monocytes into macrophages, and their uptake of lipids, leading to the formation of foam cells. Lesion progression, in the lower panels, involves the migration of SMCs from the media to the intima, the proliferation of resident intimal SMCs and media-derived SMCs, and the increased synthesis of extracellular matrix molecules such like collagen and elastin. Plaque macrophages and SMCs can die in advancing lesions leading to the accumulation of their lipids and formation of a necrotic core in the central region of a plaque. Advancing plaques also contain cholesterol crystals and microvessels and may have sites of thrombosis.

A more detailed overview of biomarkers for vulnerable atherosclerotic plaque and targeted contrast agents to image the presence of these biomarkers is presented in chapter 2.

Experimental models for atherosclerosis

The availability of clinically relevant experimental models of atherosclerosis is essential to study the underlying biological mechanisms. Wild-type mice are highly resistant to atherosclerosis as a result of high levels of HDL (anti-atherosclerotic) and low levels of LDL and VLDL (pro-atherogenic), even at advanced age, which makes them unsuitable for atherosclerosis research. The lesion-prone C57Bl/6 mice strain only develops small fatty-streak-like lesions when fed a high-cholesterol diet¹³.

Therefore, all the current mouse models for atherosclerosis are based on modulations of lipoprotein metabolism through genetic manipulations and dietary interventions. The most commonly used mouse models are the apolipoproteinE-deficient mouse (ApoE^{-/-})¹⁴ and the LDLreceptor deficient (LDLR^{-/-})¹⁵ mouse. The ApoE^{-/-} mouse develops spontaneously advanced, complex atherosclerotic lesions throughout the arterial tree, especially in the aortic arch¹⁶. Lesions are characterized by foam cell and lipid accumulation, a fibrous smooth muscle cell cap, and the presence of a necrotic core¹⁶. These lesions progress well beyond the fatty streak and resemble human lesions. This highly pro-inflammatory model is suitable to study the cellular aspects of lesion development and has been used for years to that end.

Although ApoE^{-/-} mice develop advanced lesions, they do not develop aneurysms or vulnerable plaques. To that end a double transgenic mouse has been developed; the ApoE^{-/-}-eNOS^{-/-} mouse. We used this mouse to study the treatment window of peroxisome proliferator-activated receptor gamma (PPAR γ) ligand rosiglitazone in atherosclerosis as described in chapter 8.

LDLR^{-/-} mice are based on a mutation found in patients with familial hypercholesterolemia. These mice are modestly hypercholesterolemic on a chow diet. As a result these mice develop lesions more slowly and lesions are generally more macrophage-rich and less progressed than in ApoE^{-/-} mice. Atherosclerosis development is enhanced when LDLR^{-/-} mice are fed a lipid-rich diet. The LDLR^{-/-} mouse thus represents a more moderate model than the ApoE^{-/-} model. One of the main advantages of this mouse model is the possibility to combine it with bone marrow transplantations to repopulate the hematopoietic lineage with donor bone marrow. This technique is used to specifically address the role of cells originating from the hematopoietic lineage in atherosclerosis development. An application of this method is described in chapter 5.

DETECTION OF ATHEROSCLEROTIC LESIONS

Early detection of atherosclerosis is important for preventive measures like lifestyle changes and pharmacological interventions. The diagnosis of vulnerable atherosclerotic plaques is important for screening of high-risk patients among patients with established coronary artery disease.

Our understanding of the pathogenesis of CVD has advanced considerably in the past decades and led to the development of a vast range of therapeutic and surgical interventions⁴. However, progress in the detection of both early as well as high-risk atherosclerotic lesions is lagging behind and still mainly limited to anatomical features, i.e. the degree of stenosis or vessel occlusions. However, the anatomical severity of stenosis is not sufficient to predict the risk of vascular events¹⁷. In fact vulnerable plaques are often only moderately stenotic due to outward remodeling of the vessel, and as a result difficult to recognize as presenting a high risk¹⁸. Non-invasive imaging techniques, such as magnetic resonance imaging (MRI), computed tomography (CT), positron

emission tomography (PET), single photon emission computed tomography (SPECT) and ultrasonography (US) all provide limited information on vessel wall characteristics and plaque composition. As the vulnerability of an atherosclerotic plaque is mainly dependent on plaque composition, there is an urgent need for imaging modalities capable to specifically detect vulnerable plaques.

Molecular Imaging

Over the last decade researchers worldwide have worked extensively on the development of more sensitive and more advanced imaging techniques. One of the major changes in radiology is the concept of molecular imaging. While conventional imaging techniques depict gross anatomical or functional changes, molecular imaging visualizes the molecular and cellular processes of pathology. In general, molecular imaging requires fast, sensitive and high-resolution techniques, combined with the application of contrast agents that are tailored to recognize a particular molecular target.

Two traditional imaging modalities in the field of molecular imaging are positron emission tomography (PET) and single-photon emission computed tomography (SPECT) that detect radionuclides. Both are characterized by phenomenal sensitivity with detection limits at sub-nanomolar concentrations. Yet the spatial resolution of these techniques is intrinsically low (around 5-10 mm in humans) without anatomical detail. MRI on the other hand is anticipated to become one of the prominent non-invasive imaging techniques for disease diagnosis. Its advantages include a high spatial resolution (~1 mm in humans and still improving) without the use of a ionizing radiation source. MRI can also detect multiple sources of image contrast, thereby providing both physiological and anatomical information of soft tissue. A major limitation of MRI, however, remains its inherently low sensitivity (sub-millimolar range). Only the most abundant endogenous biochemical molecules can be imaged directly by magnetic resonance spectroscopy (MRS-I). Therefore, specific and sensitive targeted contrast agents are needed to visualize molecular epitopes. To address this sensitivity problem, MRI contrast agents with a high relaxivity have been developed¹⁹. The general principle of MRI contrast agents is discussed in this chapter. Specific applications of MRI contrast agents to detect atherosclerotic lesions are presented in chapters 2 – 9.

MRI

Magnetic resonance images are predominantly produced by the detection of water protons. Water molecules can be detected due to a property of hydrogen nuclei called spin. Spin is the random spinning motion of an electric charge that produces a magnetic moment²⁰.

When a spin is placed in a strong magnetic field (B_0), these spins lose their random orientation and align within the magnetic field. For hydrogen, two energy states or orientations are possible: $N+1/2$ spin 'up' (low energy) and $N-1/2$ spin 'down' state (high energy). The Boltzmann distribution shows that at body temperature, slightly more spins occupy the lower energy state. The resulting net magnetic moment generates the MRI signal. To enable the detection of this magnetic moment of the protons within the magnetic field, an external resonant radio-frequency field is applied in the form of a short pulse, creating an additional magnetic field (B_1). This pulse causes spins to flip from their alignment with the magnetic field and turns the net magnetization towards the transverse plane. After the pulse, the generated B_1 field ceases to exist and the nuclear spins return to their equilibrium state in the main magnetic field. This process is called relaxation. The time required to return to the ground state is termed relaxation time.

Relaxation occurs through two processes named longitudinal (T1) and transverse (T2) relaxation. The return of the alignment around the z-axis to equilibrium is termed the spin-lattice or longitudinal relaxation T1. T2 relaxation is the local dephasing of spins in the transverse plane. T2* is a composite relaxation time, determined by molecular interactions (T2 relaxation) and local magnetic field non-uniformities. Due to these small differences in magnetic field the protons precess at slightly different frequencies, resulting in rapid dephasing and loss of transverse magnetization. The T1 and T2 relaxation mechanisms are independent, though T1 is inherently always longer than T2, and T2 is always longer than T2*.

T1, T2 and T2* are properties of the water environment and thus of different tissue types. They differ between tissues due to the different physicochemical microenvironments of tissues like water mobility, the presence of microstructures, macromolecules and membranes. MRI contrast may be generated by tuning the imaging parameters to optimize the T1 or T2 contrast between tissues.

MRI contrast agents

Most MRI contrast agents work by reducing the longitudinal (T1) or transverse (T2) relaxation times of the target tissue, and are thus commonly described as either "T1-agent" or "T2-agent" depending on whether their relative reduction in relaxation time is greater for the T1 or T2 relaxation times. The ability of the agent to reduce the T1 and T2 relaxation times is described by the r1 and r2 relaxivity values.

Generally speaking, T1 agents increase the spin-lattice relaxation rate ($1/T1$) of hydrogen protons in tissue. This T1 lowering effect increases the signal intensity on T1 weighted images (figure 2A). Due to the increase of signal intensity on T1-weighted images, T1 agents are also called positive contrast agents. On the other hand, T2 agents largely influence the spin-spin relaxation rate ($1/$

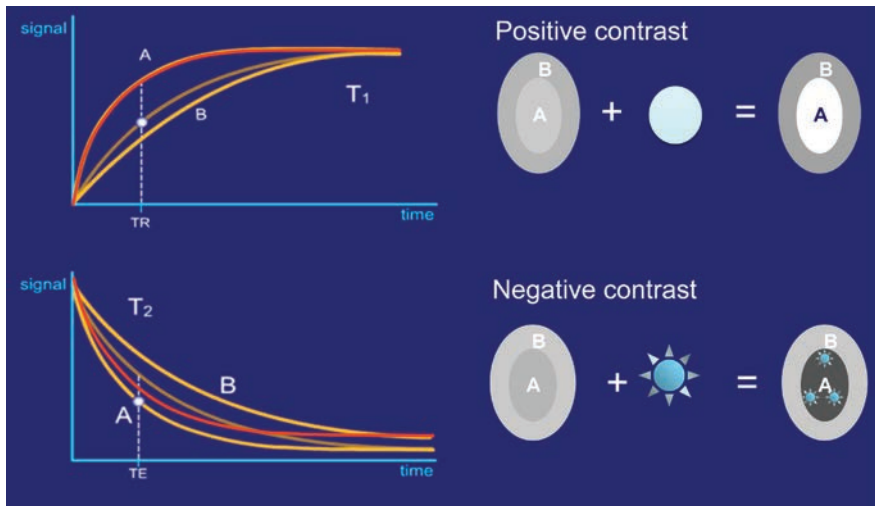


Figure 2 | T1 and T2 contrast principle. Schematic representation of the effect of positive and negative contrast agents. A. Positive contrast agents cause a reduction in the T1 relaxation time, generating spots with increased signal intensity on T1 weighted images. B. Negative contrast agents produce predominantly spin spin relaxation effects (local field inhomogeneities), which results in shorter T1 and T2 relaxation times that appear as dark spots on MRI.

T2) by decreasing T2. This results in the decrease of signal intensity on T2-weighted images (figure 2B). Thus, these agents have been named negative contrast agents.

T1 contrast agents

The most commonly used positive or T1 contrast agents are chelates of the lanthanide gadolinium (Gd³⁺). As many other metal ions, free Gd³⁺ is toxic, therefore it is used in a stable non-toxic form in a protective chelate. Several clinically approved low-molecular weight gadolinium complexes are available, including Magnevist® (Gd(DTPA)²⁻), dotarem® (Gd(DOTA)⁻) and Prohance® (Gd(HPDO3A)). The relaxivity of these compounds is sufficient to visualize the blood pool, yet too low to image sparse molecular epitopes. Nevertheless, these small compounds have been shown to enhance the vessel wall in atherosclerotic lesions using delayed contrast enhancement techniques in mouse and rabbit models of atherosclerosis^{21, 22}.

There has been considerable effort to use Gd-based probes to target specific plaque components. Gd offers the benefit of positive image contrast on T1-weighted images. The majority of work to date has been preclinical, with the exception of the fibrin-targeted probe EP-2104R, for which limited data in humans have been reported²³.

Nanoparticles, such as gadolinium-containing micelles²⁴, liposomes²⁵ and oil-in-water emulsions^{26, 27} and lipoproteins^{28, 29} have the potential to deliver high payloads of contrast generating material and are used to overcome sensitivity problems. Gd-loaded nanoparticles to image atherosclerotic lesions have been applied in chapter 3, 4 and 8.

T2 contrast agents

Most T2 contrast agents consist of a coated (mostly with dextran) iron-oxide nanoparticle in the order of 4 to 50 nm. They are also depending on their size, coating and structure referred to as superparamagnetic iron oxide particles (SPIO 60-150 nm), ultrasmall SPIO (USPIO 20-50 nm), micron-sized iron oxide particles (MPIO ~ 1 µm), very small superparamagnetic iron oxide particles (VSOP < 4 nm), monocrySTALLINE iron oxide nanoparticles (MION, 30-50 nm)³⁰ and crosslinked iron oxide (CLIO, 30-60 nm)³¹. Iron oxide particles can contain up to thousands of magnetic iron oxides and therefore these particles have a very large net magnetic moment. T2 contrast agents generate strong local field gradients, which leads to a shortening of T2 and particularly T2*, causing hypointense spots on T2-weighted MRI. On T2*-weighted images, these hypointense areas may be much larger than the actual area covered by the particles, a process called the blooming effect.

The association of iron oxide particles with cells can occur via passive or active targeting. Dextran-coated USPIO nanoparticles are inherently sequestered by monocytes/macrophages because of phagocytosis, which is therefore referred as passive targeting to monocytes/macrophages³². This is valuable for atherosclerotic plaque imaging as high macrophage content is considered a hallmark of plaques vulnerable to rupture¹. Ruehm *et al.* were the first to show that once these particles are internalized within the intraplaque macrophages, significant T2*-weighted MR signal loss occurs, allowing the detection of plaques that are macrophage rich³³. We applied this passive targeting of intraplaque macrophages in chapter 7 of this thesis, in which we assess plaque stage based on the imaging of both E-selectin and intraplaque macrophages.

Targeted MRI contrast agents

A targeted MRI contrast agent in general consists of 2 main components: 1) a ligand with high affinity for a biological relevant marker. Antibodies, peptides or other small molecules can serve as ligands for contrast agents. 2) a component that can be detected by MRI. To obtain a high

target-to-background ratio, a contrast agent should have favorable pharmacokinetics, high target-binding efficacy and specificity and low background binding. An imaging probe should also have low toxicity.

The nature of the target of choice generally dictates the type of contrast agent that can be used. Highly abundant molecular markers can be targeted using small contrast agents. Sparse molecules on the other hand require the use of high-payload contrast agents such as micelles and liposomes that deliver hundreds to thousands contrast agent moieties. The location of the target of choice is also of great importance; this determines the chance of successful targeting. During the development of atherosclerotic plaques, many potential biomarkers, such as adhesion molecules [vascular cell adhesion molecules (VCAMs), intercellular adhesion molecules (ICAMs), selectins], macrophages and their scavenger receptors, matrix metalloproteinases (MMPs), oxidized low-density lipoprotein (oxLDL), $\alpha\beta3$ integrin, extracellular matrix, and fibrin (summarized in chapter 2), are upregulated. It is important to point out that these molecules are often not unique to cardiovascular diseases, but they are present at increased levels under these disease conditions as compared to disease-free conditions.

Markers that are present on the endothelium like the leukocyte adhesion molecules VCAM-1 and E-selectin are relatively easy to reach via the blood stream with contrast agents ranging in size from very small to larger nanoparticles. In later stages of atherosclerosis the processes "specific" for that stage are generally found inside the plaque, like the scavenger receptor (SR) on macrophages as well as VCAM-1 on macrophages and vascular smooth muscle cells. These sites are not as readily accessible, and contrast agent penetration is of importance for successful targeting. The application of VCAM-1 targeted USPIO is described in chapter 6, E-selectin and SR-A1 targeted USPIO were validated in chapter 5 and chapter 7 respectively.

Outlook of molecular MRI for atherosclerosis

Targeted molecular MRI of atherosclerosis is already playing an important role in basic science, and the development and testing of novel pharmaceuticals. Although the clinical translation of these techniques holds much promise, safety, regulatory, and economic hurdles will need to be addressed.

The recent human experience with EP-2104R is in many ways encouraging.

The optimal approach to prevent cardiovascular events remains an area of significant debate and activity. It is unlikely, however, that a genomic- and biomarker-based approach alone will suffice to that end in the future, and complementary information provided by imaging techniques such as molecular MRI may ultimately become crucial.

AIM AND OUTLINE OF THE THESIS

This thesis describes the use of a variety of MRI contrast agents and vessel wall parameters to non-invasively image different stages of atherosclerosis.

Chapter 2 gives an overview of the different MRI contrast agents targeted towards the vulnerable plaque that have been presented in literature.

Chapter 3 illustrates that paramagnetic micelles and liposomes are able to accumulate in atherosclerotic plaques, yet have a complex kinetic behavior when followed for longer periods of time. This knowledge was further applied in *chapter 4* and *chapter 8* of this thesis. In *chapter 4* the use of self-gated cine MRI was validated to detect contrast agent accumulation in

atherosclerotic plaques and assess the vessel wall compliance. The potential of both techniques to monitor plaque progression and anti-atherosclerotic therapy was assessed. In *chapter 5* we developed and validated a scavenger receptor A1 targeted USPIO to detect vulnerable lesions. *Chapter 6* describes the application of a VCAM-1 targeted USPIO. Imaging at different time points after injection, allows to discriminate early plaques from advanced lesions. We show how this imaging technique could be used to monitor treatment response in ApoE^{-/-} mice. In *Chapter 7* an E-selectin targeted USPIO to detect atherosclerotic lesions was validated. This USPIO allowed discrimination of lesions rich in macrophages from early lesions. In *Chapter 8* we developed a micelle-based nanoparticle encapsulating rosiglitazone. Targeted delivery to the plaque lead to a good anti-atherosclerotic response without cardiac side-effects. Finally in *Chapter 9* the potentials and pitfalls in the histological validation of MRI contrast agents for atherosclerosis are illustrated.

The results I obtained in these studies and their (pre)clinical relevance are discussed in *General Discussion* and recommendations for future research are formulated.

REFERENCES

- Libby P. Inflammation in atherosclerosis. *Nature* 2002; 420:868-74.
- Falk E. Pathogenesis of atherosclerosis. *J Am Coll Cardiol* 2006; 47:C7-12.
- Lopez AD, Mathers CD, Ezzati M, Jamison DT, Murray CJ. Global and regional burden of disease and risk factors, 2001: systematic analysis of population health data. *Lancet* 2006; 367:1747-57.
- Libby P, Theroux P. Pathophysiology of coronary artery disease. *Circulation* 2005; 111:3481-8.
- Ross R. Atherosclerosis--an inflammatory disease. *N Engl J Med* 1999; 340:115-26.
- Naghavi M, Libby P, Falk E, et al. From vulnerable plaque to vulnerable patient: a call for new definitions and risk assessment strategies: Part I. *Circulation* 2003; 108:1664-72.
- D'Agostino RB, Sr., Vasan RS, Pencina MJ, et al. General cardiovascular risk profile for use in primary care: the Framingham Heart Study. *Circulation* 2008; 117:743-53.
- Ross R, Glomset J, Harker L. Response to injury and atherogenesis. *Am J Pathol* 1977; 86:675-84.
- Chiu JJ, Chien S. Effects of disturbed flow on vascular endothelium: pathophysiological basis and clinical perspectives. *Physiol Rev* 2011; 91:327-87.
- Stary HC, Chandler AB, Dinsmore RE, et al. A definition of advanced types of atherosclerotic lesions and a histological classification of atherosclerosis. A report from the Committee on Vascular Lesions of the Council on Arteriosclerosis, American Heart Association. *Circulation* 1995; 92:1355-74.
- Muller JE, Abela GS, Nesto RW, Toftor GH. Triggers, acute risk factors and vulnerable plaques: the lexicon of a new frontier. *J Am Coll Cardiol* 1994; 23:809-13.
- Schaar JA, Muller JE, Falk E, et al. Terminology for high-risk and vulnerable coronary artery plaques. Report of a meeting on the vulnerable plaque, June 17 and 18, 2003, Santorini, Greece. *Eur Heart J* 2004; 25:1077-82.
- Paigen B, Ishida BY, Verstuyft J, Winters RB, Albee D. Atherosclerosis susceptibility differences among progenitors of recombinant inbred strains of mice. *Arteriosclerosis* 1990; 10:316-23.
- Zhang SH, Reddick RL, Piedrahita JA, Maeda N. Spontaneous hypercholesterolemia and arterial lesions in mice lacking apolipoprotein E. *Science* 1992; 258:468-71.
- Ishibashi S, Brown MS, Goldstein JL, Gerard RD, Hammer RE, Herz J. Hypercholesterolemia in low density lipoprotein receptor knockout mice and its reversal by adenovirus-mediated gene delivery. *J Clin Invest* 1993; 92:883-93.
- Nakashima Y, Plump AS, Raines EW, Breslow JL, Ross R. ApoE-deficient mice develop lesions of all phases of atherosclerosis throughout the arterial tree. *Arterioscler Thromb* 1994; 14:133-40.
- Virmani R, Burke AP, Farb A, Kolodgie FD. Pathology of the vulnerable plaque. *J Am Coll Cardiol* 2006; 47:C13-C18.
- Virmani R, Burke AP, Kolodgie FD, Farb A. Pathology of the thin-cap fibroatheroma: a type of vulnerable plaque. *J Interv Cardiol* 2003; 16:267-72.
- Chen W, Cormode DP, Fayad ZA, Mulder WJ. Nanoparticles as magnetic resonance imaging contrast agents for vascular and cardiac diseases. *Wiley Interdiscip Rev Nanomed Nanobiotechnol* 2010.
- Hashemi RH BWLC. MRI: The Basics. 2. New York: Lippincott Williams & Wilkins 2004.
- Barkhausen J, Ebert W, Heyer C, Debatin JF, Weinmann HJ. Detection of atherosclerotic plaque with Gadofluorine-enhanced magnetic resonance imaging. *Circulation* 2003; 108:605-9.
- Yeon SB, Sabir A, Clouse M, et al. Delayed-enhancement cardiovascular magnetic resonance coronary artery wall imaging: comparison with multislice computed tomography and quantitative coronary angiography. *J Am Coll Cardiol* 2007; 50:441-7.
- Spuentrup E, Botnar RM, Wiethoff AJ, et al. MR imaging of thrombi using EP-2104R, a fibrin-specific contrast agent: initial results in patients. *Eur Radiol* 2008; 18:1995-2005.
- Mulder WJ, Strijkers GJ, van Tilborg GA, Cormode DP, Fayad ZA, Nicolay K. Nanoparticulate assemblies of amphiphiles and diagnostically active materials for multimodality imaging. *Acc Chem Res* 2009; 42:904-14.
- Meincke M, Schlorf T, Kossel E, Jansen O, Glueer CC, Mentlein R. Iron oxide-loaded liposomes for MR imaging. *Front Biosci* 2008; 13:4002-8.
- Doiron AL, Chu K, Ali A, Brannon-Peppas L. Preparation and initial characterization of biodegradable particles containing gadolinium-DTPA contrast agent for enhanced MRI. *Proc Natl Acad Sci U S A* 2008; 105:17232-7.
- Jarzyna PA, Skajaa T, Gianella A, et al. Iron oxide core oil-in-water emulsions as a multifunctional nanoparticle platform for tumor targeting and imaging. *Biomaterials* 2009; 30:6947-54.
- Frias JC, Williams KJ, Fisher EA, Fayad ZA. Recombinant HDL-like nanoparticles: a specific contrast agent for MRI of atherosclerotic plaques. *J Am Chem Soc* 2004; 126:16316-7.
- Mitsumori LM, Ricks JL, Rosenfeld ME, Schmiedl UP, Yuan C. Development of a lipoprotein based molecular imaging MR contrast agent for the noninvasive detection of early atherosclerotic disease. *Int J Cardiovasc Imaging* 2004; 20:561-7.
- Shen T, Weissleder R, Papisov M, Bogdanov A, Jr., Brady TJ. Monocrystalline iron oxide nanocompounds (MION): physicochemical properties. *Magn Reson Med* 1993; 29:599-604.
- Wunderbaldinger P, Josephson L, Weissleder R. Crosslinked iron oxides (CLIO): a new platform for the development of targeted MR contrast agents. *Acad Radiol* 2002; 9 Suppl 2:S304-S306.
- Jaffer FA, Nahrendorf M, Sosnovik D, Kelly KA, Aikawa E, Weissleder R. Cellular imaging of inflammation in atherosclerosis using magnetofluorescent nanomaterials. *Mol Imaging* 2006; 5:85-92.

-
33. Ruehm SG, Corot C, Vogt P, Kolb S, Debatin JF. Magnetic resonance imaging of atherosclerotic plaque with ultrasmall superparamagnetic particles of iron oxide in hyperlipidemic rabbits. *Circulation* 2001; 103:415-22.

ed like validated blood iron time also molecules agent
small potential sensitivity stages interventions anatomical
ques targeted arterial changes uspio chapter advanced
erotic particles micelles
wall return processes developed **Ti CO**
clinical imaging applied transverse Gd rupture
esse response
presence
oxide thesis
etect
nit levels target detection characterized field
odels nanoparticles pulse process
develop lesion early vascular cells tomography
injury use tissue E-selectin low



In press, ATVB, 2013. Modified from the submitted manuscript

Chapter 2

Molecular MRI of the vulnerable plaque Is it possible?

ABSTRACT

Recent advances in molecular resonance imaging of atherosclerosis make it possible to visualize atherosclerotic plaques *in vivo* using molecular targeted contrast agents. This offers unprecedented opportunities to use these imaging techniques to study atherosclerosis development and plaque vulnerability non-invasively to establish non-invasive tools for drug discovery. In this review paper, we discuss MRI contrast agents targeted towards the vulnerable plaque and illustrate how these new imaging platforms could assist in our understanding of atherosclerosis and aid in its treatment. In particular we highlight the challenges, including the limitations of the different contrast agent systems and the steps to be taken with the different compounds to allow them into clinical practice.

GLOSSARY OF TERMS

Term	Definition
<i>Atheroma:</i>	Accumulation of cells or cellular debris that contain lipids, calcium, and fibrous connective tissue between the endothelium lining and the smooth muscle cell-rich medial wall of arteries
<i>CLIO:</i>	Cross-linked Iron Oxide particle, iron-based T2 contrast agent with a hydrodynamic core of ~ 30 nm (see also iron oxide nanoparticle)
<i>Chelate:</i>	chemical that forms complex molecules with certain metal ions like Gd, thereby inactivating the ion so that they cannot normally react with other elements or ions converting them to a chemically inert form that can be excreted without further (toxic) interaction with the body.
<i>Fibrous cap:</i>	A layer of fibrous connective tissue in the intima
<i>Foam cells:</i>	Cells in an atheroma that consist of monocyte macrophages containing numerous lipid inclusions rich in cholesteryl esters
<i>Immunomicelle:</i>	micelle-based contrast agent coupled to an antibody (see also micelle)
<i>Intima:</i>	The innermost layer of a blood vessel
<i>Intimal thickening:</i>	Accumulation in the intima of smooth muscle cells and lipids within a matrix of proteoglycans
<i>Iron-oxide nanoparticle:</i>	A nanoparticle with a superparamagnetic iron oxide core, usually coated with dextrans (see also CLIO, MION, USPIO).
<i>Lipid-based nanoparticle:</i>	small contrast agents with a lipid layer like micelles and liposomes
<i>Liposome:</i>	A vesicle composed of a phospholipid bilayer. They may also contain mixed lipid chains with surfactant properties. Gd-chelates and targeting ligands can be incorporated in the lipid bilayer.

<i>Micelle:</i>	A spherical aggregation of a monolayer of surfactant or lipid molecules that can carry Gd-chelates and targeting ligands in the lipid layer, with a size of ~10-100 nm.
<i>MPIO:</i>	Micro Particles of Iron Oxide, T2* and T1 contrast agents with a size of ~ 1 μ m
<i>Nanoparticle:</i>	A microscopic particle having one or more dimensions of the order of 100nm or less
<i>Superparamagnetic iron oxide:</i>	microcrystalline magnetite particles with strong T2* and T1 relaxation (depending on size)
<i>Thin-cap fibroatheroma (TCFA):</i>	A thin fibrous cap infiltrated with macrophages and lymphocytes, rare smooth muscle cells, and an underlying lipid-rich necrotic core
<i>USPIO:</i>	Ultra Small Particles of Iron Oxide, superparamagnetic iron oxide particles with a hydrodynamic size of ~ 50nm. Strong T2*/T1 contrast
<i>Vulnerable plaque:</i>	A plaque with a thin fibrous cap that is prone to rupture and may cause thrombosis

INTRODUCTION

With the increased attention for preventive medicine combined with novel clinical intervention modalities, major advances have been made in the treatment of atherosclerosis¹. Yet, in the Western world atherosclerotic diseases, including acute coronary syndrome (ACS) and stroke, are responsible for nearly 50% of deaths and among the leading causes of morbidity².

One of the first known descriptions of atherosclerosis belongs to Leonardo da Vinci (1452-1519), who admirably described it as "debility through lack of blood and deficiency of the artery which nourishes the heart and other lower members". Today we know that atherosclerosis is an inflammatory disease of the arteries characterized by intimal thickening and plaque development. Although the pathology by itself is relatively benign, severe clinical complications such as angina pectoris, limb ischaemia, renal problems and hypertension are relatively common. However, the most severe complications arise from ruptured atherosclerotic plaques that can cause arterial thrombosis and precipitate acute vascular/ischemic events like myocardial infarction or ischemic stroke³. These rupture-prone plaques, also described as thin cap fibroatheromas (TCFA), are called vulnerable plaques, a term first instituted by Muller *et al*⁴.

Atherosclerotic plaque development

About 200 years ago, Joseph Hodgson already proposed that atherosclerosis is an inflammatory disease. Ultimately, it took till 1976 to revive this theory, due to the extensive studies and publications of Russel Ross (1929–1999) who introduced the "response-to-injury" concept^{5, 6}. Atherosclerotic plaques develop as a chronic inflammatory healing response, secondary to endothelial damage, as focal thickenings in lesion prone areas in the intima of large and medium-sized arteries (figure 1). Cardiovascular risk factors such as chronic smoking, hypertension and dislipidemia are risk factors for the development of dysfunctional endothelium, a crucial pathophysiological factor in the development of atherosclerosis^{7,8}.

Histopathologically, atherosclerosis is characterized by a progressive accumulation of lipoproteins, specific cell types (smooth muscle cells, monocytes, and T-lymphocytes) and deposition of extracellular matrix in the arterial wall. Subendothelial retention of lipoproteins and immune cells in the vessel wall comprises the first stage of atherosclerosis (figure 1B, 2A). As the lesion advances, upon ingestion of modified LDL, macrophages become foam cells and release inflammatory cytokines and proteases that induce fibrous cap thinning. Lipid-loaded foam cells eventually die, thereby leading to growth of the necrotic core (figure 2A). The progression of atherosclerosis from an initial fatty streak to the complex advanced lesion has been described using Stary's six-stage histological classification⁹. It is now widely established that inflammatory processes are involved in each step of the pathology.

In patients suffering from the consequences of the rupture of a previously vulnerable plaque, the necrotic lipid core is proportionally larger and eccentrically positioned in the plaque, covered by a thin fibrous cap and an increased level of intraplaque vasa vasorum angiogenesis is present³. A vulnerable plaque has specific morphological characteristics: a macrophage infiltrated thin fibrous cap, inflammatory cells, a large lipid (or necrotic) core and increased concentrations of oxidized LDL, a relatively low abundance of smooth muscle cells as well as a reduced amount of collagen. The technological development in the field of plaque imaging is making remarkable progress in the detection of different structures of the vulnerable plaques.

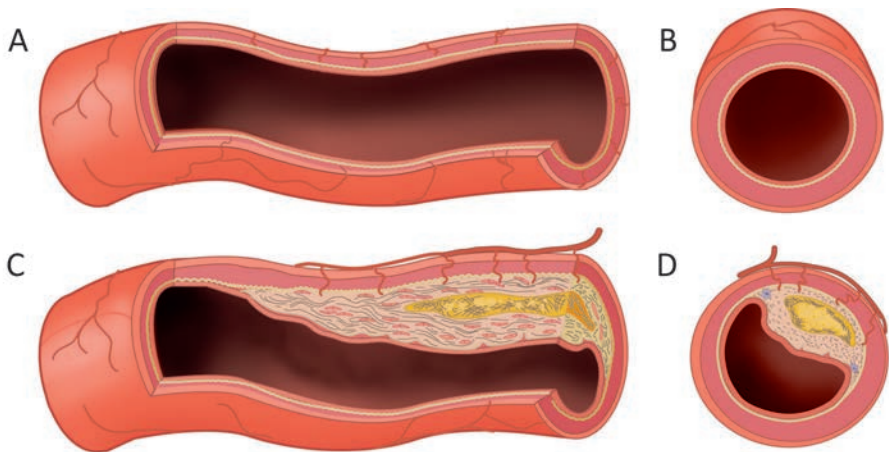


Figure 1 | Development of atherosclerosis. Atherosclerotic plaques develop as a chronic inflammatory healing response, secondary to endothelial damage. Panel A1 and A2 show a cross section of a normal muscular artery without atherosclerosis. The vessel lumen is covered by endothelial cells that rest upon a basement membrane. The vessel wall consists of 3 layers, the tunica intima, separated from the tunica media by the lamina elastica interna, and the tunica adventitia. The human intima generally consists of a layer of endothelial cells and smooth muscle cells scattered within the intimal extracellular matrix. The media consists of multiple layers of smooth muscle cells, embedded in an elastin as well as collagen-rich matrix. The adventitia, the outer layer of arteries, contains mast cells, nerve endings and microvessels. B. Endothelial dysfunction leads to fatty streak formation and thickening of the intima by recruitment of inflammatory cells and the accumulation of lipids. The initial steps of atherosclerosis include adhesion of leukocytes to activated endothelium, migration of the leukocytes into the intima, maturation of monocytes (the most numerous of the recruited leukocytes) into macrophages, and their uptake of lipids, leading to the formation of foam cells.

Plaque identification

It is increasingly recognized that the availability of noninvasive, reliable and sensitive atherosclerosis imaging techniques can be used to guide early interventional or medical therapies. In addition to that, the availability of these techniques combined with animal models of atherosclerosis provides unique opportunities for the investigation of molecular disease mechanisms, and *in vivo* monitoring of novel therapeutic approaches as well as disease progression.

Over the past decade, much effort has been put in the development of novel methods to identify vulnerable atherosclerotic plaques with different imaging techniques. If vulnerable plaques can be identified (which conventional cardiac catheterization is unable to), vulnerable plaques can be targeted for intervention (angioplasty, stent, or bypass surgery), while avoiding unnecessary treatment of the stable plaques.

Several invasive methods such as intravascular ultrasound, palpography and optical coherence tomography are currently clinically applied in patients. Because of their invasive nature these intravascular imaging modalities are not suited to screen patients with subclinical disease.

Noninvasive assessment of plaque vulnerability targets a different patient population, i.e. asymptomatic individuals who have not (yet) presented with an acute vascular event but are at risk to develop one. Relying on inflammation as a central pathogenic aspect of plaque vulnerability, circulating inflammatory biomarkers of vulnerable plaques have been identified. They provide valuable diagnostic and prognostic information¹⁰. However, they do not provide insight in the anatomic localization of individual vulnerable plaques. Thus, timely and anatomically precise imaging of vulnerable plaques is a medical need, since angiographic and pathological studies demonstrate that arteries frequently occlude acutely without preceding flow limiting stenosis^{11, 12}. These findings indeed stress that the biological characteristics of plaques rather than the degree of luminal narrowing determine the risk for clinical complications.

Traditionally the gold standard for the diagnosis and assessment of atherosclerosis severity has been X-ray angiography, which visualizes the reduction in arterial luminal diameter. However, it is increasingly recognized that significant atherosclerotic plaque can be present within the arterial wall long before the lumen is compromised^{13, 14}. Angiographic modalities, which give limited information about the vessel wall, cannot adequately delineate plaque composition and routinely underestimate atherosclerotic burden.

MRI has emerged as one of the rapidly evolving non-invasive imaging modalities of atherosclerotic disease due to its ability to assess the arterial lumen, plaque burden and plaque components in an accurate and non-invasive manner. Clinically these assessments are mainly used in the carotid arteries, but research continues to use similar MRI methods in other arteries, such as aortic, peripheral and coronary arteries. Several *in vitro* and *in vivo* studies have demonstrated the ability of MRI to differentiate the major components of atherosclerotic plaque without the use of contrast agents. In addition, MRI can accurately and reproducibly measure arterial wall dimensions. This has led to its use as the imaging efficacy end-point in therapeutic trials of plaque regression^{15, 16}.

Possibly the biggest breakthrough in the imaging field is the development of novel targeted contrast agents, thereby creating the novel field of molecular imaging. The use of molecular targeted contrast agents in combination with MRI has, albeit often still in a pre-clinical phase, already proven to be effective in detection of different stages of atherosclerosis.

In this article we review recent developments in molecular MRI concerning atherosclerosis, highlighting the detection of the vulnerable plaque as a key structure of plaque pathology, pre-view some of the new opportunities molecular MRI offers to atherosclerosis diagnosis and comment on the challenges faced by the field.

MOLECULAR MRI

High resolution MRI has emerged as the potential leading noninvasive *in vivo* imaging modality for atherosclerotic plaque characterization, in particular suitable to detect intraplaque hemorrhage, cholesterol deposits and the extend of the lipid core^{17, 18}. MRI differentiates plaque components on the basis of chemical composition, water content, physical state, and molecular motion or diffusion.

Molecular MRI offers the potential to image events at the cellular and subcellular level which has, depending on the target of choice, added value over traditional contrast agents. The introduction of targeted MR contrast agents has enabled the imaging of relatively sparsely expressed biological targets *in vivo*.

During the development of atherosclerotic plaques, many potential biomarkers, such as adhesion molecules [vascular cell adhesion molecules (VCAMs), intercellular adhesion molecules (ICAMs), selectins], macrophages and their scavenger receptors, matrix metalloproteinases (MMPs), oxidized low-density lipoprotein (oxLDL), $\alpha_v\beta_3$ integrin, extracellular matrix, and fibrin, are upregulated.

It is important to point out that these molecules are often not unique to atherosclerosis or cardiovascular diseases, but they are present at increased levels under these disease conditions as compared to disease free conditions. Moreover, these molecular targets are often present at relatively low levels (10^{-9} to 10^{-13} M/g tissue). To overcome sensitivity issues, high payload contrast agent vehicles have been developed for molecular MRI to generate sufficient signal change. Nanoparticle-facilitated imaging is at this point the most promising approach for molecular MR imaging purposes, since nanoparticles exhibit the possibility to include a high contrast agent payload, may be of relatively small size to facilitate penetration into tissue, and have a tunable circulation half-life, a large surface area available for conjugation of functional groups, and the potential to function as both imaging and therapeutic (i.e. 'theragnostic') agents.

The biological processes described above and their accompanying molecular and cellular events create numerous opportunities for targeting the atherosclerotic plaque using nanoparticles. Several novel nanoparticle platforms have emerged in molecular MRI that allow the visualization of vulnerable plaques. These will be highlighted here in the context of their relevance to plaque vulnerability.

INTRA-PLAQUE TARGETING

Lesional macrophages

A large body of evidence associates macrophages with the formation, progression, and pathogenicity of atherosclerosis. Monocytes from the peripheral circulation migrate into the plaque and differentiate there into macrophages, which in turn may engulf large quantities of low-density lipoprotein, to become resident foam cells^{19,20} (figure 2A and 2C). In mouse models it has been shown that in the absence of monocyte and macrophage migration into the vessel wall, atherosclerosis development is delayed, even in the presence of severe hyperlipidemia²¹. In man, high macrophage content in plaques is associated with vulnerability to rupture^{22, 23}. In acute coronary syndromes, the lipid core of the responsible lesions is rich in macrophage-derived foam cells and other inflammatory cells^{22, 23}. Different macrophage subsets, which differentially contribute to plaque infiltration and to atherosclerosis complications, have been identified. In the last years, it has become widely accepted that classically activated macrophages (or M1) and alternatively activated MØ (or M2) are two extremes (inflammatory versus remodelling) of a

spectrum of macrophage phenotypes that both contribute to plaque development progression and vulnerability²⁴.

M2 alternatively activated macrophages

Myeloid-related protein (Mrp)-8/14 is a member of the S100-family of Ca²⁺- modulated proteins with an important role for the Mrp complex in the inflammatory response to injury via the activation of innate immune pathways. Mrp8/14 is abundantly detected in human and mouse atherosclerotic plaques and localizes to rupture prone areas of plaque typified by large necrotic cores and high macrophage content²⁵. Indeed, a subset of macrophages (the alternatively activated M2 subset that is causally linked to plaque vulnerability) expressing dimerized Mrp have been demonstrated in human atherosclerosis and predominate in rupture-prone lesions compared to stable plaques²⁴.²⁶. Consistent with its extracellular abundance and signaling, levels of Mrp have been shown to be an independently prognostic marker of cardiovascular risk²⁷.

Recently Maiseyeu *et al.* developed a multivalent theragnostic (combination of therapeutical and diagnostical compound) nanoparticle composed of phosphatidyl-serine (PS), ω -carboxynonanoyl-cholesteryl ester and Gd lipids which were targeted to M2 macrophages using an anti-Mrp14 polyclonal antibody (IgG)²⁸. Proof of principle of the contrast agent both *in vitro* on cultured ApoE^{-/-} monocytes and *in vivo* in atherosclerotic mice showed enhanced binding potential to Mrp⁺ monocytes and endothelial cells. Although long term experiments to explore its preclinical therapeutic and diagnostic potential remains to be performed, this is the first time a contrast agent specifically targeting the vulnerable subset of macrophages has been successfully applied. Further optimization of the agent is required since the targeting vector (an IgG) may be immunogenic and the compound may target other sites than atherosclerotic plaques²⁹.

Lipoproteins

Lipoproteins are nanoparticles that are naturally present in most species, and in humans are essential to control lipid metabolism. These lipoproteins, including high-density lipoprotein (HDL) and LDL, interact with plaques through a natural conduit. Exploiting or mimicking this inherent plaque affinity of lipoproteins has been shown to be a powerful approach to target plaques. Oxidized low-density lipoprotein (oxLDL) plays a key role in the initiation, progression, and destabilization of atherosclerotic plaques and is present in macrophages and the lipid pool (figure 2C).

Targeting this oxidation epitope has been exploited with several compounds. Both Gd-based immunomicelles as well as lipid-coated iron oxide particles containing murine (malondialdehyde (MDA)-lysine MDA2 and E06) or human (IK17) antibodies that bind unique oxidation-specific epitopes (i.e. oxLDL), induced significant enhancement in MR images of the aorta wall of apoE^{-/-} mice³⁰⁻³². Similar MDA-targeted immunomicelles functionalized with manganese (Mn²⁺) chelates were recently developed in response to the finding that if Mn is delivered into a cell, interaction with intracellular components and metalloproteinase results in significant (>20-fold) increases in MR efficacy compared to the chelated form³³. *In vivo* plaque imaging findings with these Mn-based compounds were comparable with the previous results however background signal from the Mn-based contrast agent in blood was very low allowing a better plaque definition.

Lipoproteins themselves are ideal for the delivery of drug and imaging agents since they are able to circulate in the blood- stream for a significant amount of time, the hydrophobic core facilitates the incorporation of poorly soluble drugs or imaging agents, and they are highly amenable to bioconjugation.

The LDL particle itself naturally homes to a plaque after intravenous administration. LDL particles that are enriched with a hydrophobic contrast agent, manganese-mesoporphyrin, cause reduction

in T1 in foam cell pellets that were incubated with this agent³⁴. Despite the potential of these nanoparticles, extensive *in vivo* MRI of atherosclerotic plaque with these LDL nanoparticles has not (yet) been reported. Yamakoshi *et al.* recently reported the first successful *in vivo* application in both hypercholesterolemic ApoE^{-/-} and LDLR^{-/-} mice of a LDL particle functionalized with a GdDO3A-monoamide chelate³⁵.

Given the key role of LDL itself in plaque progression it is presently unclear whether an LDL based compound can be optimized for safe use in the clinic.

In contrast to the LDL, HDL forms smaller lipid nanoparticles (5–12 nm) stabilized by the interactions of surface apolipoprotein A-1 (ApoA-1). HDL nanoparticles have some advantages for atherosclerosis imaging: During reverse cholesterol transport, HDL binds to scavenger receptor B type I (SR-BI) and ATP-binding cassette transporters and thus “naturally” targets to macrophages expressing these receptors. High HDL cholesterol levels are associated with reduced atherosclerotic plaque burden and lipid content whereas LDL promotes the disease³⁶. Second, their small size (~10 nm) enables them to penetrate the vessel wall more easily than LDL. This led to the development of a vast array of HDL based contrast agents in the past decade.

The first MRI HDL particles that were synthesized contained Gd-chelating phospholipids in the lipid layer (rHDL)^{37, 38}. In hyperlipidemic apoE^{-/-} mice these paramagnetic rHDL nanoparticles showed enhanced accumulation in atherosclerotic plaques after intravenous administration.

The targeting of rHDL to macrophages may be further enhanced by the addition of P2fA2, a lipopeptide derived from the low density lipoprotein receptor (LDLR) binding domain of apoE, into the lipid layers³⁹. P2fA2-modified HDL resulted in a doubling of the enhancement ratio of the aortic vessel wall at 24 h postinjection, compared to the rHDL particle.

A clear increase in MR signal was also observed in the aortic wall of apoE^{-/-} mice *in vivo* 24 hours after injection of the paramagnetic Au HDL and QD-HDL, while a clear decrease of MR intensity in the aortic wall was observed using FeO-HDL particles⁴⁰.

Thus far the application potential of the HDL particles seems promising and due to its biological resemblance to autogenous HDL and the ease to produce the particle further development in the near future is likely to occur.

Scavenger Receptors

The macrophage scavenger receptor (SR) is a macrophage-specific cell-surface protein, and not expressed on cells in the normal vessel wall⁴¹. Both class A and B SR (SR-A and SR-B) are involved in the progression of atherosclerosis^{42, 43} (figure 1B and 2A), playing an important role in (oxidized) low-density lipoprotein uptake as well as in clearance of debris, including necrotic and apoptotic cell fragments⁴⁴. SR-A is a high-affinity receptor, in the picomolar to nanomolar range (depending on the ligand), and as macrophages are present through all stages of atherosclerosis, the scavenger receptor forms an excellent target for molecular imaging⁴⁵. Both SR-A and SR-B are instrumental in the development of atherosclerosis and collectively are responsible for binding and uptake of 75 to 90% of modified LDL uptake by macrophages⁴⁶.

Amirbekian *et al.* developed ~110 nm large immunomicelles containing Gd targeted to SR-A (CD204) via the conjugation of a monoclonal antibody⁴⁷. These micelles showed improved *in vivo* detection of murine atherosclerosis with a high correlation between the signal intensity on MRI and the number of macrophages in the region of interest⁴⁸.

Gd-loaded lipid-based nanoparticles targeting CD36, a class B scavenger receptor (SR-B), showed significant uptake by human macrophages *in vitro*, improved signal intensity of *ex vivo* aortic atherosclerotic plaque, and were shown to bind to resident macrophages in atherosclerotic

plaque using confocal microscopy⁴⁹. The CD36 labeled particles created the largest signal intensity in regions of fibrous plaque at the periphery of lipid-rich plaque. These data suggest that lipid based nanoparticles targeting CD36 may improve detection and characterization of atherosclerotic plaque and determine the degree of plaque inflammation by assessing macrophage density.

Both contrast agents were successful in the visualization of macrophages. Conjugation with a full antibody will however hamper repeated application of the agent due to an immune response. Another limitation in the use of particles targeting the scavenger receptors may be the fact that intravenous administration of this imaging agent will suffer from first pass retention in the liver due to binding to scavenger receptors expressed on the surface of Kupffer cells. For clinical application of the agent for vulnerable plaque detection these hurdles will need to be taken.

ENZYME ACTIVITY

MMPs

MMPs are a large family of zinc-dependent endopeptidases that selectively digest matrix and other key proteins during reorganization of vascular matrix scaffold, thereby facilitating cell migration. With the progression of atherosclerosis, oxidized LDL increases MMP-1 and -3 expression⁵⁰. In addition to their inherent catalytic effect, constitutive MMP expression in VSMCs is induced by inflammatory cytokines, and their expression leads to migration and phenotypic modulation of macrophages⁵⁰.

Previous histological studies demonstrated strong expression of MMPs and *in situ* matrix-degrading gelatinolytic activity in the fibrous cap of human atherosclerotic plaques⁵¹, as well as in atherosclerotic lesions that were induced in experimental models⁵². Presence of MMP-1, -3, and -9 has been observed in macrophages, VSMC, lymphocytes, and endothelial cells especially at the vulnerable shoulder region of plaques⁵¹. Recent work has demonstrated that overexpression of MMPs led to cardinal features of plaque rupture in a mouse model of atherosclerosis⁵³. Therefore, MMPs play a key role in the pathological remodeling cascade associated with the natural history of the atherosclerotic plaques, from the initial formation of lesions and outward arterial remodeling to the thinning and weakening of the extra-cellular matrix scaffold forming the fibrous cap favoring plaque instability and rupture⁵⁴.

Protease imaging has used two generic approaches: a) targeting labeled small molecules to specific protein pockets, typically the active site^{55, 56} and b) the use of 'smart' MRI probes that are bound to a synthetic graft copolymer consisting of a cleavable backbone, which become activated and detectable upon cleavage⁵⁷⁻⁵⁹.

MMP binding contrast agents

An Example of the first approach is the broad-spectrum MMP inhibiting peptide, P947, with an attached Gd-DOTA chelate (Guerbet, France) that has been developed to visualize vulnerable plaques. P947 accumulates in MMP-rich atherosclerotic plaques of ApoE^{-/-} mice^{56, 60}. Variations in MMP-related enzymatic activity in atherosclerotic plaques of rabbits subjected to dietary changes were detected *ex vivo*. Translation of this imaging technology to the clinical field could give deeper insights into the role of MMPs in arterial wall remodeling *in vivo* and a clinical modality to image and monitor markers previously associated with plaque progression and instability⁶¹.

Cleavable MMP substrates

Successful attempts of the second approach at *in vivo* MRI of matrix metalloproteinase (MMP) activity have been based on the use of MMP substrates conjugated to Gd-DOTA, with a N-terminal hydrophobic chain and a C-terminal PEG chain⁶². MMP cleaves the hydrophilic PEG from Gd-DOTA, thereby decreasing the water solubility of the remaining Gd-DOTA fragment. This approach gives a small but significant increase (approximately 0.015 s^{-1}) in proton relaxation rate due to MMP-2 activity⁵⁷ allowing *in vivo* detection of MMP-2 activity in a mouse model of mammary carcinoma. This specific probe has thus far not been applied in atherosclerosis, and though conceptually very interesting, the sensitivity of such approaches is a major issue for the *in vivo* translation of this approach.

Another MRI-dedicated MMP-2/MMP-9-sensitive probe in development uses nanoparticles loaded with gadolinium. Upon proteolysis, the nanoparticles exhibit highly cationic molecules that trigger attachment and uptake into cells^{58, 59}. Initial reports indicate a potential use for cancer targeting *in vivo*, but no study has yet assessed the utility of such agents in CVD.

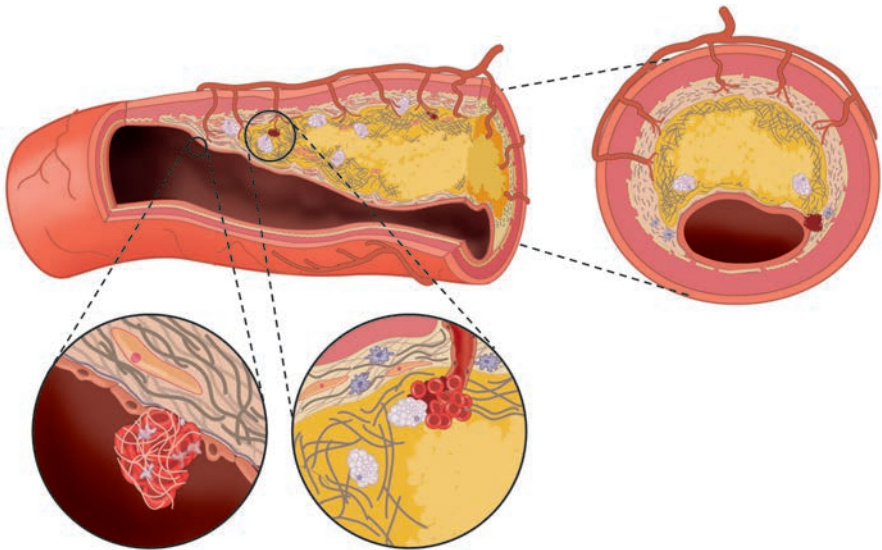


Figure 2 | Atherosclerotic plaque progression. In panel A the different steps in lesion progression are depicted. Lesion progression involves the migration of SMCs from the media to the intima, the proliferation of resident intimal SMCs and media-derived SMCs, and the increased synthesis of extracellular matrix molecules such like collagen and elastin. Plaque macrophages and SMCs can die in advancing lesions leading to the accumulation of their lipids and formation of a necrotic core in the central region of a plaque, as visualized in panel A and B2. Advancing plaques also contain cholesterol crystals and microvessels. Thrombosis, the ultimate complication of atherosclerosis, often complicates a physical disruption of the atherosclerotic plaque. In panel B1 a thrombus in the vessel lumen is depicted. In panel B2 intraplaque hemorrhage is shown, this usually occurs in the shoulder region of a plaque and is an indicator of progression towards an unstable plaque phenotype. When a plaque ruptures, blood coming in contact with the tissue factor in the plaque coagulates. Platelets activated by thrombin generated from the coagulation cascade and by contact with the intimal compartment instigate thrombus formation. Several contrast agents have been developed targeting factors in the coagulation cascade.

Myeloperoxidase

Myeloperoxidase (MPO) is involved in free radical generation with a central role in atherosclerotic plaque instability. Although generally abundant in granulocytes, MPO within atheromata originates mainly from macrophages and foam cells. MPO catalyzes chloride oxidation to hypochlorous acid (HOCl) and generates other highly reactive moieties such as chlorine, tyrosyl radicals, and aldehydes. These contribute to the microbicidal and viricidal properties of phagocytes as part of its function in innate host defense mechanisms⁶³. The reactive species formed, however, are cytotoxic and may damage normal tissues, contributing to the inflammatory injury. MPO-generated oxidants participate in multiple processes relevant to cardiovascular disease development and outcomes, including induction of foam cell formation, endothelial dysfunction, development of vulnerable plaque, and ventricular remodeling following acute myocardial infarction (reviewed in^{64, 65}).

The peptide serotonin (hydroxytryptamine), when oxidized by MPO, tends to aggregate into dimers and oligomers. This principle was used for a gadolinium-serotonin chelate, capable of sensing myeloperoxidase activity *in vivo*⁶⁶. Once the serotonin moiety in the chelate is activated by myeloperoxidase, the probe assembles into dimers, trimers and even pentamers that tend to be retained locally. This polymerization decreases the tumbling rate of Gd giving the imaging agent a significantly higher longitudinal relaxivity than the parent compound^{66, 67}. The presence of MPO has been successfully imaged *in vivo* with this probe, both in a mouse model of myositis and in a model of myocardial infarction^{67, 68} serving as a surrogate of the inflammatory response and thereby prognosis. Imaging in the context of a vulnerable atherosclerotic plaque has not been reported thus far.

LUMINAL TARGETS FOR MOLECULAR IMAGING

Thrombosis

The event of plaque rupture from a previously vulnerable plaque resulting in thrombosis plays a central role in myocardial infarction, stroke, atrial fibrillation and venous thromboembolism. Moreover, intraplaque and endothelial fibrin has recently been recognized to play an important role in the progression of atherosclerosis (figure 2A2 and 2B). A recent study showed that the leakage of fragile neovessels formed during plaque development might represent a route for fibrin to enter atherosclerotic plaque prior to rupture⁶⁹. Tavora *et al.* hypothesised that the extravasation of fibrin from newly formed blood vessels may be the defining trigger for the formation of a necrotic core and thus for the transition between early and late stage plaques⁶⁹. Fibrin is suggested to be a novel biomarker for the intraplaque necrotic core and the differentiation between pre-atheroma from atheroma.

Extensive experience with *in vivo* MRI of thrombosis has been obtained with EP2104R, currently named FTCA (Epix Pharmaceuticals, Lexington, USA), a small Gd-chelate targeted to fibrin⁷⁰. Studies with EP2104R in rabbits and swine reported the ability of the agent to detect acute and chronic arterial and venous thrombi^{71, 72}. The contrast agent was effectively applied to detect thrombi in vessels and heart chambers in 52 patients with suspected thrombosis in a phase II clinical trial, underlining its translational potential⁷³.

Recently the feasibility of intraplaque and endothelial fibrin detection using the fibrin-targeted contrast-agent was assessed *in vivo* in ApoE^{-/-} mice. The atherosclerotic plaques investigated were not associated with luminal thrombi in contrast to previous studies^{22, 74}. FTCA was selectively visualized at the location of atherosclerotic plaque in these mice, while surrounding blood and

soft tissue signal remained suppressed. Late stage atherosclerotic plaque showed the strongest signal enhancement after FTCA administration. These findings suggest that the contrast agent may not only be useful to detect thrombi but also plaques at risk, which in itself may be a contradictory imaging endpoint but represents in both cases plaques at risk of further clinical events. In 2009, EPIX Pharmaceuticals entered into an Assignment for the Benefit of Creditors. To the authors best knowledge the development and clinical trials of FTCA did not proceed thereafter.

Another fibrin-targeted contrast agent, a much larger Gd-bis-oleate nanoparticle, with a higher relaxivity, has also been shown to effectively detect thrombi *in vitro* and in an animal model, but this particle has not yet been investigated in mouse models of human atherosclerosis or patients^{75, 76}. Owing to its size, this contrast agent will be mainly suitable for the detection of luminal fibrin clots and less for the detection of intraplaque fibrin and thus for plaques at risk.

VASCULAR TARGETING: CELLULAR ADHESION MOLECULES

Dysfunctional endothelium is a crucial pathophysiological factor in atherosclerosis, causing increased permeation of macromolecules such as lipoproteins, increased expression of chemotactic molecules (for example, monocyte chemotactic protein 1) and adhesion molecules (for example, intercellular adhesion molecule 1 (ICAM-1) and vascular cell adhesion molecule 1 (VCAM-1), as well as E-selectin and P-selectin), and enhanced recruitment and accumulation of monocytes⁷.

VCAM-1 (CD106)

VCAM-1 is an appealing target as it is differentially upregulated on the endothelium related to atherosclerotic plaque and lesion prone areas of the artery⁷⁷ (figure 1B). McAteer *et al.* have recently reported a microparticle iron oxide (MPIOs) approach to VCAM-1 imaging that provides quantifiable contrast in mouse vascular inflammation^{78, 79}. Due to their size and incompressible nature, MPIO are less susceptible to nonspecific vascular egress or uptake by endothelial cells. Therefore, MPIO may be useful contrast agents for detection of strictly endovascular molecular targets by MRI.

Nahrendorf *et al.* functionalized monocrystalline iron oxide nanoparticles with vascular cell adhesion molecule-1 (VCAM-1) targeting peptides^{80, 81}. *In vivo* MR imaging revealed that the aortic root of apoE^{-/-} mice became hypointense (dark) after injection of this contrast agent, which was confirmed through fluorescence imaging both *ex vivo* and *in vitro* in macrophages that over-expressed VCAM-1.

Burtea *et al.* recently developed much smaller Gd-DOTA as well as Ultra Small Particle of Iron Oxide (USPIO) based VCAM-1 targeted compounds^{82, 83}. The Gd-based compound has shown preliminary potential in the ability to image atherosclerotic plaques in hypercholesterolemic ApoE^{-/-} mice. The strength of this approach relies in the ability of the smaller particles to penetrate into the plaque and thereby potentially target the plaque macrophage population that expresses VCAM-1. On the other hand, the Gd payload may be too low for detection of smaller plaques.

Integrin alpha_v-beta₃

Integrins are a family of heterodimeric cell surface glycoprotein adhesion molecules, that mediate cell-extracellular matrix and cell-cell interactions, and are involved in cell adhesion, proliferation, migration, differentiation, and finally serve as potential targets for imaging of vascular remodeling.

The $\alpha_v\beta_3$ integrin is among others expressed by endothelial cells (ECs), VSMCs⁸⁴, platelets, growth factor-stimulated monocytes and T lymphocytes (figure 2A)^{85, 86}. Human atherosclerotic lesions show extensive expression of $\alpha_v\beta_3$ ⁸⁷, which functions in thrombus formation⁸⁸, smooth muscle cell migration⁸⁹, (adventitial) neovascularization^{32, 33}, as well as many other processes. Although $\alpha_v\beta_3$ is expressed on a variety of cells, its expression seems to be predominant in smooth muscle cells and endothelial cells^{87, 90}. Macrophages also express $\alpha_v\beta_3$ during foam cell formation⁹¹. Most interesting is that $\alpha_v\beta_3$ expression is an early event in plaque formation^{92, 93} and is also correlated to plaque instability^{94, 95}.

The Wickline group from Washington systematically developed several integrin targeting imaging compounds over the past decade; Lanza *et al* have developed a nanoparticle with a perfluorocarbon core covered with a monolayer of lipids including paramagnetic lipids (Gd-DTPA-bis-oleate)⁹⁶. The perfluorocarbon nanoparticles targeted to the $\alpha_v\beta_3$ -integrin to detect angiogenesis in a rabbit model of atherosclerosis⁹⁷. For imaging of plaque-associated angiogenesis, Winter *et al.* have successfully developed a relatively large (273 nm) paramagnetic nanoparticle contrast agent targeted specifically to $\alpha_v\beta_3$ integrins using a Arg-Gly-Asp mimetic (RGD)⁹⁷. Although very efficient from the relaxometric point of view, this agent has the drawback of its large size that limits not only blood clearance, but also its diffusion into the targeted tissue. Based on the perfluorocarbon particles, this group not only used proton relaxation, but also direct detection of the 19F MRI signal to specifically image the contrast agent *in vivo*^{98, 99}.

A smaller, low molecular weight non-peptidic RGD mimetic covalently attached to a Gd-DTPA chelate was developed for the imaging of plaque-associated angiogenesis^{100, 101}. This contrast agent was able to penetrate the atherosclerotic plaque, allowing visualization of neovascularisation. Specificity for angiogenic vessels may be decreased, however, when diffusible rather than pure intravascular imaging probes are used because inflammatory cells and fibroblasts can express many of these integrins.

One of the major drawbacks of the previously mentioned approaches is the use of RGD-like peptides to target $\alpha_v\beta_3$ integrins. RGD-peptides are used as an imaging biomarker for both diagnosis of atherosclerosis and monitoring therapies targeting the $\alpha_v\beta_3$ integrin as well as for the development of potentially anti-angiogenic therapies in general. It has been known for a long time that RGD-peptides and small ligands can bind integrins that are not fully activated, whereas larger ligands such as fibrinogen and fibronectin cannot. More importantly, RGD is not only a potent ligand for $\alpha_v\beta_3$. All five α_v integrins, two β_1 integrins (α_5 , α_8) and $\alpha_{11b}\beta_3$ share the ability to recognise ligands containing an RGD tripeptide active site^{102, 103}. Binding specificity of RGD-nanoparticles is thus not limited to endothelial cells yet also to several (circulating) immune cells and fibroblasts.

Imaging biomarkers as widely expressed as $\alpha_v\beta_3$ integrin without plaque stage specificity need to be extensively evaluated, in particular for late-stage clinical studies, to determine whether they have any clinical relevance as read-out of therapeutic efficacy¹⁰⁴.

Anti-angiogenic therapies are postulated to provide a powerful treatment option for atherosclerotic because plaques contain angiogenic microvessels that probably play an important role in plaque development. Recently, Winter *et al* presented positive results on a theragnostic approach of MR molecular imaging and drug targeting in a rabbit model of atherosclerosis by loading fumagillin, a water-insoluble angiostatic drug, in $\alpha_v\beta_3$ -integrin-targeted liposomes¹⁰⁵. One week after the first treatment of atherosclerotic rabbits, smaller plaques were observed in the aortic wall of the rabbits treated with $\alpha_v\beta_3$ -integrin-targeted fumagillin loaded particles, which was not the case for targeted liposomes without fumagillin¹⁰⁵. In a subsequent report on these $\alpha_v\beta_3$ -targeted fumagillin

liposomes the anti-angiogenic effects appeared acute, but the effect can be prolonged when combined with atorvastatin¹⁰⁶.

Selectins

Selectins are a group of pro-inflammatory endothelial cell adhesion molecules. They mediate the first step in leucocyte adhesion, characterized by rolling and tethering of these cells to the endothelial surface (and to platelets and other leukocytes). When endothelial cells are activated during inflammation or ischemia-reperfusion damage (figure 1B), P-selectin is translocated to the endothelial cell surface^{107,108}. E-selectin expression in contrast, is linked to the attraction of Ly6C⁺ cells and as a consequence is linked to plaque vulnerability^{109,110}. The latter recent finding makes E-selectin in particular an attractive imaging target for vulnerable plaque detection as they are easily approachable in the vessel.

Kang *et al.* have functionalized cross-linked iron oxide (CLIO) nanoparticles with anti human E-selectin antibody fragments¹¹¹. A three times larger CLIO-induced MR signal decrease on T2*-weighted images was observed in human umbilical vein endothelial cells implanted into mice in response to interleukin-1 β (a cytokine that induces E-selectin expression) treatment compared to untreated controls¹¹¹.

Boutry *et al.* targeted E-selectin with a synthetic mimetic of sialyl Lewis(x) (sLe(x)), a natural ligand of E-selectin expressed on leukocytes, on the dextran coating of ultrasmall particles of iron oxide (USPIO)¹¹². *In vitro* results on endothelial cells showed a high binding affinity. *In vivo* experiments have thus far only been performed in a concavalinA-induced hepatitis model and application for the detection of atherosclerotic plaques remains to be proven.

Theoretically, the specificity of plaque targeting could be improved by using different ligands for two independent targets on the same particle. Such a dual targeted strategy has been used to image endothelial adhesion molecules in apoE^{-/-} mice, where microparticles of iron oxide were conjugated with monoclonal antibodies against VCAM-1 (VCAM-MPIO) and/or P-selectin (P-selectin-MPIO)⁷⁹. Using *ex vivo* MR imaging, dual targeted particles indeed showed higher affinity to the endothelium under flow conditions in comparison to single targeted ones, but no *in vivo* studies have been published yet.

Technical challenges

In this review, we have highlighted several contrast agent platforms for molecular imaging of atherosclerosis and in particular the vulnerable plaque. Each contrast agent and target has its own advantages and disadvantages in terms of ease of synthesis, toxicity, payload, and biodistribution. Among the nanoparticle platforms discussed, lipid-based systems, such as micelles, liposomes, and HDL, are relatively easy to synthesize. Iron oxide nanoparticles that are more complex to prepare, are on the other hand of interest since they can be degraded by the liver and therefore have low toxicity and exhibit good biocompatibility¹¹³. Gd chelates are attractive since the untargeted variants are the only clinically approved contrast agents to date.

However, the sensitivity of these small chelates is up to a factor of 10⁴ lower than that of the larger nanoparticles because the latter particles in general have a higher contrast payload. Small particles, however, can penetrate deeper into tissue, which offers advantages for targeting extravascular biomarkers in cardiovascular diseases¹¹⁴. Molecular imaging of cardiovascular disease faces several challenges as compared to other pathologies, such as cancer. First, as atherosclerosis is a systemic disease it requires investigators to focus on different anatomical structures, including the carotids, the aortic root and arch, the abdominal aorta, the renal arteries, the aortic bifurcation and femoral arteries. Moreover, movement, flow effects, the

beating of the heart, as well as the small size of vessels hamper molecular imaging sensitivity. Therefore, nanoparticles used for cardiovascular imaging usually need to be specifically designed to allow their detection with superb sensitivity and should strongly and very specifically bind to the targeted biomarker to enable sufficient accumulation of the contrast-generating material. Furthermore for these diagnostic compounds to reach clinical application contrast agents need to fulfill multiple requirements including favorable toxicity profile and elimination kinetics.

PLAQUE VULNERABILITY

The present review deals with the interplay between the complex vascular biology involved in plaque vulnerability and the potential use of MR contrast agents in this interplay. The identification of suitable target-ligand combinations specific for a vulnerable plaque (or other pathology) is a complex process. Molecular imaging requires the identification of a disease-specific target with high expression levels, and a targeting ligand with favorable binding characteristics (IC_{50} , K_d) for the target. Moreover the aspecific binding should be as low as possible, and the binding of the contrast agents should generate a robust contrast change.

Plaque rupture is a major cause of atherothrombosis; unfortunately there is no animal model for plaque rupture with consequences such as sudden death, brain or myocardial infarction and therefore the development validation pipeline for these contrast agents for the detection of vulnerable plaques is complex.

At this point multiple MRI contrast agents have been developed that allow the detection of different markers and stages in atherosclerosis. Of all the suggested markers for vulnerability, three appear to give robust pre-clinical results that should translate to the clinic. Firstly, fibrin-targeted compounds that detect thrombi provide the closest link to actual vulnerable plaques. Secondly, plaque neovascularization has shown robust results in a range of animal models. Biologically, neovascularization is not an atherosclerosis specific marker yet a robust indicator of plaque progression and vulnerability. Thirdly, VCAM-1 and ICAM-1 seem promising for early detection of endothelial activation.

As for the contrast moiety, the biodistribution of the particles will play a decisive role in ultimate translation to the clinic. Many of the nanoparticle approaches will probably not lead to clinical translation, as the kinetics of these particles are slow (in the order of hours to days), and therefore not optimal for an efficient clinical workflow. Exceptions are the small Gd-chelates and MIONS, which are cleared rapidly, and have optimal imaging time points within 1-2 hours from injection.

Apart from clinical sensitivity and practicality, the use of targeted contrast agents naturally requires an excellent safety profile: toxicity issues of many particles regarding liver uptake and Gd complex stability will have to be determined and resolved. Translation of these particles to the clinic will largely depend on the interest of imaging and nanotechnology companies to invest in the long process of FDA approval. Up to now, not a single targeted compound has successfully passed the entire approval trajectory, and future research into targeted agents will need to address the requirements for ultimate FDA approval from the very first design.

Despite these hurdles, molecular imaging of the vulnerable plaque may provide more insights in the (temporal) pathophysiological mechanisms of atherosclerosis, aiding in drug selection and monitor treatment effects. The successful implementation of molecular imaging in the clinic to detect subclinical atherosclerotic disease and to identify vulnerable plaques may profoundly impact the management of patients with atherosclerosis.

Acknowledgments Ron Slagter is thanked for the preparation of the figures. This work was supported by the European Network of Excellence Diagnostic Molecular Imaging (DIMI, LSHB-CT-2005-512146) to BdA and REP, the Netherlands Heart Foundation (NHS, 2006T106) to BdA and REP, NOW Athena (700.58.80) to LvdW.

REFERENCES

1. Ford ES, Ajani UA, Croft JB, et al. Explaining the decrease in U.S. deaths from coronary disease, 1980-2000. *N Engl J Med* 2007; 356:2388-98.
2. Roger VL, Go AS, Lloyd-Jones DM, et al. Heart disease and stroke statistics--2011 update: a report from the American Heart Association. *Circulation* 2011; 123:e18-e209.
3. Naghavi M, Libby P, Falk E, et al. From vulnerable plaque to vulnerable patient: a call for new definitions and risk assessment strategies: Part I. *Circulation* 2003; 108:1664-72.
4. Muller JE, Abela GS, Nesto RW, Tofler GH. Triggers, acute risk factors and vulnerable plaques: the lexicon of a new frontier. *J Am Coll Cardiol* 1994; 23:809-13.
5. Ross R, Glomset JA. The pathogenesis of atherosclerosis (first of two parts). *N Engl J Med* 1976; 295:369-77.
6. Ross R, Glomset JA. The pathogenesis of atherosclerosis (second of two parts). *N Engl J Med* 1976; 295:420-5.
7. Chiu JJ, Chien S. Effects of disturbed flow on vascular endothelium: pathophysiological basis and clinical perspectives. *Physiol Rev* 2011; 91:327-87.
8. Falk E. Pathogenesis of atherosclerosis. *J Am Coll Cardiol* 2006; 47:C7-12.
9. Stary HC, Chandler AB, Dinsmore RE, et al. A definition of advanced types of atherosclerotic lesions and a histological classification of atherosclerosis. A report from the Committee on Vascular Lesions of the Council on Arteriosclerosis, American Heart Association. *Circulation* 1995; 92:1355-74.
10. Zethelius B, Berglund L, Sundstrom J, et al. Use of multiple biomarkers to improve the prediction of death from cardiovascular causes. *N Engl J Med* 2008; 358:2107-16.
11. Falk E, Shah PK, Fuster V. Coronary plaque disruption. *Circulation* 1995; 92:657-71.
12. Little WC, Constantinescu M, Applegate RJ, et al. Can coronary angiography predict the site of a subsequent myocardial infarction in patients with mild-to-moderate coronary artery disease? *Circulation* 1988; 78:1157-66.
13. Glagov S, Weisenberg E, Zarins CK, Stankunavicius R, Koletlis GJ. Compensatory enlargement of human atherosclerotic coronary arteries. *N Engl J Med* 1987; 316:1371-5.
14. Virmani R, Kolodgie FD, Burke AP, Farb A, Schwartz SM. Lessons from sudden coronary death: a comprehensive morphological classification scheme for atherosclerotic lesions. *Arterioscler Thromb Vasc Biol* 2000; 20:1262-75.
15. Corti R, Fuster V, Fayad ZA, et al. Lipid lowering by simvastatin induces regression of human atherosclerotic lesions: two years' follow-up by high-resolution noninvasive magnetic resonance imaging. *Circulation* 2002; 106:2884-7.
16. Helft G, Worthley SG, Fuster V, et al. Progression and regression of atherosclerotic lesions: monitoring with serial noninvasive magnetic resonance imaging. *Circulation* 2002; 105:993-8.
17. Pasterkamp G, van der Steen AF. Intraplaque hemorrhage: an imaging marker for atherosclerotic plaque destabilization? *Arterioscler Thromb Vasc Biol* 2012; 32:167-8.
18. Choudhury RP, Fuster V, Badimon JJ, Fisher EA, Fayad ZA. MRI and characterization of atherosclerotic plaque: emerging applications and molecular imaging. *Arterioscler Thromb Vasc Biol* 2002; 22:1065-74.
19. Choudhury RP, Lee JM, Greaves DR. Mechanisms of disease: macrophage-derived foam cells emerging as therapeutic targets in atherosclerosis. *Nat Clin Pract Cardiovasc Med* 2005; 2:309-15.
20. Hansson GK. Inflammation, atherosclerosis, and coronary artery disease. *N Engl J Med* 2005; 352:1685-95.
21. Smith JD, Trojan E, Ginsberg M, Grigaux C, Tian J, Miyata M. Decreased atherosclerosis in mice deficient in both macrophage colony-stimulating factor (op) and apolipoprotein E. *Proc Natl Acad Sci U S A* 1995; 92:8264-8.
22. Kolodgie FD, Gold HK, Burke AP, et al. Intraplaque hemorrhage and progression of coronary atheroma. *N Engl J Med* 2003; 349:2316-25.
23. MacNeill BD, Jang IK, Bouma BE, et al. Focal and multi-focal plaque macrophage distributions in patients with acute and stable presentations of coronary artery disease. *J Am Coll Cardiol* 2004; 44:972-9.
24. Tabas I. Macrophage death and defective inflammation resolution in atherosclerosis. *Nat Rev Immunol* 2010; 10:36-46.
25. Croce K, Gao H, Wang Y, et al. Myeloid-related protein-8/14 is critical for the biological response to vascular injury. *Circulation* 2009; 120:427-36.
26. Ionita MG, Vink A, Dijke IE, et al. High levels of myeloid-related protein 14 in human atherosclerotic plaques correlate with the characteristics of rupture-prone lesions. *Arterioscler Thromb Vasc Biol* 2009; 29:1220-7.
27. Morrow DA, Wang Y, Croce K, et al. Myeloid-related protein 8/14 and the risk of cardiovascular death or myocardial infarction after an acute coronary syndrome in the Pravastatin or Atorvastatin Evaluation and Infection Therapy: Thrombolysis in Myocardial Infarction (PROVE IT-TIMI 22) trial. *Am Heart J* 2008; 155:49-55.
28. Maiseyeu A, Badgeley MA, Kampfrath T, et al. In Vivo Targeting of Inflammation-Associated Myeloid-Related Protein 8/14 Via Gadolinium Immunonanoparticles. *Arterioscler Thromb Vasc Biol* 2012.
29. Gauden AJ, Phal PM, Drummond KJ. MRI safety: nephrogenic systemic fibrosis and other risks. *J Clin Neurosci* 2010; 17:1097-104.
30. Briley-Saebo KC, Shaw PX, Mulder WJ, et al. Targeted molecular probes for imaging atherosclerotic lesions with magnetic resonance using antibodies that recognize oxidation-specific epitopes. *Circulation* 2008; 117:3206-15.

31. Briley-Saebo KC, Cho YS, Tsimikas S. Imaging of Oxidation-Specific Epitopes in Atherosclerosis and Macrophage-Rich Vulnerable Plaques. *Curr Cardiovasc Imaging Rep* 2011; 4:4-16.
32. Briley-Saebo KC, Cho YS, Shaw PX, et al. Targeted iron oxide particles for in vivo magnetic resonance detection of atherosclerotic lesions with antibodies directed to oxidation-specific epitopes. *J Am Coll Cardiol* 2011; 57:337-47.
33. Briley-Saebo KC, Nguyen TH, Saeboe AM, et al. In vivo detection of oxidation-specific epitopes in atherosclerotic lesions using biocompatible manganese molecular magnetic imaging probes. *J Am Coll Cardiol* 2012; 59:616-26.
34. Mitsumori LM, Ricks JL, Rosenfeld ME, Schmiel UP, Yuan C. Development of a lipoprotein based molecular imaging MR contrast agent for the noninvasive detection of early atherosclerotic disease. *Int J Cardiovasc Imaging* 2004; 20:561-7.
35. Yamakoshi Y, Qiao H, Lowell AN, et al. LDL-based nanoparticles for contrast enhanced MRI of athero plaques in mouse models. *Chem Commun (Camb)* 2011; 47:8835-7.
36. Phan BA, Chu B, Polissar N, Hatsukami TS, Yuan C, Zhao XQ. Association of high-density lipoprotein levels and carotid atherosclerotic plaque characteristics by magnetic resonance imaging. *Int J Cardiovasc Imaging* 2007; 23:337-42.
37. Frias JC, Williams KJ, Fisher EA, Fayad ZA. Recombinant HDL-like nanoparticles: a specific contrast agent for MRI of atherosclerotic plaques. *J Am Chem Soc* 2004; 126:16316-7.
38. Frias JC, Ma Y, Williams KJ, Fayad ZA, Fisher EA. Properties of a versatile nanoparticle platform contrast agent to image and characterize atherosclerotic plaques by magnetic resonance imaging. *Nano Lett* 2006; 6:2220-4.
39. Chen W, Vucic E, Leupold E, et al. Incorporation of an apoE-derived lipopeptide in high-density lipoprotein MRI contrast agents for enhanced imaging of macrophages in atherosclerosis. *Contrast Media Mol Imaging* 2008; 3:233-42.
40. Cormode DP, Skajaa T, van Schooneveld MM, et al. Nanocrystal core high-density lipoproteins: a multimodality contrast agent platform. *Nano Lett* 2008; 8:3715-23.
41. De Winther MP, Van Dijk KW, Havekes LM, Hofker MH. Macrophage scavenger receptor class A: A multifunctional receptor in atherosclerosis. *Arterioscler Thromb Vasc Biol* 2000; 20:290-7.
42. Babaev VR, Gleaves LA, Carter KJ, et al. Reduced atherosclerotic lesions in mice deficient for total or macrophage-specific expression of scavenger receptor-A. *Arterioscler Thromb Vasc Biol* 2000; 20:2593-9.
43. Sakaguchi H, Takeya M, Suzuki H, et al. Role of macrophage scavenger receptors in diet-induced atherosclerosis in mice. *Lab Invest* 1998; 78:423-34.
44. Peiser L, Mukhopadhyay S, Gordon S. Scavenger receptors in innate immunity. *Curr Opin Immunol* 2002; 14:123-8.
45. Gough PJ, Greaves DR, Suzuki H, et al. Analysis of macrophage scavenger receptor (SR-A) expression in human aortic atherosclerotic lesions. *Arterioscler Thromb Vasc Biol* 1999; 19:461-71.
46. Kunjathoor VV, Febbraio M, Podrez EA, et al. Scavenger receptors class A-I/II and CD36 are the principal receptors responsible for the uptake of modified low density lipoprotein leading to lipid loading in macrophages. *J Biol Chem* 2002; 277:49982-8.
47. Lipinski MJ, Amirbekian V, Frias JC, et al. MRI to detect atherosclerosis with gadolinium-containing immunomicelles targeting the macrophage scavenger receptor. *Magn Reson Med* 2006; 56:601-10.
48. Amirbekian V, Lipinski MJ, Briley-Saebo KC, et al. Detecting and assessing macrophages in vivo to evaluate atherosclerosis noninvasively using molecular MRI. *Proc Natl Acad Sci U S A* 2007; 104:961-6.
49. Lipinski MJ, Frias JC, Amirbekian V, et al. Macrophage-specific lipid-based nanoparticles improve cardiac magnetic resonance detection and characterization of human atherosclerosis. *JACC Cardiovasc Imaging* 2009; 2:637-47.
50. Newby AC. Dual role of matrix metalloproteinases (matrixins) in intimal thickening and atherosclerotic plaque rupture. *Physiol Rev* 2005; 85:1-31.
51. Galis ZS, Sukhova GK, Lark MW, Libby P. Increased expression of matrix metalloproteinases and matrix degrading activity in vulnerable regions of human atherosclerotic plaques. *J Clin Invest* 1994; 94:2493-503.
52. Pasterkamp G, Galis ZS, de Kleijn DP. Expansive arterial remodeling: location, location, location. *Arterioscler Thromb Vasc Biol* 2004; 24:650-7.
53. Gough PJ, Gomez IG, Wille PT, Raines EW. Macrophage expression of active MMP-9 induces acute plaque disruption in apoE-deficient mice. *J Clin Invest* 2006; 116:59-69.
54. Galis ZS, Khatri JJ. Matrix metalloproteinases in vascular remodeling and atherogenesis: the good, the bad, and the ugly. *Circ Res* 2002; 90:251-62.
55. Wu YL, Ye Q, Sato K, Foley LM, Hitchens TK, Ho C. Noninvasive evaluation of cardiac allograft rejection by cellular and functional cardiac magnetic resonance. *JACC Cardiovasc Imaging* 2009; 2:731-41.
56. Lancelot E, Amirbekian V, Brigger I, et al. Evaluation of matrix metalloproteinases in atherosclerosis using a novel noninvasive imaging approach. *Arterioscler Thromb Vasc Biol* 2008; 28:425-32.
57. Lebel R, Jastrzebska B, Theriault H, et al. Novel solubility-switchable MRI agent allows the noninvasive detection of matrix metalloproteinase-2 activity in vivo in a mouse model. *Magn Reson Med* 2008; 60:1056-65.
58. Olson ES, Aguilera TA, Jiang T, et al. In vivo characterization of activatable cell penetrating peptides for targeting protease activity in cancer. *Integr Biol (Camb)* 2009; 1:382-93.
59. Olson ES, Jiang T, Aguilera TA, et al. Activatable cell penetrating peptides linked to nanoparticles

- as dual probes for in vivo fluorescence and MR imaging of proteases. *Proc Natl Acad Sci U S A* 2010; 107:4311-6.
60. Amirbekian V, Aguinaldo JG, Amirbekian S, et al. Atherosclerosis and matrix metalloproteinases: experimental molecular MR imaging in vivo. *Radiology* 2009; 251:429-38.
 61. Hyafil F, Vucic E, Cornily JC, et al. Monitoring of arterial wall remodelling in atherosclerotic rabbits with a magnetic resonance imaging contrast agent binding to matrix metalloproteinases. *Eur Heart J* 2011; 32:1561-71.
 62. Lepage M, Dow WC, Melchior M, et al. Noninvasive detection of matrix metalloproteinase activity in vivo using a novel magnetic resonance imaging contrast agent with a solubility switch. *Mol Imaging* 2007; 6:393-403.
 63. Rosen H, Crowley JR, Heinecke JW. Human neutrophils use the myeloperoxidase-hydrogen peroxide-chloride system to chlorinate but not nitrate bacterial proteins during phagocytosis. *J Biol Chem* 2002; 277:30463-8.
 64. Brennan ML, Hazen SL. Emerging role of myeloperoxidase and oxidant stress markers in cardiovascular risk assessment. *Curr Opin Lipidol* 2003; 14:353-9.
 65. Nicholls SJ, Hazen SL. Myeloperoxidase, modified lipoproteins, and atherogenesis. *J Lipid Res* 2009; 50 Suppl:S346-S351.
 66. Chen JW, Pham W, Weissleder R, Bogdanov A, Jr. Human myeloperoxidase: a potential target for molecular MR imaging in atherosclerosis. *Magn Reson Med* 2004; 52:1021-8.
 67. Chen JW, Querol SM, Bogdanov A, Jr., Weissleder R. Imaging of myeloperoxidase in mice by using novel amplifiable paramagnetic substrates. *Radiology* 2006; 240:473-81.
 68. Nahrendorf M, Sosnovik D, Chen JW, et al. Activatable magnetic resonance imaging agent reports myeloperoxidase activity in healing infarcts and noninvasively detects the antiinflammatory effects of atorvastatin on ischemia-reperfusion injury. *Circulation* 2008; 117:1153-60.
 69. Tavora F, Cresswell N, Li L, Ripple M, Burke A. Immunolocalisation of fibrin in coronary atherosclerosis: implications for necrotic core development. *Pathology* 2010; 42:15-22.
 70. Nair SA, Kolodziej AF, Bhole G, Greenfield MT, McMurry TJ, Caravan P. Monovalent and bivalent fibrin-specific MRI contrast agents for detection of thrombus. *Angew Chem Int Ed Engl* 2008; 47:4918-21.
 71. Spuentrup E, Buecker A, Katoh M, et al. Molecular magnetic resonance imaging of coronary thrombosis and pulmonary emboli with a novel fibrin-targeted contrast agent. *Circulation* 2005; 111:1377-82.
 72. Sirol M, Fuster V, Badimon JJ, et al. Chronic thrombus detection with in vivo magnetic resonance imaging and a fibrin-targeted contrast agent. *Circulation* 2005; 112:1594-600.
 73. Spuentrup E, Botnar RM, Wiethoff AJ, et al. MR imaging of thrombi using EP-2104R, a fibrin-specific contrast agent: initial results in patients. *Eur Radiol* 2008; 18:1995-2005.
 74. Botnar RM, Buecker A, Wiethoff AJ, et al. In vivo magnetic resonance imaging of coronary thrombosis using a fibrin-binding molecular magnetic resonance contrast agent. *Circulation* 2004; 110:1463-6.
 75. Flacke S, Fischer S, Scott MJ, et al. Novel MRI contrast agent for molecular imaging of fibrin: implications for detecting vulnerable plaques. *Circulation* 2001; 104:1280-5.
 76. Winter PM, Caruthers SD, Yu X, et al. Improved molecular imaging contrast agent for detection of human thrombus. *Magn Reson Med* 2003; 50:411-6.
 77. Davies MJ, Gordon JL, Gearing AJ, et al. The expression of the adhesion molecules ICAM-1, VCAM-1, PECAM, and E-selectin in human atherosclerosis. *J Pathol* 1993; 171:223-9.
 78. McAteer MA, Sibson NR, von zur MC, et al. In vivo magnetic resonance imaging of acute brain inflammation using microparticles of iron oxide. *Nat Med* 2007; 13:1253-8.
 79. McAteer MA, Schneider JE, Ali ZA, et al. Magnetic resonance imaging of endothelial adhesion molecules in mouse atherosclerosis using dual-targeted microparticles of iron oxide. *Arterioscler Thromb Vasc Biol* 2008; 28:77-83.
 80. Nahrendorf M, Jaffer FA, Kelly KA, et al. Noninvasive vascular cell adhesion molecule-1 imaging identifies inflammatory activation of cells in atherosclerosis. *Circulation* 2006; 114:1504-11.
 81. Kelly KA, Nahrendorf M, Yu AM, Reynolds F, Weissleder R. In vivo phage display selection yields atherosclerotic plaque targeted peptides for imaging. *Mol Imaging Biol* 2006; 8:201-7.
 82. Burtea C, Laurent S, Port M, et al. Magnetic resonance molecular imaging of vascular cell adhesion molecule-1 expression in inflammatory lesions using a peptide-vectorized paramagnetic imaging probe. *J Med Chem* 2009; 52:4725-42.
 83. Burtea C, Laurent S, Mahieu I, et al. In vitro biomedical applications of functionalized iron oxide nanoparticles, including those not related to magnetic properties. *Contrast Media Mol Imaging* 2011; 6:236-50.
 84. Shattil SJ. Function and regulation of the beta 3 integrins in hemostasis and vascular biology. *Thromb Haemost* 1995; 74:149-55.
 85. Murphy JF, Bordet JC, Wyler B, et al. The vitronectin receptor (alpha v beta 3) is implicated, in cooperation with P-selectin and platelet-activating factor, in the adhesion of monocytes to activated endothelial cells. *Biochem J* 1994; 304 (Pt 2):537-42.
 86. Huang S, Endo RI, Nemerow GR. Upregulation of integrins alpha v beta 3 and alpha v beta 5 on human monocytes and T lymphocytes facilitates adenovirus-mediated gene delivery. *J Virol* 1995; 69:2257-63.
 87. Hoshiga M, Alpers CE, Smith LL, Giachelli CM, Schwartz SM. Alpha-v beta-3 integrin expression in normal and atherosclerotic artery. *Circ Res* 1995; 77:1129-35.
 88. Quinn MJ, Byzova TV, Qin J, Topol EJ, Plow EF.

- Integrin α 11 β 3 and its antagonism. *Arterioscler Thromb Vasc Biol* 2003; 23:945-52.
89. Weerasinghe D, McHugh KP, Ross FP, Brown EJ, Gisler RH, Imhof BA. A role for the α v β 3 integrin in the transmigration of monocytes. *J Cell Biol* 1998; 142:595-607.
 90. Scatena M, Almeida M, Chaisson ML, Fausto N, Nicosia RF, Giachelli CM. NF- κ B mediates α v β 3 integrin-induced endothelial cell survival. *J Cell Biol* 1998; 141:1083-93.
 91. Antonov AS, Kolodgie FD, Munn DH, Gerrity RG. Regulation of macrophage foam cell formation by α v β 3 integrin: potential role in human atherosclerosis. *Am J Pathol* 2004; 165:247-58.
 92. Winter PM, Caruthers SD, Kassner A, et al. Molecular imaging of angiogenesis in nascent Vx-2 rabbit tumors using a novel α (nu) β 3-targeted nanoparticle and 1.5 tesla magnetic resonance imaging. *Cancer Res* 2003; 63:5838-43.
 93. Blankenberg S, Barbaux S, Tiret L. Adhesion molecules and atherosclerosis. *Atherosclerosis* 2003; 170:191-203.
 94. Doyle B, Caplice N. Plaque neovascularization and antiangiogenic therapy for atherosclerosis. *J Am Coll Cardiol* 2007; 49:2073-80.
 95. Virmani R, Kolodgie FD, Burke AP, et al. Atherosclerotic plaque progression and vulnerability to rupture: angiogenesis as a source of intraplaque hemorrhage. *Arterioscler Thromb Vasc Biol* 2005; 25:2054-61.
 96. Lanza GM, Winter PM, Caruthers SD, et al. Nanomedicine opportunities for cardiovascular disease with perfluorocarbon nanoparticles. *Nanomedicine (Lond)* 2006; 1:321-9.
 97. Winter PM, Morawski AM, Caruthers SD, et al. Molecular imaging of angiogenesis in early-stage atherosclerosis with α (v) β 3-integrin-targeted nanoparticles. *Circulation* 2003; 108:2270-4.
 98. Waters EA, Chen J, Yang X, et al. Detection of targeted perfluorocarbon nanoparticle binding using 19F diffusion weighted MR spectroscopy. *Magn Reson Med* 2008; 60:1232-6.
 99. Waters EA, Chen J, Allen JS, Zhang H, Lanza GM, Wickline SA. Detection and quantification of angiogenesis in experimental valve disease with integrin-targeted nanoparticles and 19-fluorine MRI/MRS. *J Cardiovasc Magn Reson* 2008; 10:43.
 100. Burtea C, Laurent S, Murariu O, et al. Molecular imaging of α v β 3 integrin expression in atherosclerotic plaques with a mimetic of RGD peptide grafted to Gd-DTPA. *Cardiovasc Res* 2008; 78:148-57.
 101. Sulyok GA, Gibson C, Goodman SL, Holzemann G, Wiesner M, Kessler H. Solid-phase synthesis of a nonpeptide RGD mimetic library: new selective α v β 3 integrin antagonists. *J Med Chem* 2001; 44:1938-50.
 102. Humphries JD, Byron A, Humphries MJ. Integrin ligands at a glance. *J Cell Sci* 2006; 119:3901-3.
 103. Braam SR, Zeinstra L, Litjens S, et al. Recombinant vitronectin is a functionally defined substrate that supports human embryonic stem cell self-renewal via α v β 5 integrin. *Stem Cells* 2008; 26:2257-65.
 104. Katz R. Biomarkers and surrogate markers: an FDA perspective. *NeuroRx* 2004; 1:189-95.
 105. Winter PM, Neubauer AM, Caruthers SD, et al. Endothelial α (v) β 3 integrin-targeted fumagillin nanoparticles inhibit angiogenesis in atherosclerosis. *Arterioscler Thromb Vasc Biol* 2006; 26:2103-9.
 106. Winter PM, Caruthers SD, Zhang H, Williams TA, Wickline SA, Lanza GM. Antiangiogenic synergism of integrin-targeted fumagillin nanoparticles and atorvastatin in atherosclerosis. *JACC Cardiovasc Imaging* 2008; 1:624-34.
 107. Bevilacqua MP, Nelson RM. Selectins. *J Clin Invest* 1993; 91:379-87.
 108. Kanwar S, Smith CW, Kubes P. An absolute requirement for P-selectin in ischemia/reperfusion-induced leukocyte recruitment in cremaster muscle. *Microcirculation* 1998; 5:281-7.
 109. Robbins CS, Chudnovskiy A, Rauch PJ, et al. Extramedullary hematopoiesis generates Ly-6C(high) monocytes that infiltrate atherosclerotic lesions. *Circulation* 2012; 125:364-74.
 110. Woollard KJ, Geissmann F. Monocytes in atherosclerosis: subsets and functions. *Nat Rev Cardiol* 2010; 7:77-86.
 111. Kang HW, Torres D, Wald L, Weissleder R, Bogdanov AA, Jr. Targeted imaging of human endothelial-specific marker in a model of adoptive cell transfer. *Lab Invest* 2006; 86:599-609.
 112. Boutry S, Burtea C, Laurent S, Toubeau G, Vander EL, Muller RN. Magnetic resonance imaging of inflammation with a specific selectin-targeted contrast agent. *Magn Reson Med* 2005; 53:800-7.
 113. Neuwelt EA, Hamilton BE, Varallyay CG, et al. Ultrasmall superparamagnetic iron oxides (USPIOs): a future alternative magnetic resonance (MR) contrast agent for patients at risk for nephrogenic systemic fibrosis (NSF)? *Kidney Int* 2009; 75:465-74.
 114. Cormode DP, Skajaa T, Fayad ZA, Mulder WJ. Nanotechnology in medical imaging: probe design and applications. *Arterioscler Thromb Vasc Biol* 2009; 29:992-1000.

The image features a minimalist, abstract design. A large, light gray circle is partially visible on the left side, overlapping a smaller, darker gray circle. A thick, light gray arc curves from the top left towards the right. A series of small, dark gray dots forms a curved path that starts near the bottom right of the smaller circle and extends towards the right edge of the frame. The word "PLAQU" is printed in a bold, serif font across the middle of the smaller circle.

PLAQU



In Press, PLoS One, 2013

Chapter 3

Self-gated CINE MRI for combined contrast-enhanced imaging and wall-stiffness measurements of murine aortic atherosclerotic lesions

B. den Adel, L.M. van der Graaf, G.J. Strijkers, H.J. Lamb, R.E. Poelmann and L. van der Weerd

ABSTRACT

Background

High-resolution contrast-enhanced imaging of the murine atherosclerotic vessel wall is difficult due to unpredictable flow artifacts, motion of the thin artery wall and problems with flow suppression in the presence of a circulating contrast agent.

Methods and Results

We applied a 2D-FLASH retrospective-gated cine MRI method at 9.4T to characterize atherosclerotic plaques and vessel wall distensibility in the aortic arch of aged ApoE^{-/-} mice after injection of a contrast agent. The method enabled detection of contrast enhancement in atherosclerotic plaques in the aortic arch after i.v. injection of micelles and iron oxides resulting in reproducible plaque enhancement. Both contrast agents were taken up in the plaques, which was confirmed by histology. Additionally, the retrospective-gated CINE method provided images of the aortic wall throughout the cardiac cycle, from which the vessel wall distensibility could be calculated. Reduction in plaque size by statin treatment resulted in lower contrast enhancement and reduced wall stiffness.

Conclusions

The retrospective-gated CINE MRI provides a robust and simple way to detect and quantify contrast enhancement in atherosclerotic plaques in the aortic wall of ApoE^{-/-} mice. From the same scan, plaque-related changes in stiffness of the aortic wall can be determined. In this mouse model, a correlation between vessel wall stiffness and atherosclerotic lesions was found.

Abbreviations

ApoE:	apolipoprotein E
CNR:	contrast to noise ratio
ECG:	electrocardiogram
Gd-DTPA-BSA:	Gd-DTPA-bis(stearylamide)
PEG2000-DSPE:	1,2-distearoyl-sn-glycero-3-phosphoethanolamine-N [methoxy polyethyleneglycol]-2000]
NIR664-DSPE:	nearinfrared664 - 1,2-distearoyl-sn-glycero-3-phosphoethanolamine
USPIO:	ultrasmall superparamagnetic iron oxide
ROI:	region of interest

INTRODUCTION

Cardiovascular diseases, in particular carotid and other peripheral atherosclerotic diseases are the leading causes of death in the western world¹. Remodeling of the arterial wall intima, media and adventitia layers leads to the formation of an atherosclerotic plaque that may over time progress towards a vulnerable, rupture-prone phenotype². Rupture of a plaque and subsequent myocardial infarction or stroke account for more than 50% of all cardiovascular deaths¹. Clinical predictors for cardiovascular events due to vulnerable plaque rupture are plaque

components like intraplaque macrophage content and the extent of the lipid core. Apart from the composition of atherosclerotic plaques, arterial stiffness and distensibility are independent predictor of cardiac morbidity. Despite this independency, atherosclerotic plaques do contribute significantly to the vessel wall stiffness, and changes in plaque burden or aortic compliance could help to identify early cardiovascular disease in patients before an actual plaque rupture, as well as monitor the results of the therapeutic interventions^{3, 4}. Hydroxy-3-methylglutaryl coenzyme A reductase inhibitors, or statins, are well known to exert beneficial effects on the elastic properties of the arterial wall⁵. They are widely applied in both the clinic as well as in preclinical studies.

Much effort has been put into development of non-invasive techniques such as MRI to image the presence of atherosclerotic plaque directly using (targeted) contrast agents⁶⁻¹⁰. Separately, MRI techniques have been employed to image arterial stiffness, also called vascular compliance¹¹⁻¹⁶ and distensibility through cyclic strain calculations.

In this report we describe the simultaneous determination of plaque burden in the aortic arch and the stiffness and distensibility of the vessel wall of mice using retrospective-gated CINE MRI.

Retrospective-gating provides a method to depict both contrast agent enhancement in the atherosclerotic plaque at atheroprone vessels, such as the ascending aorta, which are characterized by motion due to the beating heart as well as oscillatory flow. This self-gated navigator-based CINE MRI technique is nowadays widely applied for cardiac MRI, allowing continuous acquisition of data points without the need for respiratory and ECG sensors¹⁷. The technique is based on the acquisition of a navigator signal with every k-space line, followed by sorting data points according to their origin in the cardiac and respiratory cycle¹⁸. As the vessel wall images are reconstructed separately for different phases in the cardiac cycle, cine movies can be created of vascular diameter, from which the vascular compliance can be determined.

In this study, we used the ApoE^{-/-} mouse model that spontaneously develops atherosclerotic lesions of morphology similar to that observed in humans¹⁹⁻²¹ to investigate the value of retrospective-gated CINE MRI of the aortic arch for atherosclerotic plaque detection and assessment of wall stiffness after injection of contrast agents that home to macrophages^{9, 22, 23}. Retrospective-gated MRI was done in young (12 weeks) and aged (12-14 months) ApoE^{-/-} mice with advanced atherosclerotic plaques in the bases of the aortic arch, assessing the presence of atherosclerotic plaques and vascular compliance as a function of disease progression, as well as during a therapeutic intervention with atorvastatin.

MATERIALS AND METHODS

***In vivo* Experiments**

All experiments were conducted in accordance with the Dutch guidelines for research animal care. Two groups (n=5 per group) of 12 weeks old male ApoE^{-/-} mice on a C57BL/6/Jico background were fed a normal chow diet. Four groups of 12-to-14-month-old mice (n=5 per group) were either fed (n=2 groups) a Western high fat diet (1% cholesterol, Ab Diets) or a (n=2 groups) Western diet supplemented with 0.01% wt/wt atorvastatin (Lipitor, Pfizer) (=0.1g statin / kg bodyweight) for 12 weeks.

Plaque imaging was performed with contrast enhancement using either Gd-containing micelles or ultra-small iron oxide particles. Optimal time points for contrast agent accumulation in the plaque were determined in a pilot time-course study in which contrast agent accumulation was

followed over time for 7 days with intervals ranging from 30 minutes to 6 hours (supplemental figure 1). The optimal time point was defined as the time at which the highest contrast-to-noise ratio was observed (see below), and was determined to be 12 h p.i. for the Gd-micelles²⁴, and 24 h for the USPIO particles. The blood circulation half-time of the micelles in the circulation is 8.3 hours and the half-time of the USPIOs is 10.4 hours.

Each mouse was scanned before administration of contrast agent and at the optimal time point after intravenous injection of micelles equivalent to 50 $\mu\text{mol Gd}^{3+}$ -DTPA lipid/kg bodyweight diluted in 200 μl , or 250 $\mu\text{mol Fe/kg}$ bodyweight USPIO in 200 μl dextrose solution. Mice were anesthetized with isoflurane (2% in 1:1 oxygen:air). During the examination, the respiration rate was continuously measured with a balloon pressure sensor connected to the ECG/respiratory unit. The isoflurane concentration was adjusted to keep the respiration rate between 50 and 90 respirations/min.

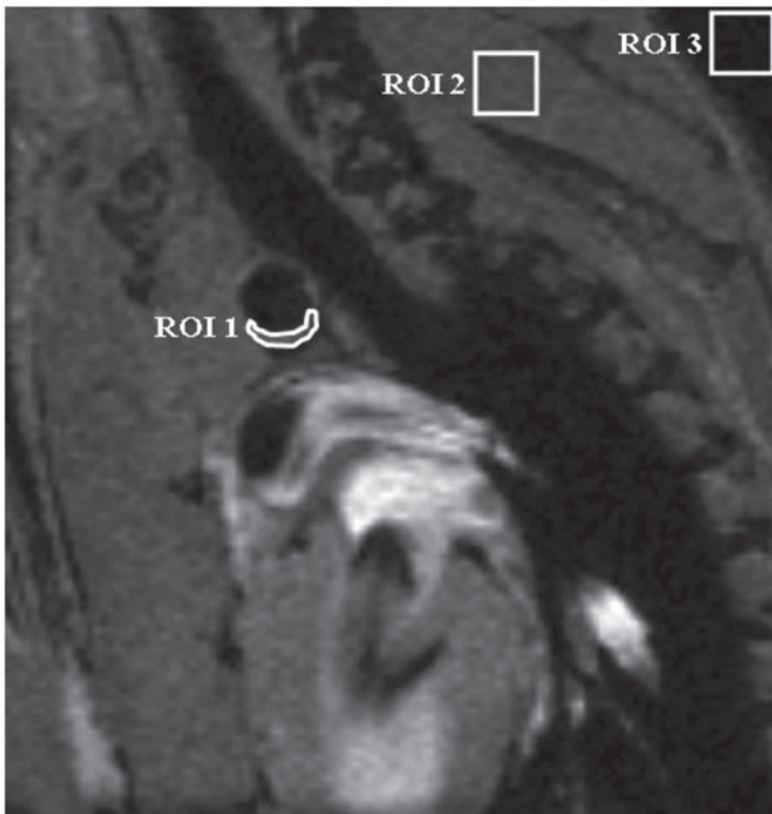


Figure 1 | Contrast-to-Noise determination in the aortic arch. Region of interest (ROI) placement in the MR images were used to determine the contrast to noise ratios (CNR) in the atherosclerotic plaques in black blood images of a cross section of the aortic arch. ROI1 is placed in the atherosclerotic plaque in the vessel wall (I_{wall}). ROI2 is positioned in a muscle and used for normalization purposes (I_{muscle}). Noise levels were determined in ROI 3, placed in a region without signal. The standard deviation of the noise ($\text{stdev}_{\text{noise}}$) was used for normalization purposes.

Contrast Agents

Gadolinium-based T1 contrast agent

Micelles were prepared by lipid film hydration²⁵. A mixture of the appropriate amounts of lipids (typically 120 mol of total lipid) was dissolved in chloroform/methanol 3:1 (v/v) and evaporated to dryness by rotary evaporation at 37°C. Gd-DTPA-BSA (Gd-DTPA-bis(stearylamide), PEG2000-DSPE (1,2-distearoyl-sn-glycero-3-phosphoethanolamine-N-[methoxy(polyethyleneglycol)-2000]) (all Avanti Polar lipids Inc) were used at a molar ratio of 1.5/1.35. For fluorescent detection, 0.1 mol% NIR664-DSPE (SyMO-CHEM B.V., Eindhoven, The Netherlands) was added. The lipid film was subsequently hydrated in HEPES buffered saline (HBS), containing 20 mM HEPES and 135 mM NaCl (pH 7.4) and vigorously stirred at 65°C for 45 min. The size and size distribution of the micelles were determined by dynamic light scattering (DLS) at 25°C with a Malvern 4700 system (Malvern ZetaSizer Nano S, Malvern, UK). The micelles had a mean size of 16 nm and a polydispersity index below 0.1, which indicates a narrow size distribution. The relaxivity was measured at 37°C and 9.4 T. The phospholipid content of the liposome preparations was determined by phosphate analysis according to Rouser after destruction with perchloric acid²⁶.

Iron-oxide-based T2 contrast agent*

ultra-small superparamagnetic iron oxides (USPIO, Sinerem®) were obtained from Guerbet (Guerbet group, Aulnay sous Bois, France). An equivalent of 250 µmol Fe/kg bodyweight was injected i.v.

MRI protocols

All experiments were performed with a vertical 89-mm bore 9.4 T magnet (Bruker, Ettlingen, Germany) supplied with an actively shielded Micro2.5 gradient system of 1 T/m and a 30 mm transmit/receive birdcage RF coil, using Paravision 4.0 software.

At the start of each examination, several 2D Fast Low Angle Shot (FLASH) scout images were recorded in the transverse and axial plane of the heart to determine the orientation of the aortic arch. A modified 2D FLASH sequence with a navigator echo (IntraGate, Bruker) was used for retrospective CINE MRI with the following parameters: Hermite-shaped RF pulse 1 ms; FA 15°; TR 31.4 ms; TE 2.96 ms; navigator echo points 64; 10 cardiac frames; FOV 1.8*1.8 cm²; matrix 128*96, zero-filled to 128*128; in-plane resolution 141 µm; 6 concomitant slices covering the inner curvature of the aortic arch; slice thickness 0.4 mm; number of repetitions 400; total acquisition time approximately 20 min. Images were positioned both perpendicular to and in line with the aortic arch according to an external placed reference to assure maintenance of the positioning plane pre and post contrast agent injection.

We performed aortic diameter measurements with 5, 8, 12, 15, 20 and 40 frames to assess the variability in the diameter measurements in a group of 3 months old (hemodynamically stable) ApoE^{-/-} mice (n=5) in relation to the frame number. All further analysis were performed using 10 reconstructed frames (supplemental figure 2).

Image Analysis

Images were analyzed using ImageJ software. For contrast to noise determination, black blood images in 3 to 4 adjacent cross-sectional slices (the ones that had the lowest signal intensity, i.e. black-blood) through the aortic arch were analyzed (Figure 1). ROIs were semi-automatically drawn around the vessel wall (I_{wall}) in all 10 movie frames. A 2nd ROI was drawn in the surrounding muscle tissue of the shoulder girdle (I_{muscle}). Furthermore, an ROI was placed outside the animal

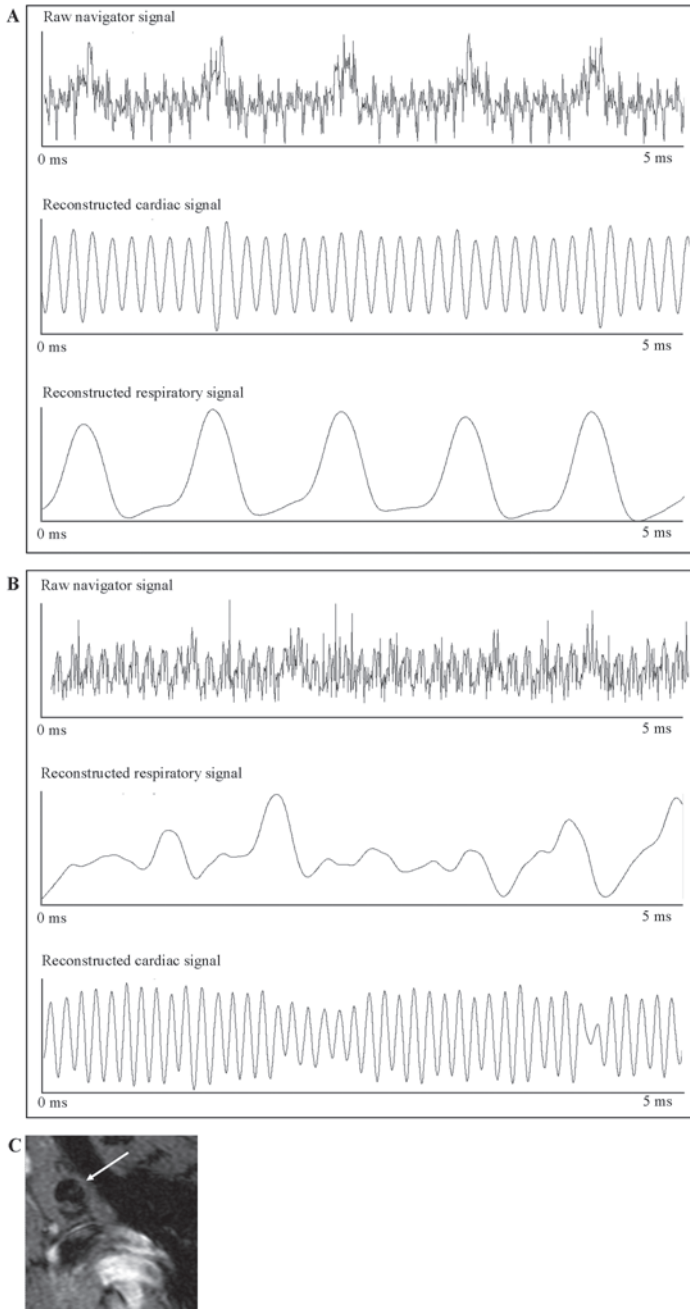


Figure 2 | Navigator signals for the reconstruction of self-gated MRI. Analysis of navigator signals for reconstruction of the self-gated MR acquisitions. A. Example of a raw navigator signal with corresponding filtered respiratory and cardiac signals. B. Under unstable physiological situations it is still possible to gather correct cardiac and respiratory traces. With the filtered reconstruction signals of both, it is possible to re-order data points in such a way a clear image of the aortic arch can still be generated. C. Representative black blood image before injection of contrast agent from the same animal shown above, with impaired cardiac and respiratory function. Retrospective gating led to a stable reconstruction of the aortic arch (arrow).

to measure the noise level (SD_{noise}). The contrast-to-noise ratio was defined in the 3 to 4 adjacent movie frames with the lowest signal intensity in the vessel lumen as follows:

$$\text{CNR} = (I_{\text{wall}} - I_{\text{muscle}}) / SD_{\text{noise}} \quad [\text{Eq1}]$$

CNR values are presented as mean \pm standard deviation.

To calculate the vessel wall stiffness, the cross-sectional diameter and area of the aortic arch were segmented manually in each frame. MRI slices were positioned orthogonal to the aortic arch, the frames that were obtained just before and after the branch of the left carotid artery had a stable circular shape and were used for this analysis (supplemental figure 3). To reduce the standard error when outlining cross-sections, all segmentations were repeated four times by the same observer (BdA). For the evaluation of the aortic stiffness β index the following formula was used:

$$\beta \text{ index} = \ln(P_{\text{sys}}/P_{\text{dias}}) / (\Delta D / D_{\text{dias}}) \quad [\text{Eq2}]$$

where P_{sys} and P_{dias} are assumed values of the systolic and diastolic arterial blood pressure in age and gender matched ApoE^{-/-} mice from literature (using a similar anesthesia setup)^{27,28}, D_{dias} is the aortic diastolic diameter, and ΔD is the difference between the systolic and diastolic diameter of the aortic arch.

For the determination of the circumferential strain as a measure of distensibility we assumed the deformation through the thickness of the vessel and in the axial direction was small compared to the circumferential deformation as described by Morrison et al.²⁹. Assuming a circular cross section of the aorta, the following expression was used to calculate the circumferential cyclic strain,

$$\epsilon_{\theta} = [A(t)/A(t0) - 1] / 2 \quad [\text{Eq3}]$$

where A is the cross sectional area of the aortic arch¹⁵.

Histology

Aortic arches were frozen in Tissue Tek® (Sakura Finetek Europe, Zoetermeer, The Netherlands) and cut into serial 5- μm sections. Sections were stained with hematoxylin and eosin for gross morphology and Oil Red O for lipid deposition as described previously³⁰, followed by bright-field microscopy. Lesion size was calculated from 8-10 consecutive H&E stained sections of the aortic arch. Iron deposits were visualized using Perl's Prussian blue staining. Presence of Gd-containing micelles was indirectly detected by staining of the DTPA chelate present in the micelles as recently described in den Adel et al.³¹. In short, sections were incubated overnight at room temperature with a rabbit polyclonal primary antibody against Gd-DTPA (1:20, BioPAL Inc). Goat-anti-rabbit conjugate (1:200, DAKO) with normal goat serum diluted in PBS was incubated for 1 h at room temperature as secondary antibody. Biotin labelling was followed by development using black alkaline phosphatase (Vector Laboratories Inc., United Kingdom) and counterstaining was done with Mayer's hematoxylin.

Statistical analysis

Data are represented as the mean \pm standard deviation. Statistical analyses were performed using SPSS 17.0.2 (SPSS, Inc., Chicago, IL, USA). Statistical significance between groups was assessed using (paired) t-test, one-way analysis of variance (ANOVA), followed by a Bonferroni correction for multiple testing in case of significance. Results were considered statistically significant at $p < 0.05$.

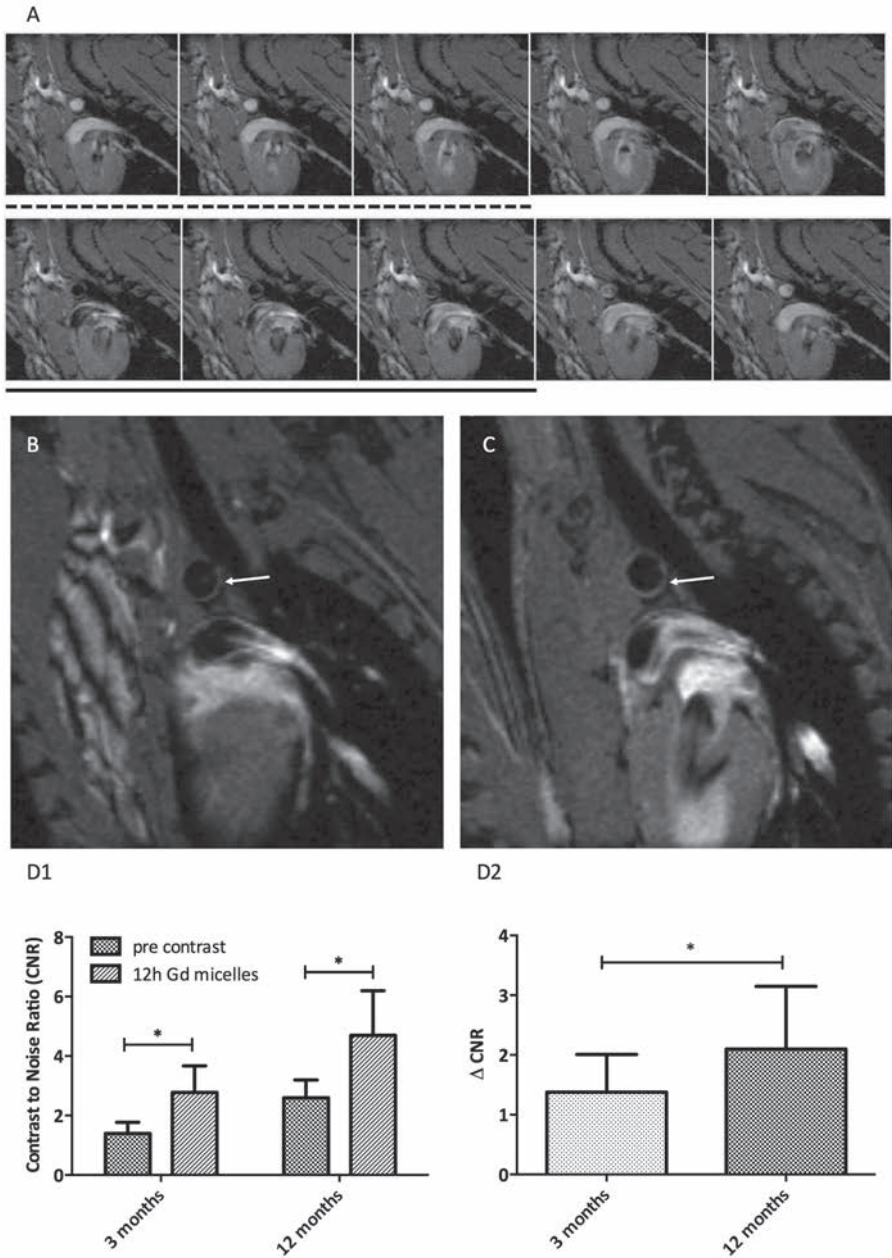


Figure 3 | Atherosclerotic plaque detection in a cross-section of the aortic arch, including the effect of Gd-loaded micelles. A. Ten movie frames of a cross section of the aortic arch are generated. The black blood images used for positive contrast agent detection in the aortic arch are typically as those in image 6-8 (underlined). Circles indicate the region of the aortic arch cross section. White blood images 1-3 (dashed line), were used for the analysis of negative contrast agents B. A cross section of the aortic arch is shown before injection of micelles. Presumptive plaque regions are difficult to discriminate (arrow). C. Cross section of the aortic arch 12 hours after injection of micelles shows contrast enhancement on the basis of the aortic arch (arrow) D. Contrast to Noise Ratio and delta CNR of atherosclerotic plaques on the inner curvature of the aortic arch in 3 months old and 12-14 months old ApoE^{-/-} mice on a western diet.

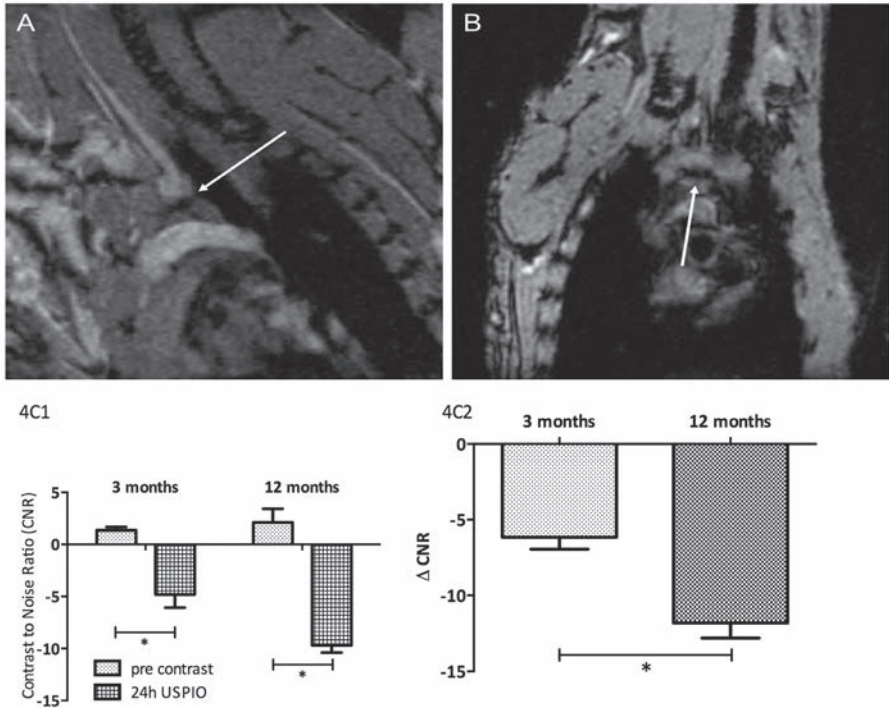


Figure 4 | Detection of atherosclerotic lesions in the aortic arch using USPIOs. T2* effects of USPIO were observed on the basis of the aortic arch 24 hours after i.v. contrast agent injection. CNR significantly decreased from 2.1 ± 1.3 before injection of contrast agent to -9.7 ± 0.7 , 24 hours after injection of micelles. The typical blooming effect by the USPIOs (arrow) was best observed in frontal views (B) of the aortic arch. C. CNR and delta CNR of both age groups before and 24 hours after USPIO injection.

RESULTS

Self-gated cine MRI in cardiovascular unstable animals

All mice included in these experiments had a relatively low variation in heart rate and respiratory rate throughout the examinations, ranging from 490 to 520 beats/min and from 50 to 80 respirations/min respectively (data not shown). The navigator echo in this sequence was used to demerge a cardiac and respiratory signal and subsequently reconstruct the sample point according to the cardiac cycle (figure 2A). However, even in cardiac and respiratory unstable mice it was feasible to obtain artifact-free MR images by specifically selecting the cardiac and respiratory weighting and periods used (figure 2B). With retrospective-gated CINE MRI, the image reconstruction could be optimized after sampling all the data points; while maintaining the usual scan time, we could still generate correct and stable images of the aortic arch allowing for plaque detection and vessel wall delineation (figure 2C).

Imaging of contrast agent uptake

The aortic arches of ApoE^{-/-} mice (young and aged) were imaged with the retrospective-gated MRI protocol pre- and post-injection of a micellar T1 contrast agent. Throughout the cardiac cycle, 10 movie frames of 6 transversal slices were made (figure 3A). Pre contrast agent injection,

the plaque burden in the inner curvature of the aorta was difficult to discriminate from healthy vessel wall, with only slightly elevated CNR in the plaque (arrow in figure 3B). After injection of Gd-containing micelles, a distinct hyperintensity was observed in the inner curvatures of the aortic arch and carotid arteries at the well-documented locations where atherosclerotic plaque is found in these ApoE^{-/-} mice (figure 3C)³². The hyper enhancement was largest in the aged animals, but could be distinguished in the younger animals as well.

The CNR values for these mice were determined after micelle injection for the images in the cardiac cycle with black blood (figure 3A, frames 6-8). Quantitative CNR values for the young and aged animals are summarized in Figure 3D. The CNR increased significantly after the injection of micelles in both groups, but both the CNR and Δ CNR of the aged animals were systematically higher than in the younger animals.

We applied a similar imaging strategy to detect the contrast changes pre- and post-injection of an ultrasmall iron-oxide particle (USPIO). Because USPIOs induce large signal voids in the artery wall, the bright blood frames of the retrospective-gated cine MRI were more suitable for CNR quantification (figure 4A&B). CNR values became negative (hypointense) after injection of the contrast agent, and as for the micelles, the enhancement was more pronounced in the aged mice (figure 4C).

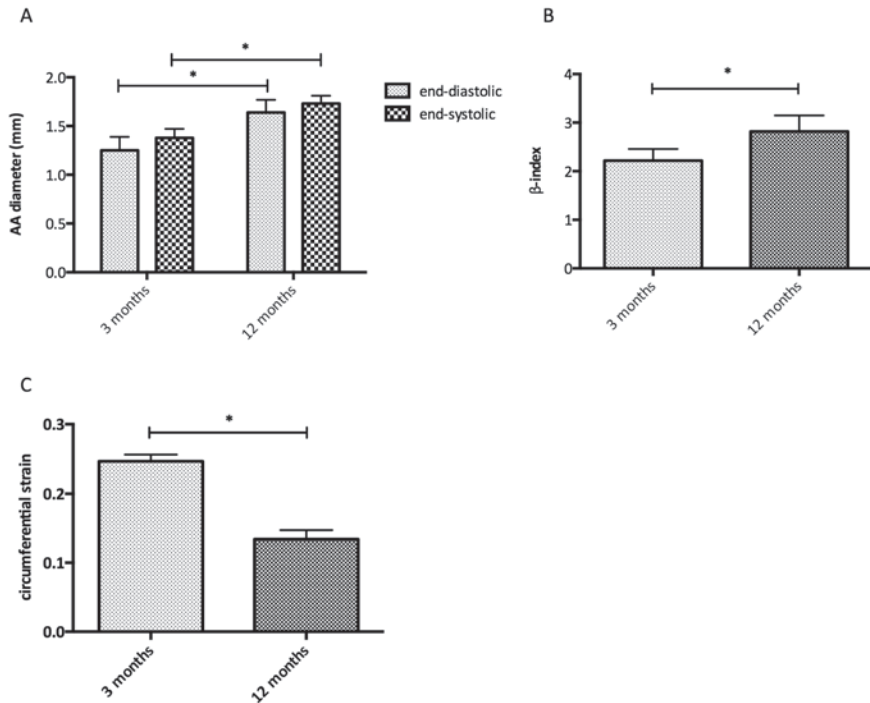


Figure 5 | Vessel wall characteristics measured by MRI. A. Diameter of the aortic arch in mm measured at end-diastole and end-systole measured in CINE MRI images from 3 months and 12 months old ApoE^{-/-} mice. B. Stiffness β' -index of the aortic arch of both age groups. C. Distensibility of the aortic arch measured by the average maximal circumferential strain calculated for both age groups.

Age related differences in vessel wall stiffness

A common consequence of atherosclerosis, observed both in humans and in animal models, is an increase in the stiffness of the aorta and major arteries, resulting in decreased vascular elasticity and compliance^{13,27}. Therefore we assessed whether we could determine the stiffness of the aortic arch based on the self-gated MRI data.

An increase in the diameter of the ascending aorta of the aged mice compared to the younger animals was observed both at end-systole and end-diastole (figure 5A). Based on the difference in diameter over the heart cycle, the aortic wall stiffness β' -index was calculated for both groups of mice (Figure 5B). Stiffness was increased by about 28% in the aged animals compared to the young animals. A significant decrease of 46% in average maximal circumferential strain values was observed between 3 and 12-month-old ApoE^{-/-} mice (figure 5C).

Effect of statin treatment on aortic plaque and vessel stiffness

We assessed whether the effects of statin therapy could be observed both on plaque level as well as the stiffness of the aortic arch in ApoE^{-/-} mice.

In aged ApoE^{-/-} mice treated for 12 weeks with a Western diet supplemented with atorvastatin plaques CNR changes were significantly smaller both in micelle injected mice as well as USPIO injected mice compared to age-matched untreated mice (figure 6A and 6B).

Diameter of the aortic arch in mm was measured at end-diastole and end-systole measured in all 3 ApoE^{-/-} treatment groups (figure 6C). The diameter at both end-diastole and end-systole was significantly decreased in the 12-months-old statin-treated mice compared to the untreated 12-months-old animals, yet still significantly higher than in the young mice. The stiffness of the aortic arch in the statin-treated group was significantly lower than for the untreated age-matched group and was slightly higher, yet not significantly different from the young animals (figure 6D). The average maximal circumferential strain calculated during the cardiac cycle shows a decrease with age (figure 6E). A statistically significant lower decrease in strain was noted after statin treatment.

Correlation between MRI contrast enhancement, aortic stiffness and histological plaque area

The plaque area in the inner curvature of the aortic arch was independently determined using histology. The anatomical position of the plaques found on MR images corresponds to the areas observed by lipid staining with Oil Red O (figure 7A & 7B). The plaque lesion sizes for the different groups are shown in figure 7C. The plaque size was smallest for the young animals, largest for the aged animals. After statin treatment, the plaque size was reduced by 28.5 %, but still significantly larger than in young ApoE^{-/-} mice. Using an anti-Gd-DTPA staining, the presence of micelles could be detected in distinct plaque areas: at the inner curvature of the aortic arch and in the intima of the vessel wall, in line with our MRI results. In contrast, the hypointense plaque regions due to iron-oxide accumulations mainly occurred in the plaque core, which was confirmed by Prussian Blue staining (figure 7D & 7E). Contrast enhancement on MRI for individual animals correlated very well ($p < 0.01$) with the lesion size as determined with histology (figure 7F), also after statin treatment, with an R^2 of 0.4203 and 0.7822 for the Gd-micelles and the USPIO respectively.

Both the aortic stiffness as well as the circumferential strain showed a linear correlation with plaque size, as determined by histology (figure 7G and 7H), with an R^2 of 0.5359 ($p < 0.01$) and 0.6465 ($p < 0.01$) respectively. Lastly, linear regression showed that both the aortic stiffness and circumferential strain were also correlated to the CNR after contrast agent administration (stiffness: figure 7I, R^2 0.2792, $p < 0.05$ and R^2 0.4019, $p < 0.05$; strain: figure 7J, R^2 0.4133 $p < 0.05$ and R^2 0.3790, $p < 0.05$).

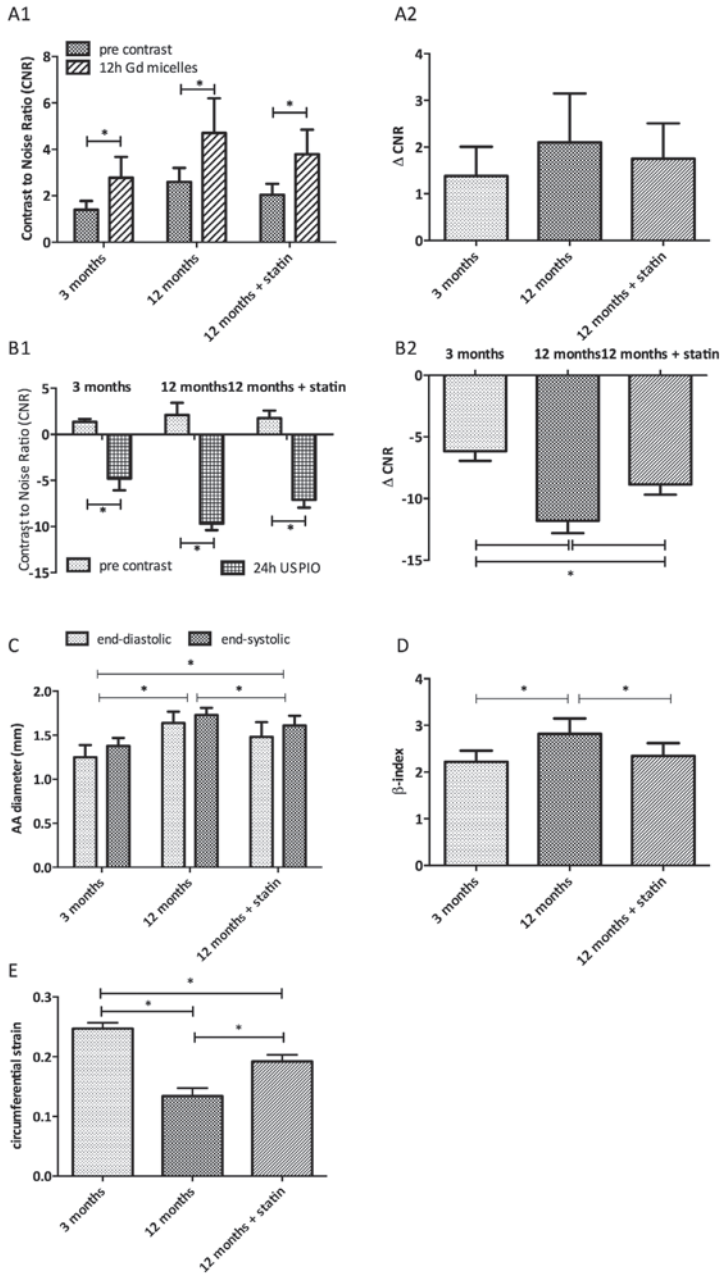


Figure 6 | The effect of atorvastatin treatment on atherosclerotic plaques. A. CNR and -CNR of atherosclerotic plaques on the inner curvature of the aortic arch of 3 months old as well as 12-14 months old ApoE^{-/-} mice on a western diet with or without supplementation with atorvastatin after micelle injection. B. CNR and -CNR of atherosclerotic plaques on the inner curvature of the 3 treatment groups after USPIO injection. C. Diameter of the aortic arch in mm measured at end-diastole and end-systole measured in CINE MRI images in all 3 ApoE^{-/-} treatment groups. D. Stiffness β -index of the aortic arch of the 3 treatment groups. E. Average maximum circumferential strain values of the 3 treatment groups.

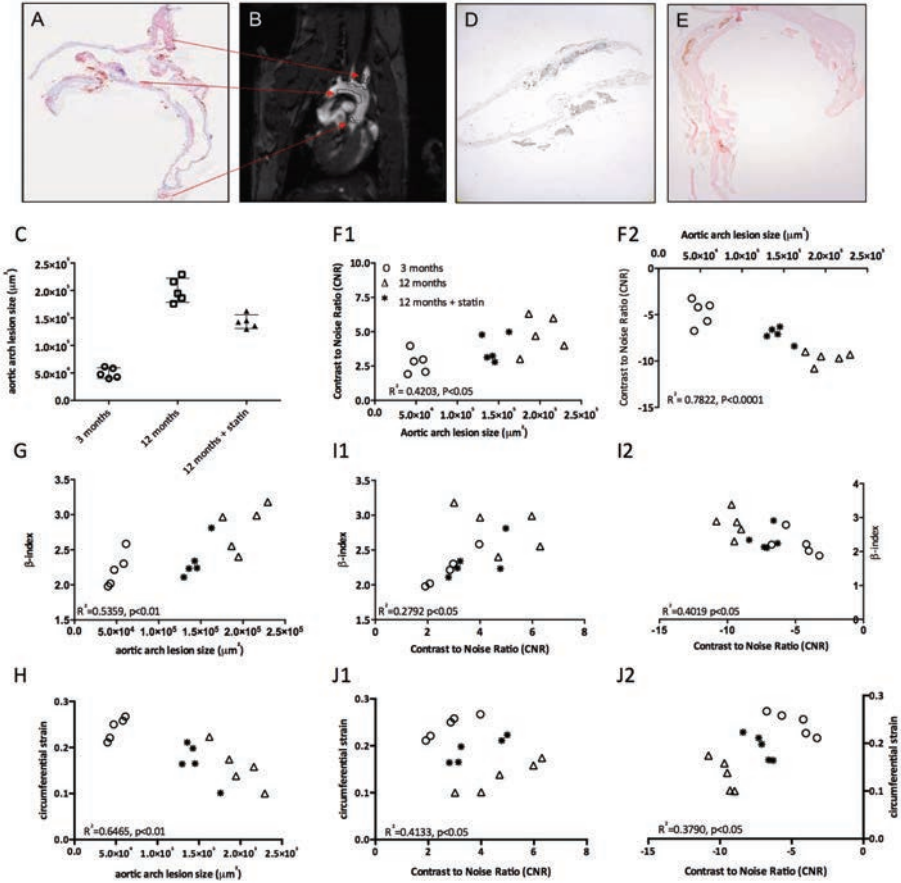


Figure 7 | Histological validation of atherosclerosis and MRI. A. Lipid depositions on the basis of the aortic arch and in the branches to the carotid and brachiocephalic arteries were shown by Oil Red O staining. B. Regions with atherosclerotic plaques corresponding to the regions in A are depicted in this MR image of the aortic arch. C. Plaque sizes of the 3 treatment groups in µm² determined on histological slices. D. Gd-DTPA localized the micelles in atherosclerotic plaques. E. Iron deposits are visualized in blue in the wall of the aortic arch. F. Correlation CNR of atherosclerotic plaques on the inner curvature of the aortic arch with plaque sizes of the 3 groups determined on histological slices. G. Correlation of the aortic arch lesion area with the β'-index. H. Correlation of the aortic arch lesion area with the circumferential strain of the 3 treatment groups. I. Correlation of the CNR of both micelles as well as USPIO with the β'-index. J. Correlation of the CNR of both micelles as well as USPIO with the circumferential strain.

DISCUSSION

Self-gated cine MRI for atherosclerotic plaque detection

Atherosclerotic plaque formation typically originates in the aortic root and progresses to the ascending aorta, the aortic arch and onward through the aorta's principal branches leading to progressive arterial stiffness⁴. These anatomical positions have one common theme; low and oscillatory (multi- or bidirectional) flow patterns, implying that plaque detection may be hampered by alterations in blood flow³⁵.

Proper visualization and quantification of atherosclerotic plaque components in both patients and animal models usually relies heavily on black-blood or bright-blood techniques with saturation slices or double inversion recovery methods^{34, 35}. However, the required steady state blood saturation can be difficult to maintain in ECG-triggered sequences¹⁸ especially in animal models. In the aortic arch, the prime site of plaque development, and carotid arteries assessment of plaques and vessel wall area becomes even more difficult, because of its proximity to the beating heart which may cause large motion artifacts on top of flow artifacts.

Classically, synchronization with the heart cycle, or prospective gating, is done using respiratory and ECG sensors to generate triggering signals³⁶. In hemodynamically unstable animals, one needs to monitor the R-R interval closely, or choose this interval conservatively, which means that the total scan time will be longer and as a consequence the influence of the imaging session on animal welfare will be higher.

Therefore, the use of a retrospective-gated cine MRI sequence provides distinct advantages over a triggered cine or single-frame sequence. Firstly, the maintenance of steady state saturation of the retrospective-gated sequence helped to reduce in-flow artifacts. Secondly, the retrospective-gated cine sequence covered the full cardiac cycle without dead time at the end of the cardiac cycle waiting for the next ECG trigger. Using the retrospective-gated cine sequence in combination with contrast agents known to accumulate in atherosclerotic plaques, micelles as well as USPIO, allowed for a good discrimination of the atherosclerotic lesion on the inner curvature of the aortic arch^{9, 10}.

Plaque burden and aortic stiffness

The finding of age-related increases in aortic stiffness, vessel diameter and aortic atherosclerosis is consistent with prior studies³⁷. Traditionally, the stiffness and compliance of conduit vessels is an estimate from the pulse wave velocity (PWV)^{38, 39}. This is routinely done in the clinic using ultrasound or MRI, yet PWV measurements in mice are feasible as shown in the group of Jakob, but challenging due to the high heart rate and difficulties to measure flow velocities *in vivo*^{15, 15, 16}. Using the stiffness of the vessel wall can be a good alternative or additional tool to characterize vessel compliance. The correlation between aortic stiffness and plaque burden is particularly interesting because the elastic properties of the aortic wall play an important role in the pathogenesis of cardiovascular disease including atherosclerosis and hypertension, and is an independent risk factor for ventricular hypertrophy and stroke. Further pathophysiological studies may include longitudinal follow-up experiments to assess the temporal relationship between vascular compliance and plaque burden as well as the ageing related increase in vessel wall diameter.

Our study showed that in a ApoE^{-/-} mouse model the histological plaque burden was closely related to both contrast-enhancement on MRI and the aortic distensibility. This correlation was preserved over a large age range, also during statin treatment (figure 7G), indicating that in this mouse model, changes in aortic stiffness are dominated by the plaque burden. Moreover the

average circumferential strain decreases with age, whereas statin treatment slows down this decrease. Together with the observation of an increase in vessel wall diameter this points at a decrease in arterial elasticity and compliance with age and in relation to the extent of atherosclerosis progression.

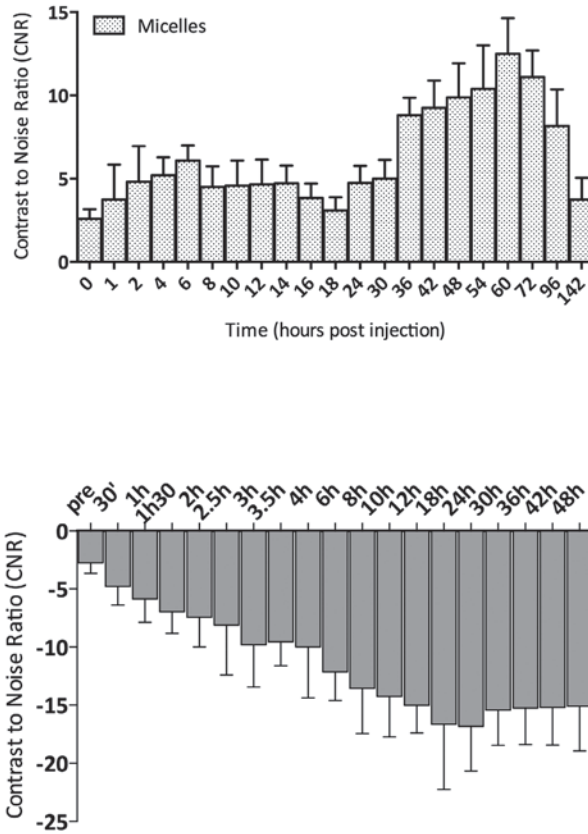
Therefore, aortic compliance measurements may be an alternative approach in this animal model to monitor subtle changes of the arterial wall elasticity to actual plaque imaging, which is still difficult and time-consuming. Aortic stiffness measurements would provide a straight-forward method to study the response to various dietary and pharmacological manipulations both in this animal models and patients^{40, 41}. One of the limitations in the current experimental setup is the lack of blood pressure measures due to the incompatibility with our MRI setup. The assumption of the blood pressure, although based on literature using animals of the same genetic background and anesthesia setup generate a bias point in our results.

Though we found a very clear correlation between aortic stiffness and plaque burden in the ApoE^{-/-} mouse, this is not necessarily the case in other mouse models, nor in patients. Arterial stiffness is an independent predictor of ventricular hypertrophy and stroke in patients, indicating that other mechanisms than plaque development may cause stiffening of the arteries. Assessing the temporal relationship between vascular compliance and plaque burden, may be particularly useful in different mouse models of atherosclerosis, including models of vascular dysfunction.

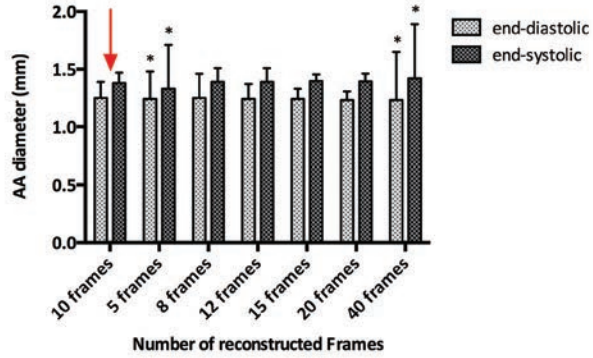
CONCLUSION

We have shown that retrospectively gated CINE MRI can be used to detect plaque burden and aortic distensibility simultaneously. Because the method can be used for both black-blood and bright-blood contrast, it is suitable for both gadolinium- and iron oxide based contrast agents. We have shown that in the ApoE^{-/-} mouse there is a high correlation between aortic stiffness, and plaque load, and both measures can be used to assess atherosclerotic plaque progression and therapeutic interventions.

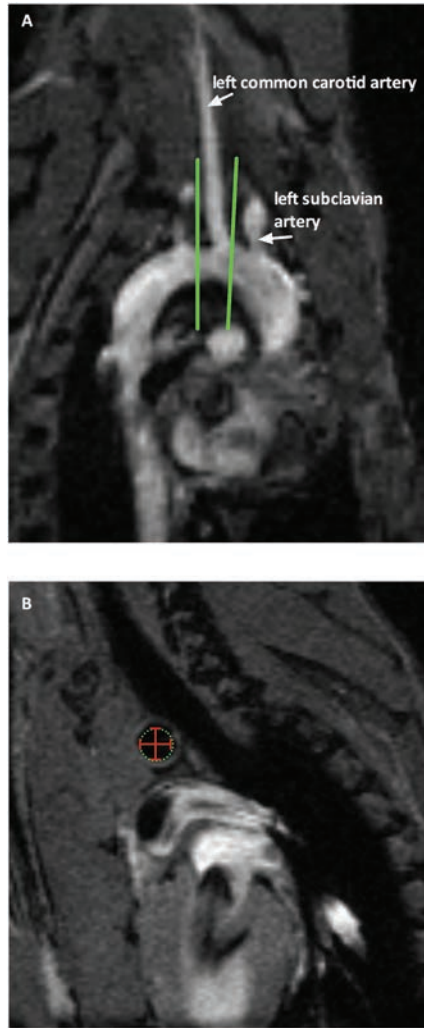
SUPPLEMENTAL FIGURES



Supplemental figure 1 | A. Time course of Gd-micelle accumulation in the inner curvature of the aortic arch of ApoE^{-/-} mice. Contrast to Noise Ratios (CNR) were determined at different time points after intravenous injection. B. CNR determined at different time points after USPIO injection in the inner curvature of the aortic arch



Supplemental figure 2 | Aortic arch diameter measurements at end-systole and end-diastole for 5, 8, 12, 15, 20 and 40 reconstructed cardiac movie frames compared to 10 movie frames. * $P < 0.05$ compared to 10 movie frames.



Supplemental figure 3 | A. Position in the aortic where frames were taken orthogonal to the aortic arch. B. Schematical depiction of determination of the diameter of the aortic arch using circular cross-sections only.

REFERENCES

1. Lloyd-Jones D, Adams RJ, Brown TM, et al. Heart disease and stroke statistics--2010 update: a report from the American Heart Association. *Circulation* 2010; 121:e46-e215.
2. Finn AV, Nakano M, Narula J, Kolodgie FD, Virmani R. Concept of vulnerable/unstable plaque. *Arterioscler Thromb Vasc Biol* 2010; 30:1282-92.
3. Virmani R, Burke AP, Kolodgie FD, Farb A. Vulnerable plaque: the pathology of unstable coronary lesions. *J Interv Cardiol* 2002; 15:439-46.
4. Laurent S, Boutouyrie P, Asmar R, et al. Aortic stiffness is an independent predictor of all-cause and cardiovascular mortality in hypertensive patients. *Hypertension* 2001; 37:1236-41.
5. John S, Schneider MP, Delles C, Jacobi J, Schmieder RE. Lipid-independent effects of statins on endothelial function and bioavailability of nitric oxide in hypercholesterolemic patients. *Am Heart J* 2005; 149:473.
6. Amirbekian V, Lipinski MJ, Briley-Saebo KC, et al. Detecting and assessing macrophages in vivo to evaluate atherosclerosis noninvasively using molecular MRI. *Proc Natl Acad Sci U S A* 2007; 104:961-6.
7. Burtica C, Laurent S, Mahieu I, et al. In vitro biomedical applications of functionalized iron oxide nanoparticles, including those not related to magnetic properties. *Contrast Media Mol Imaging* 2011; 6:236-50.
8. Yamakoshi Y, Qiao H, Lowell AN, et al. LDL-based nanoparticles for contrast enhanced MRI of athero plaques in mouse models. *Chem Commun (Camb)* 2011; 47:8835-7.
9. Klug G, Kampf T, Ziener C, et al. Murine atherosclerotic plaque imaging with the USPIO Ferumoxtran-10. *Front Biosci* 2009; 14:2546-52.
10. Morris JB, Olzinski AR, Bernard RE, et al. p38 MAPK inhibition reduces aortic ultrasmall superparamagnetic iron oxide uptake in a mouse model of atherosclerosis: MRI assessment. *Arterioscler Thromb Vasc Biol* 2008; 28:265-71.
11. Cai JM, Hatsukami TS, Ferguson MS, Small R, Polissar NL, Yuan C. Classification of human carotid atherosclerotic lesions with in vivo multicontrast magnetic resonance imaging. *Circulation* 2002; 106:1368-73.
12. Li ZY, Howarth S, Trivedi RA, et al. Stress analysis of carotid plaque rupture based on in vivo high resolution MRI. *J Biomech* 2006; 39:2611-22.
13. Lehmann ED, Hopkins KD, Jones RL, Rudd AG, Gosling RG. Aortic distensibility in patients with cerebrovascular disease. *Clin Sci (Lond)* 1995; 89:247-53.
14. Yu HY, Peng HH, Wang JL, Wen CY, Tseng WY. Quantification of the pulse wave velocity of the descending aorta using axial velocity profiles from phase-contrast magnetic resonance imaging. *Magn Reson Med* 2006; 56:876-83.
15. Herold V, Wellen J, Ziener CH, et al. In vivo comparison of atherosclerotic plaque progression with vessel wall strain and blood flow velocity in apoE(-/-) mice with MR microscopy at 17.6 T. *MAGMA* 2009; 22:159-66.
16. Parczyk M, Herold V, Klug G, Bauer WR, Rommel E, Jakob PM. Regional in vivo transit time measurements of aortic pulse wave velocity in mice with high-field CMR at 17.6 Tesla. *J Cardiovasc Magn Reson* 2010; 12:72.
17. Nahrendorf M, Wiesmann F, Hiller KH, et al. In vivo assessment of cardiac remodeling after myocardial infarction in rats by cine-magnetic resonance imaging. *J Cardiovasc Magn Reson* 2000; 2:171-80.
18. Heijman E, de GW, Niessen P, et al. Comparison between prospective and retrospective triggering for mouse cardiac MRI. *NMR Biomed* 2007; 20:439-47.
19. Faraci FM, Sigmund CD. Vascular biology in genetically altered mice : smaller vessels, bigger insight. *Circ Res* 1999; 85:1214-25.
20. Nakashima Y, Plump AS, Raines EW, Breslow JL, Ross R. ApoE-deficient mice develop lesions of all phases of atherosclerosis throughout the arterial tree. *Arterioscler Thromb* 1994; 14:133-40.
21. Plump AS, Breslow JL. Apolipoprotein E and the apolipoprotein E-deficient mouse. *Annu Rev Nutr* 1995; 15:495-518.
22. Mulder WJ, Strijkers GJ, Vucic E, Cormode DP, Nicolay K, Fayad ZA. Magnetic resonance molecular imaging contrast agents and their application in atherosclerosis. *Top Magn Reson Imaging* 2007; 18:409-17.
23. Mulder WJ, Strijkers GJ, Briley-Saboe KC, et al. Molecular imaging of macrophages in atherosclerotic plaques using bimodal PEG-micelles. *Magn Reson Med* 2007; 58:1164-70.
24. den Adel B, van der Graaf LM, Que I, et al. Contrast enhancement by lipid-based MRI contrast agents in mouse atherosclerotic plaques; a longitudinal study. *Contrast Media Mol Imaging* 2013; 8(1):63-71.
25. Mulder WJ, Strijkers GJ, Griffioen AW, et al. A liposomal system for contrast-enhanced magnetic resonance imaging of molecular targets. *Bioconjug Chem* 2004; 15:799-806.
26. Rouser G, Fkiescher S, Yamamoto A. Two dimensional thin layer chromatographic separation of polar lipids and determination of phospholipids by phosphorus analysis of spots. *Lipids* 1970; 5:494-6.
27. Wang YX, Halks-Miller M, Vergona R, et al. Increased aortic stiffness assessed by pulse wave velocity in apolipoprotein E-deficient mice. *Am J Physiol Heart Circ Physiol* 2000; 278:H428-H434.
28. Tomita H, Hagaman J, Friedman MH, Maeda N. Relationship between hemodynamics and atherosclerosis in aortic arches of apolipoprotein E-null mice on 129S6/SvEvTac and C57BL/6J genetic backgrounds. *Atherosclerosis* 2012; 220:78-85.
29. Morrison TM, Choi G, Zarins CK, Taylor CA. Circumferential and longitudinal cyclic strain of the human thoracic aorta: age-related changes. *J Vasc*

- Surg 2009; 49:1029-36.
30. Bergwerff M, Verberne ME, Deruiter MC, Poelmann RE, Gittenberger-de Groot AC. Neural crest cell contribution to the developing circulatory system: implications for vascular morphology? *Circ Res* 1998; 82:221-31.
 31. den Abel B, Bovens SM, Boekhorst BT, et al. Histological validation of iron-oxide and gadolinium based MRI contrast agents in experimental atherosclerosis: The do's and don't's. *Atherosclerosis* 2012; 225(2):274-80.
 32. Shaaban AM, Duerinckx AJ. Wall shear stress and early atherosclerosis: a review. *AJR Am J Roentgenol* 2000; 174:1657-65.
 33. Van der Heiden K, Hierck BP, Krams R, et al. Endothelial primary cilia in areas of disturbed flow are at the base of atherosclerosis. *Atherosclerosis* 2008; 196:542-50.
 34. te Boekhorst BC, Bovens SM, Rodrigues-Feo J, et al. Characterization and in vitro and in vivo testing of CB2-receptor- and NGAL-targeted paramagnetic micelles for molecular MRI of vulnerable atherosclerotic plaque. *Mol Imaging Biol* 2010; 12:635-51.
 35. Miraux S, Calmettes G, Massot P, et al. 4D retrospective black blood trueFISP imaging of mouse heart. *Magn Reson Med* 2009; 62:1099-105.
 36. Wiesmann F, Szimtenings M, Frydrychowicz A, et al. High-resolution MRI with cardiac and respiratory gating allows for accurate in vivo atherosclerotic plaque visualization in the murine aortic arch. *Magn Reson Med* 2003; 50:69-74.
 37. Mitchell GF, Parise H, Benjamin EJ, et al. Changes in arterial stiffness and wave reflection with advancing age in healthy men and women: the Framingham Heart Study. *Hypertension* 2004; 43:1239-45.
 38. Asmar RG, Topouchian JA, Benetos A, Sayegh FA, Mourad JJ, Safar ME. Non-invasive evaluation of arterial abnormalities in hypertensive patients. *J Hypertens Suppl* 1997; 15:S99-107.
 39. Hartley CJ, Taffet GE, Michael LH, Pham TT, Entman ML. Noninvasive determination of pulse-wave velocity in mice. *Am J Physiol* 1997; 273:H494-H500.
 40. Metafratzi ZM, Efremidis SC, Skopelitou AS, De RA. The clinical significance of aortic compliance and its assessment with magnetic resonance imaging. *J Cardiovasc Magn Reson* 2002; 4:481-91.
 41. Rensen SS, Niessen PM, van Deursen JM, et al. Smoothelin-B deficiency results in reduced arterial contractility, hypertension, and cardiac hypertrophy in mice. *Circulation* 2008; 118:828-36.





Contrast Media Mol Imaging. 2013 8(1):63-71

Chapter 4

Contrast enhancement by lipid-based MRI contrast agents in mouse atherosclerotic plaques; a longitudinal study

Brigit den Adel, Linda M. van der Graaf, Ivo Que, Gustav J. Strijkers, Clemens Löwik, Robert E Poelmann and Louise van der Weerd

ABSTRACT

The use of contrast-enhanced MRI to enable *in vivo* specific characterization of atherosclerotic plaques is increasing. In this study the intrinsic ability of two differently sized gadolinium-based contrast agents to enhance atherosclerotic plaques in ApoE^{-/-} mice was evaluated with MRI. We obtained a kinetic profile for contrast enhancement, as the literature data on optimal imaging time points is scarce, and assessed the more long-term kinetics. Signal enhancement in the wall of the aortic arch, following intravenous injection of paramagnetic micelles and liposomes was followed for 1 week. *In vivo* T1-weighted MRI plaque enhancement characteristics were complemented by fluorescence microscopy of NIR₆₆₄ incorporated in the contrast agents and quantification of tissue and blood Gd-DTPA. Both micelles and liposomes enhanced contrast in T1-weighted MR images of plaques in the aortic arch. The average contrast-to-noise ratio increased after liposome or micelle injection to 260% or 280%, respectively, at 24 hours after injection, compared to a pre-scan. A second wave of maximum contrast enhancement was observed around 60-72 hours after injection, which only slowly decreased towards the 1 week end-point. Confocal fluorescence microscopy and whole body fluorescence imaging confirmed MRI-findings of accumulation of micelles and liposomes. Plaque permeation of contrast agents was not strongly dependent on size in this mouse model. Our results show that intraplaque accumulation over time of both contrast agents leads to good plaque visualization for a long period. This inherent intraplaque accumulation might make it difficult to discriminate passive from targeted accumulation. This implicates that in the development of targeted contrast agents on a lipid-based backbone extensive timing studies are required.

INTRODUCTION

Atherosclerotic disease remains the primary cause of mortality in industrialized countries, despite the clinical advances that have been made in the prevention and treatment of this disease over the past 20 years¹. Studies have shown that more than two-third of acute coronary syndromes occur in patients who are classified as being at intermediate risk according to traditional Framingham Score risk-stratification methods. Based on these findings, it is clear that noninvasive diagnostic strategies are required to accurately assess the extent of cardiovascular disease in order to predict which patients most urgently need treatment.

High-resolution magnetic resonance imaging (MRI) has emerged as one of the most promising techniques for the direct and non-invasive evaluation of atherosclerotic plaques²⁻⁵. The natural differences in tissue structure between the healthy vessel wall and atherosclerotic lesions result in contrast differences on T1w, T2w and DW MRI scans⁶. However, particularly at the early stages discriminating intimal thickening and developing lesions from healthy vessels is not straightforward because of the limited sensitivity, partial volume effects and motion artifacts inherent to these scans.

Apart from the afore mentioned 'traditional' MR imaging approaches, there is increasing interest in the use of MR contrast agents that enable a more refined characterization of atherosclerotic plaques^{7,8}. Dynamic contrast-enhanced imaging using small gadolinium-based contrast agents such as gadofluorine^{9,10} and gadodiamide¹¹ has been explored to investigate plaque neo-vascularization and permeability. Although the above studies have demonstrated that imaging of plaques and even intraplaque processes is feasible in patients, these Gd chelates still have an inherently low relaxivity ($r_1 \sim 3.4 \text{ mmol}^{-1} \text{ s}^{-1}$ at 1T), resulting in only a modest signal enhancement.

A number of strategies have been developed to amplify the relaxivity and to deliver sufficient quantities of Gd *in vivo* in order to detect atherosclerotic lesions. One of these strategies is to use lipid-based nanoparticles like micelles or liposomes, carrying high payloads of amphipathic Gd chelates embedded in the outer lipid membrane. These particles may contain as many as 50,000 Gd atoms, resulting in a relaxivity per particle that is magnitudes higher than of single Gd chelates¹². Other previously explored approaches for contrast enhanced MRI of atherosclerotic plaque include perfluorocarbon nanoparticles¹³ and iron oxide particles¹⁴.

Lipid-based nanoparticles like micelles and liposomes accumulate in atherosclerotic plaques due to a leaky vasculature, ineffective lymphatic drainage, and enhanced endocytotic activity. This phenomenon provides a mechanism for passive targeting of nanoparticles to atherosclerotic sites¹⁵. The MR contrast agents used in this paper are polyethylene glycol2000 (PEG2000)-micelles and liposomes that include gadolinium diethylenetriamine pentaacetic acid (Gd-DTPA)-based lipids^{16,17}. This platform has been used to image macrophages in plaques and oxidized low-density lipoprotein (LDL). These nanoparticles have a longer half-life than regular micelles^{18,19} due to the protective "stealth" effect of the outer shell of PEG chains, which reduces recognition by opsonins and consequently clearance¹⁸, resulting in increased accumulation at inflamed sites^{20,21}.

The pharmacokinetics of these nanoparticles and the resulting concentration gradient between blood and atherosclerotic lesion determines the wash-in and washout kinetics, and thereby the timing of maximum contrast enhancement of the plaque^{20,22}. In practice, contrast-enhanced MRI using nanoparticles is typically performed at baseline and either followed for a short period of time (few hours) or measured at a single time point within 1 to 48 hours after contrast agent administration. Data on the optimal imaging time points are scarce^{23,24}. Even though the pharmacokinetics of larger liposomes, iron oxides and perfluorocarbon nanoparticles has been extensively studied²⁵⁻²⁷, very little is known about the dynamics of contrast enhancement of micelles and liposomes in atherosclerotic plaque during longer periods of time. Longitudinal follow-up of plaque development and therapy response through imaging is highly desirable and for that purpose Gd-loaded micelles and liposomes are more and more applied. In this respect, detailed information on the accumulation and clearance kinetics of contrast agents is of major importance.

In this study, we therefore aimed 1) to obtain a kinetic profile for contrast enhancement and 2) to assess the more long-term kinetics of Gd-loaded micelles and liposomes. We assessed the passive kinetic behavior of Gd-loaded micelles and liposomes in atherosclerotic plaques in the aortic arch of 1-year-old ApoE^{-/-} mice over a period of 1 week using MRI and plasma profiles. Liposomes and micelles were labeled with a fluorescent marker for validation of the MRI finding using histology and for *in vivo* whole-body biodistribution measurements.

MATERIALS AND METHODS

Hardware

All experiments were performed with a vertical 9.4 T magnet (Bruker, Ettlingen, Germany) supplied with an actively shielded Micro2.5 gradient system of 1 T/m and a 30 mm transmit/receive birdcage RF coil, using Paravision 4.0 software.

Contrast Agents

Micelles and liposomes were prepared by lipid film hydration as described previously²⁸. A mixture of the appropriate amounts of lipids (typically 120 mol of total lipid) was dissolved in chloroform/

methanol 3:1 (vol/vol) in a round-bottom flask. A lipid film was made under reduced pressure using rotary evaporation at 37 °C and dried under a stream of nitrogen. For micelles Gd-DTPA-BSA (Gd-DTPA-bis(stearylamide) and PEG2000-DSPE (1,2-distearoyl-sn-glycero-3-phosphoethanolamine-N-[methoxy(polyethyleneglycol)-2000]) were used at a molar ratio of 1.5/1.35. For fluorescent detection, 0.1 mol% NIR664-DSPE (SyMO-CHEM B.V., Eindhoven, The Netherlands) was added. The lipid film was subsequently hydrated in HEPES buffered saline (HBS), containing 20 mM HEPES and 135 mM NaCl (pH 7.4) and vigorously stirred at 65 °C for 45 min. For liposomes, Gd-DTPA-BSA (Gd-DTPA-bis(stearylamide)), DSPC (1,2-distearoyl-sn-glycero-3-phosphocholine), cholesterol, and PEG2000-DSPE were used at a molar ratio of 0.75/1.10/1/0.15 and rehydrated in HBS as described for micelles. The resulting lipid dispersion was extruded sequentially four times through polycarbonate membrane filters (Nuclepore, Pleasanton, USA) with a pore diameter of 200 nm and subsequently 10 times through filters with a pore diameter of 100 nm using a Lipofast Extruder (Avestin, Canada). The temperature during extrusion was 65°C.

The size and size distribution of the contrast agents were determined by dynamic light scattering (DLS) at 25°C with a Malvern 4700 system (Malvern ZetaSizer Nano S, Malvern, UK). The micelles had a mean size of 16 nm and liposomes had a mean size of 100 nm. Both micelles and liposomes had a polydispersity index below 0.1, which indicates a narrow size distribution. The relaxivity was measured at 37°C and 9.4 T. The phospholipid content of the liposome preparations was determined by phosphate analysis according to Rouser after destruction with perchloric acid²⁹. pH stability was assessed using DLS at different pH, ranging from 4.0 till 9.0.

***In vivo* Experiments**

All experiments were conducted in accordance with the Dutch guidelines for research animal care at our institution. A schematic overview of the experimental design and groups of mice (n=34) can be found in figure 1. Each block in this figure represents an experimental group. Thirty-four groups (n=5 per group) of aged (between 10 and 14 months old) male ApoE^{-/-} mice on a C57BL/6/J background were fed a normal chow diet. For MRI and assessment of contrast agent distribution 30 groups were used: each mouse was scanned before administration of contrast agent and every 6 hours for 142 hours (6 days) after intravenous injection of the equivalent of 50 µmol Gd³⁺-DTPA lipid/kg bodyweight (i.e. 1.25 µmol Gd/25 g body weight) in 200 µl micelles or liposomes (figure 1). Mice were anesthetized during MRI with isoflurane (± 2% in oxygen and air). At every 6 hour time-point till 30 hours post injection a group of mice (n=5) was taken out of the experiment and sacrificed by transcardial perfusion for histological validation of MRI images.

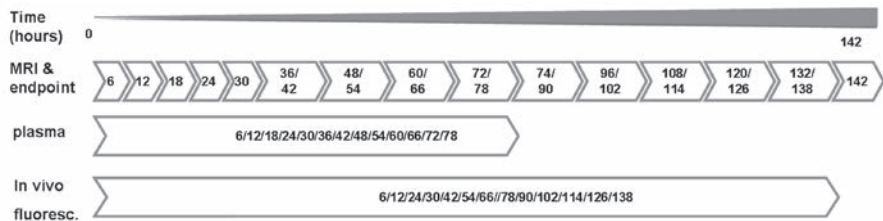


Figure 1 | A schematic overview of the *in vivo* experiments shows the distribution of different groups of animals over the experiments. Each block represents a group of 5 animals that is sacrificed at the end time indicated in the box.

After 30 hours, groups of mice were taken out of the experiment every 12 hours. In total 16 groups of mice for both micelles and liposomes were used to monitor the *in vivo* behavior of these nanoparticles.

2 separate groups of mice were used to follow kinetics of the contrast agents in blood. Moreover for *in vivo* fluorescent imaging 2 groups of mice were used.

MRI protocols

In vivo

At the start of each examination, several 2D FLASH scout images were recorded in the transverse and axial planes through the heart to determine the orientation of the aortic arch. A modified FLASH sequence with a navigator echo (IntraGate) was used for retrospective CINE MRI with the following parameters:

- 1) Cross sections of the aortic arch: RF pulse 1 ms; flip angle 15°; TR 31.4 ms; TE 2.96 ms; navigator echo points 64; 10 cardiac frames; FOV 1.8*1.8 cm²; matrix 128*128; in-plane resolution 141*141 mm²; 6 slices, slice thickness 0.4 mm; number of repetitions 400; total acquisition time approximately 20 min.
- 2) For a frontal view of the aortic arch the MR sequence was slightly adapted: TR 15.7 ms, TE 2.96 ms, 3 slices, slice thickness 0.5 mm, total acquisition time approximately 10 min.

During the examination, the respiration rate was continuously monitored using a balloon pressure sensor connected to the ECG/respiratory unit. The isoflurane concentration was adjusted to keep the respiration rate between 50 and 90 respirations/min.

Ex vivo

Blood samples were drawn from the tail vein from n=5 mice for both micelle and liposome injected mice every 6 hours for 78 hours. T1 values of plasma samples were determined using a saturation recovery protocol spin-echo sequence with the following parameters: TE 7 ms, TR 25, 20, 15, 10, 8, 6, 5, 4, 3, 2, 1.6, 1.2, 1.0, 0.8, 0.6, 0.4, and 0.3 s, matrix 128*128, resolution 195*195 μm², 2 slices, slice thickness 1 mm.

The T1 values of the various ROIs were determined using the 3-parameter fit function

$$\mathbf{M(t) = M0 (1-exp[-t/T1])}. \quad \text{[Eq1]}$$

The change in longitudinal relaxation rate ΔR1 values of the blood over time were determined by

$$\mathbf{\Delta R1(t) = (1/T1[Gd(t)]) - 1/T[0]}. \quad \text{[Eq2]}$$

The ΔR1 values were fitted using a mono-exponential decay function

$$\mathbf{\Delta R1(t) = Ae^{-ln(2)t/t_{1/2}}}. \quad \text{[Eq3]}$$

where A is the initial quantity of gadolinium, and t_{1/2} is the circulation half-life of gadolinium in the blood.

MRI Analysis

Images were analyzed using ImageJ software. Black blood images in 3 to 4 adjacent slices of cross-sections through the aortic arch were analyzed. ROIs were drawn around the plaque region in the vessel wall (*I_{wall}*). A 2nd ROI was drawn in the surrounding muscle tissue of the shoulder girdle (*I_{muscle}*). Furthermore, an ROI was placed outside the animal to measure the noise level (*stdev_{noise}*) (Figure 2).

The contrast-to-noise ratio was defined as

$$\mathbf{CNR = (I_{wall} - I_{muscle})/stdev_{noise}}. \quad \text{[Eq4]}$$

which is a measure how well the lesioned wall can be discriminated from the surrounding tissue. CNR values are shown as mean ± standard deviation.

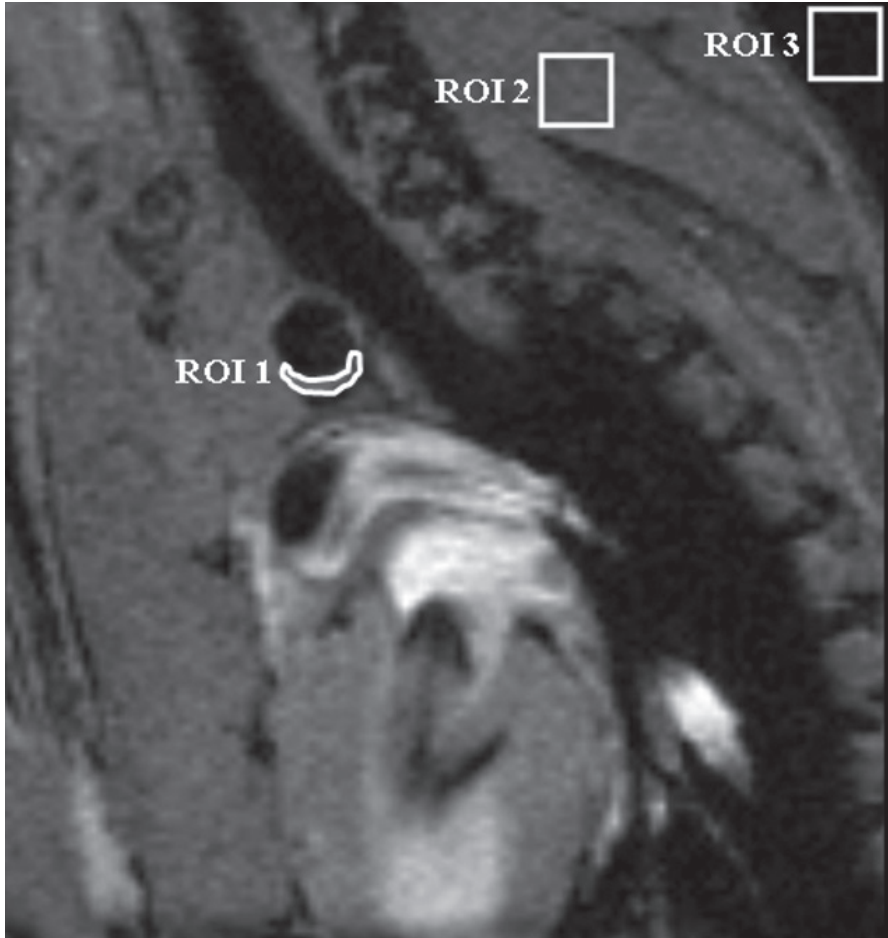


Figure 2 | Contrast to noise ratios of atherosclerotic plaques were determined in black blood images of a cross-section of the aortic arch by ROI 1, the signal intensity of the plaque in the vessel wall (I_{wall}) corrected on ROI 2, the signal intensity of surrounding muscle tissue (I_{muscle}) and ROI 3, the standard deviation of the noise ($\text{stdev}_{\text{noise}}$).

Optical Imaging

Whole body distribution of NIR664 was followed for 7 days at 12 hour intervals using 700 nm laser excitation (IVIS spectrum). OptiView software was used to create both intensity and lifetime images and a pixel-to-pixel ROI comparison.

Gd-DTPA ELISA

Gd-DTPA concentrations in tissue homogenates of liver, kidney, lungs and the aortic arch were determined using an enzyme immunoassay test kit (BioPAL Inc, Huissen, The Netherlands) with a sensitivity limit of 0.5 pg. Tissue samples (lungs, liver, kidney, spleen, heart, aortic arch) from 5 mice per contrast agent per time point were harvested at 6, 12, 18, 24, 30, 48 and 60 hours after contrast agent injection.

Histology

Aortic arches were frozen in Tissue Tek® (Sakura Finetek Europe, Zoetermeer, The Netherlands) and cut into serial 5 µm sections. Sections were stained with Oil Red O for lipid deposition and hematoxylin eosin for gross morphology, followed by bright-field microscopy.

To detect the presence of F4-80 positive macrophages sections were fixed in 10% isopropanol and incubated overnight at room temperature with a rat polyclonal primary antibody against F4-80 (1:100, SantaCruz). Rabbit anti rat conjugate (1:200, DAKO) with normal rabbit serum diluted in PBS was incubated for 1 hour at room temperature as secondary antibody. Biotin labeling was followed by development using DAB (Vector Laboratories Inc., United Kingdom) and counterstain was performed with Mayer's hematoxylin. Sections were analyzed using bright-field microscopy.

Imaging of micelle and liposome fluorescence was performed using a Leica TCS-SL confocal laser scanning microscope interfaced to a DM6000B microscope. NIR₆₆₄ was excited with a 633 nm HeNe laser, emission was filtered through a band-pass filter of 650-710 nm. Autofluorescence of elastic lamellae was detected at an emission wavelength of 450-500 nm.

Statistical analysis

Data are presented as the mean ± standard deviation. Statistical analysis was performed using SPSS 15.0 ANOVA for computations within and between groups. Results were considered statistically significant at $p < 0.05$.

RESULTS

Nanoparticle characteristics

The manufactured nanoparticles were characterized using dynamic light scattering (DLS), showing that the micelles had a mean hydrodynamic diameter of approximately 16 nm with a polydispersity index of 0.1, indicating a narrow size distribution. Liposomes were approximately 5-6 fold larger than micelles, with a mean diameter of 100 ± 0.05 nm. Micelles had a higher r_1 relaxivity per mmol Gd compared to liposomes (table 1), both at 1.41 T and 9.4 T at 37 °C and pH 7.3. For liposomes it was already known that they are stable within a physiological pH range (30). Micelles were tested for stability with changing pH; pH lowering did not compromise micelle stability. Lowering the pH to 4.0 results in only a very modest change in size distribution from 16 to 15.4 nm. Increase in pH to 9.0, however, results in increased hydrodynamic diameter of micelles, which may be explained by hypertonicity of the solvent.

Table 1. Characteristics of micelles and liposomes

pH	Hydrodynamic diameter (nm)			r_1 ($s^{-1}mM^{-1}$)	
	7.3	4.0	9.0	1.4 T, 37°C	9.4 T room temp
Micelles	16.1 ± 0.2	15.4	20.2	11.4	5.8
Liposomes	103 ± 0.4	101 ± 0.2	121 ± 0.9	6.5	2.5

***In vivo* MRI study**

In line with contrast agent concentrations applied in previous studies^{16,31}, ApoE^{-/-} mice were injected intravenously with a single dose of contrast agent at a concentration of 50 $\mu\text{mol Gd}^{3+}$ -DTPA lipid per kg bodyweight. Axial and sagittal T1w images of the aortic arch were made before contrast agent injection, as well as directly after contrast agent administration. Scans were repeated at several time points after injection, for up to 24 hours. T1-weighted MRI images showed a strong bright blood effect after an intravenous bolus injection of liposomes or micelle. The blood enhancement gradually disappeared during the 24 hours after injection due to clearance of the particles from the blood stream. Contrast enhancement was analyzed by drawing regions of interest on plaque areas at the basis of the aortic arch in black blood images (figure 2). Average CNR increased gradually after liposome or micelle injection to 260% or 280% respectively at 24 hours after micelle injection when compared to the pre-scan (figure 3A). However, the CNR had not reached a plateau at 24 hours post injection, which let us to postulate that micelles and liposomes were still circulating and entering atherosclerotic plaques after these time points.

Therefore, the fluctuations in CNR were monitored over time for a longer period of 1 week after injection, both for micelles and liposomes (figure 3B). One day after contrast agent injection, the signal intensities of both nanoparticles started to drop significantly. However, a second contrast enhancement peak was observed at around 60-72 hours after injection, which only slowly decreased towards the 1 week post injection end-point. The area in the vessel wall with clear contrast enhancement was larger at the 2nd peak contrast point than within the first 24 hours after administration (figure 3B).

Plasma kinetics

Plasma T1 values were determined to assess the amount of circulating contrast agent, using blood samples obtained from the tail vein taken at regular intervals after contrast agent injection. Plasma T1 values showed an inverse relation to the fluctuations in CNR observed in atherosclerotic plaques (figure 4A). Shortly after contrast agent injection, a sharp decrease in plasma T1 was observed, which slowly increased to almost normal plasma T1 values between 10 to 30 hours after injection. Thereafter, a second decrease in T1 values was observed for both contrast agents, which was more prominent in the case of micelles.

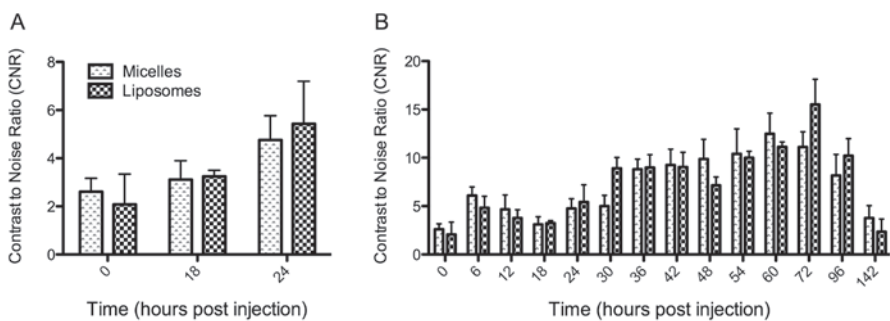


Figure 3 | Contrast to noise ratios of atherosclerotic plaques were determined at different time points after micelle or liposome injection and plotted against time. Panel A shows CNR follow-up till 24 hours post injection, whereas panel B shows CNR follow-up for several days.

Based on the $\Delta R1$ values during the first 24 hours (before recirculation), the blood circulation half-life was calculated to be 8.1 hours for micelles ($R^2 = 0.95$) and 5.3 hours ($R^2 = 0.96$) for liposomes, assuming mono-exponential behavior (figure 4B).

***In vivo* detection of whole body biodistribution**

To further assess the pharmacokinetics of the nanoparticles, we measured the biodistribution with *in vivo* fluorescence imaging using the NIR₆₆₄ fluorochrome incorporated in the lipid layer of the respective nanoparticles. In line with the enhancement pattern observed with MRI, contrast agent accumulation was observed in the region of the aortic arch, with maximum accumulation around 40 and 60 hours after injection for micelles and liposomes respectively (figure 5). However, a biphasic pattern in fluorescence, like detected with MRI in the aortic arch region could not be observed. In the first 15 min after injection, both the renal and hepatic regions became positive, indicative for primary accumulation and/or elimination via that route. Steady, but slowly fading, accumulation in the neck region (maybe the carotid arteries) and axillary lymph nodes was observed over the entire measurement period of 7 days. Apart from the expected uptake and clearance routes, the paws of all animals that were injected with micelles and liposomes showed NIR₆₆₄ fluorescence, possibly indicative of poor circulation in the paws of these aged mice. Excretion of the fluorescent dye was observed in the feces, confirming the involvement of the liver in the metabolism of the contrast agents.

Assessment of gadolinium content

An enzyme-linked immunosorbent assay (ELISA), originally developed for the detection of Gd-DTPA in serum and urine, was performed on tissue homogenates from internal organs harvested every 6 hours after contrast agent injection, i.e. directly after MRI at the respective time points. The ELISA was used to indirectly determine the biodistribution of micelles and liposomes via Gd-DTPA in liver, lungs, kidney, spleen, aortic arch and heart. 6 hours after contrast agent injection. We observed Gd accumulation in the liver of about 4% and 7% of the injected dose (ID) and spleen of about 2% and 3% of ID for micelles and liposomes respectively. The lungs and kidney showed less accumulation, in the order of 0.5-1% of the ID after 6 hours (figure 5). In all these organs, Gd was cleared over the 60 hours of the experiment. In contrast, both the heart and the aortic arch showed an initial decrease in gadolinium content followed by a steady secondary increase in Gd during the second to third day after injection, consistent with the contrast increase observed on MRI (figure 6).

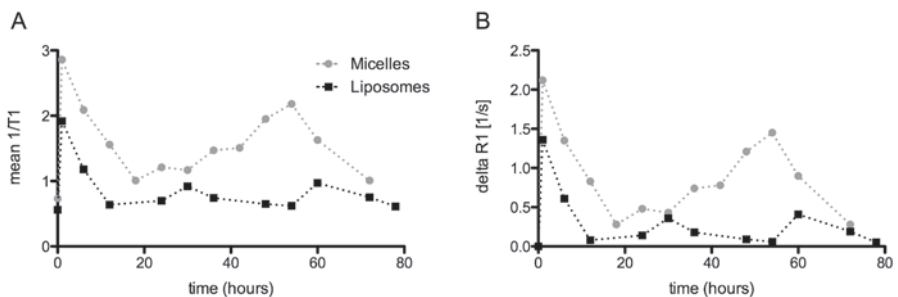


Figure 4 | 1/T1 values in panel A describes the inverted pattern of micelle and liposome blood circulation compared to the accumulation patterns observed in the aortic arch. In panel B the temporal changes in R1 values illustrate the blood circulation and circulation half-life was calculated over the first 24 hours.

Immunohistochemistry

To examine which components within atherosclerotic plaques are preferably targeted by micelles and liposomes, confocal laser scanning microscopy (CLSM) and light microscopy was performed on cryosections of the aortic arch. For CLSM, elastic lamellae were autofluorescent in the green spectrum; liposomes and micelles were already labeled with NIR₆₆₄.

Early after contrast agent injection, at 12 hours, presence of contrast agents within atherosclerotic plaques could be confirmed (figure 7). However, at this time no uptake of the nanoparticles in the macrophages or macrophage-derived foam cells could be observed. At later time points, starting 24 hours after injection, it was observed that liposomes were mainly found associated with elastic lamellae, whereas this was not the case for micelles (figure 7). Micelles were found in macrophage positive areas from 12 hours after injection onwards. Staining for smooth-muscle cells with α -actin did not show any micelle or liposome uptake in these cells (data not shown).

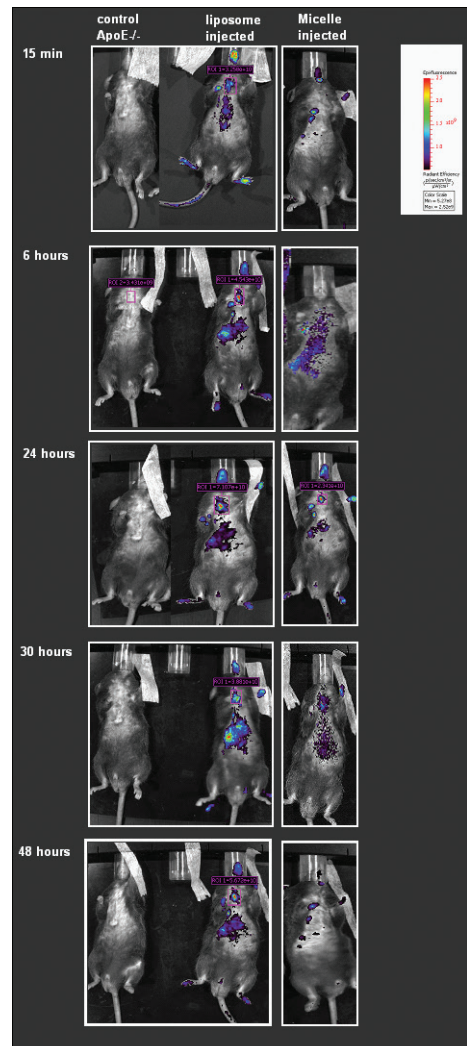


Figure 5 | Whole body fluorescence imaging of ApoE^{-/-} mice after injection of liposomes or micelles respectively shows the distribution patterns over time of the NIR₆₆₄ fluorophore incorporated in the contrast agents.

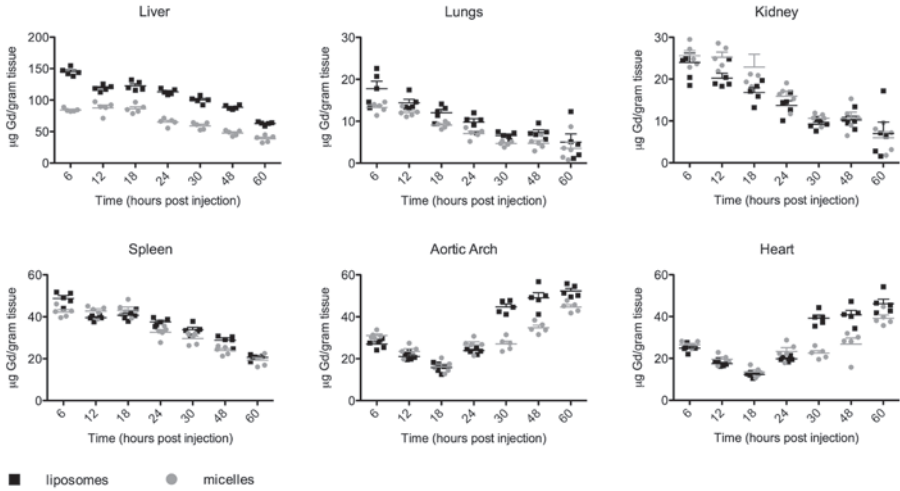


Figure 6 | Gd-DTPA accumulation was determined at several time points by ELISA on tissue homogenates in liver (A), lungs (B), kidneys (C), spleen (D), heart (E) and aortic arch (F). An increase in Gd-DTPA can be observed in the hearts and aortic arch of animals injected with both micelles and liposomes starting around 30 hours post injection.

This suggests that liposomes remain restricted to the extracellular space of the atherosclerotic plaque and that there was no cellular uptake of the contrast agent, whereas micelle retention is linked to the presence of macrophages. Some colocalization was observed for the elastic lamellae and the micelles in the atherosclerotic plaque. Although in all sections micelles and liposomes were found throughout the entire aortic plaque, the contrast agents were heterogeneously distributed, with most micelles and liposomes present in the center of the plaque early after injection, but in the cap regions of the plaque at later time points.

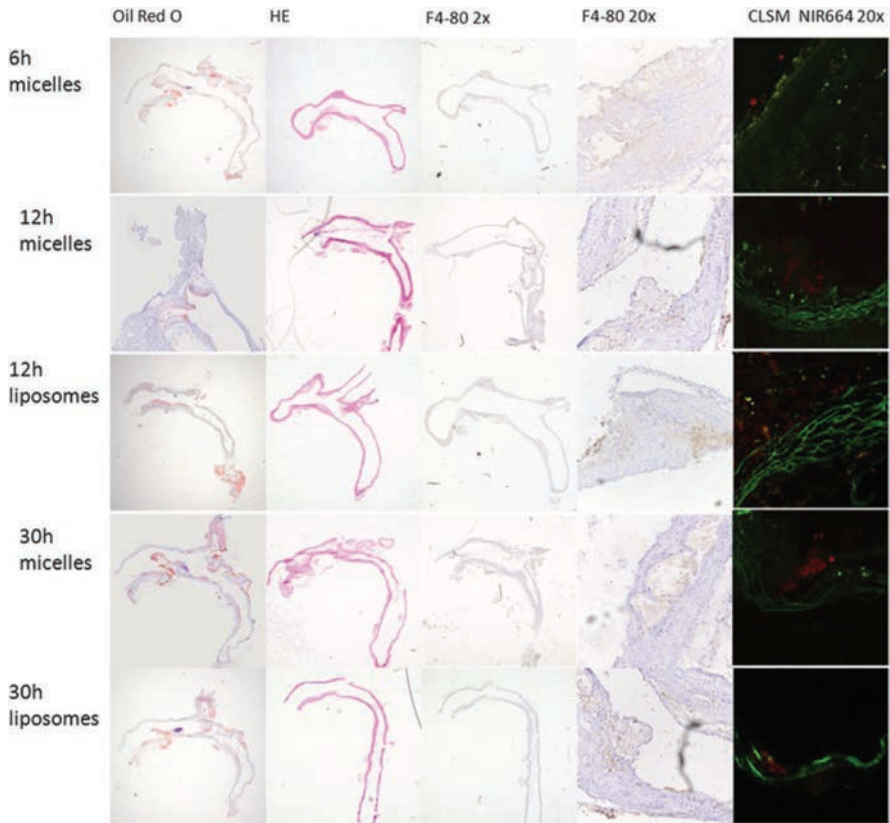


Figure 7 | Histology of aortic arch after contrast agent injection. Lipid deposition in vessel wall is visualized with Oil Red O, gross morphology with HE. Presence of macrophages in the plaques is visualized via F4-80. NIR₆₆₄ in contrast agents is visualized in corresponding plaque regions on adjacent histological slices.

DISCUSSION

Biphasic enhancement on MRI

In this study we determined the pharmacokinetics of untargeted lipid-based Gd-loaded micelles and liposomes in the ApoE^{-/-} atherosclerotic mouse. ApoE^{-/-} mice are characterized by the spontaneous and diet-induced occurrence of atherosclerosis in their arteries at sites with low and oscillatory flow patterns⁸. The occurrence of atherosclerotic plaques is preceded by damage to the endothelial layer, rendering the endothelium leaky. As a consequence molecules, but also nanoparticles like micelles and liposomes, can pass the endothelial lining and penetrate atherosclerotic plaques where they may be retained.

Here we show that in the unaffected vessel wall no MR contrast enhancement occurred, whereas at the classical atherosclerosis-prone sites increased signal intensity was observed with peak contrast enhancement at two time points around 12 and around 60 hours after injection in ApoE^{-/-} mice. Previous studies already mention peak contrast points shortly after injection (minutes) which can be attributed to a first passage effect and peak enhancements in the period of 12-24 hours after contrast agent injection, with contrast agent follow-up ranging from 24 to 48 hours^{24,32}.

The difference between the previous described and our recent observations may be attributed to imaging timing (much later time points than previously) and possibly also increased sensitivity to the detection of contrast enhancement by the use of cine MRI.

This biphasic kinetic pattern was present for both liposomes and micelles. For all time points, the areas of MRI contrast enhancement showed good agreement with the Gd-DTPA concentration in tissues and the presence of NIR664 on the histological sections, suggesting that the paramagnetic and fluorescent lipids remain co-localized for the entire observation period.

During the second wave of enhancement, we still observed co-localization of the fluorescence and Gd signal. When contrast agents are administered intravenously there may be some local extravasation encouraged by mass action, owing to particle size and loading dose. The second contrast wave may also be due to slow release of these particles from the liver or more likely from contrast agent loaded macrophages migrating out of the spleen in the days following contrast agent injection, as previously observed with ^{19}F in the early days of RES imaging³³. At this time point, the micelles and liposomes were probably no longer intact, but one could easily interpret the results differently because we did not observe differences in the time course or localization within the plaque of the fluorescent and Gd components based on the histological evaluation. Whether or not the particles were still intact, this second contrast wave should be considered for longitudinal experiments, as it will be a confounding factor in follow-up studies.

Passive accumulation in plaques: micelles versus liposomes

From the microscopic analysis, it became apparent that the uptake mechanism of micelles in atherosclerotic plaque was most likely related to passive diffusion of the micelles over the abnormal endothelial lining followed by uptake into phagocytic cells like monocytes and macrophages. Liposomes were also found inside the plaque, but mainly outside cells and close to the elastic laminae.

No significant liposome or micelle uptake was observed in normal vessel walls of ApoE^{-/-} mice with MRI or histology. LSCM showed a predominant first uptake of the contrast agents into the extracellular space of the plaque on the laminar side of the lesion in ApoE^{-/-} mice indicative for the enhanced permeability of the vessel wall. Furthermore, colocalization of the micelles with cell nuclei and F4-80 positive cells revealed that micelles were retained in the plaque by uptake in cells, whereas this was not the case for liposomes. We did not observe ingestion of the nanoparticles within circulating monocytes or macrophages in the first hours after injection, as determined by blood smears. This however does not rule out that ingestion does occur at a low percentage and that these cells then migrate into the plaque.

Finally, maximum signal enhancement of the plaque occurred at relatively late time points suggestive for slow uptake and accumulation of both liposomes and micelles in the plaque. The difference in behavior inside the plaque of the particles may be due to the difference in size which makes it favorable to phagocytose micelles but not liposomes³⁴

Clearance and distribution pathways

During the first phase after injection, contrast agents that were cleared from the blood accumulated in various organs, as shown by the *in vivo* whole body biodistribution studies, and the Gd- content in tissue homogenates.

Both micelles and liposomes are metabolized through the liver and to a much lesser extent by the kidneys. The liver may serve as a reservoir for the nanoparticles as the fluorescence and Gd-DTPA content remains high over time and clearance from this organ is slow. Compared to micelles, liposomes accumulated more in the spleen, liver and lungs of mice, possibly due to the fact that

liposomes are a magnitude larger than micelles and therefore get trapped in the capillary beds in these organs. At atherosclerotic areas this difference disappears as the damaged endothelial lining of atherosclerotic layer allows easier passage of particles. Both in micelle- as well as liposome-injected mice a steady decline in Gd content in the spleen was observed, which suggests involvement of the spleen in the redistribution of the Gd-lipids.

We did not observe a biphasic enhancement pattern for the aortic plaques in the *in vivo* fluorescence study. However, this does not imply it is not present. On MRI images we report differences in T1 in the plaque with high sensitivity and spatial accuracy, and thereby indirectly on the fluctuations in the amount of contrast agent internalized in the plaque. In contrast, specific quantification of the fluorescent signal in the aortic arch was not possible due to the low spatial resolution of *in vivo* fluorescence cameras and the relatively large amount of micelle and liposome uptake in the entire thoracic region (i.e. in the heart, lymph nodes and large arteries). As reported previously, liposomes and micelles did not produce a sufficient signal to visualize the plaques in its anatomical context *in vivo*, presumably because of insufficient tissue penetration of the exciting and emitted signals³⁵. *Ex vivo* visualization of the aortic arch however showed increased fluorescence in the aortic tree and at the basis of the aortic arch in line with our histological findings. Overall we observed no real differences in tissue distribution between micelles and liposomes, which is in line with previous studies using other nanoparticles^{26,27,32,36}.

CONCLUSIONS

The maximum enhancement for Gd-loaded micelles and liposomes was shown to be dependent on contrast agent size and blood circulation kinetics, which underscores that plaque enhancement by nontargeted and targeted contrast agents must be interpreted with care. Our results indicate that the timing of contrast-enhanced MRI is of utmost importance and will need to be optimized for every novel contrast agent and animal model.

REFERENCES

- 1 Sanz J, Moreno PR, Fuster V. The year in atherothrombosis. *J Am Coll Cardiol* 2008 Mar 4;51(9):944-55.
- 2 Choudhury RP, Fuster V, Fayad ZA. Molecular, cellular and functional imaging of atherothrombosis. *Nat Rev Drug Discov* 2004 Nov;3(11):913-25.
- 3 Itskovich VV, Samber DD, Mani V, Aguinaldo JG, Fallon JT, Tang CY, et al. Quantification of human atherosclerotic plaques using spatially enhanced cluster analysis of multicontrast-weighted magnetic resonance images. *Magn Reson Med* 2004 Sep;52(3):515-23.
- 4 Ruehm SG, Corot C, Vogt P, Kolb S, Debatin JF. Magnetic resonance imaging of atherosclerotic plaque with ultrasmlal superparamagnetic particles of iron oxide in hyperlipidemic rabbits. *Circulation* 2001 Jan 23;103(3):415-22.
- 5 Yuan C, Hatsukami TS, Cai J. MRI plaque tissue characterization and assessment of plaque stability. *Stud Health Technol Inform* 2005;113:55-74.
- 6 Sanz J, Fayad ZA. Imaging of atherosclerotic cardiovascular disease. *Nature* 2008 Feb 21;451(7181):953-7.
- 7 Saraste A, Nekolla SG, Schwaiger M. Cardiovascular molecular imaging: an overview. *Cardiovasc Res* 2009 Sep 1;83(4):643-52.
- 8 Van der Heiden K, Hierck BP, Krams R, de CR, Cheng C, Baiker M, et al. Endothelial primary cilia in areas of disturbed flow are at the base of atherosclerosis. *Atherosclerosis* 2008 Feb;196(2):542-50.
- 9 Barkhausen J, Ebert W, Heyer C, Debatin JF, Weinmann HJ. Detection of atherosclerotic plaque with Gadofluorine-enhanced magnetic resonance imaging. *Circulation* 2003 Aug 5;108(5):605-9.
- 10 Sirol M, Itskovich VV, Mani V, Aguinaldo JG, Fallon JT, Misselwitz B, et al. Lipid-rich atherosclerotic plaques detected by gadofluorine-enhanced in vivo magnetic resonance imaging. *Circulation* 2004 Jun 15;109(23):2890-6.
- 11 Kerwin WS, O'Brien KD, Ferguson MS, Polissar N, Hatsukami TS, Yuan C. Inflammation in carotid atherosclerotic plaque: a dynamic contrast-enhanced MR imaging study. *Radiology* 2006 Nov;241(2):459-68.
- 12 Mulder WJ, Strijkers GJ, van Tilborg GA, Griffioen AW, Nicolay K. Lipid-based nanoparticles for contrast-enhanced MRI and molecular imaging. *NMR Biomed* 2006 Feb;19(1):142-64.
- 13 Tran TD, Caruthers SD, Hughes M, Marsh JN, Cyrus T, Winter PM, et al. Clinical applications of perfluorocarbon nanoparticles for molecular imaging and targeted therapeutics. *Int J Nanomedicine* 2007;2(4):515-26.
- 14 Burtea C, Laurent S, Mahieu I, Larbanoix L, Roch A, Port M, et al. In vitro biomedical applications of functionalized iron oxide nanoparticles, including those not related to magnetic properties. *Contrast Media Mol Imaging* 2010 Dec 29.
- 15 Peer D, Karp JM, Hong S, Farokhzad OC, Margalit R, Langer R. Nanocarriers as an emerging platform for cancer therapy. *Nat Nanotechnol* 2007 Dec;2(12):751-60.
- 16 Mulder WJ, Strijkers GJ, Briley-Saboe KC, Frias JC, Aguinaldo JG, Vucic E, et al. Molecular imaging of macrophages in atherosclerotic plaques using bimodal PEG-micelles. *Magn Reson Med* 2007 Dec;58(6):1164-70.
- 17 Mulder WJ, Griffioen AW, Strijkers GJ, Cormode DP, Nicolay K, Fayad ZA. Magnetic and fluorescent nanoparticles for multimodality imaging. *Nanomedicine (Lond)* 2007 Jun;2(3):307-24.
- 18 Lukyanov AN, Torchilin VP. Micelles from lipid derivatives of water-soluble polymers as delivery systems for poorly soluble drugs. *Adv Drug Deliv Rev* 2004 May 7;56(9):1273-89.
- 19 Torchilin VP. Structure and design of polymeric surfactant-based drug delivery systems. *J Control Release* 2001 Jun 15;73(2-3):137-72.
- 20 Chono S, Tauchi Y, Deguchi Y, Morimoto K. Efficient drug delivery to atherosclerotic lesions and the antiatherosclerotic effect by dexamethasone incorporated into liposomes in atherogenic mice. *J Drug Target* 2005 May;13(4):267-76.
- 21 Metselaar JM, Storm G. Liposomes in the treatment of inflammatory disorders. *Expert Opin Drug Deliv* 2005 May;2(3):465-76.
- 22 Neubauer AM, Sim H, Winter PM, Caruthers SD, Williams TA, Robertson JD, et al. Nanoparticle pharmacokinetic profiling in vivo using magnetic resonance imaging. *Magn Reson Med* 2008 Dec;60(6):1353-61.
- 23 Klink A, Lancelot E, Ballet S, Vucic E, Fabre JE, Gonzalez W, et al. Magnetic resonance molecular imaging of thrombosis in an arachidonic acid mouse model using an activated platelet targeted probe. *Arterioscler Thromb Vasc Biol* 2010 Mar;30(3):403-10.
- 24 Beilvert A, Cormode DP, Chaubet F, Briley-Saebo KC, Mani V, Mulder WJ, et al. Tyrosine polyethylene glycol (PEG)-micelle magnetic resonance contrast agent for the detection of lipid rich areas in atherosclerotic plaque. *Magn Reson Med* 2009 Nov;62(5):1195-201.
- 25 McGoron AJ, Pratt R, Zhang J, Shiferaw Y, Thomas S, Millard R. Perfluorocarbon distribution to liver, lung and spleen of emulsions of perfluorotributylamine (FTBA) in pigs and rats and perfluorooctyl bromide (PFOB) in rats and dogs by 19F NMR spectroscopy. *Artif Cells Blood Substit Immobil Biotechnol* 1994;22(4):1243-50.
- 26 Waters EA, Chen J, Yang X, Zhang H, Neumann R, Santeford A, et al. Detection of targeted perfluorocarbon nanoparticle binding using 19F diffusion weighted MR spectroscopy. *Magn Reson Med* 2008 Nov;60(5):1232-6.
- 27 Waters EA, Chen J, Allen JS, Zhang H, Lanza GM, Wickline SA. Detection and quantification of angiogenesis in experimental valve disease with integrin-targeted nanoparticles and 19-fluorine MRI/MRS. *J Cardiovasc Magn Reson* 2008;10:43.
- 28 Mulder WJ, Strijkers GJ, Griffioen AW, van BL, Molema G, Storm G, et al. A liposomal system for

- contrast-enhanced magnetic resonance imaging of molecular targets. *Bioconjug Chem* 2004 Jul;15(4):799-806.
- 29 Rouser G, Fkeischer S, Yamamoto A. Two dimensional then layer chromatographic separation of polar lipids and determination of phospholipids by phosphorus analysis of spots. *Lipids* 1970 May;5(5):494-6.
- 30 Sabin J, Prieto G, Ruso JM, Hidalgo-Alvarez R, Sarmiento F. Size and stability of liposomes: a possible role of hydration and osmotic forces. *Eur Phys J E Soft Matter* 2006 Aug;20(4):401-8.
- 31 Briley-Saebo KC, Amirbekian V, Mani V, Aguinaldo JG, Vucic E, Carpenter D, et al. Gadolinium mixed-micelles: effect of the amphiphile on in vitro and in vivo efficacy in apolipoprotein E knockout mouse models of atherosclerosis. *Magn Reson Med* 2006 Dec;56(6):1336-46.
- 32 van Bochove GS, Paulis LE, Segers D, Mulder WJ, Krams R, Nicolay K, et al. Contrast enhancement by differently sized paramagnetic MRI contrast agents in mice with two phenotypes of atherosclerotic plaque. *Contrast Media Mol Imaging* 2011 Jan;6(1):35-45.
- 33 Ratner AV, Hurd R, Muller HH, Bradley-Simpson B, Pitts W, Shibata D, et al. 19F magnetic resonance imaging of the reticuloendothelial system. *Magn Reson Med* 1987 Dec;5(6):548-54.
- 34 Roerdink F, Wassef NM, Richardson EC, Alving CR. Effects of negatively charged lipids on phagocytosis of liposomes opsonized by complement. *Biochim Biophys Acta* 1983 Sep 21;734(1):33-9.
- 35 Peters D, Kastantin M, Kotamraju VR, Karmali PP, Gujraty K, Tirrell M, et al. Targeting atherosclerosis by using modular, multifunctional micelles. *Proc Natl Acad Sci U S A* 2009 Jun 16;106(24):9815-9.
- 36 Mulder WJ, Strijkers GJ, Briley-Saboe KC, Frias JC, Aguinaldo JG, Vucic E, et al. Molecular imaging of macrophages in atherosclerotic plaques using bimodal PEG-micelles. *Magn Reson Med* 2007 Dec;58(6):1164-70.

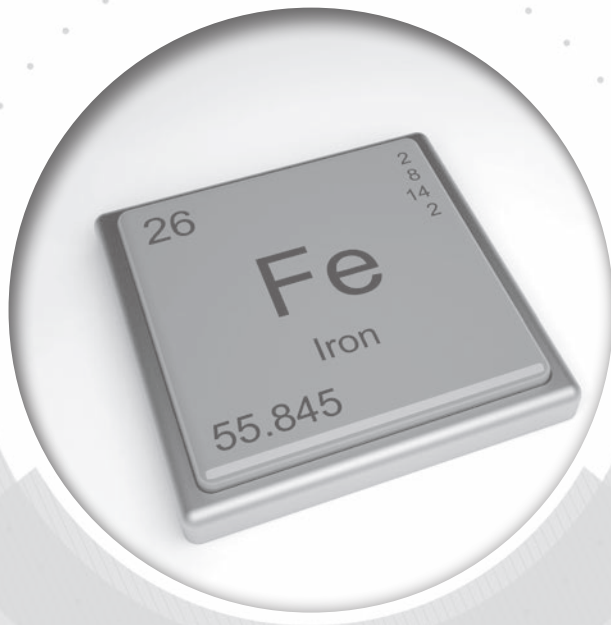


Fe

Iron

55.845

26
55.845



Under revision

Chapter 5

Scavenger receptor-AI targeted iron oxide nanoparticles for *in vivo* MRI detection of atherosclerotic lesions

Filip M.E. Segers, Brigit den Adel, Ilze Bot, Linda M. van der Graaf, Walter Gonzalez, Isabelle Raynal, Menno de Winther, Robert E. Poelmann, Theo J.C. van Berkel, Louise van der Weerd and Erik A.L. Biessen

ABSTRACT

Rationale

Several MRI studies have shown atherosclerosis can be detected both in humans and animal models. Uptake of non-targeted contrast agents (CA) in the leaky endothelium of atherosclerotic plaque gives good plaque enhancement yet without discrimination of the different plaque components.

Objective

In search of molecular imaging modalities for specific detection of inflammatory atherosclerotic plaques, we explored the potential of targeting scavenger receptor-AI (SR-AI), which is highly expressed by lesional macrophages and linked to an effective internalization machinery.

Methods and Results

Ultrasmall Superparamagnetic Iron Oxide (USPIO) particles were conjugated to a peptidic SR-AI ligand (0.371mol Fe/L and 0.018mol PP1/L). *In vitro* incubation of human or murine macrophages with SR-AI targeted USPIO led to significantly higher iron uptake *in vitro* than with non-targeted USPIO, as judged from quantitative atomic absorption spectroscopy and Perl's staining. Incremental uptake was strictly mediated by scavenger receptors. SR-AI targeted USPIO displayed accelerated plasma decay, and a 3.5 fold increase ($p=0.01$) in atherosclerotic plaque accumulation upon *i.v.* injection into ApoE^{-/-} mice, as compared to non-targeted USPIO. In keeping, atherosclerotic humanized LDLr^{-/-} chimeras with leukocyte expression of human SR-AI showed a significant improvement in contrast-to-noise ratio (2.7-fold; $p=0.003$) in the atherosclerotic aortic arch plaques 24h after injection of SR-AI targeted USPIO compared to chimeras with leukocyte SR-AI deficiency.

Conclusion

Collectively, our data provides several lines of evidence that SR-AI targeted molecular imaging of USPIO based contrast agents holds great promise for *in situ* detection of inflammatory plaques in manifest atherosclerosis.

ABBREVIATIONS

T-USPIO – Targeted Ultrasmall Superparamagnetic Iron Oxide particles

hSR-AI ki – human Scavenger Receptor-AI knock in

ROI – Region of Interest

INTRODUCTION

Despite recent advancement in our understanding of the pathogenesis of acute cardiovascular syndromes (ACS), the current imaging diagnostic modalities are primarily appropriate for detecting the degree of stenosis, but lack the desired specificity to identify those atherosclerotic plaques that are at risk of becoming clinically symptomatic. Non-invasive detection methods, such as magnetic resonance imaging (MRI), have shown to enable early tracking of subclinical lesions, characterization of plaque composition, and accurate discrimination between stable and unstable

lesions. To augment the inherent low sensitivity of MRI, superparamagnetic contrast agents have been developed and are to date widely used as contrast agents for molecular and cellular imaging¹. An example of such an agent is Ferumoxtran-10, an ultrasmall superparamagnetic iron-oxide nanoparticle (USPIO). USPIOs have already been applied for detection of metastases^{2, 3}, multiple sclerosis lesions^{4, 5}, inflammatory foci in the central nervous system⁶ and atherosclerotic plaques^{7, 8}. USPIO particles are only slowly cleared from the bloodstream, potentially via nonspecific receptor mediated endocytosis⁹ by macrophages, and as a result of this long circulation time end up in lymph node macrophages and peripheral tissue macrophages^{10, 11}. Nevertheless, plaque uptake is rather inefficient, possibly due to USPIO's inherent low affinity for the major elimination receptors. The dextran coating is progressively degraded and almost exclusively eliminated via the urinary system, whereas iron is assimilated in the body's iron pool, progressively incorporated in red blood cells (haemoglobin) and finally eliminated via faeces with a half-life of 84 days¹. While advantageous for some imaging purposes, a prolonged biological half-life may be accompanied by cytotoxic effects on the long run¹². USPIO were reported to reside in the lysosomal compartment for up to 7 days *in vitro*¹³ before complete degradation.

A hallmark in the pathogenesis of atherosclerosis is monocyte infiltration, their differentiation into macrophages and foam cells, and subsequent activation in the arterial intima¹⁴. Plaque macrophages highly express class A scavenger receptors (SR-A), which have been suggested to play a crucial role in atherosclerotic lesion development¹⁵⁻¹⁸. Scavenger-receptor-mediated uptake of modified lipoproteins is deemed instrumental in foam cell formation and activation, promoting a pro-inflammatory phenotype of lesional macrophages¹⁹. Abundant scavenger receptor expression was found in lesion-specific foam cells and vascular smooth muscle cells but not in the healthy vessel wall^{20, 21}. Relevant to vulnerable plaque detection, abundant SR-AI expression was shown in macrophage enriched inflammatory foci in the advanced, atherosclerotic lesion. Combined with efficient receptor-mediated endocytosis of bound substrates this qualifies SR-AI as promising target for plaque-directed molecular imaging and drug delivery approaches. Due to the complex chemical nature of known macromolecular SR-AI substrates, attempts in ligand design for this receptor have so far been rather unsuccessful. We recently identified a 15-mer peptide PP1 by phage display library screening, which shows high *in vitro* and *in vivo* affinity and specificity for both human and murine macrophage scavenger receptor class A²².

In the current study we report the development and validation of SR-AI targeted USPIO functionalized with the aforementioned SR-A specific peptide. The targeted USPIO was not only tested *in vitro* on mouse and human macrophages but also *in vivo* in an established mouse model for atherosclerosis (aged chow fed ApoE^{-/-} mice), as well as in a humanized model of atherosclerosis (western type diet fed LDLr^{-/-} chimera with leukocyte expression of human SR-A1).

MATERIALS AND METHODS

Cell culture

RAW264.7 murine macrophage cells and human THP-1 monocyte cells (gift from Guerbet Group, France) were grown at 37°C in a humidified atmosphere (5% CO₂) in Dulbecco's Modified Eagle's Medium (DMEM) and RPMI 1640 medium, respectively, supplemented with 10% Fetal Bovine Serum (FBS) (Heat-inactivated, 30min 56°C), 2mmol/L L-glutamine, 100 U/ml Penicillin and 100µg/ml streptomycin (all from PAA, Cölbe, Germany). THP-1 monocytes were differentiated into macrophages by incubation with phorbol 12-myristate, 13-acetate (PMA, 100nM, o.n.)

(Sigma, Zwijndrecht, The Netherlands). Fucoidan (Sigma, Zwijndrecht, The Netherlands) was used as an inhibitor for SR-AI.

Animals

All animal work was conducted in compliance with the Dutch government guidelines. ApoE^{-/-} (1-year old) and female LDLr^{-/-} mice (aged 8-12 weeks) were obtained from the local animal breeding facility. SR-AI^{-/-} mice were from Jacksons Laboratory (Bar Harbor, Maine, USA) and transgenic mice with human SR-A overexpression on a SR-AI deficient background were obtained from Dr. Menno de Winther, Maastricht University Medical Center, the Netherlands. All mice were kept under standard laboratory conditions. Diet and water were provided *ad libitum* throughout the experiment.

Bone Marrow Transplantation and induction of hypercholesterolemia

Female LDLr^{-/-} mice were lethally irradiated by a single dose of 9 Gy (0.19 Gy/min, 200 kV, 4 mA) total body irradiation, using an Andrex Smart 225 Röntgen source (YXLON Int, Copenhagen, Denmark) equipped with a 6-mm aluminium filter. Donor bone marrow was isolated by flushing femurs and tibias with phosphate-buffered saline (PBS). Single-cell suspensions were prepared by passing the cells through a 30- μ m nylon gauze. Irradiated recipients received 0.5×10^7 bone marrow cells by intravenous injection into the tail vein. After a recovery of 6 weeks animals received a semisynthetic high-cholesterol diet containing 15% (w/w) fat and 0.25% (w/w) cholesterol (Diet W; Abdiets, Woerden, The Netherlands) for 12-18 weeks. Drinking water was supplemented with antibiotics (83 mg/L ciprofloxacin and 67 mg/L polymyxin B sulfate) and 6.5 g/L sucrose. Mouse health and weight was monitored during the experiment and blood samples were collected by tail bleeding every 2-3 weeks for assessment of plasma cholesterol levels. Total cholesterol levels were quantified spectrophotometrically using an enzymatic procedure (Roche Diagnostics, Germany). Precipath standardized serum (Boehringer, Germany) was used as an internal standard.

Preparation of functionalized USPIO

The PP1 peptide was synthesized as previously described²². PP1 peptide was conjugated to USPIO through their amino-terminal groups (5%; 0.018mol PP1/L and 0.371mol Fe/L) by Guerbet (Aulnay-sous-Bois, France). PEG-NH₂ (Mw =750 g/mol; Sigma) was conjugated to the free carboxyl groups exposed by the particles and the pH was finally adjusted to 7.6. In order to remove the free non-conjugated molecules, the solution was exhaustively dialyzed.

The physico-chemical characterization was carried out as previously described²³. Briefly, the mean diameter of coated USPIO-PP1 (T-USPIO) was about 22nm measured by photon correlation spectroscopy (PCS) on a Malvern system (Zétasizer nanoseries ZEN 3600). USPIO were of comparable size, namely 24.1nm. Iron concentration was determined by ICP-AES after mineralization in acidic conditions (HNO₃, 80°C).

Relaxivity

The relaxivities (r₁, r₂) were measured in water at 60 and 20 MHz at 37°C on a Bruker Minispec (respectively mq60 and mq20) by Guerbet (Aulnay-sous-Bois, France). Before the *in vivo* experiments, the transverse r₂ relaxivity was determined from the slope of a linear regression curve of T₂ measurements of several contrast agent concentrations on the *in vivo* MRI system (9.4T) at 37°C.

***In vivo* MRI**

All experiments were performed on a 9.4T (400 MHz) vertical 89-mm bore MR magnet interfaced to a Bruker AVANCE (Bruker BioSpin MRI GmbH, Ettlingen, Germany) MR imaging console equipped with ParaVision 5.0 software, with an actively shielded Micro2.5 gradient system (1 T/m). Mice were scanned in a transmit/receive birdcage radiofrequency coil with an inner diameter of 3.0 cm (Bruker BioSpin MRI GmbH, Ettlingen, Germany).

In vivo MRI was performed on the animals described above (ApoE^{-/-} and bone marrow transplanted LDLr^{-/-} mice). For *in vivo* imaging mice were anesthetized with isoflurane (2% in air). During the examination, the respiration rate was continuously measured with a balloon pressure sensor using a respiration cushion under the mouse chest connected to the ECG/respiratory unit (SA Instruments, Inc., Stony Brook, NY). The isoflurane concentration was adjusted to keep the respiration rate between 50 and 80 respirations/min. The mice were randomly divided into two groups injected with targeted (T-USPIO) or non-targeted contrast agent (USPIO).

To determine the optimal imaging time point 2 groups (n=5 per group) of aged ApoE^{-/-} mice were injected with 250 µmol Fe/kg bodyweight SR-A1 targeted or control USPIO. Animals were imaged with 30 minutes intervals for the first 3 hours and thereafter every 2.5 hours to find the optimal imaging time point. The optimal imaging time point is defined as the moment where the highest difference in blooming effect was observed between the 2 contrast agents. At 24 hours after injection contrast enhancement was largest using the T-USPIOs (supplemental figure 1).

At the start of each examination, several 2D FLASH scout images were recorded in the transverse and axial plane of the heart to determine the orientation of the aortic arch. The following parameters were used for the scout scans: Hermite-shaped RF pulse 1.000 ms; flip angle (FA) 10; repetition time (TR) 14.7 ms; echo time (TE) 1.8 ms; sample rate 40 kHz; echo position 30%; field of view (FOV) 1.8*1.8 cm²; matrix 128*128; in-plane resolution 0.141 mm; slice thickness 0.4 mm; number of repetitions 64; total acquisition time approximately 2 min.

A modified FLASH sequence with a navigator echo (IntraGate) was used for retrospective CINE MRI with the following parameters:

Hermite-shaped RF pulse 1.000 ms; FA 15°; TR 15.7 ms; TE 2.96 ms; sample rate 40 kHz; echo position 30%; navigator echo points 64; 10 cardiac frames; FOV 2.56*2.56 cm²; matrix 128*128; in-plane resolution 0.2 mm; slice thickness 0.5 mm; number of repetitions 400; total acquisition time approximately 14 min.

Image Analysis

For each time point, bright blood images were selected and 3 to 4 adjacent slices of cross-sections of the aortic arch were manually analyzed using ImageJ software. Regions of Interest (ROIs) were drawn around the vessel wall (I_{wall}). A 2nd ROI was drawn in the muscle tissue of the shoulder region (I_{muscle}). Furthermore, an ROI was placed outside the animal to measure the noise level (stdevnoise) (Supplemental Figure 1).

The contrast to noise ratio was defined as:

$$\text{CNR} = (I_{\text{wall}} - I_{\text{muscle}}) / \text{stdev}_{\text{noise}} \quad [\text{Eq1}]$$

Histology and Morphometry

Cryostat sections (10µm) were prepared of the aortic valve area and lipid deposits were stained with Oil Red O. Mean lesion area was calculated from 8-10 consecutive Oil Red O (ORO) stained sections. Lesional macrophage content was determined after immunohistochemical staining with a macrophage specific antigen antibody (MoMa-2, monoclonal rat IgG₂, dilution 1:50; Serotec,

Oxford, UK). Secondary antibody goat-anti- rat IgG-AP (1:100; Sigma, St-Louis, MO) and enzyme substrate Nitro Blue Tetrazolium – 5-Bromo-4-Chloro-3-Idolyl Phosphate (NBT-BCIP) (Dako, Glostrup, Denmark) were used. Iron deposits were visualized by hemosiderin staining according to the Perl's method.

Morphometric analysis on Oil Red O and MoMa-2 stained sections was performed using Leica Qwin image analysis software and a Leica-DM-RE microscope (Leica imaging systems, Cambridge, UK). Perl's positive cells were counted manually in a blinded manner.

Quantitative analysis of iron dosages in plasma and organs

Blood samples were collected by tail vein puncture and plasma was isolated. Upon sacrifice, mice were anesthetized and underwent *in situ* PBS perfusion via the left cardiac ventricle. Organs of interest were isolated and stored at -80°C until further analysis. Iron content of cell cultures and tissue was determined by inductively coupled plasma atomic emission spectroscopy (ICP-AES) (Optima 3300 RL, Perkin Elmer, Courtaboeuf, France).

RESULTS

Relaxivity analysis

The contrast agent relaxivities were measured at 37°C at 20, 60 and 400 MHz respectively (Table 1). The transverse relaxivities of the SR-A1 and control particle did not differ significantly nor did the longitudinal relaxivity.

Increased uptake of scavenger receptor targeted USPIO by macrophages *in vitro*

The kinetics of basal uptake, processing and detection of USPIO *in vitro* and *in vivo* by macrophages have been subject of numerous studies⁹. Here we sought to investigate whether USPIO uptake by (plaque associated) macrophages could be augmented by conjugation to a newly devised peptide ligand for SR-A1²², a receptor previously shown to be highly expressed by this leukocyte subset in inflammatory foci within the plaque²⁴. As a measure of USPIO uptake by RAW264.7 cells (300 μg Fe/ml) cell-associated iron was assessed using quantitative atomic absorption spectroscopy analysis. SR-A1 targeted USPIO (T-USPIO) showed a markedly increased uptake by macrophages than non-targeted USPIO (1729 \pm 152 versus 805 \pm 111ng Fe/g cell pellet, $p < 0.001$, figure 1.A). *In vitro* uptake studies in human THP-1 macrophages revealed a comparable increase in cellular uptake of T-USPIO (600 \pm 35) over USPIO (343 \pm 48 ng Fe/g cell pellet, $p = 0.01$). T-USPIO uptake could be blocked to a large extent by pre-incubation of the cells with fucoidan, an established

Table 1. Relaxivity analysis (r1 and r2) for USPIO and targeted USPIO (T-USPIO) particles

	20 MHz water 37°C		60 MHz water 37°C		400 MHz saline 37°C	
	USPIO	T-USPIO	USPIO	T-USPIO	USPIO	T-USPIO
R1 $\text{mM}^{-1}\cdot\text{s}^{-1}$	34.1	40.0	16.1	17.0	$0.47 \cdot 10^2$	$0.5 \cdot 10^2$
R2 $\text{mM}^{-1}\cdot\text{s}^{-1}$	91.3	82.0	90.7	78.7	$5.0 \cdot 10^2$	$5.3 \cdot 10^2$

inhibitor of SR-AI/II²⁵. Fucoidan also diminished the uptake of non-targeted USPIO, which is consistent with the previously suggested role of scavenger receptors in USPIO phagocytosis. (figure 1.B). Of note, the targeted USPIO uptake remains significantly higher than the uptake of its untargeted counterpart.

The increased T-USPIO accumulation by THP-1 cells translated in a decreased T₂ relaxation time (65.4 ± 0.6 msec; $p=0.01$) compared to cells incubated with USPIO (72.5 ± 1.4 msec) (Figure 1.C). Again, incubation with fucoidan neutralized the decrease in T₂ relaxation of T-USPIO, albeit to a lesser extent also of USPIO-incubated macrophages. In fact, T₂ relaxation times after fucoidan treatment were comparable to that of the control samples.

In keeping with these *in vitro* MRI data, Perl's staining of THP-1 macrophages confirmed the more abundant presence of iron deposits in T-USPIO incubated macrophages (figure 1.D-E). Our results thus indicate that peptide targeted USPIO display significantly increased, SR-AI dependent uptake by macrophages *in vitro*.

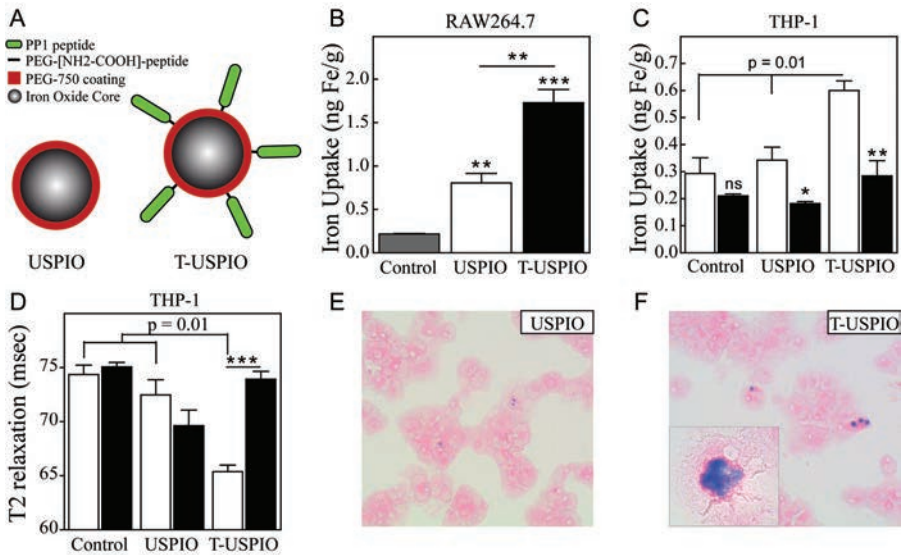


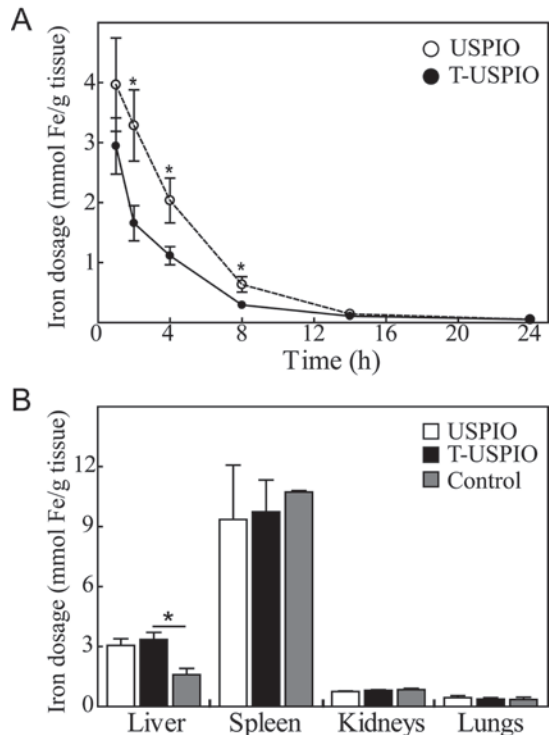
Figure 1 | Scavenger receptor targeted USPIO display improved uptake by macrophages *in vitro* compared to untargeted USPIO. Cellular uptake of targeted (T-USPIO; 300 μ g Fe/ml; A right) and non-targeted USPIO (USPIO, 300 μ g Fe/ml; A left) was assessed in different *in vitro* macrophage cell cultures. (B) RAW264.7 macrophages were incubated with T-USPIO or USPIO for 24h. Cells without contrast agents served as control. Cell pellets were collected and quantitatively analyzed by inductively coupled plasma atomic emission spectroscopy (ICP-AES). (C) THP-1 macrophages with (■) or without (□) inhibitor (Fucoidan; 0.5mg/ml) were incubated for 24h with USPIO and T-USPIO. Uptake of (T-)USPIO was determined by ICP-AES based iron analysis of cell lysates and corrected for protein content. (D) T₂ relaxation times from cell pellets were analyzed by MRI. Iron uptake was reflected by signal loss in T₂-weighted MRI analysis of cell pellets. THP-1 incubated with USPIO (E) and T-USPIO (F) were stained for iron with Perl's staining to visualize intracellular iron deposition. Data are shown as mean \pm SEM. (* $p<0.05$, ** $p<0.01$ and *** $p<0.001$)

Increased plasma clearance and increased signal *in vivo* upon targeted delivery of USPIO in ApoE^{-/-} mice

As a next step, we investigated the optimal imaging window and the fate of plaque accumulation of the SR-AI targeted T-USPIO *in vivo* in aged (1y) ApoE^{-/-} mice (N=14) with established advanced atherosclerotic lesions. Mice were imaged every 30 minutes for the first 3 hours after contrast agent injection and thereafter followed every 2.5 hours until 48 hours after injection. Gradually increasing uptake in the plaque on the inner curvature of the aortic arch was observed until a significant difference in uptake between the T-USPIO and USPIO was observed 24 hours after injection.

A subset of mice received a single intravenous injection with T-USPIO (250µmol Fe/kg, N=6) while the control group received plain USPIO (250µmol Fe/kg, N=6). The remaining mice were used to determine endogenous tissue iron content. Kinetic analysis of plasma iron levels by inductively coupled plasma atomic emission spectroscopy (ICP-AES) (figure 2.A) pointed to an increased plasma clearance of T-USPIO ($T_{1/2} = 1.7\text{h}$) compared to USPIO ($T_{1/2} = 2.9\text{h}$; $P < 0.05$). Plasma iron levels declined to baseline within 24h after administration of T-USPIO or USPIO. Analysis of macrophage-rich organs such as liver, spleen and lungs, as well as kidney 24h after injection (figure 2.B), showed increased iron accumulation in liver, the primary eliminating organ, in USPIO ($3.1 \pm 0.3\mu\text{mol Fe/g}$; NS) and even more so in T-USPIO treated mice ($3.4 \pm 0.4\mu\text{mol Fe/g tissue}$; $p < 0.05$) compared to the endogenous tissue iron concentrations ($1.6 \pm 0.3\mu\text{mol Fe/g}$). *In vivo* MRI of the aortic arch 24 hours after injection of contrast agent revealed increased accumulation of T-USPIO compared to non-targeted USPIO in atherosclerotic plaques on the basis of the innercurvature of the aortic arch (T-USPIO Contrast-to-Noise Ratio (CNR) -14.0 ± 1.7 , USPIO -9.8

Figure 2 | Targeted USPIO show faster kinetics in blood and improved accumulation in macrophage-rich organs. Aged ApoE^{-/-} (1-year old) mice received USPIO (N=6; white bars) or targeted USPIO (T-USPIO; N=6; black bars) by intravenous injection. Mock injected mice served as control and were used to determine endogenous tissue iron concentrations (gray bars). (A) Plasma samples were subjected to ICP-AES atomic absorption spectroscopy and iron content in mice treated with T-USPIO (●) and untargeted USPIO (○) was determined. (B) At 24h after administration, organs of interest were harvested and analyzed for iron uptake by ICP-AES. Data are shown as mean±SEM. (* $p < 0.05$)



± 0.7 , $p < 0.05$) (figure 3.A-C). Except for liver, biodistribution profiles of T-USPIO and USPIO were essentially similar and did not significantly differ from that of untreated controls (figure 2.B). Lesion prone artery segments (aortic valve area, figure 3) were also analyzed *ex vivo* for lesion size, monocyte/macrophage content and iron accumulation. As expected, no differences were observed in lesion size (figure 3.J-K) and monocyte/macrophage content (figure 3.G-I). However, in line with the aforementioned results obtained by MRI, visualization of iron uptake by Perl's staining (figure 3.D-F) revealed a significant, 3.3-fold increase in Perl's positive cells in lesions of T-USPIO injected mice compared to those injected with USPIO ($P = 0.01$). Our data thus demonstrate that targeted contrast agents combine accelerated plasma clearance with increased accumulation in advanced atherosclerotic lesions.

T-USPIO show superior accumulation in plaques in a humanized mouse model of atherosclerosis

In initial studies we already showed that the SR-AI targeting peptide PP1 had higher affinity for human derived THP-1 macrophages than for murine macrophages, suggesting that PP1 may be, at least, equally effective in a human setting²². To address its potential for human plaque imaging we generated LDLr^{-/-} chimeras with hematopoietic human SR-AI (hSR-AI) expression by bone marrow transplantation (>90% bone marrow reconstitution after 6 weeks). Chimeras with hematopoietic SR-AI deficiency (SR-AI^{-/-}) and wild type bone marrow transplanted LDLr^{-/-} mice served as control. After a recovery period of 6 weeks, atherogenesis was induced by high cholesterol diet feeding. After 3 months of diet exposure, all groups of mice received a single intravenous dose of PP1-targeted contrast agent (T-USPIO; 250 μ mol Fe/kg). After 24h, mice were anesthetized and subjected to *in vivo* magnetic resonance imaging at 9.4T. In keeping with previous findings^{26, 27} morphometric analysis did not reveal any differences in plaque size between SR-AI^{-/-} and hSR-AI mice (figure 4.G; representative pictures of the Oil-Red-O staining in online supplement figure 2) Importantly, plaque monocyte/macrophage content of the atherosclerotic lesions did also not differ (figure 4.D-F). *In vivo* MRI analysis of the aortic arch revealed a significantly decreased contrast-to-noise ratio in mice overexpressing human SR-AI (-17.4 ± 2.3) compared to SR-AI^{-/-} controls (-6.4 ± 0.5 ; $p = 0.004$) and control BM animals (figure 4A-D). Moreover the signal voids in MR images pointed to augmented iron uptake in hSR-AI overexpressing mice. These results clearly illustrate the improved capacity of SR-AI targeted contrast agents to accumulate in atherosclerotic lesions in a SR-AI dependent manner.

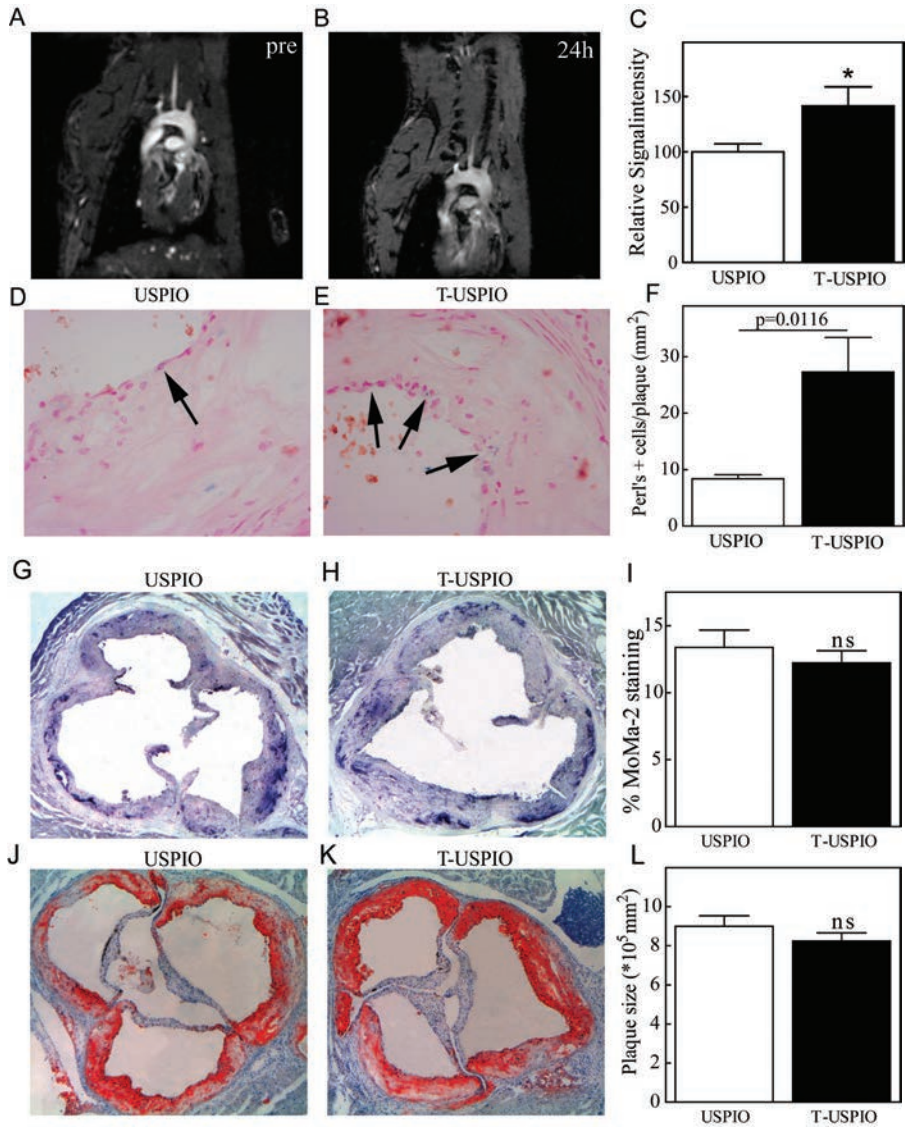


Figure 3 | SR-AI targeting of contrast agents results in increased uptake in advanced atherosclerotic plaques in ApoE^{-/-} mice. Aged ApoE^{-/-} (1-year old) mice received an intravenous injection of non-targeted (USPIO; white) or targeted USPIO (T-USPIO; black). After 24h mice underwent *in vivo* MRI analysis (A-C) and were sacrificed and sections were made of the atherosclerotic lesion prone aortic root. These sections were subsequently stained for Perl's (D-F), MoMa-2 (G-H) and Oil-Red-O (J-L). Perl's staining was analyzed in a blinded manner and Perl's+ cells were individually scored (data presented as # Perl's+ cells/plaque area). Data are shown as mean±SEM. (* $p < 0.05$)

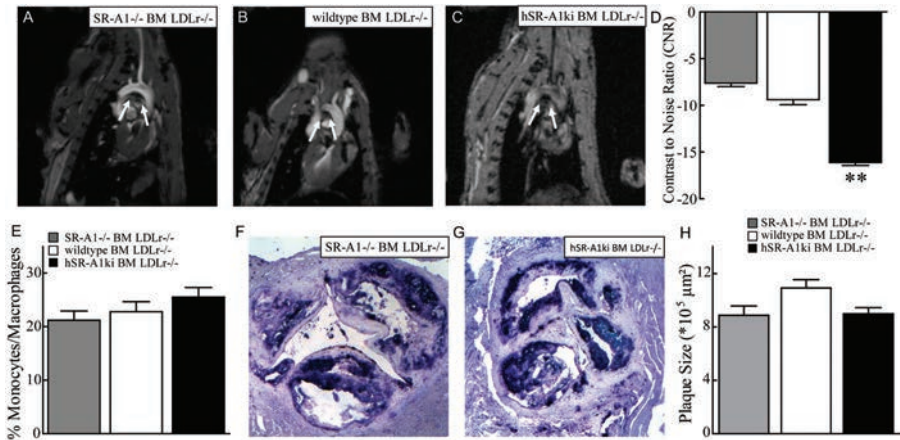


Figure 4 | In vivo Magnetic Resonance Imaging of the aortic arch reveals increased lesional uptake of targeted USPIO in hSR-A overexpressing LDLr^{-/-} chimeras. After bone marrow transplantation, LDLr^{-/-} chimeras were fed a high cholesterol diet to induce atherosclerotic plaque formation. SR-A^{-/-}, hSR-A overexpressing and WT (control) bone marrow recipients received a single administration with targeted USPIO. At 24h after injection, mice were subjected to *in vivo* magnetic resonance imaging and subsequently sacrificed. Contrast-to-Noise Ratio (CNR) was determined by computer assisted analysis of MRI images (A-C). For each mouse three images were analyzed and mean CNR was determined (D). Cryosections were made from the atherosclerotic lesion prone aortic root and subsequently stained SEMa-2 (E) and for atherosclerotic plaque size (G). Data are shown as mean \pm SEM. (** $p < 0.01$)

DISCUSSION

The data of the current study show that conjugation of PP1 to USPIO particles could provide a useful molecular imaging tool for noninvasive imaging of atherosclerotic plaques. We not only show induced delivery of this PP1 conjugated USPIO to macrophages *in vitro* and *in vivo*, but also enhanced MRI image contrast in macrophage rich atherosclerotic plaques in a humanized model of atherosclerosis.

Ultra-small superparamagnetic iron oxide particles (USPIO) have been used in non-invasive clinical imaging to enhance image contrast in detection of malignancies²⁸, inflammatory multiple sclerosis lesions, CNS pathologies and atherosclerotic lesions⁷. One of the major challenges in cardiovascular imaging is the clinically relevant distinction between stable and unstable rupture-prone lesions. The abundant presence of macrophages is a hallmark feature of the latter plaques²⁹. This renders macrophages primary targets in diagnostic strategies for vulnerable plaque detection. The current study provides several lines of evidence for effective scavenger receptor A1 directed targeting of plaque macrophages. Firstly USPIO particles equipped with the SR-A1 specific peptide ligand PP1, T-USPIO, show preferential and SR-A1 dependent uptake by murine and human macrophages *in vitro*. Secondly T-USPIO had accelerated plasma decay and augmented accumulation by atherosclerotic plaques in aged ApoE^{-/-} mice and in western type diet fed LDLR^{-/-} with human SR-A1. Thirdly, T-USPIO was capable of visualizing inflammatory aortic arch plaques by MRI *in vivo*.

The marked expression of SR-A1 in macrophage enriched sites of inflammation and the fact that this receptor mediates efficient endocytosis of its substrates renders it an interesting

candidate for targeted delivery to inflammatory plaques^{15, 30, 31}. Recently, our group successfully identified a small 15-mer peptide (PP1) with high specificity and affinity for scavenger receptor class AI, which is better fit as homing device for contrast agents²². Concordant with our previous study, PP1 conjugated USPIO are preferentially taken up by macrophages in a scavenger-receptor dependent manner as fucoidan coinubation blunted the incremental uptake. Macrophage uptake of conventional USPIO was partly inhibited as well, fueling the notion that SR-A can also mediate untargeted USPIO uptake to some extent⁹. Further support for SR-AI specificity was derived from the sharply diminished accumulation of T-USPIO in LDLr^{-/-} chimeras deficient in leukocyte SR-AI²⁶.

Another important issue is whether the effective macrophage targeting observed in our study is reflective of its effectiveness in a human context. Our data in a humanized model of atherosclerosis, i.e. LDLr^{-/-} mice with macrophage-specific overexpression of the human macrophage scavenger receptor class A^{27, 32, 33} clearly corroborate the plaque macrophage imaging potential of PP1 equipped USPIO for humans. From histological plaque analysis we can exclude differences in lesion size or plaque characteristics between the different groups, confirming that the increased image contrast is attributable to increased T-USPIO ingestion by SR-AI expressing plaque macrophages.

Although the targeting efficacy of T-USPIO in hSR-AI->LDLr^{-/-} chimeras and ApoE^{-/-} was largely the same, we did notice minor differences. These may well relate to issues other than species differences in SR-AI receptor binding, such as progression stage of lesions (higher in ApoE^{-/-}), the level of neovascularisation (higher in ApoE^{-/-})³⁴, plaque inflammation and cap fibrosis, all of which potentially affecting the penetration of T-USPIO particles into the plaque³⁵.

The biodistribution profile of T-USPIO was consistent with that of [¹²⁵I]-labeled PP1²². The faster plasma decay of T-USPIO and increased hepatic uptake relative to USPIO, likely due to accelerated elimination by SR-A1 on liver cells and endothelial cells³⁶ will have beneficial and adverse effects on plaque imaging. On the one hand it may constrain the penetration of T-USPIO into the plaque, and may enhance USPIO deposition in cells of the reticulo-endothelial system for metabolization, with the associated risk of toxicity¹². On the other hand it may be accompanied by even faster normalization of blood signal intensity, and will reduce nonspecific USPIO accumulation by surrounding tissue, which both will augment contrast-to-noise ratio in the vessel wall. With regard to the latter, it will be of great interest for future studies to optimize the circulation time of the particles for maximum specificity and minimum toxicity, e.g. by using larger iron oxide particles³⁷.

Several reports have been published so far on targeted imaging of inflammation and of vulnerable atherosclerotic plaques. Macrophages remain an important target for imaging as they are key effectors in atherosclerosis²⁹ and their high abundance in plaque was associated with a high risk of clinical complications³⁸⁻⁴⁰. Currently two major approaches exist for imaging intraplaque macrophage density. Macrophages have been targeted in a passive manner, be it after penetration of USPIO into the plaque and ingestion in situ, or via circulating USPIO laden monocytes which after plaque invasion differentiate into macrophages⁴¹. Alternatively, for molecular imaging of inflammatory plaques the potential of active targeting of plaque leukocyte subsets (detailed review see⁴²) have been explored, often using scavenger receptors as route of entry^{43,44}.

Synthetic PP1 may contrast favourably to the homing devices used in the latter studies. It shows a similar to even higher in vivo accumulation ratio than macrophage targeted immunomicelles⁴⁵, MDA2⁴⁶, OxLDL targeted⁴⁶ and tyrosine PEG-micelles⁴⁷ and HDL based contrast agent⁴⁸. While at least equally effective and synthetically flexible, these peptide based homing vehicles display higher receptor specificity (compared to PEG micelles, HDL-based contrast agents), are less

immunogenic (vs MDA2 micelles, synthetic HDL), or do not give rise to cell activation (vs liposomes)⁴⁹. PP1 equipped contrast agents (PET or MRI) may thus represent effective screening tools to detect macrophage-rich atherosclerotic lesions in the patient at risk, and, in more general sense, inflammatory foci, precisely mapping location and extent of inflammation. How scavenger receptor directed imaging of inflammatory atherosclerotic plaques compares to that the imaging of other vulnerable plaque components or processes such as apoptosis, necrosis, neovascularization, extracellular matrix and MMP's (for a review see⁵⁰) remains to be investigated yet the plaque macrophage specificity of SR-A1 gives this contrast agent an important advantage over the imaging of other more general biological processes .

In conclusion, we here show the successful development of an SR-AI targeted iron-oxide-based MRI contrast agent that shows increased and SR-AI dependent uptake by macrophages *in vitro* as well as *in vivo* in an established atherosclerotic mouse model. The SR-AI targeted USPIO combines rapid blood decay with effective SR-AI dependent plaque macrophage uptake, due to its high affinity for SR-AI. Importantly it displays a favorable contrast-to-noise ratio in MRI aided detection of atherosclerotic plaques in a humanized model of atherosclerosis. With these features, PP1 targeted USPIO constitutes a promising new platform for the non-invasive detection of macrophage-rich foci in chronic inflammatory diseases such as the atherosclerotic plaque and might even allow selective discrimination of unstable plaques.

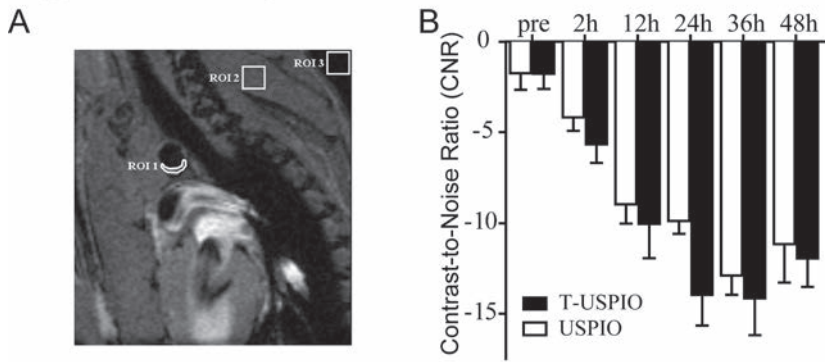
Sources of funding

This study was supported by Guerbet Group, manufacturer of USPIO and PP1-Targeted USPIO. This work was supported by the European Network of Excellence Diagnostic Molecular Imaging (DIMI, LSHB-CT-2005-512146) to BdA, REP, LvdW, LvdG and Dutch Organisation for Scientific Research (NWO) Athena grant (700.58.80) to LvdW . EALB and REP were supported by the Netherlands Heart Foundation (EALB from grant 2003T.201 and REP 2006T.106).

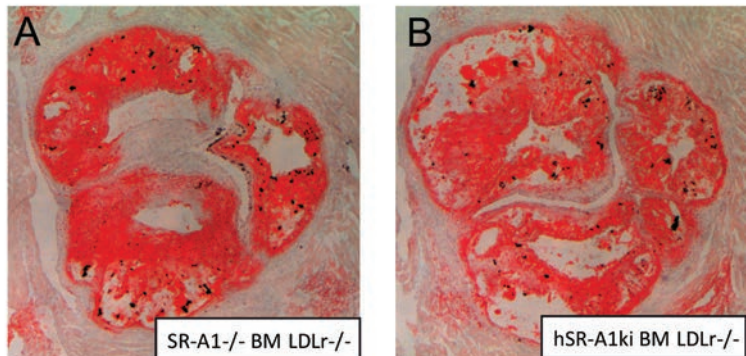
Disclosures

Conflict of interest: W.G. and I.R. were employees of Guerbet Group during performance of the study.

SUPPLEMENTAL FIGURES



Supplemental Figure 1 | A) Schematic overview of the ROI's used for MRI Image analysis. (B) Contrast enhancement measurements before and at regular time intervals after intravenous injection of USPIO and T-USPIO in 1y-old ApoE^{-/-} mice.



Supplemental Figure 2 | Oil Red O staining of the aortic root of SR-A1^{-/-} and hSR-A1 ki bone marrow transplanted LDLr^{-/-} mice.

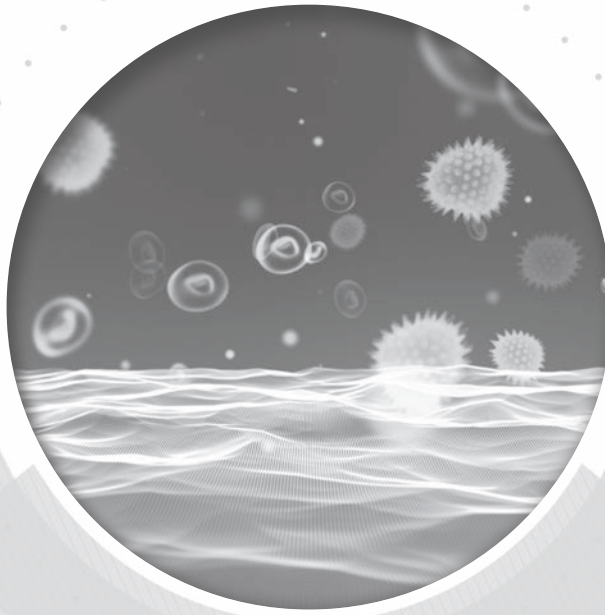
REFERENCES

- Corot C, Robert P, Idee JM, Port M. Recent advances in iron oxide nanocrystal technology for medical imaging. *Adv Drug Deliv Rev.* 2006;58:1471-1504
- Anzai Y, Piccoli CW, Outwater EK, Stanford W, Bluemke DA, Nurenberg P, Saini S, Maravilla KR, Feldman DE, Schmiedl UP, Brunberg JA, Francis IR, Harms SE, Som PM, Tempny CM. Evaluation of neck and body metastases to nodes with ferumoxtran 10-enhanced mr imaging: Phase iii safety and efficacy study. *Radiology.* 2003;228:777-788
- Harisinghani MG, Barentsz J, Hahn PF, Deserno WM, Tabatabaei S, van de Kaa CH, de la Rosette J, Weissleder R. Noninvasive detection of clinically occult lymph-node metastases in prostate cancer. *N Engl J Med.* 2003;348:2491-2499
- Rausch M, Hiestand P, Baumann D, Cannet C, Rudin M. Mri-based monitoring of inflammation and tissue damage in acute and chronic relapsing eae. *Magn Reson Med.* 2003;50:309-314
- Rausch M, Hiestand P, Foster CA, Baumann DR, Cannet C, Rudin M. Predictability of fty720 efficacy in experimental autoimmune encephalomyelitis by in vivo macrophage tracking: Clinical implications for ultrasmall superparamagnetic iron oxide-enhanced magnetic resonance imaging. *J Magn Reson Imaging.* 2004;20:16-24
- Pirko I, Johnson A, Ciric B, Gamez J, Macura SI, Pease LR, Rodriguez M. In vivo magnetic resonance imaging of immune cells in the central nervous system with superparamagnetic antibodies. *FASEB J.* 2004;18:179-182
- Corot C, Petry KG, Trivedi R, Saleh A, Jonkmanns C, Le Bas JF, Blezer E, Rausch M, Brochet B, Foster-Gareau P, Baleriaux D, Gaillard S, Dousset V. Macrophage imaging in central nervous system and in carotid atherosclerotic plaque using ultrasmall superparamagnetic iron oxide in magnetic resonance imaging. *Invest Radiol.* 2004;39:619-625
- Kooi ME, Cappendijk VC, Cleutjens KB, Kessels AG, Kitslaar PJ, Borgers M, Frederik PM, Daemen MJ, van Engelsehoven JM. Accumulation of ultrasmall superparamagnetic particles of iron oxide in human atherosclerotic plaques can be detected by in vivo magnetic resonance imaging. *Circulation.* 2003;107:2453-2458
- Raynal I, Prigent P, Peyramaure S, Najid A, Rebuzzi C, Corot C. Macrophage endocytosis of superparamagnetic iron oxide nanoparticles: Mechanisms and comparison of ferumoxides and ferumoxtran-10. *Invest Radiol.* 2004;39:56-63
- Weissleder R, Elizondo G, Wittenberg J, Rabito CA, Bengel HH, Josephson L. Ultrasmall superparamagnetic iron oxide: Characterization of a new class of contrast agents for mr imaging. *Radiology.* 1990;175:489-493
- Bourrinet P, Bengel HH, Bonnemain B, Dencausse A, Idee JM, Jacobs PM, Lewis JM. Preclinical safety and pharmacokinetic profile of ferumoxtran-10, an ultrasmall superparamagnetic iron oxide magnetic resonance contrast agent. *Invest Radiol.* 2006;41:313-324
- Muller K, Skepper JN, Posfai M, Trivedi R, Howarth S, Corot C, Lancelot E, Thompson PW, Brown AP, Gillard JH. Effect of ultrasmall superparamagnetic iron oxide nanoparticles (ferumoxtran-10) on human monocyte-macrophages in vitro. *Biomaterials.* 2007;28:1629-1642
- Schulze E, Ferrucci JT, Jr., Poss K, Lapointe L, Bogdanova A, Weissleder R. Cellular uptake and trafficking of a prototypical magnetic iron oxide label in vitro. *Invest Radiol.* 1995;30:604-610
- Ross R. Atherosclerosis--an inflammatory disease. *N Engl J Med.* 1999;340:115-126
- Hiltunen TP, Luoma JS, Nikkari T, Yla-Herttuala S. Expression of ldl receptor, vldl receptor, ldl receptor-related protein, and scavenger receptor in rabbit atherosclerotic lesions: Marked induction of scavenger receptor and vldl receptor expression during lesion development. *Circulation.* 1998;97:1079-1086
- Kunjathoor VV, Febbraio M, Podrez EA, Moore KJ, Andersson L, Koehn S, Rhee JS, Silverstein R, Hoff HF, Freeman MW. Scavenger receptors class a-i/ii and cd36 are the principal receptors responsible for the uptake of modified low density lipoprotein leading to lipid loading in macrophages. *J Biol Chem.* 2002;277:49982-49988
- van Berkel TJ, Out R, Hoekstra M, Kuiper J, Biessen E, van Eck M. Scavenger receptors: Friend or foe in atherosclerosis? *Curr Opin Lipidol.* 2005;16:525-535
- Suzuki H, Kurihara Y, Takeya M, Kamada N, Kataoka M, Jishage K, Ueda O, Sakaguchi H, Higashi T, Suzuki T, Takashima Y, Kawabe Y, Cynshi O, Wada Y, Honda M, Kurihara H, Aburatani H, Doi T, Matsumoto A, Azuma S, Noda T, Toyoda Y, Itakura H, Yazaki Y, Horiuchi S, Takahashi K, Kruijt JK, van Berkel TJ, Steinbrecher UP, Ishibashi S, Maeda NY, Gordon S, Kodama T. A role for macrophage scavenger receptors in atherosclerosis and susceptibility to infection. *Nature.* 1997;386:292-296
- Moore KJ, Freeman MW. Scavenger receptors in atherosclerosis: Beyond lipid uptake. *Arterioscler Thromb Vasc Biol.* 2006;26:1702-1711
- Gough PJ, Greaves DR, Suzuki H, Hakkinen T, Hiltunen MO, Turunen M, Herttuala SY, Kodama T, Gordon S. Analysis of macrophage scavenger receptor (sr-a) expression in human aortic atherosclerotic lesions. *Arterioscler Thromb Vasc Biol.* 1999;19:461-471
- de Winther MP, van Dijk KW, Havekes LM, Hofker MH. Macrophage scavenger receptor class a: A multifunctional receptor in atherosclerosis. *Arterioscler Thromb Vasc Biol.* 2000;20:290-297
- Segers FM, Yu H, Molenaar TJ, Prince P, Tanaka T, van Berkel TJ, Biessen EA. Design and validation of a specific scavenger receptor class ai binding peptide for targeting the inflammatory atherosclerotic plaque. *Arterioscler Thromb Vasc Biol.* 2012;32:971-978

23. Burtea C, Laurent S, Mahieu I, Larbanoix L, Roch A, Port M, Rousseaux O, Ballet S, Murariu O, Toubreau G, Corot C, Vander Elst L, Muller RN. In vitro biomedical applications of functionalized iron oxide nanoparticles, including those not related to magnetic properties. *Contrast Media Mol Imaging*. 2011;6:236-250
24. Matsumoto A, Naito M, Itakura H, Ikemoto S, Asaoka H, Hayakawa I, Kanamori H, Aburatani H, Takaku F, Suzuki H, Kobari Y, Miyai T, Takahashi K, Cohen EH, Wydro R, Housman DE, Kodama T. Human macrophage scavenger receptors: Primary structure, expression, and localization in atherosclerotic lesions. *Proc Natl Acad Sci U S A*. 1990;87:9133-9137
25. Platt N, Gordon S. Scavenger receptors: Diverse activities and promiscuous binding of polyanionic ligands. *Chem Biol*. 1998;5:R193-203
26. de Winther MP, Gijbels MJ, van Dijk KW, van Gorp PJ, Suzuki H, Kodama T, Frants RR, Havekes LM, Hofker MH. Scavenger receptor deficiency leads to more complex atherosclerotic lesions in apoE3 transgenic mice. *Atherosclerosis*. 1999;144:315-321
27. Van Eck M, De Winther MP, Herijgers N, Havekes LM, Hofker MH, Groot PH, Van Berkel TJ. Effect of human scavenger receptor class a overexpression in bone marrow-derived cells on cholesterol levels and atherosclerosis in apoE-deficient mice. *Arterioscler Thromb Vasc Biol*. 2000;20:2600-2606
28. Islam T, Josephson L. Current state and future applications of active targeting in malignancies using superparamagnetic iron oxide nanoparticles. *Cancer Biomark*. 2009;5:99-107
29. Libby P. Inflammation in atherosclerosis. *Nature*. 2002;420:868-874
30. Yla-Herttuala S, Rosenfeld ME, Parthasarathy S, Sigal E, Sarkioja T, Witztum JL, Steinberg D. Gene expression in macrophage-rich human atherosclerotic lesions. 15-lipoxygenase and acetyl low density lipoprotein receptor messenger rna colocalize with oxidation specific lipid-protein adducts. *J Clin Invest*. 1991;87:1146-1152
31. Hiltunen TP, Yla-Herttuala S. Expression of lipoprotein receptors in atherosclerotic lesions. *Atherosclerosis*. 1998;137 Suppl:S81-88
32. de Winther MP, van Dijk KW, van Vlijmen BJ, Gijbels MJ, Heus JJ, Wijers ER, van den Bos AC, Breuer M, Frants RR, Havekes LM, Hofker MH. Macrophage specific overexpression of the human macrophage scavenger receptor in transgenic mice, using a 180-kb yeast artificial chromosome, leads to enhanced foam cell formation of isolated peritoneal macrophages. *Atherosclerosis*. 1999;147:339-347
33. Oswald P, Clement O, Chambon C, Schouman-Claeys E, Frija G. Liver positive enhancement after injection of superparamagnetic nanoparticles: Respective role of circulating and uptaken particles. *Magn Reson Imaging*. 1997;15:1025-1031
34. Moulton KS, Vakili K, Zurakowski D, Soliman M, Butterfield C, Sylvan E, Lo KM, Gillies S, Javaherian K, Folkman J. Inhibition of plaque neovascularization reduces macrophage accumulation and progression of advanced atherosclerosis. *Proc Natl Acad Sci U S A*. 2003;100:4736-4741
35. Briley-Saebo KC, Amirbekian V, Mani V, Aguinaldo JG, Vucic E, Carpenter D, Amirbekian S, Fayad ZA. Gadolinium mixed-micelles: Effect of the amphiphile on in vitro and in vivo efficacy in apolipoprotein e knockout mouse models of atherosclerosis. *Magn Reson Med*. 2006;56:1336-1346
36. Daugherty A, Cornicelli JA, Welch K, Sendobry SM, Rateri DL. Scavenger receptors are present on rabbit aortic endothelial cells in vivo. *Arterioscler Thromb Vasc Biol*. 1997;17:2369-2375
37. McAteer MA, Sibson NR, von Zur Muhlen C, Schneider JE, Lowe AS, Warrick N, Channon KM, Anthony DC, Choudhury RP. In vivo magnetic resonance imaging of acute brain inflammation using microparticles of iron oxide. *Nat Med*. 2007;13:1253-1258
38. Choudhury RP, Fuster V, Fayad ZA. Molecular, cellular and functional imaging of atherothrombosis. *Nat Rev Drug Discov*. 2004;3:913-925
39. Jaffer FA, Weissleder R. Seeing within: Molecular imaging of the cardiovascular system. *Circ Res*. 2004;94:433-445
40. Jaffer FA, Libby P, Weissleder R. Molecular and cellular imaging of atherosclerosis: Emerging applications. *J Am Coll Cardiol*. 2006;47:1328-1338
41. Tang TY, Muller KH, Graves MJ, Li ZY, Walsh SR, Young V, Sadat U, Howarth SP, Gillard JH. Iron oxide particles for atheroma imaging. *Arterioscler Thromb Vasc Biol*. 2009;29:1001-1008
42. Choudhury RP, Fisher EA. Molecular imaging in atherosclerosis, thrombosis, and vascular inflammation. *Arterioscler Thromb Vasc Biol*. 2009;29:983-991
43. de Vries HE, Moor AC, Dubbelman TM, van Berkel TJ, Kuiper J. Oxidized low-density lipoprotein as a delivery system for photosensitizers: Implications for photodynamic therapy of atherosclerosis. *J Pharmacol Exp Ther*. 1999;289:528-534
44. Lipinski MJ, Amirbekian V, Frias JC, Aguinaldo JG, Mani V, Briley-Saebo KC, Fuster V, Fallon JT, Fisher EA, Fayad ZA. Mri to detect atherosclerosis with gadolinium-containing immunomicelles targeting the macrophage scavenger receptor. *Magn Reson Med*. 2006;56:601-610
45. Amirbekian V, Lipinski MJ, Briley-Saebo KC, Amirbekian S, Aguinaldo JG, Weinreb DB, Vucic E, Frias JC, Hyafil F, Mani V, Fisher EA, Fayad ZA. Detecting and assessing macrophages in vivo to evaluate atherosclerosis noninvasively using molecular mri. *Proc Natl Acad Sci U S A*. 2007;104:961-966
46. Briley-Saebo KC, Shaw PX, Mulder WJ, Choi SH, Vucic E, Aguinaldo JG, Witztum JL, Fuster V, Tsimikas S, Fayad ZA. Targeted molecular probes for imaging atherosclerotic lesions with magnetic resonance using antibodies that recognize oxidation-specific epitopes. *Circulation*. 2008;117:3206-3215

47. Beilvert A, Cormode DP, Chaubet F, Briley-Saebo KC, Mani V, Mulder WJ, Vucic E, Toussaint JF, Letourneur D, Fayad ZA. Tyrosine polyethylene glycol (peg)-micelle magnetic resonance contrast agent for the detection of lipid rich areas in atherosclerotic plaque. *Magn Reson Med*. 2009;62:1195-1201
48. Cormode DP, Briley-Saebo KC, Mulder WJ, Aguinaldo JG, Barazza A, Ma Y, Fisher EA, Fayad ZA. An apo-a-i mimetic peptide high-density-lipoprotein-based mri contrast agent for atherosclerotic plaque composition detection. *Small*. 2008;4:1437-1444
49. Haxby JA, Kinsky CB, Kinsky SC. Immune response of a liposomal model membrane. *Proc Natl Acad Sci U S A*. 1968;61:300-307
50. Briley-Saebo KC, Mulder WJ, Mani V, Hyafil F, Amirbekian V, Aguinaldo JG, Fisher EA, Fayad ZA. Magnetic resonance imaging of vulnerable atherosclerotic plaques: Current imaging strategies and molecular imaging probes. *J Magn Reson Imaging*. 2007;26:460-479





submitted

Chapter 6

Vascular cell adhesion molecule-1 targeted nanoparticles discriminate between atherosclerotic plaque stages in disease progression and therapy

Brigit den Adel, Ernst Suidgeest, Carmen Burtea, Kim van der Heiden, Marieke Stammes, Sophie Laurent, Kim van Gaalen, Frank Gijsen, Robert N Muller, Robert E Poelmann and Louise van der Weerd

ABSTRACT

Rationale

Non-invasive determination of atherosclerotic plaque composition is essential for diagnosis, monitoring and treatment of atherosclerosis. We and others have observed that Vascular Cell Adhesion Molecule-1 (VCAM-1) is weakly expressed in healthy vessels but rapidly induced on vascular endothelium in early atherosclerotic plaques. In later plaque stages VCAM-1 is expressed on vascular smooth muscle cells and macrophages. The aim of this study was to image selective enhancement of VCAM-1 positive atherosclerotic plaque using VCAM-1 targeted USPIO. Secondly, we hypothesized that endothelial and intraplaque VCAM-1 expression could be distinguished based on the biokinetics of VCAM-1-USPIO.

Methods and Results

First, targeting of VCAM-1-USPIO versus a non-targeted control USPIO was assessed in aortic arch plaques of aged ApoE^{-/-} mice. VCAM-1-USPIO contrast on MRI was significantly increased when compared to control particles, and colocalized with VCAM-1 expression. Secondly, plaque progression was imaged at 3, 6 and 9 weeks after placement of a carotid artery collar to induce plaque formation in young ApoE^{-/-} mice. VCAM-1 targeted USPIO enhancement at 1.5 hours after i.v. injection showed enhanced uptake of the contrast agent (CA) in the vessel wall of all mice. 6 hours after injection, intraplaque binding of the CA was apparent in mice with more advanced lesions. The CNR ratio between early (1.5 hr) and late (6 hrs) imaging time points allowed us to discriminate reliably between different plaque stages. To test the potential of VCAM-1-USPIO to monitor therapy response, ApoE^{-/-} mice were exposed to a western diet with or without atorvastatin. A clear correlation was observed between the therapy response and intraplaque VCAM-1-USPIO accumulation.

Conclusion

VCAM-1 targeted USPIO holds great promise for *in vivo* non-invasive determination of atherosclerotic plaque composition and stage. Ultimately this technology might be an effective tool for diagnosis and monitoring of disease progression in patients.

INTRODUCTION

Clinically as well as pre-clinically, it is of great interest to identify and characterize vulnerable atherosclerotic lesions timely, since early diagnosis may prevent progression towards vascular events, including myocardial infarction (MI) or ischemic stroke. Current non-invasive clinical imaging technologies largely focus on luminal narrowing¹ and do not provide information on plaque composition. However, more and more studies show that the anatomical severity of stenosis is a poor predictor for plaque rupture, and thereby for the risk of vascular events². More sophisticated molecular imaging techniques are now rapidly evolving, providing direct information on plaque composition and the biological processes involved in plaque progression and plaque vulnerability^{1, 3, 4}.

To achieve this, targeted contrast agents are needed that can identify molecules of interest with high specificity, while conveying sufficient contrast to be easily distinguished from unenhanced tissue. MRI is a promising imaging modality as it is non-invasive and provides excellent soft tissue contrast, high spatial resolution and structural definition. The sensitivity for contrast agent

detection using MRI is inherently low compared to other molecular imaging modalities such as positron emission tomography (PET). Nevertheless, for indications such as atherosclerotic plaques, with highly abundant targets that are readily accessible, MRI using targeted contrast agents has been shown to be a viable imaging technique⁵⁻⁷.

In atherosclerotic plaques, numerous potential molecular imaging targets are expressed either by endothelial cells and / or by cells within the wall of the artery. Ideally, a molecule of interest is differentially expressed from early lesion formation to advanced plaques^{5, 8}.

Early markers of atherogenesis include endothelial cell adhesion molecules, such as P- and E-selectin (CD62-E), and vascular cell adhesion molecule-1 (VCAM-1: CD106), which facilitate mononuclear leukocyte recruitment to activated endothelium and subsequent transmigration into the subendothelial space^{9, 10}. VCAM-1 expression particularly plays a cardinal role in atherosclerotic plaque progression¹¹⁻¹³. The adhesion molecule is present on the endothelium at atherosclerosis-prone sites even before macroscopic disease is apparent. As the lesion advances, VCAM-1 expression persists, but shifts from the endothelium to intraplaque sites, i.e. lesional macrophages and smooth muscle cells¹¹⁻¹³.

We¹⁴⁻¹⁶ and others¹⁷⁻²² have already successfully demonstrated that VCAM-1 targeted nanoparticles can detect atherosclerotic plaques and other inflammatory processes using MRI or nuclear techniques. Using VCAM-1-targeted ultrasmall superparamagnetic iron oxide (USPIO), robust contrast enhancement could be demonstrated in aortic plaque in the ApoE^{-/-} mouse model^{16, 18}. However, the feasibility to distinguish intraplaque and endothelial VCAM-1 expression by *in vivo* MRI, has not yet been investigated, nor the relation between these expression sites and plaque progression and therapy response.

The aim of this study was to test whether it is feasible to differentiate early and advanced plaques using VCAM-1 targeted USPIOs. To that extend, we compared the VCAM-1-targeted contrast enhancement at different time points after injection. We hypothesized that early imaging time points favor the enhancement of endothelial VCAM-1 expression, whereas imaging at later time points visualizes USPIO binding both at the endothelial layer and inside the plaque, thus providing a method to differentiate between early and advanced plaque. In addition, we hypothesized that this method could be used to monitor atherosclerotic plaque progression over time and the effect of an anti-atherosclerotic therapy in the ApoE^{-/-} mouse model.

MATERIALS AND METHODS

Contrast agents

USPIO were prepared as previously described^{15, 16}. In short, a VCAM-1-targeted cyclic heptapeptide was conjugated to USPIO (USPIO-R832 hereafter called VCAM-1 USPIO), and VCAM-1 binding was first confirmed on human umbilical vein endothelial cells (HUVEC) stimulated with TNF-alpha. The control imaging probe was represented by USPIO vectorized by a non-specific peptide (USPIO-NSP, called control USPIO). The size of functionalized USPIO was ~30 nm. Further characterization of these particles can be found in¹⁶.

MRI Hardware

All experiments were performed on a vertical 89-mm bore 9.4T magnet (Bruker, Ettlingen, Germany) with an actively shielded Micro2.5 gradient system of 1T/m and a 30 mm transmit/receive birdcage RF coil, using Paravision 5.0 software.

Animal experiments

All experiments were conducted in accordance with the Dutch guidelines for research animal care. In total 12 groups of $n=5$ (with the exception of 2 groups of $n=8$) male ApoE^{-/-} mice on a C57BL/6/Jico background were used for the experiments. Supplemental figure 1 gives an overview of the experimental groups. All mice were housed in groups and allowed ad libitum access to food and water. The given diet was either chow or a Western diet, depending on the experiments, as described below.

Contrast enhancement over time

Optimal time points for plaque accumulation of both the VCAM-1-targeted as well as the untargeted USPIO were determined in a pilot time-course study in 2 groups (group A, supplemental figure 1) of 12-14 months old male ApoE^{-/-} mice in which contrast agent accumulation and wash-out was followed over time for 48 hours. Each mouse was scanned before administration of USPIO and at several time points after intravenous injection of 0.05 mmol Fe/kg bodyweight in 200 μ l dextrose solution. From 0-4 hours after USPIO injection mice were scanned every 30 minutes, thereafter every 2 hours from 4-12 hours after injection and every 6 hours from 12-48 hours after injection. Mice were anesthetized during MRI with isoflurane (\pm 2% in oxygen and air). During the examination, the respiration rate was continuously monitored using a balloon pressure sensor connected to the ECG/respiratory unit. The isoflurane concentration was adjusted to keep the respiration rate between 50 and 90 respirations/min.

The optimal time point was defined as the time at which the largest contrast-to-noise ratio (see below) difference was observed.

In vivo toxicity was assessed after injection of the USPIO in these latter mice. Acute adverse effects were assessed by monitoring changes in heart rate and respiration after injection. Animals were sacrificed 48 hours after contrast agent injection. In each group organs were harvested and inspected for gross abnormalities by a trained animal pathologist (heart, aorta, liver, lungs, spleen and kidneys). No signs of toxicity were observed during this observation period (data not shown).

Supplemental figure 1. Overview of the experimental groups of ApoE^{-/-} mice that were included in the study.

	Group	Age
Optimal imaging time point	A (n=5 VCAM USPIO, n=5 control USPIO)	12-14 months old ApoE ^{-/-} mice
Plaque imaging at 1.5 & 6 hrs	B (n=5 VCAM USPIO, n=5 control USPIO)	12-14 months old ApoE ^{-/-} mice
Collar model plaque stages	C1 (n=5 per age group, 3, 6 & 9 wks) MRI	12 wks old ApoE ^{-/-} mice
	C2 (n=3 per age group, 3, 6 & 9 wks) Western blotting	12 wks old ApoE ^{-/-} mice
Atorvastatin therapy	D (n=5 per age groups, 3, 6 & 9 weeks)	12 wks old ApoE ^{-/-} mice
Plasma half-time	E (n=5 VCAM USPIO, n=5 control USPIO)	12-14 months old ApoE ^{-/-} mice

Plaque imaging in aged ApoE^{-/-} mice

2 groups (n=5 per group, group B) of 12-to-14-month-old male ApoE^{-/-} mice were fed a normal chow diet. Each mouse was scanned before administration of contrast agent to visualize the aortic arch without contrast enhancement. The groups were injected with either VCAM-1 or untargeted USPIO and scanned at two time points after injection: 1.5 hours and 6 hours. These time points had been determined from the pilot time course experiment to be the optimal time points for endothelial enhancement and intraplaque enhancement respectively.

Imaging of plaque stage in ApoE^{-/-} mice with carotid cuff

3 groups (n=8) of 12-week-old male ApoE^{-/-} mice were exposed to a Western diet (1% Cholesterol, Ab-diets, The Netherlands). Four weeks later, at the age of 16 weeks, a restrictive collar was placed around the left carotid artery, to mechanically induce the formation of atherosclerotic plaques around the collar. Mice were randomized for 3, 6 or 9 week follow-up of plaque formation, corresponding to early, intermediate and advanced plaque formation stages respectively. At each time point a group of 5 mice (group C1) was scanned before contrast agent injection and 1.5 and 6 hours thereafter. The remaining mice (n=3, group C2) were sacrificed and the left carotid artery was dissected for western blot analysis.

Imaging of the effect of atorvastatin therapy on plaque development

Finally, 3 groups (n=5, group D) of 12-week-old male ApoE^{-/-} mice were exposed to a Western diet with or without the addition of 0.01% wt/wt atorvastatin (Lipitor, Pfizer) (=0.1g statin / kg bodyweight) for a period of 4 weeks. After 4 weeks, at the age of 16 weeks, the restrictive collar was placed around the left carotid artery. Mice were randomized for 3, 6 or 9 week follow-up of plaque formation, subsequently mice were scanned 1.5 and 6 hours after i.v. injection of VCAM-1 targeted USPIO.

MRI protocols

At the start of each *in vivo* examination, several 2D Fast Low Angle Shot (FLASH) scout images were recorded in the transverse and axial plane of the heart to determine the orientation of the aortic arch.

A modified 2D FLASH sequence with a navigator echo (IntraGate, Bruker) was used for retrospective CINE MRI with the following parameters:

T1 weighted images: hermite-shaped RF pulse 1 ms; FA 15°; TR 31.4 ms; TE 2.96 ms; navigator echo points 64; 10 cardiac frames; FOV 1.8*1.8 cm²; matrix 128*128; in-plane resolution 141 μm; slice thickness 0.4 mm; number of repetitions 400.

T2 weighted images:* hermite-shaped RF pulse 1 ms; FA 10°, TR 34 ms, TE 6 ms, navigator echo points 64; 10 cardiac frames; FOV 1.8*1.8 cm²; matrix 256*256; in-plane resolution 70 μm; slice thickness 0.4 mm; number of repetitions 400.

Image Analysis

Images were analyzed using ImageJ software. Bright blood images were analyzed in 3 to 4 adjacent cross-sectional slices through the aortic arch as described previously ((23)in press). ROIs were semi-automatically drawn around the vessel wall (I_{wall}) in all 10 movie frames. A 2nd ROI was drawn in the surrounding muscle tissue of the shoulder girdle (I_{muscle}). Furthermore, an ROI was placed outside the animal to measure the noise level (SD_{noise}).

The contrast-to-noise ratio was defined in the 3 to 4 adjacent bright-blood movie frames as following:

$$\text{CNR} = (I_{\text{wall}} - I_{\text{muscle}}) / \text{SD}_{\text{noise}} \quad [\text{Eq1}]$$

which is a measure to what extend the lesioned wall can be discriminated from the surrounding tissue.

Histology

Mouse Tissue

After MRI, mice were terminally anesthetized with a intraperitoneal injection of 5 mg/kg midazolam (dormicum®, Roche), 0.5 mg/kg medetomidine (domitor®, Orion corporation, Finland) and 0.05 mg/kg fentanyl (Janssen-Cilag, Belgium) followed by transcardial perfusion with saline; arteries were taken out for histological validation. Aortic arches and carotid arteries were frozen in Tissue Tek® (Sakura Finetek Europe, Zoetermeer, The Netherlands) and cut into serial 5 µm sections. Sections were stained with Oil Red O for lipid deposition and counterstained with hematoxylin, followed by bright-field microscopy. Iron deposits were visualized using Perl's Prussian blue method with DAB enhancement as described previously²⁴. Slides were first incubated with fresh 2% potassium ferrocyanide (Sigma Aldrich) in water, mixed with equal volumes of 2% hydrochloric acid for up to 20 minutes at room temperature. Slides were washed, incubated in methanol/H₂O₂ and subsequently the iron staining was enhanced using 3,3'-diaminobenzidine (DAB) (Sigma-Aldrich). Slides were counterstained with nuclear fast red (Vector Laboratories, Burlingame, USA), and mounted in Vectashield (Vector laboratories).

VCAM-1 was visualized by incubating the sections overnight with rabbit-anti-mouse VCAM-1 (Santa Cruz, H276). Slides were subsequently incubated with biotinylated goat-anti-rabbit (Vector laboratories Inc, United Kingdom) in 1.5% goat serum (Vector Laboratories Inc., United Kingdom). Biotin labelling was followed by development using red alkaline phosphatase substrate (Vector Laboratories Inc., United Kingdom) according to the manufacturer's instructions, and as described in ((25) in press). Counterstaining was performed with Mayer's hematoxylin.

Human coronary artery

Human left anterior descending (LAD) coronary artery was obtained post-mortem. Approval was given by the Institutional Review Board of the Erasmus MC, and informed consent was obtained. The LAD was frozen in Tissue Tek® and cut into serial 5 µm sections. Oil Red O and immunohistochemical staining for CD31/CD34 (clone Jc/70A, Abcam and QBEND-10, Sanbio) as well as CD68 (clone KP1, Abcam) was performed, followed by light microscopical analysis. Furthermore, slices were incubated for 30 minutes with 5 µM VCAM-1 or control USPIO, followed by Prussian blue iron staining as described above.

Western immunoblotting for VCAM-1

Left carotid arteries from group C2 were cleaned and homogenized in cold lysis buffer (100 mmol/L K₂HPO₄, 1 mmol/L phenylmethylsulfonyl fluoride, and 0.2% Triton X-100). Protein concentration was determined by the bicinchoninic acid (BCA) protein assay (Pierce) using bovine serum albumin (2 mg/ml, Pierce, USA) as a standard. Equal amount of protein preparations (10 µg in 25µL buffer) were run on SDS-PAGE, using NuPage 12% Bis-Tris gels (Invitrogen), electro-transferred overnight to polyvinylidene difluoride filter (PVDF) membrane (Hybond-P, GE Healthcare, the Netherlands). To reduce non-specific binding, the PVDF membrane was blocked for 1 h at room temperature with blocking buffer (ECL Advance blocking agent, GE Healthcare) in TBST solution composed of 10 mmol/l Tris-HCl, 0.05% Tween-20, 150 mmol/l NaCl, pH 8.0.

Thereafter, the PVDF membrane was incubated with primary antibodies diluted 1:50,000 in blocking buffer at room temperature for 60 min, washed four times in TBST solution, and incubated with horseradish peroxidase- conjugated secondary antibodies diluted 1:35,000 in blocking buffer at room temperature for 60 min. Bands were visualized with the enhanced chemiluminescence detection system (ECL Advance western blotting detection kit, GE Healthcare), exposed to X-ray film (GE Healthcare).

Molecular band intensity (arbitrary units relative to β -actin) was determined by densitometry using ImageJ. Primary antibodies used were: rabbit-anti-mouse VCAM-1 (Santa Cruz, H276) and rabbit-anti-mouse β -actin (Santa Cruz). Secondary antibody used was goat anti-rabbit IgG conjugated to HRP (Santa Cruz Biotechnology).

Blood half life

Blood circulation half-lives were determined for both USPIO using 2 groups of n=5 (group E) 12-14 months old ApoE^{-/-} mice. Blood samples from the tail vein were collected in heparin-coated vials at regular intervals before and up to 48 hours after contrast agent administration (0h, 15, 30, 45 min, 1h, 2h, 3h, 4h, 6h, 8h, 12h, 16h, 24h, 32h, 40h, 48h). T1 values of plasma samples and USPIO were determined using a saturation recovery protocol (multi slice multi echo (msme) sequence) with the following parameters: TE 7 ms, TR: 25-20-15-10-8-6-5-4-3-2-1.6-1.2-1.0-0.8-0.6-0.4-0.3 s, excitation hermite 1 ms, ref hermite 0.75 ms, band width 100kHz, matrix 128*128, resolution (195)² μ m, 2*1mm slices.

The T1 values of the various ROIs were determined using a 3-parameter fit function:

$$M(t) = M0 (1 - \exp(-t/T1)) \quad [\text{Eq2}]$$

T2 was measured using a MSME sequence with TR 2000 ms, TE 9-300 ms in 32 steps. hermite-shaped RF pulse 1 ms, ref hermite 0.75 ms, BW 100kHz, matrix 128*128, resolution (195)² μ m, 2*1mm slices. The T2 values of the various ROIs were determined using

$$M[t]=M0*\exp(-t/T2) \quad [\text{Eq3}]$$

The change in the relaxation rate ($\Delta R2$) of the blood over time was determined by:

$$\Delta R2, \text{blood}(t) = (1/T2, \text{blood}(t)) - (1/T2, \text{blood}(0)) \quad [\text{Eq4}]$$

The $\Delta R2$ change over time was fitted using a mono-exponential decay function:

$$\Delta R2, \text{blood}(t) = A e^{-\ln(2)t/t_{1/2}} \quad [\text{Eq5}]$$

where A is the initial R2 change upon USPIO injection, and t_{1/2} is the circulation half-life of USPIO in the blood.

Soluble VCAM-1 measurements

At baseline and after 2 and 4 weeks, serum concentrations of sVCAM-1 from all mice at a Western diet with or without the addition of atorvastatin (group C1 and D) were determined with an ELISA kit from R&D Systems (Minneapolis, MN, USA) according to the manufacturer's protocol.

Statistical analysis

Data are presented as the mean \pm standard deviation. Statistical analysis was performed using SPSS 15.0 ANOVA for computations within and between groups. Results were considered statistically significant at p < 0.05.

RESULTS

VCAM-1 expression in atherosclerotic plaques

Understanding the spatial and temporal expression patterns of atherosclerosis markers may result in identification of novel diagnostic cues to tailor atherosclerosis therapy. The extracellular adhesion molecule VCAM-1 is reported to be present at atherosclerosis-prone sites in humans even before macroscopic disease is apparent, with persistent expression in more advanced lesions¹¹⁻¹³.

To assess whether the VCAM-1 expression patterns observed in human plaques can be recapitulated in a mice model suitable for longitudinal MRI studies we placed a constrictive collar around the left carotid artery in hypercholesterolemic ApoE^{-/-} mice (figure 1A). In these mice plaque development around the collar is progressive over the course of several weeks and well characterized²⁶. Histological H&E stained sections of typical plaques proximal to the collar are shown in figure 1B, corresponding histological measurement of plaque area is shown in figure 1C. In early plaques, the presence of VCAM-1 was confined to the luminal area (endothelium) (figure 1D). As the atherosclerotic lesion progressed, VCAM-1 positive areas were visible inside the plaque (figure 1E&F). This mouse model thus allows for a controlled induction of early and advanced lesions together with a changing VCAM-1 pattern. Western blot analysis of carotid artery homogenates confirmed our histological finding that total VCAM-1 protein expression increases significantly during collar-induced plaque development (figure 1G).

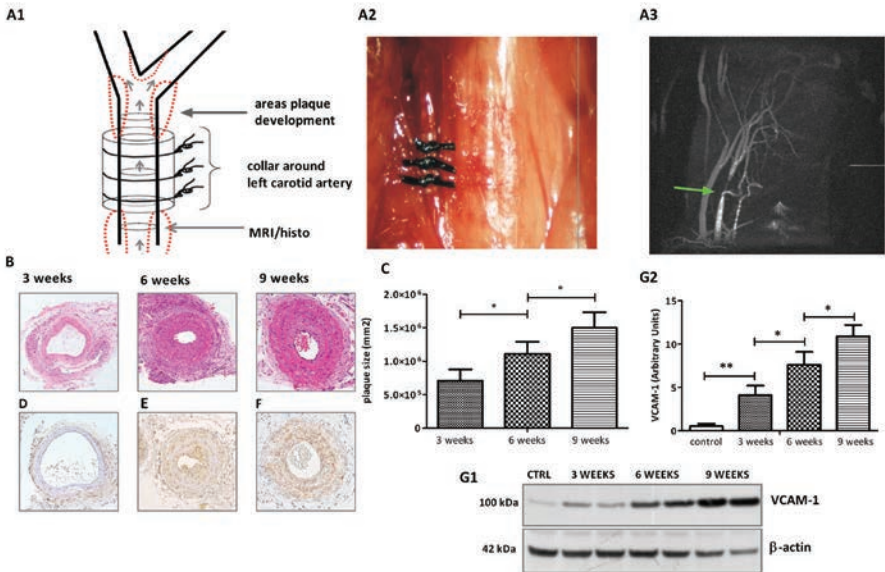


Figure 1 | VCAM-1 expression in atherosclerotic lesions. A1. Schematic depiction of the left carotid artery with a collar. The areas with stimulated plaque development are indicated in red. The grey arrow (corresponding to the green arrow in panel A3) points at the region we used for planning the MRI imaging plane as well as the histological sections. A2. Photo of a collar *in situ* in an ApoE^{-/-} mouse directly after placement. A3. Angiogram of the arterial tree after placement of a collar. B. H&E stainings of sections of the left carotid artery of ApoE^{-/-} mice 3, 6 and 9 weeks after collar placement. C. Histological measurement of the plaque size. D, E and F. VCAM-1 immunohistochemical staining of the left carotid artery of ApoE^{-/-} mice 3, 6 and 9 weeks after collar placement respectively. G1. Western blot for VCAM-1 and β -actin of an undiseased carotid artery and the left carotid artery of ApoE^{-/-} mice 3, 6 and 9 weeks after collar placement. G2. Quantification in arbitrary units of the VCAM-1 Western blot shown in panel G1.

We¹⁴⁻¹⁶ and others¹⁷⁻²¹ have already successfully demonstrated that VCAM-1 targeted nanoparticles can detect atherosclerotic plaques and other inflammatory processes using MRI or nuclear techniques. Here, we attempt to take VCAM-1 imaging to the next level by assessing the feasibility of *in vivo* intraplaque and endothelial VCAM-1 imaging, and its relation to plaque development and therapy response.

Relaxivity of USPIO at 9.4T

Relaxivity measurements yield information on the strength of the contrast agent at a given MRI field strength. The r1 and r2 relaxivity were calculated based on relaxation time measurements at 9.4T. VCAM-1 USPIO r1 relaxivity was 0.850 s⁻¹ mM⁻¹ and r2 121.8. s⁻¹ mM⁻¹ versus r1 of 0.948 s⁻¹ mM⁻¹ and r2 of 131.46. s⁻¹ mM⁻¹ for control USPIO at 37 °C respectively (Table1). The r2/r1 ratio was 141.95 and 138.6 for VCAM-1 USPIO and control USPIO respectively, indicating that these particles will result mainly in T2 and T2* contrast.

Blood half-life in aged ApoE^{-/-} mice

Next, we assessed the *in vivo* properties of the VCAM-1 and control USPIO in aged ApoE^{-/-} mice. Blood samples obtained at different time points after intravenous injection were used to measure the blood circulation half-life of VCAM-1 and control USPIO. Relaxation rates (R2) of the different blood samples were measured and T_{1/2} was calculated accordingly. Control USPIO had a blood circulation half-life of ~7.5 ± 0.8 hours. VCAM-1 USPIOs had a slightly shorter blood circulation half-life of 5.9 ± 1.3 hours (Table 1).

Atherosclerotic plaque detection in aged ApoE^{-/-} mice

Having established the compound kinetics, we assessed the *in vivo* targeting of plaques in the aortic arch of 12-14 months old ApoE^{-/-} mice. Before USPIO injection, the contrast to noise ratio (CNR) of atherosclerotic plaques in the aortic arch to surrounding muscle was -2.75 ± 0.85, and plaques were not easily discernible on T1 or T2* weighted images (figure 2A T1 weighted image). As early as 0.5 hours after injection, VCAM-1 USPIO caused a marked MRI contrast effect in the inner curvature of the aortic arch, evident as focal hypointense areas on T₂*-weighted self-gated images of the aortic arch (figure 2B). The contrast enhancement persisted for over 24 hours and was observed in atheroprone areas, as confirmed by post-mortem Oil Red O stainings of the same animals (figure 2C and 2D). At the earliest time points, however, the blood plasma levels were too high to clearly visualize the vessel wall (figure 2B). The largest difference in contrast enhancement of VCAM-1 USPIOs compared to control USPIOs was observed at 1.5 hours after intravenous injection (figure 2E).

Table 1. Ex vivo relaxivity measurements, in vivo circulation half-time and peak contrast enhancement of VCAM-1 and control USPIO at 9.4T.

	VCAM-1 USPIO	Control USPIO
r1 (s ⁻¹ mM ⁻¹)	0.858	0.948
r2 (s ⁻¹ mM ⁻¹)	121.816	131.46
T _{1/2} (hours)	5.9 ± 1.3	7.5 ± 0.8
Peak contrast <i>in vivo</i> (hours)	1.5	

At this time point the USPIO accumulation could mainly be observed at the endothelium, as illustrated by the iron staining of the aortic arch (figure 2F). Note that USPIO binding is only observed in the areas with atherosclerotic lesions, not on the contralateral side of the artery. As it takes time for USPIOs to infiltrate a plaque, we postulated that imaging later after injection would favor imaging of intraplaque binding. Imaging 6 hours after injection unveiled higher VCAM-1 USPIO uptake inside the plaque as illustrated by iron staining of the aortic arch harvested immediately after MRI at the 6 hour time point (figure 2G). 24 hours after injection, the CNR in the lesional areas is still high, but did not differ significantly anymore between control and VCAM-1 USPIO injected ApoE^{-/-} mice, indicating that passive USPIO accumulation is dominating the enhancement at this stage.

Plaque staging - Endothelial versus intraplaque VCAM-1 imaging

We used the hypercholesterolemic ApoE^{-/-} mouse model with a constrictive collar to assess whether it is possible to differentiate early from more advanced lesions using VCAM-1 targeted USPIO. CNR was determined on T2*-weighted MRI 1.5 and 6 hours after VCAM-1 USPIO injection at 3, 6 or 9 weeks after collar placement in different groups to assess early, intermediate or late plaque stages respectively (figure 3A). Highest decrease in CNR on 1.5 hour post-injection MR images (early) was observed 3 weeks after collar placement, i.e. in an early plaque stage. The CNR change became smaller with plaque progression. 9 weeks after collar placement the CNR shows an

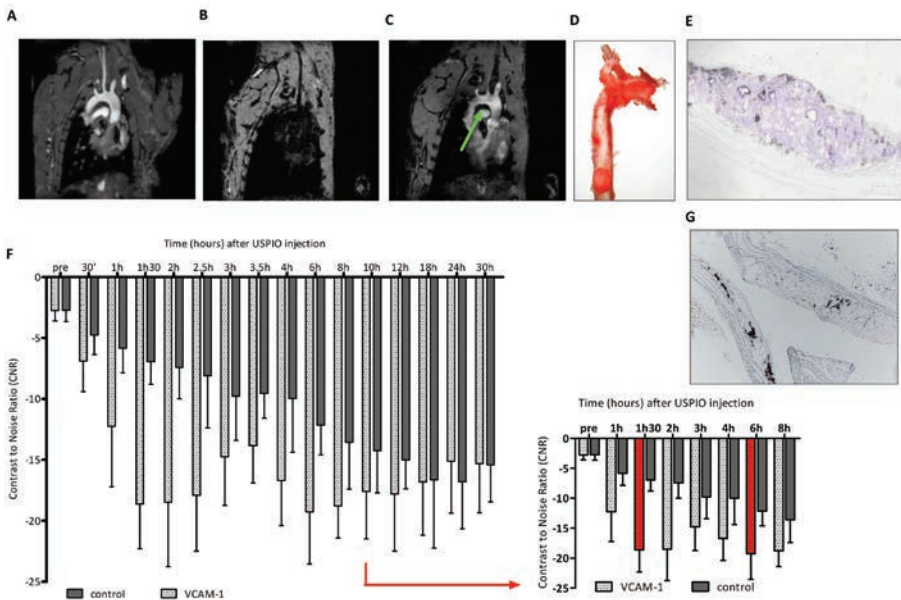


Figure 2 | Atherosclerotic plaque detection in ApoE^{-/-} mice with VCAM-1 USPIO. A. T1 weighted MRI of the aortic arch of a 12-14 months old ApoE^{-/-} mouse without injection of USPIO. B. T2* weighted MRI of the same aortic arch as in panel A, 30 minutes after VCAM-1 USPIO injection. C. Contrast enhancement on the inner curvature of the aortic arch 24 hours after VCAM-1 USPIO injection. The green arrow points at a plaque region. D. Corresponding Oil Red O staining of the aortic arch and descending aorta of a 12-14 months old ApoE^{-/-} mouse. E. Iron staining of an atherosclerotic lesion in the aortic arch 1.5 hours after VCAM-1 USPIO injection. F. Kinetics in Contrast to Noise Ratio (CNR) after injection of either control or VCAM-1 targeted USPIO. A zoom of a selection of time points is shown for clarity. In red are the optimal imaging time points

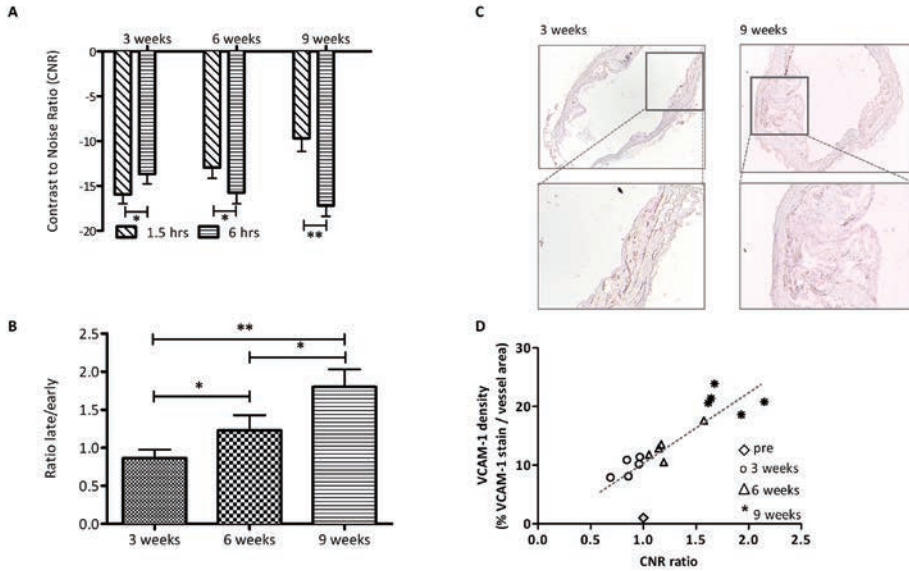


Figure 3 | VCAM-1 targeted imaging of different stages of atherosclerosis. A. CNR measured 1.5 and 6 hours after VCAM-1 USPIO injection in carotid arteries of ApoE^{-/-} mouse with a collar around the left carotid artery at 3, 6 and 9 weeks after placement. B. Ratio of late versus early imaging time points CNR in carotid arteries of ApoE^{-/-} mouse with a collar around the left carotid artery at 3, 6 and 9 weeks after placement. C. Immunohistochemical assessment of VCAM-1 (in red) and VCAM-1 USPIO (in brown) staining in the carotid artery of ApoE^{-/-} mice. D. Correlation between the *in vivo* VCAM-1 USPIO enhancement signal and the *ex vivo* VCAM-1 density in the plaque.

opposite trend, with advanced plaques, having a larger CNR change than early lesions at 6 hours after injection. The ratio of the late (6h) over early (1.5h) CNR is indicative for the plaque stage in this model (figure 3B). In the collar-induced plaque model an early plaque was characterized by a late/early ratio <1, whereas advanced plaques had a ratio > 1.5.

Immediately after MRI, the left carotid arteries were harvested for immunohistochemical assessment of VCAM-1 USPIO distribution and VCAM-1 distribution. Areas with positive staining for VCAM-1 were shown to be associated with areas where VCAM-1-USPIO was present (figure 3C). We found a significant correlation ($R^2 = 0.6945$, $p < 0.001$) between the *in vivo* VCAM-1 USPIO enhancement (CNR ratio on T2*w-MRI) and *ex vivo* VCAM-1 density in the plaque respectively (figure 3D)

Atorvastatin therapy

To assess the potential of VCAM-1 targeted molecular imaging for therapy follow-up, ApoE^{-/-} mice were fed a Western diet supplemented with atorvastatin. The mice were injected with VCAM-1 targeted USPIO at 3, 6 or 9 weeks after collar placement, and as before MRI was performed 1.5 and 6 hours after contrast agent injection.

Statin treatment significantly decreased the CNR change of VCAM-1 USPIO at 1.5 hours after injection (figure 4A), indicating reduced VCAM-1 USPIO binding to the endothelial layer in the left carotid artery in all plaque stages. The effect of statin therapy on the CNR at 6 hours after injection was even more pronounced, with CNR changes becoming significantly smaller over time, indicating reduced intraplaque targeting (figure 4A). The late/early CNR ratio after therapy was

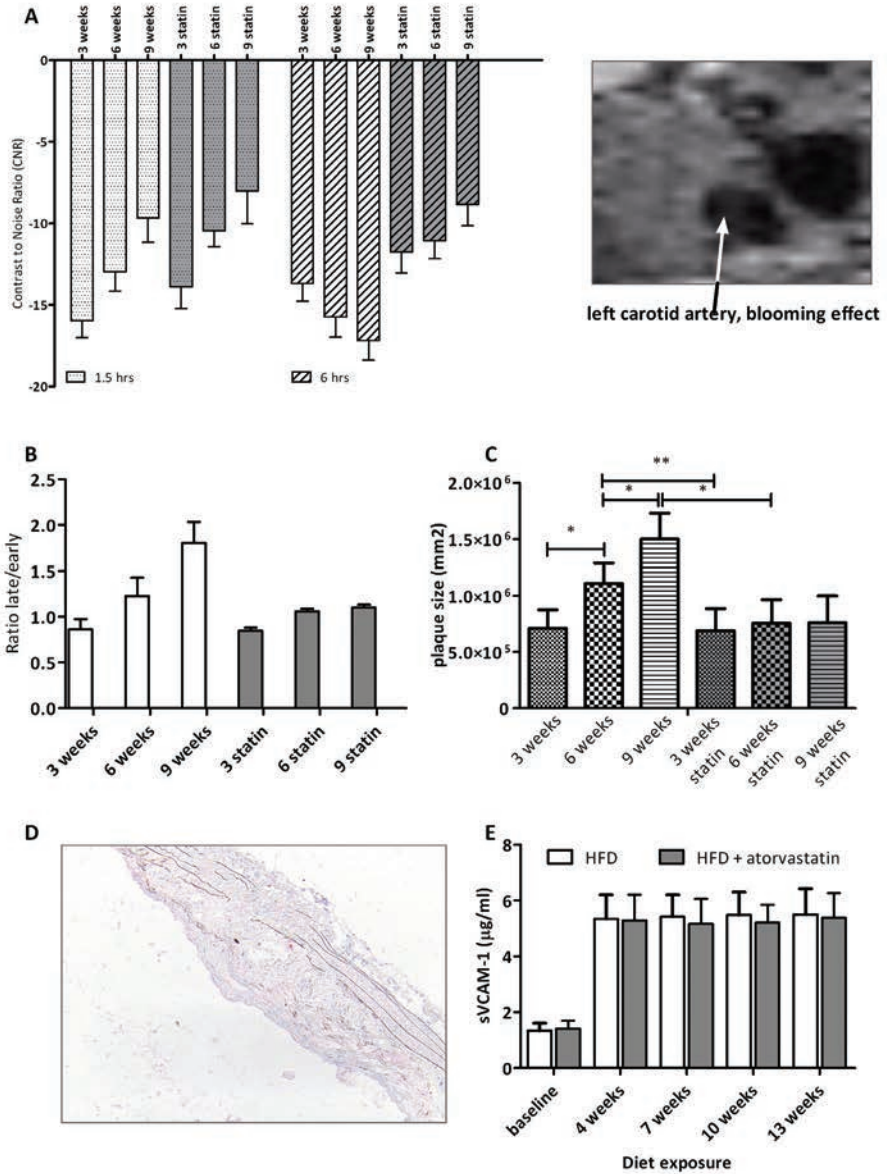


Figure 4 | VCAM-1 targeted imaging for atorvastatin therapy follow-up. A. CNR measured 1.5 and 6 hours after VCAM-1 USPIO injection in carotid arteries of ApoE^{-/-} mouse with a collar around the left carotid artery at 3, 6 and 9 weeks after placement. Mice were either fed a Western diet (dotted bars) or a Western diet supplemented with atorvastatin (striped bars). B. Late/early imaging ratio to assess the plaque phenotype in mice with a collar around the left carotid artery. Mice were either fed a Western diet (white bars) or a Western diet supplemented with atorvastatin (grey bars). C. Immunohistochemical measurement of the plaque area in plaques in the carotid artery at 3, 6 and 9 weeks after collar placement, with (grey bars) or without (white bars) atorvastatin treatment respectively. D. VCAM-1 staining in an atherosclerotic lesion after atorvastatin treatment. E. Circulating sVCAM-1 levels determined by ELISA in plasma samples taken at baseline, 4, 7, 10 and 13 weeks of diet exposure.

around 1 during all time points, indicating a less advanced plaque phenotype (figure 4B). Immunohistochemical assessment of plaque area showed that plaque growth was reduced (figure 4C). Also VCAM-1 expression was less prominent in the atorvastatin-treated mice compared to the control mice, with the largest effect inside the plaque (figure 4D).

Atorvastatin potentially could affect the amount of VCAM-1 shedding into the blood stream, thereby influencing the kinetics and binding potential of VCAM-1 USPIO. Therefore, we assessed soluble VCAM-1 levels in plasma samples taken at 4, 7, 10 and 13 weeks of Western diet exposure, but no significant differences in circulating VCAM-1 were observed between treated and non-treated animals (figure 4E).

Confirmation of VCAM-1 imaging of atherosclerotic lesions in humans

As initial evidence of the potential for VCAM-1-USPIO imaging in humans, we incubated human obduction material of a LAD with both USPIO. Typical USPIO binding could be observed on the surface of an atherosclerotic plaque after incubation with VCAM-1 USPIO (figure 5A) in areas where VCAM-1 could be detected by immunohistochemistry (figure 5B) but not after incubation with control USPIO (figure 5C). Plaque morphology was further illustrated using Oil Red O (figure 5D), macrophage content by CD68 staining (figure 5E), and endothelium by CD31 staining (figure 5F).

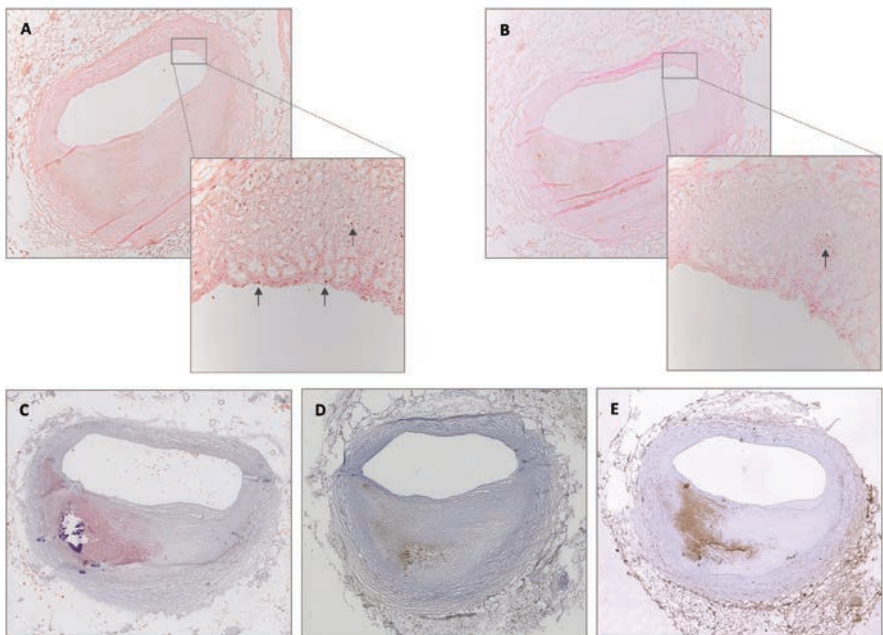


Figure 5 | VCAM-1 USPIO imaging on human vessels. A. Prussian blue staining of VCAM-1 USPIO that were incubated on a human LAD. Arrows point at DAB positive areas with clusters of USPIO. B. VCAM-1 immunostaining on human LAD. C. Prussian blue staining of control USPIO that were incubated on a human LAD. Arrows point at DAB positive areas with clusters of USPIO. Plaque morphology was further illustrated using D. Oil Red O E. CD68 staining and F. CD31 staining (figure 5E).

DISCUSSION

Feasibility of VCAM-1-targeted molecular imaging

In the current study we successfully demonstrated the feasibility of endothelial and intraplaque VCAM-1 MR imaging in an ApoE^{-/-} mouse model of atherosclerosis using VCAM-1 USPIO. The biodistribution of VCAM-1 USPIO proved favorable: VCAM-1 was specifically visualized at the area of atherosclerotic plaques, whereas contrast enhancement in undiseased vessels and the blood pool (at the optimal imaging time points) signal were low. VCAM-1 USPIO selectively targeted areas of atherosclerotic plaque with high VCAM-1 expression, as confirmed by histology.

Early stage atherosclerotic plaques showed the largest contrast change at 1.5 hours after VCAM-1 USPIO injection. The reverse was true for advanced lesions: the largest contrast change was observed at 6 hours after injection of VCAM-1 USPIO. The ratio between early and late enhancement provides a reliable measure of plaque progression.

Atorvastatin treatment, known to reduce VCAM-1 expression²⁷, diminished VCAM-1 USPIO accumulation *in vivo*.

The dose of USPIO administered in our study was 0.05 mmol Fe/kg body weight (corresponding to 2.8 mg/kg body weight), which is similar to that used clinically for non-targeted iron contrast agents in oncological imaging (2.6 mg/kg)²⁸ and significantly lower than some ultrasmall particles of iron oxide doses used experimentally for imaging animal models such as rabbits (11–56 mg/kg)²⁹.

Role of VCAM-1 in atherosclerosis

The recognition that inflammation drives the development and complication of atherosclerosis offers several potential imaging targets; vascular cell adhesion molecule-1 (VCAM-1) has gained considerable attention in this regard. Furthermore, like many other diseases, atherosclerosis is most amenable to treatment at an early stage. Efforts are underway to create novel therapies aimed at interrupting the inflammatory events that initiate plaque formation. If treatment is to be initiated years to decades before atherosclerosis becomes clinically evident, then a method for accurately detecting vascular inflammation is a critical asset.

Lipid lowering (LDL) with statins (3-hydroxy-3-methylglutaryl coenzyme A reductase inhibitors) is an established therapy in the primary and secondary prevention of atherosclerotic disease³⁰. Although the LDL lowering does not occur in ApoE^{-/-} mice^{31, 32} statins also have beneficial effect on the inflammatory process involved in atherosclerosis plaque formation and progression both in mice and men³³. As VCAM-1 is one of these markers of inflammation, we used this well-known clinical drug, atorvastatin, to assess treatment response in ApoE^{-/-} mice with different plaque stages.

Previous studies on VCAM-1 imaging have used several different molecules like affinity ligands detected by ultrasound (coupled to microbubbles)^{34, 35}, by MRI (attached to iron oxides^{16, 18, 20, 36} or using F-19³⁷), or by nuclear imaging (derivatized with F-18²¹). This earlier work provided evidence for the feasibility in several imaging modalities, addressed the imaging of therapeutic efficiency, and explored a variety of applications. Our work is unique in the sense that we apply a VCAM-1 targeted USPIO to differentiate early from advanced atherosclerotic lesions by tuning the imaging timing to detect different origins of contrast enhancement.

Endothelial and intraplaque VCAM-1 expression

Understanding the spatial and temporal expression patterns of atherosclerosis markers may result in identification of novel diagnostic cues to tailor atherosclerosis therapy. The extracellular

adhesion molecule VCAM-1 is present at atherosclerosis-prone sites in humans even before macroscopic disease is apparent, with persistent expression in more advanced lesions¹¹⁻¹³. In later plaque stages, VCAM-1 expression shifts from the endothelial layer to lesional macrophages and smooth muscle cells. The collar model used in this study results in VCAM-1 expression patterns that closely resemble the expression during human plaque development.

The early induction, confinement of expression to atherosclerotic lesions, and accessible position in proximity to the blood pool render VCAM-1 an attractive imaging biomarker for early stage plaque identification. Moreover, the presence of the adhesion molecule on lesional macrophages and smooth muscle cells in later plaque stages make VCAM-1 an attractive candidate to image advanced atherosclerotic plaques.

While the role of VCAM-1 as mediator of monocyte chemotaxis is rather well understood^{9,13}, the role of VCAM-1 expression inside the plaque in advanced lesions remains speculative. VCAM-1 expressed by vascular smooth muscle cells (SMCs) may facilitate the accumulation of transmigrated leukocytes within the vascular wall¹³. Indeed, in advanced human plaques, VCAM-1 expression is not often observed on the endothelial cells in the arterial lumen, but it is prevalent at the base of plaques^{38, 39}. VCAM-1 expression on SMCs in the intima and media is most prominent in fibrous plaques and advanced atherosclerotic lesions⁴⁰. Macrophages on the other hand are known to express VCAM-1 in lipid-containing plaques⁴¹, implying that no clear VCAM-1 expression pattern is associated with either stable or unstable atherosclerotic lesions.

Despite the lack of knowledge of the exact role of intraplaque VCAM-1, response to therapy can be evaluated using this VCAM-1 specific contrast agent. VCAM-1 USPIO could theoretically be useful in patients in which atherosclerotic lesions already have been identified with conventional imaging techniques. In these patients, VCAM-1 USPIO could serve as a tool for *in vivo* differentiation between early lesions and more advanced potentially "unstable" atherosclerotic lesions. In our study, we started atorvastatin therapy at an early plaque stage, thereby preventing plaque growth and reducing the pro-inflammatory status. Clinically, it would be of interest to study the effect of statins on the inflammatory response in more advanced plaques, to be able to follow longitudinally whether a reduction in VCAM-1 expression is (directly) associated with a reduced risk for vascular events.

Comparison to other VCAM-1 targeting imaging agents

One of the most successful applications of VCAM-1 contrast agents thus far has been the development of 18F-4V, a hybrid PET-CT tracer, by Nahrendorf *et al*²¹. While PET has higher detection sensitivity (picomolar range) than MRI, and better tissue penetration than ultrasound or OCT, the disadvantages of PET are its limited spatial resolution, logistics of isotope provision, substantial radiation exposure and costs. Similar to our findings, endothelial targeting of 18F-4V is optimal between 60-120 minutes after injection. However, because of the short blood half-life of 18F-4V and the fast decay of the radio isotope, intraplaque targeting is not feasible with this compound.

For molecular MR imaging of endovascular VCAM-1, large iron oxide particles (MPIO) have proven to be very useful⁴². The relatively large size of MPIO makes them less susceptible to non-specific uptake than smaller particles⁴³, thus retaining specificity for endothelial molecular targets. However, this is at the same time the major disadvantage for plaque staging with these particles, as they are not taken up into the plaque. Their use thus remains restricted to the detection of early pro-inflammatory plaques.

Study limitations

The exact role of VCAM-1 in the development and progression of atherosclerotic plaques in ApoE^{-/-} mice has not been fully elucidated. Whether the expression of VCAM-1 on vascular smooth muscle cells and macrophages in advanced lesions represents a marker of stability, instability or only of lesion stage is a matter of ongoing research.

While the current preclinical findings are encouraging, a number of hurdles must be overcome before agents such as VCAM-1 USPIO can be used clinically; perhaps the most important will be the development of fully biodegradable USPIO, together with full toxicological testing of the humanized and biodegradable agent

CONCLUSION

This study demonstrated that molecular MRI using VCAM-1 USPIO allows selective imaging and quantification of endothelial and intraplaque VCAM-1 expression in ApoE^{-/-} mice. VCAM-1 targeted imaging may therefore be a useful approach for *in vivo* detection and staging of atherosclerotic lesions, as well as for monitoring of a therapeutic response.

Acknowledgments

The authors would like to acknowledge Guerbet Group France for providing USPIOs. This work was supported by the European Network of Excellence Diagnostic Molecular Imaging (DIMI, LSHB-CT-2005-512146) to BdA, REP and LvdW, the Netherlands Heart Foundation Grant (NHF, 2006T106) to BdA, and REP, NWO Athena (700.58.80) to LvdW, NOW VENI (916.11.015) to KvdH, Actions de Recherche Concertées (00/05-258 and 05/10-335) and ENCITE (European Network for cell imaging and tracking expertise to CB, SL and RNM. The support and sponsorship concerted by COST Actions (TD1004 and CM1006) and of the EMIL program are acknowledged. The authors thank the Center for Microscopy and Molecular Imaging (CMMI, supported by the European Regional Development Fund and the Walloon Region.

REFERENCES

1. Sanz J, Fayad ZA. Imaging of atherosclerotic cardiovascular disease. *Nature* 2008; 451:953-7.
2. Falk E, Shah PK, Fuster V. Coronary plaque disruption. *Circulation* 1995; 92:657-71.
3. Cyrus T, Lanza GM, Wickline SA. Molecular imaging by cardiovascular MR. *J Cardiovasc Magn Reson* 2007; 9:827-43.
4. Jaffer FA, Libby P, Weissleder R. Molecular imaging of cardiovascular disease. *Circulation* 2007; 116:1052-61.
5. Choudhury RP, Fuster V, Fayad ZA. Molecular, cellular and functional imaging of atherothrombosis. *Nat Rev Drug Discov* 2004; 3:913-25.
6. Amirbekian V, Lipinski MJ, Briley-Saebo KC, et al. Detecting and assessing macrophages in vivo to evaluate atherosclerosis noninvasively using molecular MRI. *Proc Natl Acad Sci U S A* 2007; 104:961-6.
7. Spuentrup E, Botnar RM, Wiethoff AJ, et al. MR imaging of thrombi using EP-2104R, a fibrin-specific contrast agent: initial results in patients. *Eur Radiol* 2008; 18:1995-2005.
8. Choudhury RP. Atherosclerosis and thrombosis: identification of targets for magnetic resonance imaging. *Top Magn Reson Imaging* 2007; 18:319-27.
9. Cybulsky MI, Gimbrone MA, Jr. Endothelial expression of a mononuclear leukocyte adhesion molecule during atherogenesis. *Science* 1991; 251:788-91.
10. Galkina E, Ley K. Leukocyte influx in atherosclerosis. *Curr Drug Targets* 2007; 8:1239-48.
11. Iiyama K, Hajra L, Iiyama M, et al. Patterns of vascular cell adhesion molecule-1 and intercellular adhesion molecule-1 expression in rabbit and mouse atherosclerotic lesions and at sites predisposed to lesion formation. *Circ Res* 1999; 85:199-207.
12. Li H, Cybulsky MI, Gimbrone MA, Jr., Libby P. Inducible expression of vascular cell adhesion molecule-1 by vascular smooth muscle cells in vitro and within rabbit atheroma. *Am J Pathol* 1993; 143:1551-9.
13. Libby P, Li H. Vascular cell adhesion molecule-1 and smooth muscle cell activation during atherogenesis. *J Clin Invest* 1993; 92:538-9.
14. Burtea C, Laurent S, Port M, et al. Magnetic resonance molecular imaging of vascular cell adhesion molecule-1 expression in inflammatory lesions using a peptide-vectorized paramagnetic imaging probe. *J Med Chem* 2009; 52:4725-42.
15. Burtea C, Laurent S, Mahieu I, et al. In vitro biomedical applications of functionalized iron oxide nanoparticles, including those not related to magnetic properties. *Contrast Med. Mol. Imaging* 2011; 6: 236-250.
16. Burtea C, Ballet S, Laurent S, et al. Development of a magnetic resonance imaging protocol for the characterization of atherosclerotic plaque by using vascular cell adhesion molecule-1 and apoptosis-targeted ultrasmall superparamagnetic iron oxide derivatives. *Arterioscler Thromb Vasc Biol* 2012; 32:e36-e48.
17. Kelly KA, Allport JR, Tsourkas A, Shinde-Patil VR, Josephson L, Weissleder R. Detection of vascular adhesion molecule-1 expression using a novel multimodal nanoparticle. *Circ Res* 2005; 96:327-36.
18. Nahrendorf M, Jaffer FA, Kelly KA, et al. Noninvasive vascular cell adhesion molecule-1 imaging identifies inflammatory activation of cells in atherosclerosis. *Circulation* 2006; 114:1504-11.
19. Behm CZ, Kaufmann BA, Carr C, et al. Molecular imaging of endothelial vascular cell adhesion molecule-1 expression and inflammatory cell recruitment during vasculogenesis and ischemia-mediated arteriogenesis. *Circulation* 2008; 117:2902-11.
20. McAteer MA, Sibson NR, von Zur MC, et al. In vivo magnetic resonance imaging of acute brain inflammation using microparticles of iron oxide. *Nat Med* 2007; 13:1253-8.
21. Nahrendorf M, Keliher E, Panizzi P, et al. 18F-4V for PET-CT imaging of VCAM-1 expression in atherosclerosis. *JACC Cardiovasc Imaging* 2009; 2:1213-22.
22. Broisat A, Hernot S, Toczek J, et al. Nanobodies Targeting Mouse/Human VCAM1 for the Nuclear Imaging of Atherosclerotic Lesions. *Circ Res* 2012; 110:927-37.
23. den Adel B, van der Graaf LM, Que I, et al. Contrast enhancement by lipid-based MRI contrast agents in mouse atherosclerotic plaques; a longitudinal study. *Contrast Media Mol Imaging* 2012.
24. Moos T, Mollgard K. A sensitive post-DAB enhancement technique for demonstration of iron in the central nervous system. *Histochemistry* 1993; 99:471-5.
25. den Adel B, Bovens SM, te Boekhorst B, et al. Histological validation of iron-oxide and gadolinium based MRI contrast agents in experimental atherosclerosis: The do's and don't's. *Atherosclerosis* 2012 ; 225(2):274-80.
26. Von Der Thusen JH, Van Berkel TJ, Biessen EA. Induction of rapid atherogenesis by perivascular carotid collar placement in apolipoprotein E-deficient and low-density lipoprotein receptor-deficient mice. *Circulation* 2001; 103:1164-70.
27. Aikawa M, Sugiyama S, Hill CC, et al. Lipid lowering reduces oxidative stress and endothelial cell activation in rabbit atheroma. *Circulation* 2002; 106:1390-6.
28. Gough PJ, Gomez IG, Wille PT, Raines EW. Macrophage expression of active MMP-9 induces acute plaque disruption in apoE-deficient mice. *J Clin Invest* 2006; 116:59-69.
29. Schmitz SA, Coupland SE, Gust R, et al. Superparamagnetic iron oxide-enhanced MRI of atherosclerotic plaques in Watanabe hereditary hyperlipidemic rabbits. *Invest Radiol* 2000; 35:460-71.
30. Shepherd J, Cobbe SM, Ford I, et al. Prevention of coronary heart disease with pravastatin in men with

- hypercholesterolemia. West of Scotland Coronary Prevention Study Group. *N Engl J Med* 1995; 333:1301-7.
31. Grothusen C, Bley S, Selle T, et al. Combined effects of HMG-CoA-reductase inhibition and renin-angiotensin system blockade on experimental atherosclerosis. *Atherosclerosis* 2005; 182:57-69.
 32. Nachtigal P, Pospisilova N, Pospechova K, et al. MDOC and atorvastatin have potential antiinflammatory effects in vascular endothelium of apoE-/- mouse model of atherosclerosis. *Life Sci* 2006; 78:1983-9.
 33. Nachtigal P, Jamborova G, Pospisilova N, et al. Atorvastatin has distinct effects on endothelial markers in different mouse models of atherosclerosis. *J Pharm Pharm Sci* 2006; 9:222-30.
 34. Ferrante EA, Pickard JE, Rychak J, Klibanov A, Ley K. Dual targeting improves microbubble contrast agent adhesion to VCAM-1 and P-selectin under flow. *J Control Release* 2009; 140:100-7.
 35. Kaufmann BA, Sanders JM, Davis C, et al. Molecular imaging of inflammation in atherosclerosis with targeted ultrasound detection of vascular cell adhesion molecule-1. *Circulation* 2007; 116:276-84.
 36. McAteer MA, von Zur MC, Anthony DC, Sibson NR, Choudhury RP. Magnetic resonance imaging of brain inflammation using microparticles of iron oxide. *Methods Mol Biol* 2011; 680:103-15.
 37. Southworth R, Kaneda M, Chen J, et al. Renal vascular inflammation induced by Western diet in ApoE-null mice quantified by ¹⁹F NMR of VCAM-1 targeted nanobeacons. *Nanomedicine* 2009; 5:359-67.
 38. O'Brien KD, Allen MD, McDonald TO, et al. Vascular cell adhesion molecule-1 is expressed in human coronary atherosclerotic plaques. Implications for the mode of progression of advanced coronary atherosclerosis. *J Clin Invest* 1993; 92:945-51.
 39. O'Brien KD, McDonald TO, Chait A, Allen MD, Alpers CE. Neovascular expression of E-selectin, intercellular adhesion molecule-1, and vascular cell adhesion molecule-1 in human atherosclerosis and their relation to intimal leukocyte content. *Circulation* 1996; 93:672-82.
 40. Kasper HU, Schmidt A, Roessner A. Expression of the adhesion molecules ICAM, VCAM, and ELAM in the arteriosclerotic plaque. *Gen Diagn Pathol* 1996; 141:289-94.
 41. Davies MJ, Gordon JL, Gearing AJ, et al. The expression of the adhesion molecules ICAM-1, VCAM-1, PECAM, and E-selectin in human atherosclerosis. *J Pathol* 1993; 171:223-9.
 42. McAteer MA, Mankia K, Ruparella N, et al. A leukocyte-mimetic magnetic resonance imaging contrast agent homes rapidly to activated endothelium and tracks with atherosclerotic lesion macrophage content. *Arterioscler Thromb Vasc Biol* 2012; 32:1427-35.
 43. Briley-Saebo KC, Johansson LO, Hustvedt SO, et al. Clearance of iron oxide particles in rat liver: effect of hydrated particle size and coating material on liver metabolism. *Invest Radiol* 2006; 41:560-71.





under revision

Chapter 7

E-selectin targeted MRI visualizes progression of atherosclerotic plaques

Brigit den Adel, Ernst Suidgeest, Carmen Burtea, Marieke Stammes, Kim van der Heiden, Sophie Laurent, Robert E Poelmann, Robert N Muller and Louise van der Weerd

ABSTRACT

Rationale

Molecular imaging using specific markers for atherosclerotic plaque stage may substantially improve the diagnosis, monitoring and treatment of atherosclerosis. E-selectin is weakly expressed in healthy vessels but rapidly induced on vascular endothelium in early atherosclerotic plaques with increasing expression during plaque progression. We hypothesized that E-selectin targeted ultrasmall particles of iron oxide (E-selectin USPIO) would be a suitable candidate for molecular MRI of atherosclerotic plaque composition and stage.

Methods and Results

We assessed E-selectin USPIO uptake in aortic arch plaques of aged ApoE^{-/-} mice, and in collar-induced plaques in carotid arteries of young ApoE^{-/-} mice. MRI performed 1.5 hours after i.v. injection of E-selectin USPIO showed enhanced uptake of the contrast agent (CA) on the vessel wall in aged mice. Uptake of E-selectin USPIO 1.5 h after injection was significantly increased in mice 3 weeks post collar placement. At later stages after collar placement we observed a higher change in CNR. Passive USPIO uptake imaged 24 hours after USPIO injection gradually increased with increasing plaque size. To test the potential of E-selectin USPIO to monitor therapy response, ApoE^{-/-} mice were exposed to a western diet with or without atorvastatin or fenofibrate. Mice on western diet had large, advanced plaques with a high E-selectin expression. Atorvastatin therapy reduced both plaque burden as well as E-selectin expression on the endothelium. Mice treated with fenofibrate had a smaller change in E-selectin CNR at 1.5 hours after USPIO injection but not less late CA uptake.

Conclusion

E-selectin targeted USPIO holds great promise for *in vivo* non-invasive determination of atherosclerotic plaque composition, progression and stage. Ultimately this technology might be an effective tool for diagnosis and monitoring of disease progression in patients.

INTRODUCTION

Atherosclerosis is a complex arterial disease that affects the large and medium-sized arteries. Cholesterol deposition, oxidative stress, degradation of the extracellular matrix, chronic inflammation, and thrombus formation all play major roles in progression towards clinical events¹. The disease is quickly becoming the leading cause of mortality worldwide, accounting for a fifth of all deaths^{2,3}. Disease progression is usually slow and remains asymptomatic until stenosis occurs and thereby reduced blood supply, or a plaque rupture occurs precipitating clinical events resulting in myocardial infarction or stroke.

Today's clinical imaging technologies focus on the severity of luminal narrowing, yet do not provide information on plaque composition⁴. However, the anatomical severity of stenosis is not sufficient to predict the risk of vascular events⁵. A priori detection of vulnerable or advanced lesions is an increasing clinical need, requiring molecular imaging techniques that provide information on plaque composition and the biological processes associated with progression and destabilization. Because of its high anatomical details, magnetic resonance imaging (MRI) has emerged as a promising technique for both the direct assessment of plaque burden and the evaluation of plaque composition^{6,7}.

In atherosclerosis, a vast range of molecular targets is expressed both at the endothelial surface and within the vessel wall with a differential expression from early lesions to advanced and vulnerable plaques. One of these markers is E-selectin (CD-62E), an endothelial cell adhesion molecule expressed on activated endothelium involved in the recruitment of leukocytes⁸. E-selectin is expressed in the endothelium of human atherosclerotic lesions, particularly when lesions are associated with subendothelial leukocytic infiltrates^{9, 10}. An *et al.* have described that Gr1⁺/Ly6C^{high} “pro-inflammatory” monocytes preferentially accumulate at sites of endothelial activation and thrombosis¹¹, leading to the accumulation of lipid-laden macrophages in apoE-deficient (ApoE^{-/-}) mice¹². The extent of E-selectin expression is related to atherosclerosis development. Soluble E-selectin levels, like other inflammatory markers, is of prognostic value for cardiovascular risk prediction¹³. Also within the plaque, inflammation, particularly monocyte and macrophage infiltration at plaque rupture-sensitive sites (i.e. fibrous cap and areas of erosion) has been shown to be associated with plaque vulnerability¹⁴⁻¹⁶.

Previously, we and others have provided proof-of-concept for E-selectin targeted MRI contrast agents to image endothelial activation in inflammation¹⁷⁻²⁰. Here we tested the ability of the E-selectin targeted USPIOs to detect progression of atherosclerotic lesions. We assessed active targeting of E-selectin using sialyl Lewis X (sLeX) USPIO and control particles by imaging 1.5 hours after USPIO injection. Secondly, we hypothesized that these particles are being engulfed by macrophages whether they are targeted or not. We therefore also imaged the same animals at 24 hours, to assess the macrophage pool^{21, 22}. Lastly, we treated groups of ApoE^{-/-} mice with atorvastatin or fenofibrate, hypothesizing these therapies differentially influence the macrophage pool of atherosclerotic lesions, and assessed the potential of E-selectin targeted molecular imaging to monitor anti-atherosclerotic therapy.

MATERIALS AND METHODS

Contrast agents

USPIO-PEG750-sLeX was prepared as described previously by Radermacher *et al.*¹⁹ Briefly, nanoparticles with carboxylated groups on their surface were modified in 2 steps. Briefly, nanoparticles with carboxylated groups on their surface were first coupled to sLeX mimetic and then to AminoPEG750 by using N-(3-dimethylaminopropyl)-N'-ethylcarbodiimide hydrochloride as an activator reagent. After each step of conjugation, the mixture was ultrafiltered on a 30 kD membrane to remove low-molecular weight material. The control imaging probe was a USPIO vectorized with a non-specific peptide (USPIO-NSP).

MRI Hardware

All experiments were performed with a vertical 89-mm bore 9.4T magnet (Bruker, Ettlingen, Germany) supplied with an actively shielded Micro2.5 gradient system of 1T/m and a 30 mm transmit/receive birdcage RF coil, using Paravision 5.0 software.

Animal experiments

The experiments were conducted in accordance with the Dutch guidelines for research animal care. Protocols were approved by the Dier Experimentele commissie (Committee for laboratory animal use) at the Leiden University Medical Center under DEC protocol number 10136. In total 17 groups of n=5 male ApoE^{-/-} mice were used for the experiments (see Table 1).

Table 1. Overview of the experimental groups of ApoE^{-/-} mice that were included in the study

Experiment	Group	Nanoparticle	Time points	Age	Diet
Plasma half-time	A1 (n=5)	E-selectin USPIO	16	12-14 months	Chow
	A2 (n=5)	control USPIO	from 0-48h		
Optimal imaging time point	B1 (n=5)	E-selectin USPIO	16 from 0-48h	12-14 months	Chow
	B2 (n=5)	control USPIO			
Plaque imaging at 1.5 & 24 hrs	C1 (n=5)	E-selectin USPIO	1.5h	12-14 months	Chow
	C2 (n=5)	control USPIO			
	C3 (n=5)	E-selectin USPIO	1.5h, 24h		
	C4 (n=5)	control USPIO			

Experiment	Group	Nanoparticle	Time after cuff	Age start	
Collar model plaque stages: MRI & histology	D1 (n=5)	E-selectin USPIO	3 weeks	12 wks	Western
	D2 (n=5)	E-selectin USPIO	6 weeks		
	D3 (n=5)	E-selectin USPIO	9 weeks		
Collar model plaque stages: western blotting	D4 (n=3)		3 weeks	12 wks	Western
	D5 (n=3)		6 weeks		
	D6 (n=3)		9 weeks		

Experiment	Group	Nanoparticle	Treatment	Age	
Atorvastatin /	E1 (n=5)	E-selectin USPIO	None	12-14 months	Western
Fenofibrate	E2 (n=5)	E-selectin USPIO	Atorvastatin		
therapy	E3 (n=5)	E-selectin USPIO	Fenofibrate		

Blood half life

Blood circulation half-lives were determined for the different USPIO using 2 groups (n=5) 12-14 months old ApoE^{-/-} mice (group A). Blood samples from the tail vein were collected in heparin-coated vials at regular intervals before and up to 48 hours after contrast agent administration (0h, 15, 30, 45 min, 1h, 2h, 3h, 4h, 6h, 8h, 12h, 16h, 24h, 32h, 40h, 48h).

The change in longitudinal relaxation rate $\Delta R2$ of the blood over time was determined by:

$$\Delta R2(t) = 1/T2(t) - 1/T2(0) \quad [\text{Eq1}]$$

The $\Delta R2$ change over time was fitted using a mono-exponential decay function:

$$\Delta R2(t) = A e^{-\ln(2)t/t_{1/2}} \quad [\text{Eq2}]$$

where A is the initial R2 change upon USPIO injection, and $t_{1/2}$ is the circulation half-life of USPIO in the blood.

Contrast enhancement over time

Optimal time points for plaque accumulation of both the E-selectin USPIO as well as the control USPIO were determined in 2 groups of n=5 (group B) 12-14 months old ApoE^{-/-} mice in a pilot time-course study in which contrast agent accumulation was followed for 48 hours. Each mouse was scanned before administration of USPIOs and at several time points after intravenous injection of 0.05 mmol Fe/kg bodyweight in 200 μ l dextrose solution. From 0-4 hours after USPIO injection mice were scanned every 30 minutes, and thereafter every 4 hours from 4-48 hours after injection. Mice were anesthetized during MRI with isoflurane (\pm 2% in oxygen and air). During the examination, the respiration rate was continuously monitored using a balloon pressure sensor connected to the ECG/respiratory unit (SA Instruments, New York). The isoflurane concentration was adjusted to keep the respiration rate between 50 and 90 respirations/min.

The optimal time point was defined as the time at which the highest contrast-to-noise ratio (see below) was observed.

Plaque imaging in aged ApoE^{-/-} mice

4 groups (n=5 per group, group C) of 12-to-14-month-old male ApoE^{-/-} mice on a C57BL/6/Jico background were fed a normal chow diet. Each mouse was scanned before administration of contrast agent to visualize the aortic arch without contrast enhancement. Two of these groups were injected with either E-selectin USPIO or control USPIO and scanned at the optimal time point for endothelial binding, 1.5 hours after contrast agent injection. The other 2 groups were also injected with E-selectin USPIO or control USPIO, but these animals were scanned at both 1.5 hours and 24 hours after contrast agent injection.

Imaging of plaque stage in ApoE^{-/-} mice with carotid collar

3 groups (n=8, group D) of 12-week-old male ApoE^{-/-} mice were exposed to a Western diet (1% Cholesterol, Ab-diets, Woerden, The Netherlands). Four weeks later, at the age of 16 weeks, a restrictive collar was placed around the left carotid artery to mechanically induce the formation of atherosclerotic plaques around the collar. Mice were randomized for 3, 6 or 9 week follow-up of plaque formation, corresponding to early, intermediate and advanced plaque formation stages respectively. At each time point a group of 5 mice (group D1-D3) was scanned before contrast agent injection and at 1.5 hours and 24 hours thereafter. The remaining mice (n=3 per group, group D4-D6) were sacrificed and the left carotid artery was dissected for western blot analysis.

Imaging the effect of atorvastatin or fenofibrate therapy on plaque inflammation

Finally 3 groups (group E) of 12-14 months old male ApoE^{-/-} mice were exposed to a Western diet for 4 weeks. After a 4-hour fasting period, body weight was determined and EDTA plasma (Sarstedt, Nümbrecht, Germany) was collected via the tail vein. Total plasma cholesterol and triglyceride levels were measured (Roche Diagnostics, Almere, The Netherlands). Mice were randomized to 3 treatment groups based on the cholesterol and lipid levels. Mice were subsequently exposed to E1: 4 weeks of Western diet, E2: Western diet with the addition of 0.01% wt/wt atorvastatin (=0.1g / kg bodyweight, Lipitor, Pfizer) or E3: Western diet with 0.05% w/w fenofibrate (= 0.1g / kg bodyweight, Abbott Laboratories) for a period of 4 weeks. After 4 weeks of treatment, body weight was determined and EDTA plasma was collected via the tail vein. The mice were scanned with the same MRI protocol and timing as described above after i.v. injection of E-selectin targeted USPIOs.

After the final MRI scan all mice were terminally anesthetized with a mixture of midazolam (dormicum®, Roche), medetomidine (domitor®, Orion corporation, Espoo, Finland) and fentanyl (Janssen-Cilag, Beerse, Belgium) followed by transcatheter perfusion; arteries were taken out for histological validation.

MRI protocols

At the start of each *in vivo* examination, several 2D Fast Low Angle Shot (FLASH) scout images were recorded in the transverse and axial plane of the heart to determine the orientation of the aortic arch.

A modified FLASH sequence with a navigator echo (IntraGate, Bruker) was used for retrospective CINE MRI with the following parameters:

T1 weighted images: hermite-shaped RF pulse 1 ms; FA 15°; TR 31.4 ms; TE 2.96 ms; navigator echo points 64; 10 cardiac frames; FOV 1.8*1.8 cm²; matrix 128*128; in-plane resolution 141 μm; slice thickness 0.4 mm; number of repetitions 400.

T2 weighted images:* hermite-shaped RF pulse 1 ms; FA 10°, TR 34 ms, TE 6 ms, navigator echo points 64; 10 cardiac frames; FOV 1.8*1.8 cm²; matrix 256*256; in-plane resolution 70 μm; slice thickness 0.4 mm; number of repetitions 400.

Relaxivity measurements

T1 measurements

T1 values of plasma samples and USPIO were determined using a saturation recovery protocol (multi slice multi echo (MSME) sequence) with the following parameters: TE 7 ms, TR: 25-20-15-10-8-6-5-4-3-2-1.6-1.2-1.0-0.8-0.6-0.4-0.3 s, excitation hermite 1 ms, ref hermite 0.75 ms, band width 100kHz, matrix 128*128, resolution (195)² μm, 2*1mm slices.

The T1 values of the various ROIs were determined using a 3-parameter fit function:

$$M(t) = M0 (1 - \exp(-t/T1)) \quad [\text{Eq3}]$$

T2 measurements

MSME sequence with TR 2000 ms, TE 9-300 ms in 32 steps. hermite-shaped RF pulse 1 ms, ref hermite 0.75 ms, BW 100kHz, matrix 128*128, resolution (195)² μm, 2*1mm slices. The T2 values of the various ROIs were determined using

$$M[t]=M0*\exp(-t/T2) \quad [\text{Eq4}]$$

Image Analysis

Images were analyzed using ImageJ software. Bright blood images of 3 to 4 adjacent cross-sectional slices through the aortic arch were analyzed. ROIs were semi-automatically drawn around the vessel wall (I_{wall}) in all 10 movie frames. A 2nd ROI was drawn in the surrounding muscle tissue of the shoulder girdle (I_{muscle}). Furthermore, an ROI was placed outside the animal to measure the noise level (SD_{noise}) (Figure 1).

The contrast-to-noise ratio was defined in the 3 to 4 adjacent movie frames with the lowest signal intensity inside the vessel as following:

$$\text{CNR} = (I_{\text{wall}} - I_{\text{muscle}}) / SD_{\text{noise}} \quad [\text{Eq5}]$$

which is a measure of how well the lesioned wall can be discriminated from the surrounding tissue. CNR are shown as mean ± standard deviation.

Histology

Aortic arches and carotid arteries were frozen in Tissue Tek[®] (Sakura Finetek Europe, Zoetermeer, The Netherlands) and cut into serial 5 μm sections. Sections were stained with Oil Red O for lipid deposition, counterstained with hematoxylin and assessed by bright-field microscopy.

USPIO were visualized using the Perl's Prussian blue method with DAB enhancement as described previously²³. Slides were first incubated with fresh 2% potassium ferrocyanide (Sigma Aldrich, St Louis, MO, USA) in water mixed with equal volumes of 2% hydrochloric acid for up to 20 minutes at room temperature. Slides were washed, incubated in methanol/H₂O₂ and subsequently the iron staining was enhanced using 3,3'-diaminobenzidine (DAB) (Sigma-Aldrich). Slides were counterstained with nuclear fast red (Vector Laboratories, Burlingame, USA), and mounted.

For E-selectin staining slides were incubated overnight with rat-anti-mouse E-selectin (Pharmingen, San Diego, CA, USA), for macrophage staining slides were incubated with rat-anti-mouse F4-80

(clone A3-1, Serotec, Düsseldorf, Germany). Subsequently slides were incubated with horse radish peroxidase (HRP) -labelled or biotinylated goat-anti-rat (Vector laboratories Inc, Peterborough United Kingdom) in 1.5% goat serum (Vector Laboratories Inc.). Biotin labelling was followed by development using red alkaline phosphatase substrate (Vector Laboratories Inc.) according to the manufacturer's protocol, and as described in den Adel *et al*²⁴. HRP labeling was followed by 3,3'-diaminobenzidine development. Counterstaining was performed with Mayer's hematoxylin.

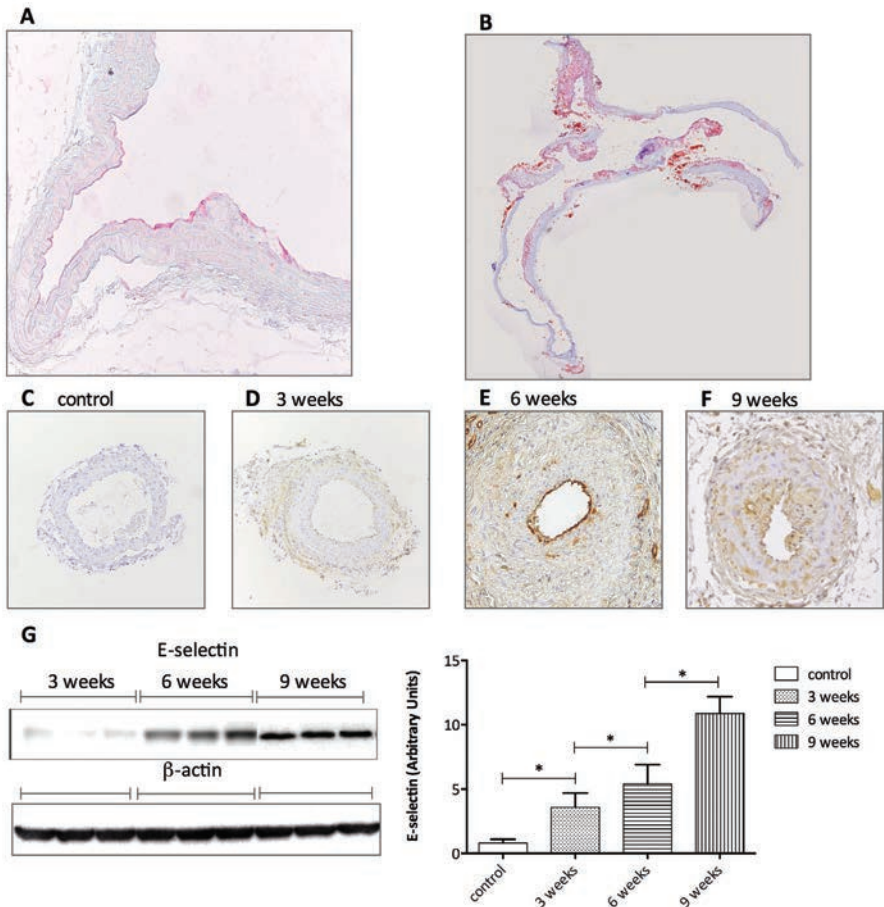


Figure 1 | E-selectin expression in atherosclerotic lesions. A. E-selectin (red alkaline phosphatase) immunohistochemical staining of the aortic arch of a 12-14 months old ApoE^{-/-} mouse, 40x magnification B Oil Red O staining of the aortic arch and descending aorta of a 12-14 months old ApoE^{-/-} mouse depicting lesion areas in red. 2x magnification C-F. E-selectin DAB immunohistochemical staining of the left carotid artery of ApoE^{-/-} mice before (C), 3 (D), 6 (E) and 9 (F) weeks after collar placement respectively. 40x magnifications. G. Western blot for E-selectin and β-actin of an undiseased carotid artery and the left carotid artery of ApoE^{-/-} mice 3, 6 and 9 weeks after collar placement. Quantification in arbitrary units of the VCAM-1 Western blot is shown in the right-sided panel. * p < 0.05.

Human coronary artery

Human left anterior descending (LAD) coronary artery was obtained post-mortem. Approval was given by the Institutional Review Board of the Erasmus MC, and informed consent was obtained. The LAD was frozen in Tissue Tek® and cut into serial 5 µm sections. Oil Red O, HE, RF and immunohistochemical staining for E-selectin and CD68 (clone KP1, Abcam) was performed, followed by light microscopical analysis. Furthermore, slices were incubated for 30 minutes with 5 µM E-selectin or control USPIO, followed by Prussian blue iron staining as described above.

E-selectin Western blotting

Left carotid arteries from group D4-D6 were cleaned and homogenized in cold lysis buffer (100 mmol/L K₂HPO₄, 1 mmol/L phenylmethylsulfonyl fluoride, and 0.2% Triton X-100). Protein concentration was determined by the bicinchoninic acid (BCA) protein assay (Pierce, Rockford, IL, USA) using bovine serum albumin (2 mg/ml, Pierce) as a standard. Equal amount of protein preparations (10 µg in 25µL buffer) were run on SDS-PAGE, using NuPage 12% Bis-Tris gels (Invitrogen, Carlsbad, CA), electro-transferred overnight to polyvinylidene difluoride filter (PVDF) membrane (Hybond-P, GE HealthcareDiegem, Belgium). To reduce non-specific binding, the PVDF membrane was blocked for 1 h at room temperature with blocking buffer (ECL Advance blocking agent, GE Healthcare) in TBST solution. Thereafter, the PVDF membrane was incubated with primary antibodies diluted 1:50,000 in blocking buffer at room temperature for 60 min, washed four times in TBST solution, and incubated with horseradish peroxidase- conjugated secondary antibodies diluted 1:35,000 in blocking buffer at room temperature for 60 min. Bands were visualized with the enhanced chemiluminescence detection system (ECL Advance western blotting detection kit, GE Healthcare), exposed to X-ray film (GE Healthcare).

Molecular band intensity (arbitrary units relative to β-actin) was determined by densitometry using ImageJ. Primary antibodies used were: rat-anti-mouse E-selectin (Pharmingen) and rabbit- anti-mouse β-actin (Santa Cruz Biotechnology, Heidelberg, Germany). Secondary antibody used were goat anti-rat IgG and goat anti-rabbit IgG conjugated to HRP (Santa Cruz Biotechnology).

Statistical analysis

Data are presented as the mean ± standard deviation. Statistical analysis was performed using SPSS 15.0 ANOVA for computations within and between groups. Results were considered statistically significant at $p < 0.05$.

RESULTS

E-selectin expression on atherosclerotic plaques

The extracellular adhesion molecule E-selectin is reported to be present at atherosclerosis-prone sites in humans even before overt disease is apparent, with persistent expression concomitant with macrophage accumulation in more advanced lesions. We first assessed whether the E-selectin expression patterns observed in human plaques can be recapitulated in the ApoE^{-/-} mice model often used for longitudinal MRI studies in atherosclerosis. Histological sections of the aortic arch confirmed the presence of E-selectin positive areas on the luminal side of the atherosclerotic lesion on the inner curvature of the aortic arch (figure 1A). Corresponding Oil Red O staining shows the lesional area on the inner curvature (figure 1B). In hypercholesterolemic ApoE^{-/-} mice with a constrictive collar around the left carotid artery, plaque development around the collar is progressive over the course of several weeks and well characterized²⁵. In control mice before

exposure to a Western diet no E-selectin was observed in the endothelium (figure 1C). In early plaques (3 weeks after collar placement), E-selectin was observed in the endothelium (figure 1D). As the atherosclerotic lesions developed and became larger, E-selectin positive areas were clearly visible in the endothelium and at the latest plaque stage also inside the plaque (figure 1E and 1F). Western blot analysis of aortic arch and carotid artery homogenates confirmed our histological findings that during plaque development, both spontaneous as well as after collar placement, total E-selectin protein expression increased significantly (figure 1G). This distinction in E-selectin expression allowed us to use the ApoE^{-/-} mouse model to assess the feasibility of *in vivo* E-selectin imaging, and its relation to plaque development and therapy response.

Characterization of E-selectin USPIO at 9.4T

Relaxivities were calculated from T1 and T2 relaxation time measurements to characterize the E-selectin and control USPIO at 400 MHz. E-selectin USPIO r1 relaxivity was 1.170 s⁻¹.mM⁻¹ and r2 212.78 s⁻¹.mM⁻¹ versus r1 of 0.948 s⁻¹.mM⁻¹ and r2 of 131.46 s⁻¹.mM⁻¹ for control USPIO at 37°C respectively (Table 2). These values were well within expected ranges.

Blood half life

Next we assessed the *in vivo* properties of the E-selectin and control USPIO in ApoE^{-/-} mice. Blood samples obtained at different time points after intravenous injection were used to measure the blood pool half-life of E-selectin and control USPIO. Relaxation rates (R2) of the different blood samples were measured and T_{1/2} was calculated according to equation 1 and 2. Control USPIO had a blood circulation half-life of ~7.2 ± 0.7 hours. The half-life of E-selectin USPIOs was similar at 6.63 ± 1.1 hours after intravenous administration in aged ApoE^{-/-} mice (Table 2).

Imaging of E-selectin in aged ApoE^{-/-} mice

We next addressed the potential of the E-selectin-USPIO to detect atherosclerotic lesions in aged male ApoE^{-/-} mice. Before USPIO injection, the contrast to noise ratio (CNR) in the inner curvature of the aortic arch of 12 to 14-month-old ApoE^{-/-} mice was low, and atherosclerotic plaques were not readily discernible from the surrounding tissue (figure 2A T1 weighted image). Shortly after USPIO injection, the CNR decreases and plaques can be discriminated from the surrounding tissue as focal hypointense areas. We followed the CNR of E-selectin USPIO to control USPIO over time to determine the optimal imaging window (figure 2B). The largest difference in contrast enhancement of E-selectin USPIO compared to control USPIO was observed between 1 and 2 hours after intravenous injection (arrow in figure 2B). This time point is optimal for endothelial binding, as illustrated by the iron staining of the aortic arch 1.5 hours after injection (figure 2C).

Table 2.

	E-selectin USPIO	Control USPIO
r1 (s ⁻¹ mM ⁻¹)	1.170	0.948
r2 (s ⁻¹ mM ⁻¹)	212.78	131.46
T _{1/2} (hours)	6.63 ± 1.1	7.2 ± 0.7
Peak contrast <i>in vivo</i> (hours)	1.5-2 hours	24 hours

Ex vivo relaxivity measurements, *in vivo* circulation half-time and peak contrast enhancement of E-selectin and control USPIO at 9.4T. None of the values were significantly different between the two contrast agents.

USPIO binding was not observed in non-diseased areas of the artery. The contrast enhancement in the plaques persisted for over 24 hours and was observed in areas where atherosclerotic lesions were detectable on Oil Red O staining (figure 2D and 1B). However, at 24 hours after injection, the CNR did not differ significantly anymore between control and E-selectin USPIO injected ApoE^{-/-} mice (figure 2B), indicating that passive USPIO accumulation due to particle engulfment by macrophages inside the plaque is dominating the enhancement at this stage (figure 2E). We therefore chose this time point to image the plaque macrophage content.

Plaque staging

To assess the possibility to differentiate early from more advanced lesions using E-selectin targeted USPIOs we used the model of hypercholesterolemic ApoE^{-/-} mice with a constrictive collar around the left carotid artery. CNR was determined on T2*-weighted MRI of the carotids at 1.5 and 24 hours after E-selectin USPIO injection, and at 3, 6 and 9 weeks after collar placement cross-sectionally to assess early, intermediate or late plaque stages respectively (figure 3A). We observed the highest CNR decrease at 9 weeks after collar placement for both the 1.5 hour scan and the 24 hour scan after E-selectin USPIO injection, indicating a progressive increase in both E-selectin expression on the endothelium and macrophage content in the plaque.

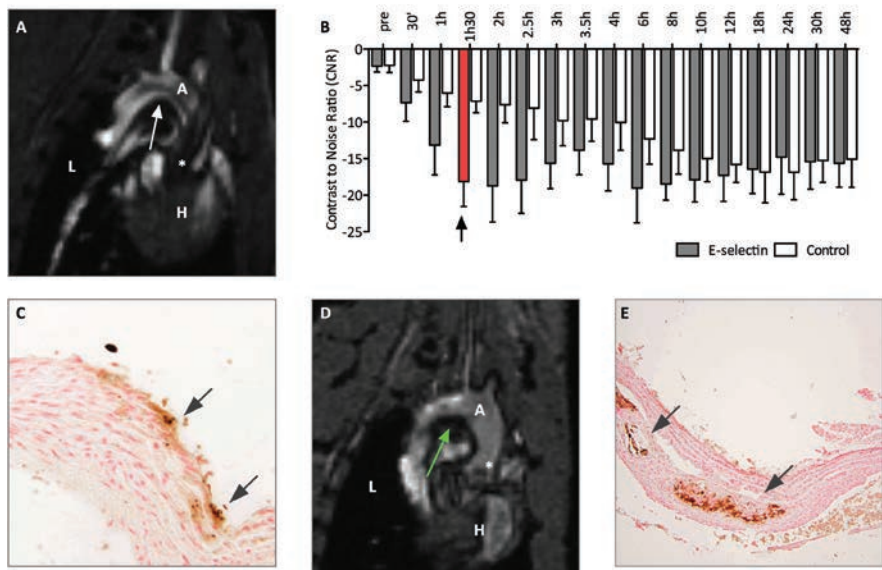


Figure 2 | Atherosclerotic plaque detection in ApoE^{-/-} mice with E-selectin USPIO. A. T1 weighted MRI of the aortic arch of a 12-14 months old ApoE^{-/-} mouse without injection of USPIO. Arrow points at a plaque region in the inner curvature of the aortic arch. A= aortic arch, L = lungs, * aortic valves, H=heart. B. Kinetics of Contrast to Noise Ratio (CNR) after injection of either control or E-selectin targeted USPIO. The arrow represents the time point with highest CNR difference between control and E-selectin USPIO. C. DAB enhanced Iron staining (brown) of an atherosclerotic lesion in the aortic arch 1.5 hours after E-selectin USPIO injection, 40 x magnification. Arrows point at DAB positive areas D. Contrast enhancement on the inner curvature of the aortic arch 24 hours after E-selectin USPIO injection. The green arrow points at a plaque region with contrast enhancement in the inner curvature of the aortic arch. A= aortic arch, L = lungs, * aortic valves, H=heart. E DAB enhanced Iron staining (brown) of an atherosclerotic lesion in the aortic arch 24 hours after E-selectin USPIO injection, 40 x magnification. Arrows point at DAB positive areas.

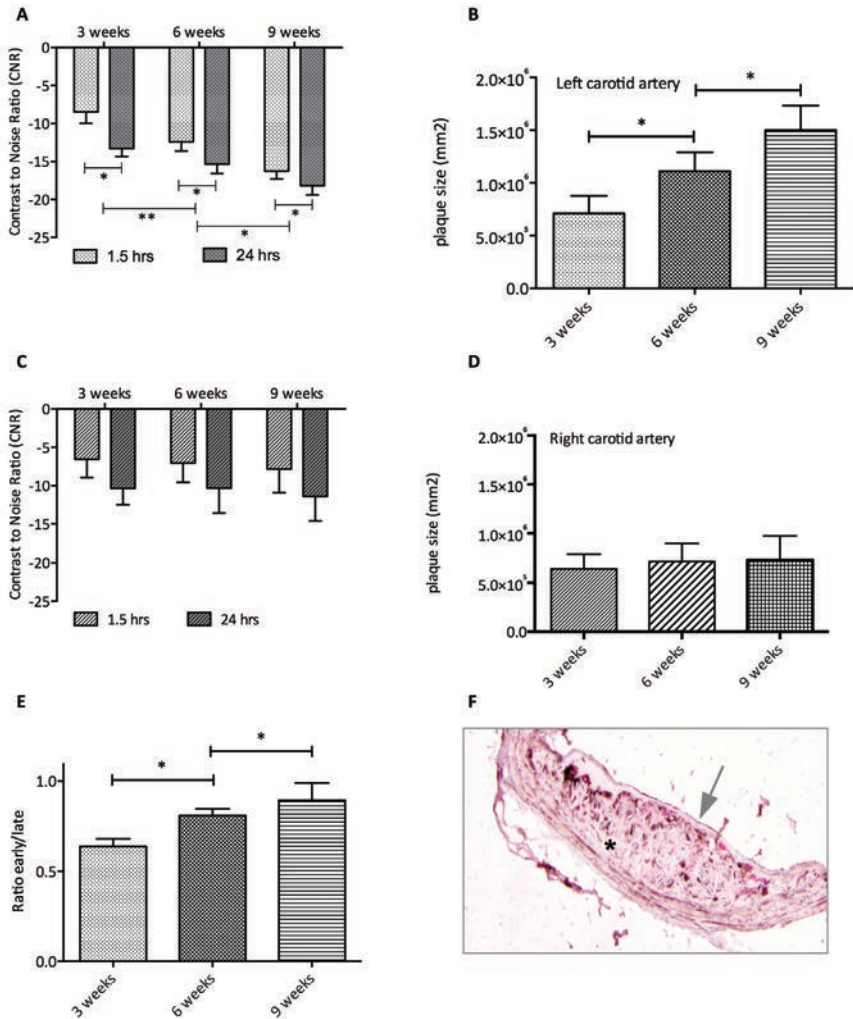


Figure 3 | E-selectin targeted imaging of different stages of atherosclerosis. A. CNR measured 1.5 and 24 hours after E-selectin USPIO injection in carotid arteries of ApoE^{-/-} mouse with a collar around the left carotid artery at 3, 6 and 9 weeks after placement. B. Histological measurement of the plaque size. C. CNR measured 1.5 and 24 hours after E-selectin USPIO injection in right collateral carotid arteries of ApoE^{-/-} mouse (thus without a collar around the left carotid artery) at 3, 6 and 9 weeks after surgery. D. Histological measurement of the plaque size of the right carotid artery at 3, 6 and 9 weeks after surgery. E. Ratio of early versus late imaging time points CNR in carotid arteries of ApoE^{-/-} mouse with a collar around the left carotid artery at 3, 6 and 9 weeks after placement. F. Immunohistochemical staining of the left carotid artery 24 hours after E-selectin USPIO injection, 9 weeks after collar placement. E-selectin in red (alkaline phosphatase, indicated by the arrow), and iron staining in brown (DAB, indicated with an asterisk). * $p < 0.05$, ** $p < 0.01$

Corresponding histological measurements of the plaque area proximal to the collar are shown in figure 3B, confirming the progressive increase in plaque development. This steady increase in CNR change was not observed in the contralateral right-sided carotid artery, where plaques also develop due to the Western diet, but slower and less predictable (figure 3C). Plaque size does not increase progressively in the right carotid artery, in line with the observation CNR change is not

progressive with plaque progression (figure 3D). To generate a single measure of plaque stage, we calculated the ratio of early contrast enhancement over late enhancement, hypothesizing that late enhancement would be dominating as plaque stage progresses due to the mere bulk of the macrophage pool (figure 3E, histology in figure 3F). The calculated ratio indeed increased with progressing plaque stage.

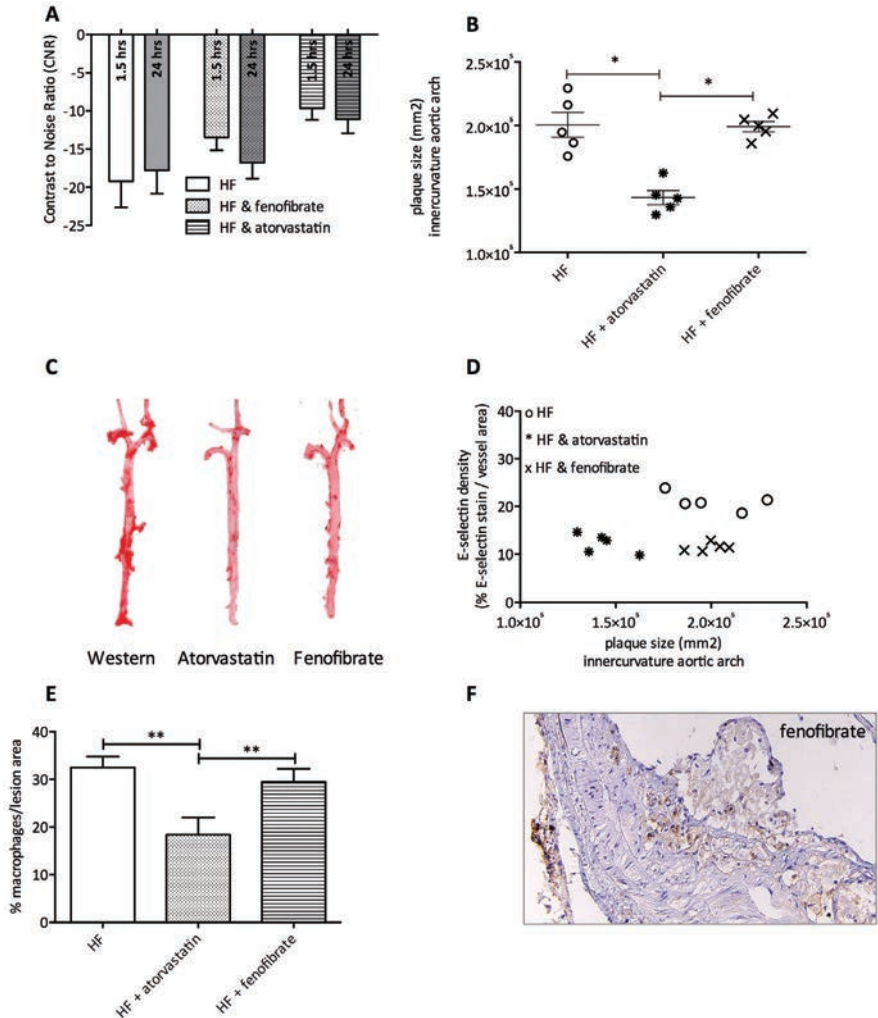


Figure 4 | E-selectin targeted imaging of therapy follow-up. A. CNR was measured 1.5 and 24 hours after E-selectin USPIO injection in the inner curvature of the aortic arch of ApoE^{-/-} mouse. Mice were either fed a Western diet (transparent bars) or a Western diet supplemented with fenofibrate (dotted bars) or a Western diet supplemented with atorvastatin (striped bars). B. Histological measurement of the plaque size after diet exposure. C. Oil Red O staining of the aortic arch and descending aorta of ApoE^{-/-} mice exposed to a Western diet, a Western diet supplemented with atorvastatin, or a Western diet supplemented with fenofibrate. D. Plot depicting the relation between the plaque size of ApoE^{-/-} mice after diet exposure on the innercurvature of the aortic arch and the histologically determined E-selectin density in the plaque. E. Percentage of F4-80 positive macrophages in the lesion area in the inner curvature of the aortic arch. F. DAB staining of F4-80 of a fenofibrate treated ApoE^{-/-} mouse. * p < 0.05, ** p < 0.01

Anti-atherosclerotic therapy

To assess the potential of E-selectin targeted molecular imaging for therapy follow-up, mice were exposed to two commonly prescribed anti-atherosclerotic drugs with a different mechanism of action. Aged male ApoE^{-/-} mice were fed a Western diet for 4 weeks. After 4 weeks plasma lipids were measured (table 3) and mice were randomized into 3 groups that received another 4 weeks of Western diet, Western diet supplemented with atorvastatin or Western diet supplemented with fenofibrate.

Atorvastatin treatment significantly reduced both the early E-selectin-USPIO induced contrast enhancement as well as the late USPIO enhancement (figure 4A). In mice treated with fenofibrate, the early E-selectin USPIO induced CNR change 1.5 hours after contrast agent injection was also significantly reduced compared to untreated animals. However, the measurement 24 hours after E-selectin USPIO injection did not show a significant difference compared to untreated mice, suggesting that plaque size or macrophage content did not change after fenofibrate treatment (figure 4A). Immunohistochemical assessment of plaque area (Oil Red O) and E-selectin distribution confirmed the MRI results. After atorvastatin therapy, the lesion area was significantly reduced in mice exposed to a Western diet supplemented with atorvastatin compared to untreated mice (figure 4B). In contrast, lesion area in fenofibrate treated mice was not significantly reduced, although the lipid content was decreased (figure 4C). Presence of E-selectin on the endothelium was reduced in both atorvastatin and fenofibrate treated mice compared to the untreated mice (figure 4D). Macrophage content was significantly decreased in mice treated with atorvastatin, whereas the percentage of F4-80⁺ cells did not change with fenofibrate treatment compared to untreated Western diet fed mice (figure 4E and 4F). As expected, neither treatment resulted in a significant decrease of plasma lipids (Table 3).

Table 3. Body weight and plasma lipids

	Western diet	Atorvastatin	Fenofibrate
At randomization			
Body weight (gram)	34.2 ± 1.8	33.9 ± 1.9	34.5 ± 2.1
Cholesterol (mg/dL)	914 ± 24	923 ± 22	917 ± 27
Triglycerides (mg/dL)	148 ± 12	147 ± 14	150 ± 16
At sacrifice			
Body weight (gram)	38.7 ± 2.1 *	31.4 ± 2.2 *	31.8 ± 1.9 *
Cholesterol (mg/dL)	1094 ± 38	931 ± 27	925 ± 25
Triglycerides (mg/dL)	179 ± 15	146 ± 14	144 ± 17

Body weight and plasma lipids of ApoE^{-/-} mice were measured after 4 weeks of Western diet exposure, at randomization into 3 treatment groups, and 4 weeks later, at sacrifice. Atorvastatin treatment and fenofibrate treatment did not significantly influence plasma cholesterol or triglycerides. Body weight decreased significantly (*, p < 0.05) upon atorvastatin treatment as well as fenofibrate treatment, whereas Western diet exposure significantly increased the body weight compared to at randomization.

Confirmation of E-selectin imaging potential of atherosclerotic lesions in humans

As initial evidence of the potential for E-selectin USPIO imaging in humans, we exposed a human LAD tissue slice to E-selectin and control USPIO. Typical USPIO-induced dots were observed on the surface of atherosclerotic plaques after incubation with E-selectin USPIO (figure 5A) in contrast to control USPIO (figure 5B). E-selectin expression on the endothelium (figure 5C) was confirmed by immunohistochemistry and the anatomical setting was described using HE, RF, CD 68 and Oil Red O stainings (figure 5D - G)

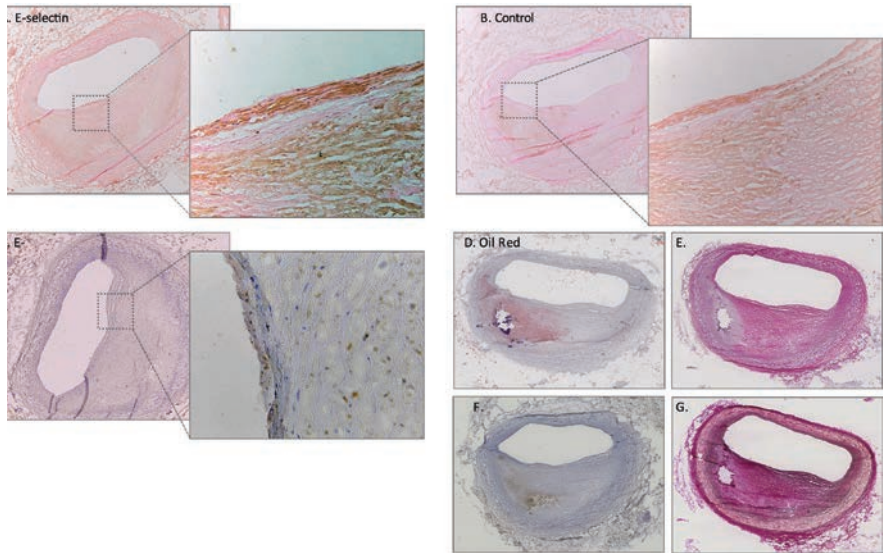


Figure 5 | E-selectin USPIO imaging on human vessels. A. Prussian blue staining of E-selectin USPIO that were incubated on a human LAD. Arrows point at DAB positive areas with clusters of USPIO. 20x, zoom 400x. B. Prussian blue staining of control USPIO that were incubated on a human LAD. Arrows point at DAB positive areas with clusters of USPIO. C. Confirmation of E-selectin expression on the endothelium by immunohistochemistry. Plaque morphology was further illustrated using D. Oil Red O, E. Haematoxylin Eosin, F. CD68 staining and G. RF staining.

DISCUSSION

Feasibility of E-selectin-targeted molecular imaging

In the current study we successfully demonstrated the feasibility of endothelial E-selectin and plaque macrophage MR imaging in an ApoE^{-/-} mouse model of atherosclerosis using a combination of two imaging time points after contrast agent injection. The biodistribution of E-selectin USPIO proved favorable for early time points after injection (1.5 hours), as it was specifically visualized at the endothelium of atherosclerotic plaques. Contrast enhancement in undiseased vessel wall (as can be seen in part of figure 2D) and the blood pool (at the optimal imaging time points) were low. E-selectin USPIO selectively targeted areas of atherosclerotic plaque with high E-selectin expression, showing a quantitative correlation with histology of atherosclerotic plaques on excised carotids and aortic arches. At later imaging time points (24 h) after injection, non-specific USPIO uptake by macrophages is dominating the contrast.

Both statin and fenofibrate treatment are known to reduce E-selectin expression²⁵, and indeed diminished *in vivo* E-selectin USPIO accumulation at 1.5 hours after contrast agent injection. However, only statins reduced the actual plaque size and macrophage pool, corresponding to a reduced CNR change at 24 hours. Fenofibrate treatment did not significantly alter the plaque size, which was also observed as unchanged contrast enhancement at 24 hours.

Role of E-selectin in atherosclerosis

The recognition that inflammation drives the development and complication of atherosclerosis paved the way to assess several early inflammatory markers of atherosclerosis. E-selectin is such an early marker of atherosclerosis expressed in the endothelium of human atherosclerotic lesions, particularly when lesions are associated with subendothelial leukocytic infiltrates^{9, 10}. The extent of E-selectin expression is related to atherosclerosis development and soluble E-selectin levels are of prognostic value for cardiovascular risk prediction¹³. Therefore, imaging its presence on individual plaques would allow a risk prediction for individual lesions, and could thus complement serological tests. Here we present proof-of-concept of how E-selectin guided imaging offers insight in plaque progression.

Imaging therapy response

Lipid (LDL) lowering with statins (3-hydroxy-3-methylglutaryl coenzyme A reductase inhibitors) has been established as an important therapy in the primary and secondary prevention of atherosclerotic disease²⁶. LDL lowering does not occur in ApoE^{-/-} mice (Table 3), although beneficial effect on the inflammatory process involved in atherosclerosis plaque formation and progression both in mice and men have been reported, including a reduction of the macrophage pool^{27, 28}. Peroxisome Proliferator-Activated Receptor- α (PPAR α) agonists like fenofibrate also affects lipid metabolism and inflammation, modulating pathophysiological pathways implicated in fatty liver disease and atherosclerosis. As is the case for statins, ApoE^{-/-} mice treated with fibrates do not respond to PPAR α agonists as humans, displaying no change²⁹ or even an increase³⁰ in plasma lipids upon fibrate treatment (Table 3). The pleiotropic anti-inflammatory effects such as the effect on the E-selectin expression remains conserved. Recently, it became apparent that despite the beneficial effects of fibrates on atherosclerosis, lesion size does not decrease, a phenomenon also observed in our study. As current diagnostic imaging mainly focusses on lesion size, it is of importance to keep in mind that therapy response may exist without a significant decrease in lesional area. As demonstrated in this study, imaging the endothelium activation status and/or plaques macrophage content may then provide mechanistic insights.

Role of macrophages in the plaque

Inflammation plays a pivotal role in all stages of atherosclerosis. E-selectin targeted early imaging allows to visualize the inflammatory status of the endothelium. The response to therapy is currently assessed by imaging the atherosclerotic lesion size or the luminal narrowing. Our current findings indicate that imaging the macrophage pool in a plaque gives complementary information on therapy response.

Both in murine and human atherosclerotic lesions different macrophage phenotypes co-exist³¹. Macrophage phenotypic polarization is thought to play a role in the fate of an atherosclerotic lesion. Classically activated macrophages (or M1) and alternatively activated macrophages (or M2) are two extremes representing inflammatory and reparative macrophage phenotypes^{32, 33}. Several recent studies have suggested that pharmacological treatments may skew macrophage polarization toward the M2 phenotype, thereby stabilizing atherosclerotic lesions even without reducing the

macrophage pool^{32, 36}. We hypothesize that the difference in macrophage content between animals on Western diet, atorvastatin or fenofibrate is not only related to a simple reduction in the number of macrophages, but also to a change in macrophage phenotype. Of course, this mode of action is still speculative and requires further thorough investigation of the exact effects of different pharmacological treatments on macrophage polarization in the context of atherosclerosis. In this context it would be very interesting to use contrast agents that are targeted specifically towards either M1 or M2 macrophages. Using our strategy of early imaging to visualize active M1 or M2 targeting combined with late imaging of the passive engulfment of USPIO in the plaque macrophage pool would in theory allow an assessment of the M1/M2 balance *in vivo*.

Comparison to other E-selectin targeting imaging agents

The imaging field has provided several proof-of-concept studies for E-selectin imaging in (experimental) atherosclerosis in the past decade. Molecular MRI of E-selectin was performed to image neuro-inflammation to visualize the upregulation of the endothelial leukocyte adhesion molecules P- and E-selectin³⁷. The paramagnetic contrast agent Gd-DTPA (Magnevist[®]) was functionalized with a mimetic of sialyl Lewis X (sLe X) that binds to P- or E-selectin. Changes in longitudinal MR relaxation time T1 were modest, but MRI revealed specific binding of Gd-DTPA-(sLe X).

Kang *et al.* have functionalized cross-linked iron oxide (CLIO) nanoparticles with anti human E-selectin antibody fragments³⁸. Boutry *et al.* targeted E-selectin with a synthetic mimetic of sialyl Lewis(x) (sLe(x)), a natural ligand of E-selectin expressed on leukocytes, conjugated to Gd-DTPA or to USPIO¹⁷⁻¹⁹. This last approach has been used in the current work. Following *in vivo* injection of these targeted USPIOs, significant hypointensities on T2* -weighted MR images were observed at sites of injury during hepatitis¹⁷.

Our work is unique as we apply an E-selectin USPIO to detect atherosclerosis and thereby differentiate early from advanced atherosclerotic lesions by tuning the imaging timing detecting both active E-selectin targeting and passive targeting of the macrophage load.

Study limitations

The exact role of E-selectin in the development, progression and regression of atherosclerotic plaques in ApoE^{-/-} mice has not been fully elucidated. Whether the expression of E-selectin on the endothelium in advanced lesions represents a marker of stability or instability by its role in the attraction of inflammatory cells is a matter of ongoing research. As P-selectin also plays a pivotal role in leukocyte tethering during plaque development, dual targeting of both selectins could have been of interest in the current application of the USPIO, although the expression of P-selectin is broader, potentially limiting the imaging specificity.

While the current preclinical findings are encouraging, a number of hurdles must be overcome before agents such as E-selectin USPIO can be used clinically; perhaps the most important will be the development of fully biodegradable USPIO, together with full toxicological testing of the humanized and biodegradable agent. Nevertheless, to date we have observed no toxicological effects of the E-selectin USPIO used in mice

CONCLUSION

In conclusion, this study demonstrated that molecular MRI using E-selectin USPIO allows selective imaging and quantification of endothelial E-selectin on the aortic arch as well as the carotid

arteries in ApoE^{-/-} mice. E-selectin imaging combined with macrophage imaging in the plaque represents a tool to monitor plaque progression, regression and treatment response *in vivo*. E-selectin targeted imaging may therefore be a useful marker for *in vivo* detection and staging of atherosclerotic lesions.

Acknowledgments

The authors would like to acknowledge Guerbet Group France for providing USPIOs. This work was supported by the European Network of Excellence Diagnostic Molecular Imaging (DIMI, LSHB-CT-2005-512146) to BdA, REP and LvdW, the Netherlands Heart Foundation Grant (NHF, 2006T106) to BdA, and REP, NWO Athena (700.58.80), NWO VENI (916.11.015) to KvdH, Actions de Recherche Concertées (00/05-258 and 05/10-335) and ENCITE (European Network for cell imaging and tracking expertise to CB, SL and RNM). The support and sponsorship concerted by COST Actions (TD1004 and CM1006) and of the EMIL program are acknowledged. The authors thank the Center for Microscopy and Molecular Imaging (CMMI, supported by the European Regional Development Fund and the Walloon Region)

REFERENCES

1. Libby P. Inflammation in atherosclerosis. *Nature* 2002; 420:868-74.
2. Falk E. Pathogenesis of atherosclerosis. *J Am Coll Cardiol* 2006; 47:C7-12.
3. Lopez AD, Mathers CD, Ezzati M, Jamison DT, Murray CJ. Global and regional burden of disease and risk factors, 2001: systematic analysis of population health data. *Lancet* 2006; 367:1747-57.
4. Sanz J, Fayad ZA. Imaging of atherosclerotic cardiovascular disease. *Nature* 2008; 451:953-7.
5. Virmani R, Burke AP, Farb A, Kolodgie FD. Pathology of the vulnerable plaque. *J Am Coll Cardiol* 2006; 47:C13-C18.
6. Cai J, Hatsukami TS, Ferguson MS, et al. In vivo quantitative measurement of intact fibrous cap and lipid-rich necrotic core size in atherosclerotic carotid plaque: comparison of high-resolution, contrast-enhanced magnetic resonance imaging and histology. *Circulation* 2005; 112:3437-44.
7. Desai MY, Lima JA. Imaging of atherosclerosis using magnetic resonance: state of the art and future directions. *Curr Atheroscler Rep* 2006; 8:131-9.
8. Ley K. The role of selectins in inflammation and disease. *Trends Mol Med* 2003; 9:263-8.
9. Davies MJ, Gordon JL, Gearing AJ, et al. The expression of the adhesion molecules ICAM-1, VCAM-1, PECAM, and E-selectin in human atherosclerosis. *J Pathol* 1993; 171:223-9.
10. van der Wal AC, Das PK, Tigges AJ, Becker AE. Adhesion molecules on the endothelium and mononuclear cells in human atherosclerotic lesions. *Am J Pathol* 1992; 141:1427-33.
11. An G, Wang H, Tang R, et al. P-selectin glycoprotein ligand-1 is highly expressed on Ly-6Chi monocytes and a major determinant for Ly-6Chi monocyte recruitment to sites of atherosclerosis in mice. *Circulation* 2008; 117:3227-37.
12. Swirski FK, Libby P, Aikawa E, et al. Ly-6Chi monocytes dominate hypercholesterolemia-associated monocytois and give rise to macrophages in atheromata. *J Clin Invest* 2007; 117:195-205.
13. Pai JK, Pischon T, Ma J, et al. Inflammatory markers and the risk of coronary heart disease in men and women. *N Engl J Med* 2004; 351:2599-610.
14. Davies MJ, Richardson PD, Woolf N, Katz DR, Mann J. Risk of thrombosis in human atherosclerotic plaques: role of extracellular lipid, macrophage, and smooth muscle cell content. *Br Heart J* 1993; 69:377-81.
15. van der Wal AC, Becker AE, van der Loos CM, Das PK. Site of intimal rupture or erosion of thrombosed coronary atherosclerotic plaques is characterized by an inflammatory process irrespective of the dominant plaque morphology. *Circulation* 1994; 89:36-44.
16. Virmani R, Burke AP, Kolodgie FD, Farb A. Pathology of the thin-cap fibroatheroma: a type of vulnerable plaque. *J Interv Cardiol* 2003; 16:267-72.
17. Boutry S, Burtea C, Laurent S, Toubeau G, Vander EL, Muller RN. Magnetic resonance imaging of inflammation with a specific selectin-targeted contrast agent. *Magn Reson Med* 2005; 53:800-7.
18. Boutry S, Laurent S, Elst LV, Muller RN. Specific E-selectin targeting with a superparamagnetic MRI contrast agent. *Contrast Media Mol Imaging* 2006; 1:15-22.
19. Radermacher KA, Beghein N, Boutry S, et al. In vivo detection of inflammation using pegylated iron oxide particles targeted at E-selectin: a multimodal approach using MR imaging and EPR spectroscopy. *Invest Radiol* 2009; 44:398-404.
20. Reynolds PR, Larkman DJ, Haskard DO, et al. Detection of vascular expression of E-selectin in vivo with MR imaging. *Radiology* 2006; 241:469-76.
21. Hyafil F, Laissy JP, Mazighi M, et al. Ferumoxtran-10-enhanced MRI of the hypercholesterolemic rabbit aorta: relationship between signal loss and macrophage infiltration. *Arterioscler Thromb Vasc Biol* 2006; 26:176-81.
22. Ruehm SG, Corot C, Vogt P, Kolb S, Debatin JF. Magnetic resonance imaging of atherosclerotic plaque with ultrasmall superparamagnetic particles of iron oxide in hyperlipidemic rabbits. *Circulation* 2001; 103:415-22.
23. Moos T, Mollgard K. A sensitive post-DAB enhancement technique for demonstration of iron in the central nervous system. *Histochemistry* 1993; 99:471-5.
24. den Adel B, Bovens SM, Boekhorst BT, et al. Histological validation of iron-oxide and gadolinium based MRI contrast agents in experimental atherosclerosis: The do's and don't's. *Atherosclerosis* 2012 ; 225(2):274-80.
25. Von Der Thusen JH, Van Berkel TJ, Biessen EA. Induction of rapid atherogenesis by perivascular carotid collar placement in apolipoprotein E-deficient and low-density lipoprotein receptor-deficient mice. *Circulation* 2001; 103:1164-70.
26. Shepherd J, Cobbe SM, Ford I, et al. Prevention of coronary heart disease with pravastatin in men with hypercholesterolemia. West of Scotland Coronary Prevention Study Group. *N Engl J Med* 1995; 333:1301-7.
27. Nachtigal P, Jamborova G, Pospisilova N, et al. Atorvastatin has distinct effects on endothelial markers in different mouse models of atherosclerosis. *J Pharm Pharm Sci* 2006; 9:222-30.
28. Nachtigal P, Pospisilova N, Pospechova K, et al. MDOC and atorvastatin have potential antiinflammatory effects in vascular endothelium of apoE-/- mouse model of atherosclerosis. *Life Sci* 2006; 78:1983-9.
29. Duez H, Chao YS, Hernandez M, et al. Reduction of atherosclerosis by the peroxisome proliferator-activated receptor alpha agonist fenofibrate in mice. *J Biol Chem* 2002; 277:48051-7.
30. Fu T, Kashireddy P, Borensztajn J. The peroxisome-proliferator-activated receptor alpha agonist ciprofibrate severely aggravates hypercholesterolaemia and accelerates the

- development of atherosclerosis in mice lacking apolipoprotein E. *Biochem J* 2003; 373:941-7.
31. Khallou-Laschet J, Varthaman A, Fornasa G, et al. Macrophage plasticity in experimental atherosclerosis. *PLoS One* 2010; 5:e8852.
 32. Bouhrel MA, Derudas B, Rigamonti E, et al. PPARgamma activation primes human monocytes into alternative M2 macrophages with anti-inflammatory properties. *Cell Metab* 2007; 6:137-43.
 33. Mantovani A, Sica A, Sozzani S, Allavena P, Vecchi A, Locati M. The chemokine system in diverse forms of macrophage activation and polarization. *Trends Immunol* 2004; 25:677-86.
 34. Loke P, Gallagher I, Nair MG, et al. Alternative activation is an innate response to injury that requires CD4+ T cells to be sustained during chronic infection. *J Immunol* 2007; 179:3926-36.
 35. Khallou-Laschet J, Caligiuri G, Groyer E, et al. The proatherogenic role of T cells requires cell division and is dependent on the stage of the disease. *Arterioscler Thromb Vasc Biol* 2006; 26:353-8.
 36. Odegaard JI, Chawla A. Alternative macrophage activation and metabolism. *Annu Rev Pathol* 2011; 6:275-97.
 37. Barber PA, Foniok T, Kirk D, et al. MR molecular imaging of early endothelial activation in focal ischemia. *Ann Neurol* 2004; 56:116-20.
 38. Kang HW, Torres D, Wald L, Weissleder R, Bogdanov AA, Jr. Targeted imaging of human endothelial-specific marker in a model of adoptive cell transfer. *Lab Invest* 2006; 86:599-609.
 39. van Kasteren SI, Campbell SJ, Serres S, Anthony DC, Sibson NR, Davis BG. Glyconanoparticles allow pre-symptomatic in vivo imaging of brain disease. *Proc Natl Acad Sci U S A* 2009; 106:18-23.

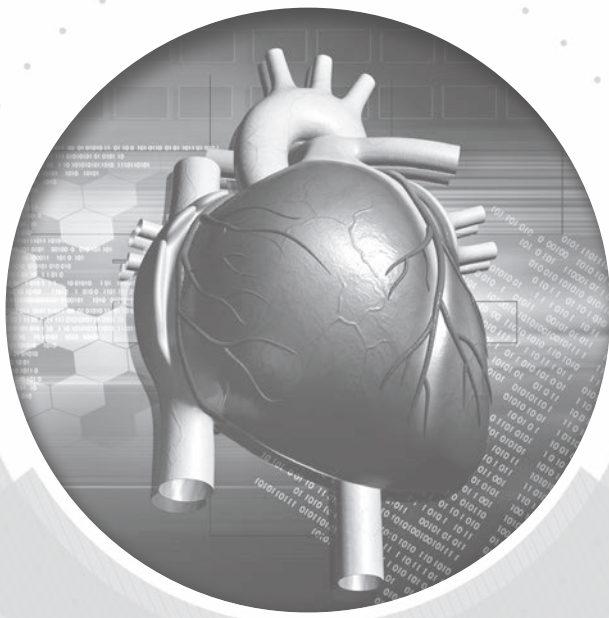


11 01 10 0 101 0110 01 01 1011 01 0101
0101 10
101011011
010 1110110101

101
01 10011
1110 10 2
011010
11 01 10 0
010 10
010 1103

10101 001 10 11 01
01 1010 10 1
10101011 01010101
• 1010

10101



Manuscript in preparation

Chapter 8

Micelle-mediated rosiglitazone treatment of atherosclerosis

Brigit den Adel, Sandra Bovens, Ernst Suidgeest, Gustav J Strijkers, Robert E Poelmann, Gerard Pasterkamp and Louise van der Weerd

ABSTRACT

Atherosclerosis is an inflammatory disease causing considerable morbidity and mortality in the Western world. Rosiglitazone is an effective anti-diabetic drug that also has anti-atherosclerotic potential, but is controversial because of reported cardiac side effects. Therefore, a nanomedicinal micelle formulation of this drug was developed to improve targeted delivery. Micelle-mediated delivery of rosiglitazone was validated *in vitro* and *in vivo* in ApoE^{-/-} and ApoE^{-/-}-eNOS^{-/-} mice. The PPAR- γ activating potential of rosiglitazone micelles was assessed by a firefly luciferase expression assay responsive to activation of the PPAR- γ pathway. Contrast-enhanced magnetic resonance imaging was applied to assess micelle targeting and determine the therapeutic efficacy longitudinally. Significant anti-atherosclerotic effects and reduction in mortality were observed upon treatment with rosiglitazone micelles and rosiglitazone. However, micelle-mediated delivery resulted in less side effects (weight gain, plasma cholesterol increase) than conventional rosiglitazone. No significant changes were found for untreated animals or mice treated with control micelles. These findings were corroborated by immunohistochemical analysis of lesion size. In conclusion, this study evaluates a powerful strategy for efficient treatment of atherosclerosis that includes nanomedical therapy of atherosclerotic plaques and the application of noninvasive and clinically approved imaging techniques to monitor delivery and therapeutic responses. We demonstrate anti-atherosclerotic effects in atherosclerotic lesions after micelle-mediated rosiglitazone therapy, while reducing common side effects associated with rosiglitazone.

INTRODUCTION

Cardiovascular disease (CVD) is the leading cause of morbidity and mortality in the Western world leading to clinical events such as myocardial infarction, stroke or aortic aneurysm rupture¹. Atherosclerosis is considered as the single most important contributor to CVD, characterized by a chronic inflammation of the arterial wall with concomitant accumulation of lipids, fibrous components and debris in the vessel wall^{2,3}. Both pre-clinical and clinical studies have reported that the insulin sensitizers thiazolidinediones (TZD), which exert their action mainly through binding to peroxisome proliferator-activated receptor γ receptors, inhibit the development and progression of atherosclerosis *in vivo*⁴⁻⁸. These anti-atherosclerotic effects are thought to occur independent of their metabolic effects^{5,6}. Moreover, TZD have a marked effect on both aneurysm development and rupture⁹.

Despite its proven success in the treatment of diabetes, TZD therapy is hampered by its undesirable (cardiac) side effects. Rosiglitazone, a TZD, was recently even put under selling restrictions in the US and withdrawn from the market in Europe due to an increased risk of cardiovascular events. Therefore, TZDs have not been seriously considered for clinical treatment of atherosclerosis, probably because they exhibit a poor pharmacokinetic profile, resulting in relatively low drug concentrations at sites of intended action.

More efficient delivery of rosiglitazone to the atherosclerotic lesions may improve its biodistribution and allow lowering of the therapeutic dose, thus producing an anti-atherosclerotic effect while reducing the side effects of this drug. Nanoparticle delivery has been shown to be a viable method to improve therapeutic efficacy, with liposomal doxorubicin as key example of a successful nanoparticles that received clinical approval¹⁰. Lipid-soluble drugs, such as rosiglitazone phosphate, can be encapsulated in micelles, coated with poly(ethylene) glycol (PEG) to enhance their circulation half-life, thereby increasing their accumulation at sites where the endothelium

is leaky (EPR effect) such as atherosclerotic lesions¹¹. This approach is particularly attractive, as micellar nanoparticles may be used not only for drug delivery to the atherosclerotic plaque, but also as an imaging platform by adding MRI-sensitive moieties such as gadolinium-DTPA, allowing a theragnostic approach to vascular disease¹¹.

In the present study, micelle-mediated rosiglitazone delivery is explored as a tool towards theragnostic imaging and treatment of atherosclerotic lesions. Two mouse models were used: hyperlipidemic ApoE^{-/-} mice, which develop extensive atherosclerotic lesions, and ApoE^{-/-}-eNOS^{-/-} mice¹², which develop both plaques and aneurysms. The objectives of this study were: (1) to assess whether micelle-encapsulated rosiglitazone could be delivered preferentially to sites of atherosclerotic plaques, (2) to assess whether plaque progression could be inhibited by micelle-mediated rosiglitazone therapy and (3) to assess whether the gadolinium-labelled micelles allowed a noninvasive follow-up assessment of the effect of rosiglitazone delivery on plaque progression.

MATERIALS AND METHODS

Preparation of rosiglitazone micelles

Preparation of rosiglitazone micelles was performed by modification of a conventional lipid film hydration method¹¹.

A mixture of the appropriate amounts of lipids (typically 120 mol of total lipid) was dissolved in chloroform/methanol 3:1 (vol/vol) in a round-bottom flask. A lipid film was made under reduced pressure using rotary evaporation at 37 °C and dried under a stream of nitrogen. Gd-DTPA-BSA (Gd-DTPA-bis(stearylamide) and PEG2000-DSPE (1,2-distearoyl-sn-glycero-3-phosphoethanolamine-N-[methoxy(polyethyleneglycol)-2000]) were used at a molar ratio of 1.5/1.35. For fluorescent detection, 0.1 mol% NIR664-DSPE (SyMO-CHEM B.V., Eindhoven, The Netherlands) was added. 0.02 mmol rosiglitazone (Cayman Chemicals) was incorporated. The lipid film was subsequently hydrated in 135 mM NaCl (pH 7.4) and vigorously stirred at 65 °C for 45 min.

The size and size distribution of the contrast agents were determined by dynamic light scattering (DLS) at 25 °C with a Malvern 4700 system (Malvern ZetaSizer Nano S, Malvern, UK). The micelles had a mean size of 16 nm and a polydispersity index below 0.1, which indicates a narrow size distribution. The relaxivity was measured at 37 °C and 9.4T.

The emission spectra of the probes were recorded using a fluorescence spectrophotometer (Fluorolog FII A Spectrofluorimeter, Spex Inc., NJ, USA) to confirm integration of rosiglitazone in the micelles as described previously¹³.

In vitro PPAR-γ activation measurements

Rosiglitazone activity and incorporation into micelles was confirmed by *in vitro* cell culture experiments. An osteoblast cell line, U02S, without PPAR-γ expression, was seeded into 12-wells plates. When the cells had a confluence of 70% they were transfected with the PPARγ-reporter, containing a dual luciferase (Signal PPAR Reporter (luc) kit, SABiosciences. Transfection results in continuous expression of Renilla luciferase, with firefly luciferase co-expression after activation of the PPAR-γ pathway. Rosiglitazone was used as a positive control. Control micelles, rosiglitazone micelles (containing 2.5 μM rosiglitazone), rosiglitazone (2.8 μM) were incubated for 24 hours after which the cells were lysed and luciferase expression was measured. Data was expressed as the ratio between Renilla and Firefly luciferase. All experiments were performed *in duplo*.

In vitro monocyte activation measurements

Monocyte activation was determined by flow cytometry (FC500, Beckman Coulter, Fullerton, CA, USA) following incubation of human whole blood from healthy donors with rosiglitazone (2.8 μM), rosiglitazone micelles (with 2.5 μM rosiglitazone), control micelles, or PBS. At different timepoints (30–240 minutes) blood samples were incubated with FACS antibodies for 30 minutes, red blood cells were lysed and FACS analysis was performed. CD14-PC5 (mouse anti-human IgG2a, A07765, Beckman-Coulter) was used for monocyte selection; CD11b-PE-Cy7 (mouse anti-human IgG1, 22-0118-42, eBioscience) and CD62L-ECD (L-selectin, mouse anti-human IgG1, IM2713U, Beckman-Coulter) were used to determine cell activation. CD14 positive cells were used and the percentage of the cells positive for CD11b and negative for CD62L were used to determine monocyte activation.

Animal experiments

Animal experiments were conducted in accordance with the Dutch guidelines for research animal care. The experiments have been approved by the institutional Animal Ethics Committee (DEC) at the Leiden University Medical Center, permit number 11180. In total 6 groups of male ApoE^{-/-} and 6 groups of male ApoE^{-/-}eNOS^{-/-} mice on a C57Bl6Jico background were included in this study (table 1). Mice were housed in isolator cages and given free access to food unless stated otherwise and acidified drinking water. All knockout mice were backcrossed for 10 generations to the C57Bl/6J genetic background. To generate ApoE^{-/-}-eNOS^{-/-} mice, eNOS^{-/-} mice and ApoE^{-/-} mice (Jackson laboratories, Bar Harbor, ME, USA) were crossed. These double heterozygous mice were subsequently crossed and the offspring genotyped for eNOS and ApoE by polymerase chain reaction to select ApoE^{-/-}-eNOS^{-/-} mice.

In vivo passive targeting of micelles to atherosclerotic lesions

To test the potential of rosiglitazone and control micelles to passively target atherosclerotic plaques, 2 groups (A) of 12–14 months old ApoE^{-/-} and 2 groups (B) of 10–12 months old ApoE^{-/-}eNOS^{-/-} were exposed to a Western diet (Ab-diets, The Netherlands) for 4 weeks. Each mouse was subsequently scanned before administration of rosiglitazone micelles or control micelles and 24 hours after intravenous injection of micelles (50 $\mu\text{mol Gd}^{3+}$ -DTPA lipid/kg bodyweight in 200

Table 1. Overview of the experimental groups of mice that were included in the analysis of the study

	ApoE ^{-/-}	ApoE ^{-/-} -eNOS ^{-/-}
Plaque imaging potential	A (n=5 rosiglitazone micelles, n=5 control micelles)	B (n=5 rosiglitazone micelles, n=5 control micelles)
4 weeks Western diet followed by		
6 weeks Western diet	C (n=5)	D (n=5)
6 weeks Western diet with rosiglitazone	E (n=5)	F (n=5)
6 weeks Western diet with control micelles	G (n=5)	H (n=5)
6 weeks Western diet with rosiglitazone micelles	I (n=5)	J (n=5)

μ l dextrose solution). The 24 hour time-point was determined in previous work as the optimal time point for passive targeting of micelles to the plaques¹⁴.

Effect of rosiglitazone therapy on plaque inflammation and aneurysm formation

To assess the therapeutic potential of rosiglitazone micelles 4 groups of ApoE^{-/-} and 4 groups of ApoE^{-/-}-eNOS^{-/-} mice were exposed to a Western diet for 4 weeks. After a 4-hour fasting period, body weight was determined and EDTA plasma (Sarstedt, Germany) was collected via the tail vein. Total plasma cholesterol and triglyceride levels were measured (Roche Diagnostics). The ApoE^{-/-} and ApoE^{-/-}-eNOS^{-/-} mice were subsequently randomized according to their body weight and plasma lipid levels (table 2). One group of animals for each genotype was fed for another 6 weeks a Western diet (C, D), one group was exposed to a Western diet supplemented with rosiglitazone (Ab diets, 0.018% w/w rosiglitazone, ~10 mg/kg bw/day (GSK, Zeist, The Netherlands) (E, F), the third and fourth group of mice was fed a Western diet for 6 weeks and received micelles through mini-osmotic pumps (Alzet, USA). Animals had an osmotic pump inserted subcutaneously in the interscapular region that released either control micelles (G, H) or rosiglitazone micelles (~10 mg/kg bw/day) (I, J). As significant mortality was expected, 15 mice were included per treatment group. Of the surviving animals, 5 mice per group were randomly selected for analysis after the treatment period.

Table 2. Overview of the plasma cholesterol and lipid values, as well as the body weight of the experimental groups of mice included in the study.

	Western diet	Western diet & rosiglitazone	Western diet & control micelles	Western diet & rosiglitazone micelles
ApoE^{-/-} mice				
At randomization				
Body weight (gram)	33.8 ± 1.8	33.1 ± 2.4	33.5 ± 2.8	34.5 ± 2.1
Cholesterol (mg/dL)	934 ± 24	923 ± 22	932 ± 21	917 ± 27
Triglycerides (mg/dL)	148 ± 12	147 ± 14	151 ± 9	150 ± 16
6 weeks treatment				
Body weight (gram)	36.7 ± 2.1 *	42.4 ± 3.2 *	37.0 ± 3.0 *	37.8 ± 1.9 *
Cholesterol (mg/dL)	1014 ± 38	1092 ± 29 *	1000 ± 23	994 ± 25
Triglycerides (mg/dL)	171 ± 14	196 ± 15	173 ± 13	174 ± 17
ApoE^{-/-}-eNOS^{-/-} mice				
At randomization				
Body weight (gram)	29.4 ± 1.6	28.7 ± 1.3	29.2 ± 2.0	28.9 ± 1.8
Cholesterol (mg/dL)	984 ± 48	978 ± 45	982 ± 39	987 ± 26
Triglycerides (mg/dL)	124 ± 11	135 ± 16	128 ± 15	132 ± 14
6 weeks treatment				
Body weight (gram)	32.6 ± 1.2	41.7 ± 2.8	33.4 ± 1.9	34.8 ± 2.4
Cholesterol (mg/dL)	1008 ± 35	1123 ± 25 *	1007 ± 41	1058 ± 37
Triglycerides (mg/dL)	182 ± 9	211 ± 14	175 ± 7	187 ± 16

Body weight, total cholesterol and triglycerides significantly increased compared to mice in other groups with rosiglitazone treatment. * p < 0.05

Imaging hardware

All MRI experiments were performed with a vertical 9.4 T magnet (Bruker, Ettlingen, Germany) supplied with an actively shielded Micro2.5 gradient system of 1 T/m and a 30 mm transmit/receive birdcage RF coil, using Paravision 5.0 software.

MRI protocols

In vivo

At the start of each examination, several 2D FLASH scout images were recorded in the transverse and axial planes through the heart to determine the orientation of the aortic arch. A modified FLASH sequence with a navigator echo (IntraGate) was used for retrospective CINE MRI with the following parameters:

1) *Cross sections of the aortic arch:*

RF pulse 1 ms; flip angle 15°; TR 31.4 ms; TE 2.96 ms; navigator echo points 64; 10 cardiac frames; FOV 1.8*1.8 cm²; matrix 128*128; in-plane resolution 141*141 μm²; 6 slices, slice thickness 0.4 mm; number of repetitions 400; total acquisition time approximately 20 min.

2) *For a frontal view of the aortic arch the MR sequence was slightly adapted:*

TR 15.7 ms, TE 2.96 ms, 3 slices, slice thickness 0.5 mm, total acquisition time approximately 10 min.

During the examination, the respiration rate was continuously monitored using a balloon pressure sensor connected to the ECG/respiratory unit (SA instruments, Stony Brook, NY, USA). The isoflurane concentration was adjusted to keep the respiration rate between 50 and 90 respirations/min.

After the final MRI scan all mice were terminally anesthetized with a mixture of midazolam (dormicum®, Roche), medetomidine (domitor®, Orion corporation, Finland) and fentanyl (Janssen-Cilag, Belgium) followed by transcardial perfusion; arteries were taken out for histological validation.

Ex vivo

Relaxivity measurements:

T1 values of micelles were determined using a saturation recovery protocol (multi slice multi echo (msme) sequence) with the following parameters: TE 7 ms, TR: 25-20-15-10-8-6-5-4-3-2-1.6-1.2-1.0-0.8-0.6-0.4-0.3 s, excitation hermite 1 ms, ref hermite 0.75 ms, band width 100kHz, matrix 128*128, resolution (195)² μm, 2*1mm slices.

The T1 values of the various ROIs were determined using a 3-parameter fit function:

$$M(t) = M0 (1 - \exp(-t/T1)) \quad [\text{Eq1}]$$

MRI Analysis

Aortic arch images were analyzed using ImageJ software. Black blood images in 3 to 4 adjacent slices of cross-sections through the aortic arch were analyzed. ROIs were drawn around the plaque region in the vessel wall (I_{wall}). A 2nd ROI was drawn in the surrounding muscle tissue of the shoulder girdle (I_{muscle}). Furthermore, an ROI was placed outside the animal to measure the noise level ($\text{stdev}_{\text{noise}}$) (Figure 2).

The contrast-to-noise ratio was defined as

$$\text{CNR} = (I_{\text{wall}} - I_{\text{muscle}}) / \text{stdev}_{\text{noise}} \quad [\text{Eq2}]$$

which is a measure how well the lesioned wall can be discriminated from the surrounding tissue. CNR values are shown as mean ± standard deviation.

Histology

Aortic arches, aortae and carotid arteries were fixed in 4% PFA, subsequently paraffin embedded and cut into serial 5 μm sections. Sections were stained with hematoxylin and eosin (H&E), followed by bright-field microscopy.

Statistical analysis

Data are represented as the mean \pm standard deviation. Statistical analyses were performed using SPSS 17.0.2 (SPSS, Inc., Chicago, IL, USA). Statistical significance between all four groups was assessed using one-way analysis of variance (ANOVA), followed by a Bonferroni correction for multiple testing in case of significance. Results were considered statistically significant at $p < 0.05$.

RESULTS

Nanoparticle characteristics

The mean size of the rosiglitazone micelles was 16.8 nm, the control micelles were 16.1 nm. Both batches had a polydispersity index of 0.1, indicating a narrow size distribution, as was determined by dynamic light scattering. Longitudinal relaxation values (r_1) obtained at 9.4 T at room temperature was $5.67 \text{ s}^{-1} \text{ mM}^{-1}$ for rosiglitazone micelles which was comparable to the relaxivity of $5.8 \text{ s}^{-1} \text{ mM}^{-1}$ of control micelles, in line with what we recently described¹⁴. Fluorescence spectra recorded for both micelles indicated that the amount of fluorescent near-infrared 664 was similar for both formulations.

In vitro PPAR- γ activation measurements

Human blood was incubated up to 240 minutes with rosiglitazone, PBS, rosiglitazone micelles, control micelles or PBS. Both rosiglitazone and rosiglitazone micelles had the potential to activate monocytes (CD11b⁺CD62L⁻ cells of CD14⁺ population (figure 1A). The percentage of CD11b⁺CD62L⁻ monocytes increased up to 92.04% of the CD14⁺ cell population after rosiglitazone micelle incubation similar to free rosiglitazone in solution. The PBS control did not show any activation; neither did the control micelles without rosiglitazone.

Subsequently, we tested the capacity to activate PPAR- γ transcription. A PPAR- γ deficient osteoblast cell-line transfected with a dual luciferase construct was used to assess PPAR- γ activating potential. Rosiglitazone (positive control) showed an increase in PPAR- γ activation. Two different batches of rosiglitazone micelles showed similar activation of PPAR- γ . The control micelles (without rosiglitazone) showed no activation after 24 hours of incubation (figure 1B).

In vivo passive targeting of micelles to atherosclerotic plaques.

The *in vivo* passive targeting of Gd-containing rosiglitazone micelles was investigated ApoE^{-/-} and ApoE^{-/-}-eNOS^{-/-} mouse models of experimental atherosclerosis on a high fat diet. Figure 2A and B depict representative MRI images of the aortic arch from ApoE^{-/-} and ApoE^{-/-}-eNOS^{-/-} animals obtained before (figure 2A) and 24 hours (figure 2B) after injection of micelles. There was approximately a 5 fold increase in enhancement of the aortic arch wall compared to muscle with both control and rosiglitazone micelles in ApoE^{-/-} and ApoE^{-/-}-eNOS^{-/-} mice (figure 2C). Contrast enhancement was observed in areas where atherosclerotic lesions were detectable on HE staining (figure 2D). No contrast enhancement was observed in areas without atherosclerotic lesions, demonstrating that both formulations are selectively retained in areas with endothelial damage.

Therapeutic properties of rosiglitazone micelles

Having demonstrated the passive homing of rosiglitazone micelles to atherosclerotic lesions, and the capacity of rosiglitazone micelle to activate PPAR- γ *in vitro*, we further explored whether rosiglitazone micelle can serve as targeted therapeutics for atherosclerosis.

ApoE^{-/-} and ApoE^{-/-}-eNOS^{-/-} mice were exposed to a Western diet. Subsequently, from both genotypes mice were randomized in 4 groups according to their body weight and plasma lipid levels (table 2). Mice were exposed for 6 weeks to either 1) a Western diet alone, or a Western diet with 2) control micelles, 3) rosiglitazone micelles or 4) oral rosiglitazone supplementation. At the end of the 6-week-therapeutical intervention period all ApoE^{-/-} mice were alive. ApoE^{-/-}-eNOS^{-/-} mice are known to have a high mortality, therefore groups of n=15 mice were initially used. Mice were exposed to either a Western diet supplemented with rosiglitazone or a Western diet with rosiglitazone micelles had a significantly higher survival chance than ApoE^{-/-}-eNOS^{-/-} mice exposed to a Western diet or a Western diet supplemented with control micelles (figure 3A). Five surviving mice per group were analyzed. Mice from both genotypes exposed to a Western diet supplemented with rosiglitazone developed a ruffled fur after ~ 4 weeks of exposure (figure 3B). Body weight of the control mice and of those receiving control micelles increased over the 6-week-intervention period (table 2). Mice exposed to a Western diet supplemented with rosiglitazone, gained significantly more weight than control animals, a known side-effect of rosiglitazone treatment. Also plasma cholesterol levels were increased compared to control mice (table 2). Interestingly, the weight gain and plasma cholesterol of mice on micelle-mediated rosiglitazone treatment and Western diet was similar to that of the control groups). MRI was performed after 6 weeks therapeutic intervention. Contrast-to-noise ratios (CNR) of atherosclerotic lesions on the inner curvature of the aortic arch were determined (figure 3C). ApoE^{-/-}-eNOS^{-/-} mice had significantly higher CNR and larger atherosclerotic lesions than ApoE^{-/-} mice. Treatment with rosiglitazone supplemented in the diet as well as rosiglitazone micelles led to a decrease in lesion area and consequently in CNR compared to mice exposed to a Western diet. Immunohistochemical assessment of plaque area (HE) and CD68 distribution confirmed the MRI results. The lesion area was significantly reduced in mice exposed to a Western diet supplemented with rosiglitazone and in mice exposed to rosiglitazone micelles compared to untreated mice (figure D and E). Both on MRI images and *ex vivo* the occurrence of aortic aneurysms was assessed. As expected, no aneurysms could be observed in the groups of ApoE^{-/-} mice. In ApoE^{-/-}-eNOS^{-/-} mice exposed to a Western diet or a Western diet with control micelles, aneurysms were detected in the abdominal aorta of all mice (figure 3F). Aneurysms were significantly reduced in size in mice treated with rosiglitazone micelles, and to a lesser extent also in mice exposed to a Western diet supplemented with rosiglitazone.

DISCUSSION

In the current study we successfully demonstrated the feasibility of a theragnostic approach using micelles as a carrier system for efficient anti-atherosclerotic drug delivery to atherosclerotic lesions as well as for plaque MR imaging in both the ApoE^{-/-} and ApoE^{-/-}-eNOS^{-/-} mouse model of atherosclerosis. Using MRI, we showed that homing of micelles to undiseased vessel walls was low, whereas micelles passively accumulated in atherosclerotic lesions. Both *ex vivo* tests and *in vivo* imaging showed that micelles are suitable as drug carrier for delivery of rosiglitazone to atherosclerotic lesions. The method of "targeted" delivery and accumulation is attributed to the enhanced permeability and retention (EPR) effect^{13,14} that is observed in atherosclerotic lesions

characterized by a disrupted endothelial layer. Moreover, we demonstrated that rosiglitazone micelle treatment led to decreased mortality, reduced plaque load and reduced aneurysm formation, similar to rosiglitazone, while preventing significant weight gain during the treatment.

Nanoparticles as imaging and drug carriers

Long-circulating particles, such as PEGylated micelles, are able to extravasate from the bloodstream and subsequently accumulate at sites with leaky endothelium where they are retained and act locally^{11,15}. This targeting effect results in an enhanced delivery of the drug to the desired site, which theoretically enables the use of lower dosages to achieve the same efficacy. Due to the long-circulating properties of the micelles, a higher proportion of the injected dose of the micelle-encapsulated drug as compared to the orally delivered drug ends up in the atherosclerotic plaques. As a next step, targeted delivery of drugs to sites with enhanced permeability can be even further improved by conjugation of targeting ligands to the micelle surface. Several studies have shown that micelles can be actively targeted to entities of interest by conjugating targeting molecules to the surface^{15,16}. To that end, it is also possible to actively target atherosclerotic plaques by e.g. targeting macrophages via the macrophage scavenger receptor¹⁵, neovessels via $\alpha v\beta_3$ -integrin^{16,17} or any other target of choice that is up-regulated in atherosclerotic lesions¹⁷.

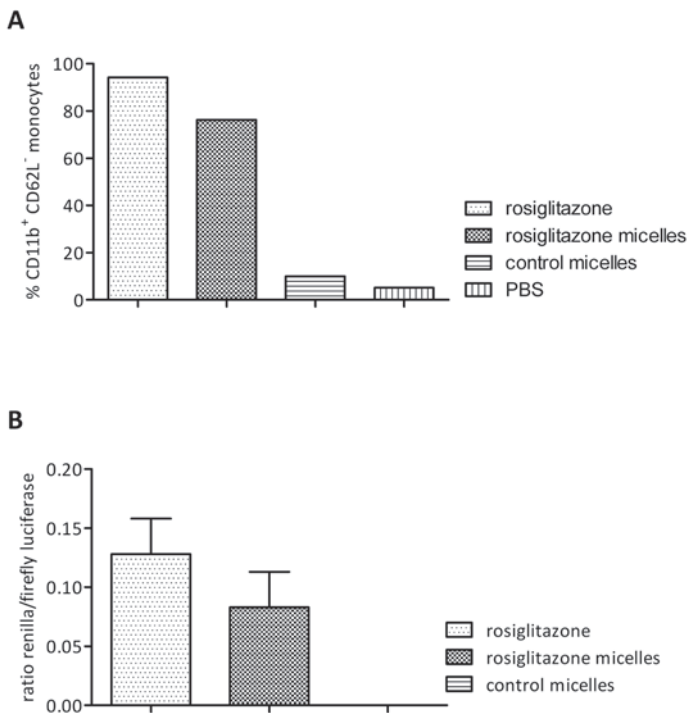


Figure 1 | In vitro validation of rosiglitazone micelles. A. Fraction activated CD11b⁺ CD62L⁻ monocytes from the CD14⁺ population after 2 hours incubation with rosiglitazone, rosiglitazone micelles, control micelles or PBS. B. Activating potential of rosiglitazone and rosiglitazone micelles was tested in a PPAR- γ deficient osteoblast cell-line transfected with a dual luciferase construct was used to assess PPAR- γ activating potential

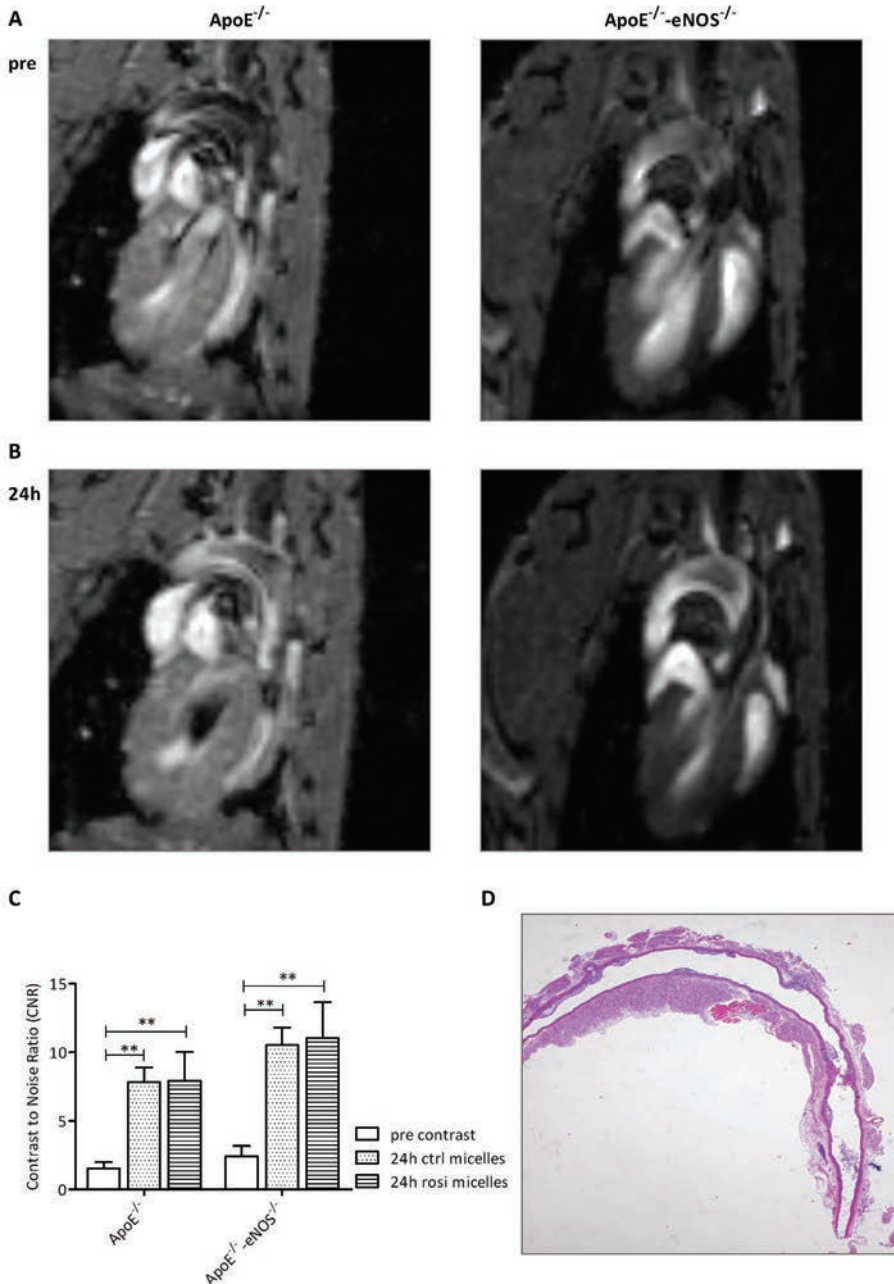


Figure 2 | Proof of principle of imaging potential of Gd-loaded rosigitazone and control micelles. A. T1 weighted MRI of the aortic arch before injection of micelles. B. T1 weighted MRI 24 hours after rosigitazone micelle injection. C. Contrast-to-Noise ratios of ApoE^{-/-} and ApoE^{-/-} eNOS^{-/-} mice 24 hours after injection of either control micelles or rosigitazone micelles. D. Representative Haematoxylin Eosin staining of the inner curvature of the aortic arch of an ApoE^{-/-} eNOS^{-/-} mouse. Atherosclerotic plaques are observed in areas with contrast enhancement on MRI. ** p < 0.01.

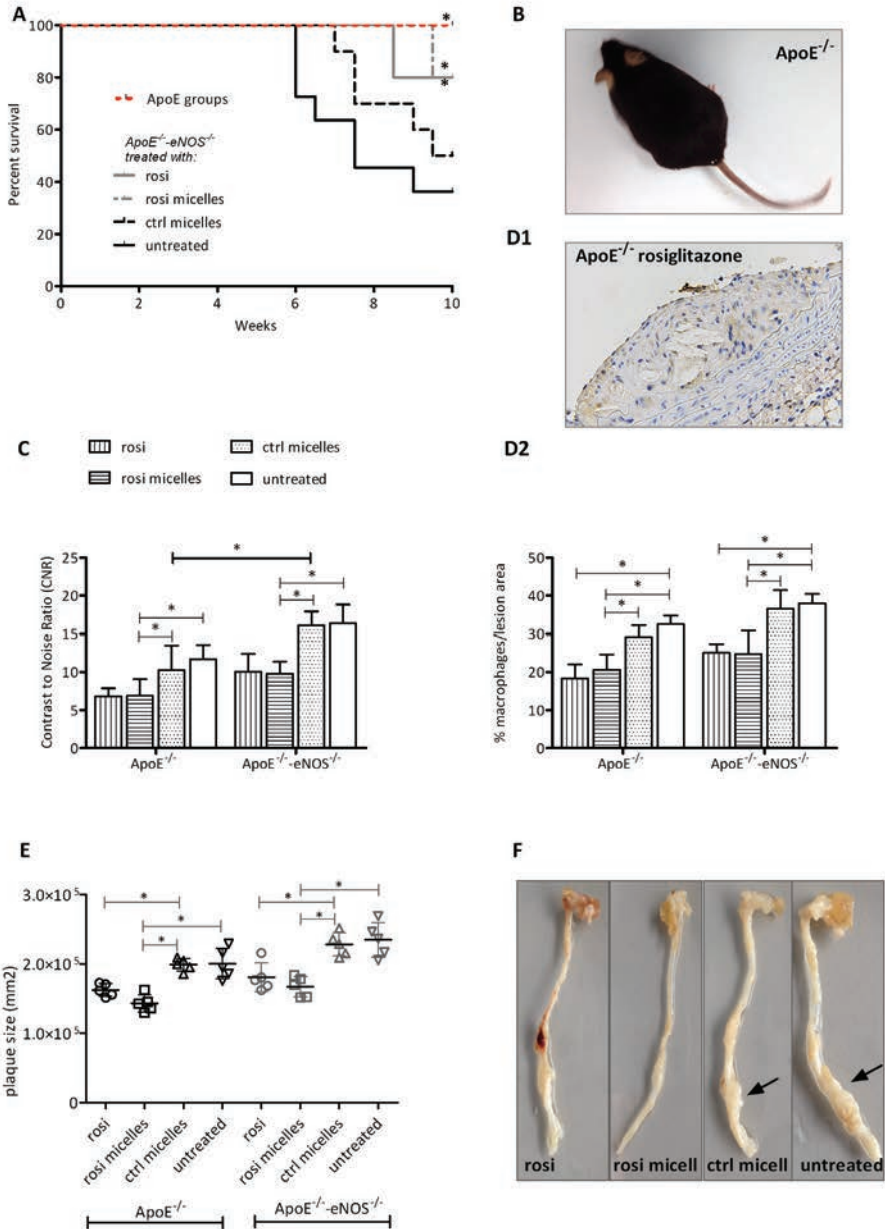


Figure 3 | The effect of rosiglitazone on atherosclerosis and aneurysm formation. A. Kaplan-Meier survival curve of ApoE^{-/-} (in red) and ApoE^{-/-}eNOS^{-/-} (in black/gray) mice exposed for 4 weeks to a Western diet and subsequently treated with rosiglitazone, rosiglitazone micelles, control micelles or left untreated. B. Ruffled fur of an ApoE^{-/-} mouse exposed to a Western diet supplemented with rosiglitazone. C. Contrast to Noise Ratios of the different groups of animals after 6 weeks treatment. D. D1 Immunohistochemical DAB staining of the aortic arch of a rosiglitazone treated ApoE^{-/-} mouse, 400x. D2. Percentage CD68+ cells per lesion area on the innercurvature of the aortic arch of the different treatment groups. E. Histological determination of plaque size in the different treatment groups. F. *En face* preparation of the aortic arch and aorta of ApoE^{-/-}eNOS^{-/-} mice from the 4 treatment groups. * p< 0.05

Nevertheless, “simple” long circulating micelles without the conjugation of targeting ligands are attractive for several reasons. They are easier to synthesize, less expensive, more generally applicable, less immunogenic, and most importantly can be translated relatively fast to the clinic. In the past this has already led to the approval and clinical application of a variety of lipid-based drugs in the field of oncology like clodronate liposomes^{21,22}. In this study, the micelles were administered using osmotic pumps to facilitate the experimental design. However, micelle formulations can in principle be stabilized with a sufficiently long shelf life for oral administration. Previously, microsphere delivery of rosiglitazone in diabetic rats already showed that nanoparticle delivery allows for better glycemic control at lower dose than immediate-release formulations¹⁸, suggesting that our current approach could also be an interesting alternative for a large group of patients with comorbid diabetes and vascular disease.

Rosiglitazone in the treatment of atherosclerosis

In this study we successfully applied rosiglitazone in a micelle formulation to treat experimental atherosclerosis and the occurrence of aneurysms. Rapidly increasing amounts of evidence have underscored the importance of PPAR- γ in cardiovascular disease¹⁹, in particular in diabetes mellitus²⁰ and atherosclerosis²¹. Treatment with PPAR- γ agonists leads to a reduction of insulin resistance by sensitizing muscle, liver, and adipose tissue to insulin. Largely consistent results from preclinical studies using *in vivo* and *in vivo* models, suggest that PPAR- γ and its selective agonists including rosiglitazone have an atheroprotective role via their effect on inflammatory cells, endothelial cells and lipid metabolism²². These mechanisms are also the basis of its potential to reduce the occurrence of aneurysms⁹. We confirmed the potential of rosiglitazone to modulate the immune system *ex vivo* by facs analysis of circulating monocytes/macrophages as well as *in vivo* by addressing the plaques macrophage load.

Treatment with rosiglitazone has been associated with weight gain in patients with type 2 diabetes as well as in animal models, mainly attributable to an increase in abdominal adipose tissue without a significant gain in body water^{23,24}. Moreover, an increase in total cholesterol and triglyceride plasma levels occurs with rosiglitazone treatment. We observe indeed an increase in body weight and plasma cholesterol and triglyceride levels in mice treated with a western diet supplemented with rosiglitazone. In contrast, this effect was not observed though in the groups of mice exposed to a Western diet and treated with rosiglitazone micelles. This suggests the mode of action of the rosiglitazone micelles on atherosclerosis progression is indeed a local rather than a systemic effect. It would be of interest to assess whether the insulin-sensitizing mode of action is also still present using rosiglitazone micelles. The slow-release study by Kamila *et al.* and the pharmacokinetic profile of micelles (long circulation times, clearance via the liver¹⁴ would suggest that it is very well possible that micelle-mediated delivery also has a beneficial effect on glycaemic control.

In this study we administered a similar dose of rosiglitazone orally and in micelles to the mice. The effect on atherosclerotic lesions and mortality was comparable. The effect on systemic side-effects remains to be investigated, although the lack of weight gain and cholesterol increase in the rosiglitazone micelle-treated group is an indication that severe edema probably does not occur. We observed a significant increase in survival chance in ApoE^{-/-}-eNOS^{-/-} mice treated with rosiglitazone. Several ApoE^{-/-}-eNOS^{-/-} mice exposed to a Western diet died, probably because of myocardial infarction and aneurysm rupture, which introduced a bias in the control group, as we chose to maintain the group size at n=5 after the 6 weeks treatment period. The strongest mice were thus included in the analysis of the treatment effects, and therefore we are probably underestimating the treatment effect.

The effects of TZDs on vascular disease in clinical trials are at this stage conflicting. Several studies have reported a beneficial effect on atherosclerosis progression, whereas other studies reported no effect²². Recent meta-analyses even suggest an increased risk of myocardial infarction using rosiglitazone²³. Unveiling the background of these confusing clinical results will be complicated given that the patient population often suffers from multiple morbidities and receives several drugs. A nanoparticle approach may help to locally treat the atherosclerotic lesion, allowing image guided follow-up as well as lower dosing and thereby reducing the risk of severe adverse effects.

Comparison to other theragnostic particles

A combined approach of MR imaging and drug targeting has recently gained more attention and has been demonstrated previously in experimental atherosclerosis. Lobatto *et al.* recently developed liposomes loaded with anti-inflammatory glucocorticoids^{27,28}. The liposomes were intravenously applied in a rabbit model of atherosclerosis. 18F-fluoro-deoxy-glucose positron emission tomography and dynamic contrast enhanced MRI, were applied to longitudinally assess therapeutic efficacy. Significant anti-inflammatory effects were observed as early as 2 days that lasted up to at least 7 days after administration of a single dose of liposomes.

Winter *et al.* documented results on a combined approach of molecular MRI and drug targeting of atherosclerosis using $\alpha_3\beta_3$ -specific nanoparticles^{29,30}. They used these nanoparticles to target atherosclerotic lesions of rabbits. For therapeutic purposes, they included fumagillin in the lipid monolayer of the nanoparticles and observed an anti-angiogenic effect with MRI that was confirmed histologically. Moreover Maiseyeu *et al.* developed a multivalent theragnostic nanoparticle composed of phosphatidyl-serine (PS), ω -carboxynonanoyl-cholesteryl ester and Gd lipids which were targeted to M2 macrophages using an anti-Mrp14 polyclonal antibody^{30,31}. Overall, these studies as well as this current work hold great promise for nanoparticles-based treatment of atherosclerosis.

REFERENCES

- Lopez, A. D.; Mathers, C. D.; Ezzati, M.; Jamison, D. T.; Murray, C. J. Global and regional burden of disease and risk factors, 2001: systematic analysis of population health data. *Lancet* 2006, 367 (9524), 1747-1757.
- Falk, E. Pathogenesis of atherosclerosis. *J. Am. Coll. Cardiol.* 2006, 47 (8 Suppl), C7-12.
- Libby, P. Inflammation in atherosclerosis. *Nature* 2002, 420 (6917), 868-874.
- Li, A. C.; Brown, K. K.; Silvestre, M. J.; Willson, T. M.; Palinski, W.; Glass, C. K. Peroxisome proliferator-activated receptor gamma ligands inhibit development of atherosclerosis in LDL receptor-deficient mice. *J. Clin. Invest* 2000, 106 (4), 523-531.
- Levi, Z.; Shaish, A.; Yacov, N.; Levkovitz, H.; Trestman, S.; Gerber, Y.; Cohen, H.; Dvir, A.; Rhachmani, R.; Ravid, M.; Harats, D. Rosiglitazone (PPARgamma-agonist) attenuates atherogenesis with no effect on hyperglycaemia in a combined diabetes-atherosclerosis mouse model. *Diabetes Obes. Metab* 2003, 5 (1), 45-50.
- Calkin, A. C.; Forbes, J. M.; Smith, C. M.; Lassila, M.; Cooper, M. E.; Jandeleit-Dahm, K. A.; Allen, T. J. Rosiglitazone attenuates atherosclerosis in a model of insulin insufficiency independent of its metabolic effects. *Arterioscler. Thromb. Vasc. Biol.* 2005, 25 (9), 1903-1909.
- Chen, Z.; Ishibashi, S.; Perrey, S.; Osuga, J.; Gotoda, T.; Kitamine, T.; Tamura, Y.; Okazaki, H.; Yahagi, N.; Iizuka, Y.; Shionoiri, F.; Ohashi, K.; Harada, K.; Shimano, H.; Nagai, R.; Yamada, N. Troglitazone inhibits atherosclerosis in apolipoprotein E-knockout mice: pleiotropic effects on CD36 expression and HDL. *Arterioscler. Thromb. Vasc. Biol.* 2001, 21 (3), 372-377.
- Gerstein, H. C.; Ratner, R. E.; Cannon, C. P.; Serruys, P. W.; Garcia-Garcia, H. M.; van Es, G. A.; Kolatkar, N. S.; Kravitz, B. G.; Miller, D. M.; Huang, C.; Fitzgerald, P. J.; Nesto, R. W. Effect of rosiglitazone on progression of coronary atherosclerosis in patients with type 2 diabetes mellitus and coronary artery disease: the assessment on the prevention of progression by rosiglitazone on atherosclerosis in diabetes patients with cardiovascular history trial. *Circulation* 2010, 121 (10), 1176-1187.
- Jones, A.; Deb, R.; Torsney, E.; Howe, F.; Dunkley, M.; Gnanaswaran, Y.; Gaze, D.; Nasr, H.; Loftus, I. M.; Thompson, M. M.; Cockerill, G. W. Rosiglitazone reduces the development and rupture of experimental aortic aneurysms. *Circulation* 2009, 119 (24), 3125-3132.
- Slingerland, M.; Guchelaar, H. J.; Gelderblom, H. Liposomal drug formulations in cancer therapy: 15 years along the road. *Drug Discov. Today* 2012, 17 (3-4), 160-166.
- Mulder, W. J.; Strijkers, G. J.; Briley-Saboe, K. C.; Frias, J. C.; Aguinaldo, J. G.; Vucic, E.; Amirbekian, V.; Tang, C.; Chin, P. T.; Nicolay, K.; Fayad, Z. A. Molecular imaging of macrophages in atherosclerotic plaques using bimodal PEG-micelles. *Magn Reson. Med.* 2007, 58 (6), 1164-1170.
- Chen, J.; Kuhlencordt, P. J.; Astern, J.; Gyurko, R.; Huang, P. L. Hypertension does not account for the accelerated atherosclerosis and development of aneurysms in male apolipoprotein e/endothelial nitric oxide synthase double knockout mice. *Circulation* 2001, 104 (20), 2391-2394.
- Sarkar, A.; Banerjee, P.; Bhattacharya, S. C. Substituent effect on the emission behavior of thiazolidinedione derivatives in cationic and anionic micellar media. *J. Colloid Interface Sci.* 2009, 329 (1), 160-166.
- den Adel, B.; van der Graaf, L. M.; Que, I.; Strijkers, G. J.; Lowik, C.; Poelmann, R. E.; van der Weerd, L. Contrast enhancement by lipid-based MRI contrast agents in mouse atherosclerotic plaques; a longitudinal study. *Contrast. Media Mol. Imaging* 2013 Jan;8(1):63-71.
- Beilvert, A.; Cormode, D. P.; Chaubet, F.; Briley-Saboe, K. C.; Mani, V.; Mulder, W. J.; Vucic, E.; Toussaint, J. F.; Letourneur, D.; Fayad, Z. A. Tyrosine polyethylene glycol (PEG)-micelle magnetic resonance contrast agent for the detection of lipid rich areas in atherosclerotic plaque. *Magn Reson. Med.* 2009, 62 (5), 1195-1201.
- van Tilborg, G. A.; Vucic, E.; Strijkers, G. J.; Cormode, D. P.; Mani, V.; Skajaa, T.; Reutelingsperger, C. P.; Fayad, Z. A.; Mulder, W. J.; Nicolay, K. Annexin A5-functionalized bimodal nanoparticles for MRI and fluorescence imaging of atherosclerotic plaques. *Bioconjug. Chem.* 2010, 21 (10), 1794-1803.
- Majmudar, M. D.; Nahrendorf, M. Cardiovascular molecular imaging: the road ahead. *J. Nucl. Med.* 2012, 53 (5), 673-676.
- Kamila MM; Mondal N; Ghosh LK; Gupta BK . Multiunit Floating Drug Delivery System of Rosiglitazone Maleate: Development, Characterization, Statistical Optimization of Drug Release and In Vivo Evaluation. 10(3), 887-899. 9-9-2009.
- Viberti, G. C. Rosiglitazone: potential beneficial impact on cardiovascular disease. *Int. J. Clin. Pract.* 2003, 57 (2), 128-134.
- Nicholson, G.; Hall, G. M. Diabetes mellitus: new drugs for a new epidemic. *Br. J. Anaesth.* 2011, 107 (1), 65-73.
- Wang, N.; Yin, R.; Liu, Y.; Mao, G.; Xi, F. Role of peroxisome proliferator-activated receptor-gamma in atherosclerosis: an update. *Circ. J.* 2011, 75 (3), 528-535.
- Dandona, P.; Chaudhuri, A.; Ghanim, H. Rosiglitazone, thiazolidinediones and atherosclerosis. *Atherosclerosis* 2010, 211 (2), 384-385.
- Bourg, C. A.; Phillips, B. B. Rosiglitazone, myocardial ischemic risk, and recent regulatory actions. *Ann. Pharmacother.* 2012, 46 (2), 282-289.





Atherosclerosis. 2012; 225(2):274-80

Chapter 9

Histological validation of iron-oxide and gadolinium based MRI contrast agents in experimental atherosclerosis: the do's and don't's

Brigit den Adel*, Sandra M. Bovens*, Bernard te Boekhorst, Gustav J. Strijkers, Robert E. Poelmann, Louise van der Weerd and Gerard Pasterkamp

ABSTRACT

MRI using targeted contrast agents (CA) has emerged as a promising technique to study atherothrombotic disease *in vivo*. Particularly, the use of targeted Gd and lipid-based nanoparticles has enabled detailed *in vivo* imaging of various molecular markers of atherosclerotic plaque pathophysiology. For validation purposes, it is crucial that nanoparticle accumulation in the plaque, cellular association and localization can be assessed by *ex vivo* immuno-histology or fluorescence microscopy of tissue sections.

In this review we discuss the various methods that are available for histological evaluation of targeted MRI contrast agents such as lipid-based nanoparticles and iron oxide particles. We discuss the detection of these contrast agents in paraffin-embedded and in cryopreserved tissue sections of atherosclerotic plaques. During the embedding procedure in paraffin, most components of targeted lipid-based nanoparticles are generally washed out, though the actual targeting moieties may be retained in the embedded sections. Therefore staining of the antibody-antigen complex provides a suitable way to visualize the presence of the nanoparticle in the plaque. Cryopreservation preserves nanoparticle presence in the plaque. In cryosections, the localization of nanoparticles can be assessed directly by measuring the fluorescence of an incorporated fluorophore or by secondary stainings of the Gd-containing DTPA lipids or the iron oxide particles. With certain secondary stainings, be it for the contrast agent or for co-localization with the target, the contrast agent itself may interfere with standard histological protocols, yielding false positive results.

The here presented techniques enable proper visualization of MR contrast agent accumulation and localization in atherosclerotic plaque, which will provide the validation necessary to advance these lipid-based nanoparticles to the clinic.

INTRODUCTION

Atherosclerosis and its thrombotic complications are a major cause of morbidity and mortality in the industrialized countries, despite the clinical advances that have been made over the past 20 years in the prevention and treatment of this disease¹. The main components of the atherothrombotic plaques are: (i) connective tissue extracellular matrix, including collagen, proteoglycans, fibronectin, and elastic fibers; (ii) crystalline cholesterol, cholesteryl esters, and phospholipids; (iii) cells including monocyte-derived macrophages, T-lymphocytes, and smooth muscle cells, and in advanced or ruptured plaques (iv) thrombotic material with platelets and fibrin. Varying proportions of these components are present in different plaques, thus giving rise to heterogeneity of the lesions²⁻⁴. Vulnerable plaques, which are prone to rupture, contain a high frequency of inflammatory cells and may cause clinically manifest problems. Vulnerable plaque composition varies depending on the anatomical site, with striking heterogeneity even within the same individual. Therefore reliable non-invasive clinically available imaging is needed, which is able to detect and characterize atherothrombotic disease in its various stages and at different anatomical sites⁵. An ideal clinical imaging modality for atherosclerotic vascular disease is safe, inexpensive, non- or minimally invasive, accurate, and reproducible, while the imaging readouts should correlate with the extent of atherosclerotic disease and have high predictive value for the occurrence of future clinical events^{5,6}.

In this respect, high-resolution magnetic resonance imaging (MRI) has emerged as a promising technique to study atherothrombotic disease *in vivo*⁷. MRI does not involve ionizing radiation and provides high-resolution images of various vascular regions. An MR image is based on

radiofrequency signals, typically from water protons, following administration of a radiofrequency pulse, while the subject is placed in a strong magnetic field. The emitted signal varies according to the water concentration and the relaxation times (T1 and T2). Using combined analysis of different tissue signal intensities generated by the application of T1-weighted (T1W), T2-weighted (T2W), and proton-density-weighted (PDW) images, it is possible to generate detailed images of plaque anatomy and morphology⁸. The use of (targeted) contrast agents enables visualization of plaque permeability and disease-specific cellular and molecular processes.

In the past decade, the development of MRI contrast agents has seen a tremendous progress. The application of T1 and T2 non-targeted and targeted contrast agents (CA) is commonly explored in animal models of human atherosclerosis⁷. Currently, there are no clinically established methods to non-invasively differentiate between stable and vulnerable plaques and to identify rupture prone plaques. Therefore, there has been much activity in the development of targeted MRI contrast agents (9). Validation of the MR molecular images in pre-clinical models of atherosclerosis by comparison with "gold standard" histology images is at these stages of utmost importance. In many cases histological validation is difficult or even flawed because of several reasons. First of all, the tissue preparation method, such as embedding in paraffin or freezing, may render detection of contrast agent in a native state impossible. Secondly, lipid-based nanoparticles generally consist of a mixture of building blocks – e.g. phospholipids, targeting ligands, fluorescent moieties, Gd-containing lipids, cholesterol. Histological visualization of one of these components, e.g. the targeting ligand, does not automatically imply copresence of the other components. Thirdly, autofluorescence of tissue may interfere with specific detection of fluorescent moieties in tissue. Fourthly, the contrast agent itself may interfere with standard histological protocols.

This review will discuss several existing strategies and validated histological methods for the detection of contrast agents in tissue sections of mouse atherosclerotic plaque. We will discuss Gd-based nanoparticle contrast agents that generate contrast on T1W MR images (T1 contrast agents), as well as FeO-based agents, which are more suitable for detection using T2W MR imaging techniques (T2 contrast agents).

T1 contrast agents

Most clinically applied MRI contrast agents are based on Gd³⁺-DTPA or -DOTA chelates. Because the potency of one Gd-DTPA molecule to generate contrast in the MR images (i.e. the relaxivity) is rather low, (preclinically) the Gd is often incorporated in nanoparticles, such as micelles and liposomes, to increase the payload and improve the detection sensitivity. It becomes more and more apparent that post-processing techniques of harvested tissues determine to a large extent whether one can validate the accumulation of these lipid-based nanoparticles; they generally wash out during embedding in paraffin, however any incorporated peptide/antibody remains attached to its ligand. To verify ligand binding, embedding in paraffin and subsequent staining of the antibody-antigen complex is a suitable approach. However, to verify whether the entire lipid-based nanoparticle entered the vessel wall, cryopreservation is required to either stain for the presence of DTPA or to visualize an incorporated fluorophore in the nanoparticle.

Ex vivo histological visualization of Gd in tissue sections is complicated. Indirect detection is possible by replacing Gd with Europium (Eu), which enables imaging of the Eu chelate by fluorescence microscopy¹⁰ or as paraCEST agent¹¹. Inductively coupled plasma mass spectroscopy (ICP-MS) of tissue homogenates can also be used to quantify Gd content in tissues. However, with this technique information on the cellular localization of the CA is lost¹².

Recently several anti-DOTA and anti-DTPA antibodies became commercially available that allow detection of Gd-chelates in their native cellular environment¹². Staining of the Gd-chelate requires

the presence of a stable and accessible chelate (without spherical hindrance) in the contrast agent. Here we report for the first time on the use of these antibodies to detect the Gd-chelates in atherosclerotic plaque. Figure 1 demonstrates the application of anti-DTPA antibodies with diaminobenzidine (DAB) enhancement to stain cryosections of plaques in the carotid artery of an ApoE^{-/-} mouse that was injected with Gd-DTPA containing micelles. DAB positive areas (figure 1A and C) in tissue cryosections of the carotid arteries were in agreement with a positive signal enhancement observed on *in vivo* MR images (figure 1B and D). This Gd staining method may not be suitable for tissue sections prepared by paraformaldehyde fixation and paraffin embedding, as Gd-DTPA will wash out during preparation.

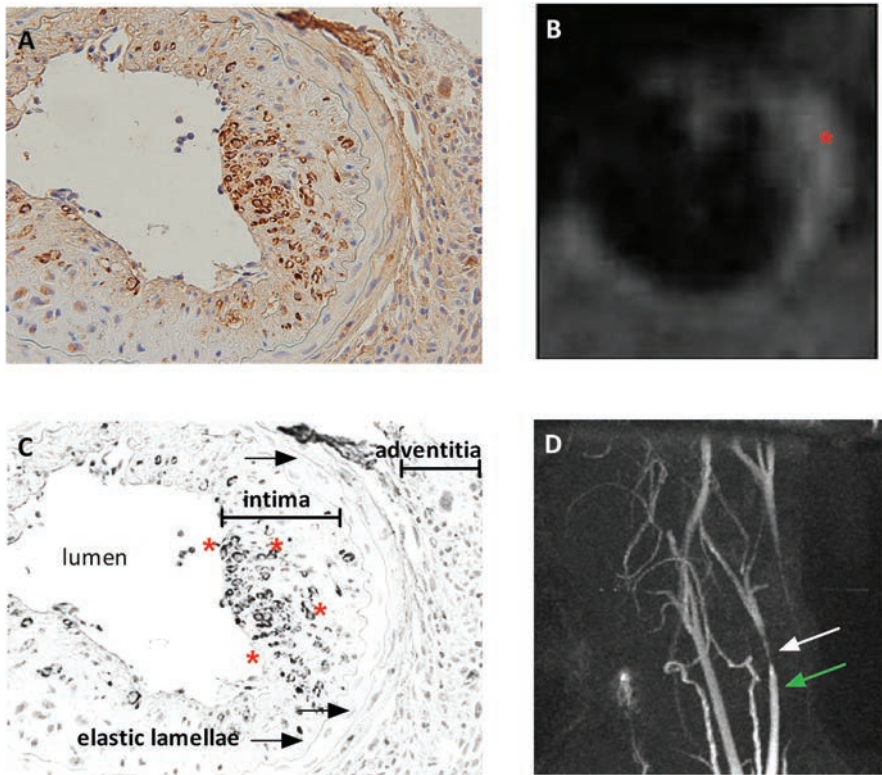


Figure 1 | Detection of Gd-DTPA in an atherosclerotic plaque of an ApoE^{-/-} mouse. Application of anti-DTPA antibodies to stain cryosections of plaques in the carotid artery of an ApoE^{-/-} mouse that was injected with Gd-DTPA containing micelles. In panel A DAB positive areas showing Gd-DTPA micelles in tissue cryosections of the carotid arteries are visible in the intima of the carotid artery. Red asterisk in panel B indicates the area with positive contrast enhancement in an MR image of a mouse carotid artery with atherosclerosis after injection of Gd-containing micelles. The area with positive contrast enhancement is in agreement with the DAB positive area in panel A. In panel C, an enhanced version of the histological slide of panel A for better distinction of lumen, intima and adventitia of the histological slide from panel A indicates the vessel lumen, intima and adventitia. Arrows point at the elastic lamellae. The asterisks contour the DAB positive area. In panel D an MR angiogram of an ApoE^{-/-} mouse is shown. The white arrow indicates the area where a constrictive collar has been placed around the left carotid artery to induce atherosclerosis. The green arrow points at the region of the left carotid artery where the histological slices originate from.

Most of the micellar and liposomal Gd-based MRI contrast agents also contain a lipid-bound fluorophore in the membrane for *ex vivo* visualization by fluorescence microscopy. Originally, rhodamine-PE was the fluorophore of choice¹³. However, detection of rhodamine-PE in atherosclerotic plaques in ApoE^{-/-} mice fails due to autofluorescence of elastic lamellae at approximately the same emission wavelength (580 nm), leading to images that are difficult to interpret¹⁴. As an alternative, a near infrared fluorophore (NIR-664) has been used to visualize micelles accumulated in atherosclerotic plaques in the carotid arteries of ApoE^{-/-} mice¹⁵. Autofluorescence of tissue is now an advantage as it enables visualization of the elastic lamellae without additional stainings. Figure 2B shows a confocal microscopy image of an aortic arch (figure 2A) plaque with in green the elastic lamellae and in red the NIR-664 lipids of the micelles. The corresponding MRI of the aortic arch with positive contrast enhancement on the inner curvature of the aortic arch is shown in figure 2C. When using a different atherosclerotic mouse model (ApoE^{-/-}eNOS^{-/-} double knockout mice¹⁶ in which intra-plaque hemorrhage and the spontaneous development of aneurysms (in males) can be observed, erythrocytes cause additional autofluorescence, especially in the near infrared spectral region (figure 2D). Therefore, in this mouse model fluorescence microscopy in the NIR regime does not completely solve the problem with autofluorescence.

To circumvent flawed histological validation due to autofluorescence overlapping with the fluorescent spectrum of fluorophores incorporated in nanoparticles, a different approach could be used to detect micelles/liposomes indirectly with a secondary histological staining of the targeting ligands (e.g. antibodies). Antibodies bound to a target survive the paraffin embedding procedure and therefore a secondary antibody can be applied, after which a DAB or alkaline phosphatase (AF) step visualizes the bound antibodies and thus indirectly reveals the presumed location of the micelles¹⁷. An example of this staining method is shown in figure 3. NGAL staining displayed a wide-spread distribution of this protein in the plaque (figure 3A). The staining to detect bound primary antibodies, previously coupled to the injected micelles (figure 3B), showed a partial overlap in AF signal. We conclude that the micelles specifically binds to NGAL, yet the target is also present in different areas of the plaque that do not show the presence of micelles, possible because the micelles do not penetrate into these areas.

Van Tilborg *et al.*¹⁸ designed a targeting approach in tumors with liposomes containing lipids conjugated to biotin or streptavidin. An avidin chase was used *in vivo* to increase the clearance rate of unbound particles. However, when these particles were used for histological evaluation using an avidin method it gave rise to considerable background staining. Normally, a blocking step is used to block biotin in any staining procedure (both cryo- or paraffin-sections). However, this is not suitable to stain the biotin present in the nanoparticle contrast agent. So though this method may be very useful *in vivo* in experimental animals, it cannot be used in conjunction with standard histological validation of contrast agents.

Another promising approach to circumvent hindrance by autofluorescence in atherosclerotic vessels is the development of dual histology/MRI contrast agents in which the same molecule acts as an MRI contrast agent and as an optical histological stain. Thus far this has only been described for brain MRI contrast agents^{19,20}. Luxol Fast Blue (LFB), a classical staining for myelin, contains copper, a paramagnetic metal that acts as an MRI contrast agent. Both the macroscopic and microscopic distributions of LFB were found to mimic those of traditional histological preparations and the *ex vivo* use of the compound allowed detailed co-registration of histology and MRI. Congo Red, a histological fluorescent staining for amyloid plaque, was modified by Higuchi *et al.* to contain 19F for 19F-MRI and T1W detection. *In vivo* and *ex vivo* MRI and histology

showed targeting of fibrillar plaques using this agent. We postulate that a similar approach could be used with a modified Oil Red O stain or classical collagen staining to detect atherosclerotic plaques.

T2 contrast agents

USPIO (18-30 nm) and SPIO (100-200 nm) are superparamagnetic particles made of an iron-oxide crystalline core. Because of their large magnetic moment, the iron-oxide containing particles create strong local magnetic field gradients, which leads to rapid signal loss in T2 weighted images.

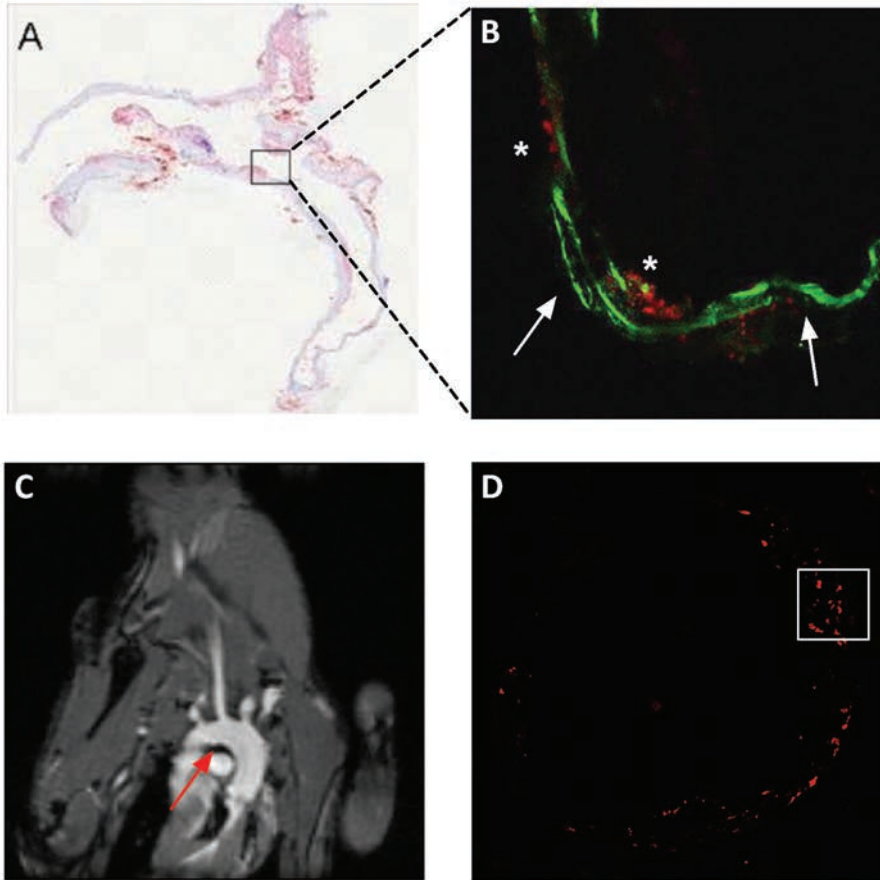


Figure 2 | Detection of NIR664 lipid in an atherosclerotic plaque of atherosclerotic mice. A: Oil Red O staining of the entire aortic arch of an ApoE^{-/-} mouse displaying lipid depositions in red. B: confocal microscopy image (zoomed frame of A, indicated by dashed lines), depicting the elastic lamellae in green (white arrows) and the micelles with a NIR664 lipid in red (asterisks). C: MRI of the aortic arch depicted in A and B after injection of Gd-containing micelles. Positive contrast enhancement of the micelles is observed on the inner curvature of the arch (red arrow), correlating to the regions where atherosclerotic plaques can be observed in panel A. D: In ApoE^{-/-} eNOS^{-/-} mouse autofluorescence of excessive lipid deposition and intraplaque hemorrhage generate autofluorescence in the vessel thereby preventing detection of NIR664. Autofluorescence can be observed at several wavelengths due to the presence of intra-plaque erythrocytes: red (ex543, em590), green (ex488, em518), and far red (ex633, em670), overlapping with the emission spectrum of NIR664. Ex: excitation; em: emission

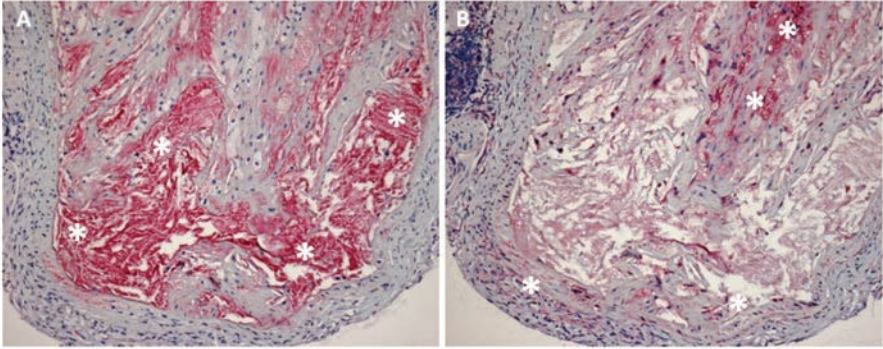


Figure 3 | NGAL and micelle staining in an atherosclerotic plaque from a ApoE^{-/-}/eNOS^{-/-} mouse. A: NGAL staining is depicted in red (AF) in an atherosclerotic plaque, red areas are indicated with asterisks; B: micelle staining depicted in red (AF)(white asterisks). Some overlap between the staining can be observed, with more NGAL present than micelles. NGAL: *neutrophil gelatinase-associated lipocalin*; AF: *alkaline phosphatase*

In black, negative contrast in the surrounding of the particle the classical dipole shape can be recognized, which is coined the “blooming” effect²¹. This blooming effect stresses the need to histologically validate the cellular localization of the contrast agent, as the blooming effect is often too large to appreciate the exact location of the particles in the MR images. Iron oxide nanoparticles are typically classified according to their size, which impacts their magnetic and biological properties. The coating is often dextran, citrate, or a polymer such as polyethylene glycol or polyvinyl alcohol.

Iron oxide-based contrast agents can be reliably detected using a Prussian blue staining, if needed with an amplification step. When using molecularly targeted iron oxides it is difficult to discriminate specific binding from aspecific cellular uptake. Therefore it is preferable to combine the widely applied Prussian blue staining to detect iron with a secondary staining for the molecular target of the CA. Staining with 3,3'-diaminobenzidine (DAB), a commonly used chromogen for immunohistochemical stainings, is widely applied as secondary detection method for a molecular target, in the presence of iron oxides²². However, development of a DAB staining requires a redox reaction to obtain its typical brown color. The redox reaction is performed with a peroxidase enzyme, yet iron oxides may also act as a reducing agent. We tested this hypothesis on aortic arch tissue of ApoE^{-/-} mice that were injected with USPIOs and subsequently sacrificed. We found that a DAB step in the presence of iron oxide nanoparticles leads to false-positive results for the secondary staining and difficulties to discriminate between the presence of the molecular target or merely the iron particle (figure 4A). To circumvent this problem, we tested several other classical staining methods. Double staining of iron oxide particles with Prussian blue and a molecular target with alkaline phosphatase substrate turned out to be the most suitable method for detection of multiple targets without interference of iron oxides with the secondary staining (figure 4B and 4C).

Imaging gene expression

An emerging new imaging field is the use of (MRI) contrast agents that can be activated by the expression of an endogenous receptor or enzyme. Alternatively, reporter genes are used that are co-expressed with the gene of interest. MRI reporter genes are unique among all reporter genes used with the various imaging modalities because they can provide information on gene expression that can be co-registered with anatomic/histological and functional information²³.

This approach, of course purely used for research purposes, is already commonly used in the optical-imaging field, where GFP transgenic mice have been utilized to visualize a myriad of genes²⁴. For MRI, this field is relatively new. A number of candidate reporter genes have previously been used for detection of gene expression by MRI. Several groups have presented candidate MRI-detectable substrates for classical reporter genes, such as the histologically applied β -galactosidase^{25,26} and the enzymes arginine and creatine kinase^{27,28}. The principle of these agents is based on a change in MR relaxivity of the probe after cleavage by the reporter enzyme, leading to a local contrast change in the image. Though potentially very interesting, the sensitivity of these probes is currently too low for routine use.

As an alternative to the use of activatable probes, reporter genes have been proposed to image gene expression directly. For MRI recent advances have allowed the use of genes associated with iron homeostasis such as the transferrin receptor^{29,30}, tyrosinase³¹ and ferritin^{32,33}, resulting in (endogenous) iron accumulation at the site of gene expression, which can be visualized using T2W or T2*W sequences *in vivo*, and Prussian Blue stainings in post-mortem histological material. Obviously, as described above, the presence of high concentrations of iron in the tissue may result in false-positive DAB enhancement of histological stainings.

Outlook

Histological validation of contrast agent accumulation is an essential step in the validation process of a contrast agent. Evaluation of the specificity of targeted contrast agent accumulation to detect atherosclerotic lesions can be challenging because the enhanced permeability of the plaque itself also may lead to significant amounts of non-specific uptake and retention of contrast agents, and the balance between target-specific and aspecific contrast agent enhancement is strongly dependent on the time passed after injection. To discriminate specific uptake from non-specific uptake, the timing of imaging and tissue harvesting after the administration of the contrast agent is of utmost importance to assure that the interpretation of MRI data is not obscured by changes in contrast agent accumulation over time or ambiguity in the histology.

Different mouse models of atherosclerosis ask for different validation solutions. Although this review is written in the context of atherosclerosis, extrapolation of these findings to other tissue types and pathologies is possible as autofluorescence, washing out of particles and chemical interferences are general challenges encountered when working with MRI contrast agents.

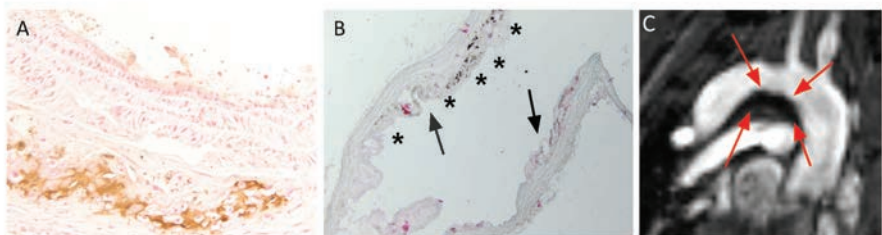


Figure 4 | Staining of USPIO in an atherosclerotic plaque from an ApoE^{-/-} mouse. A: A false positive double staining (both stainings turn brown) for macrophages due to reactivity of USPIO and DAB. Note that the USPIOs and CD68⁺ cells cannot be differentiated from each other in this panel. B: Double staining of USPIO with Prussian Blue and secondary CD68⁺ target with alkaline phosphatase allows visualization of both USPIO and CD68 in the same histological slice. Black arrows indicate the CD68⁺ cells, black asterisks indicate the USPIO. C: T2* weighted MR image of the aortic arch, the red arrows indicate the region with the USPIO induced Blooming effect in the inner curvature of the aortic arch. USPIO: ultra small particle of iron oxide; AF: alkaline phosphatase

The use of contrast agents for the *in vivo* detection of atherosclerotic plaques, either targeted or non-targeted, has so far not reached the clinic. However, molecular MRI is one of the most promising non-invasive screening tools for identification of patients at risk of a clinical event. Before clinical implementation of molecular MRI of atherosclerosis 3 main aspects need to be considered: 1) technical constraints that currently hamper clinical applications, in particular for imaging of the coronary arteries, 2) potential toxic or adverse effects of the *in vivo* use of MR contrast agents and 3) the potential clinical impact in terms of managing strategies to ultimately reduce the occurrence of cardiac events. These translational challenges are enormous, and many of the developed contrast agent will fail to reach the clinic, but the few nanoparticles that so far have reached clinical status show substantial benefit over conventional imaging approaches³⁴. One of the main concerns for the clinical application of MRI contrast agents as diagnostic compound for atherosclerosis is the potential toxicity. Gd-based contrast agents are associated with rare cases of nephrogenic systemic fibrosis (NSF) in patients with renal failure^{35,36}. The exact mechanism of gadolinium-induced skin fibrosis in these patients is unknown, although it is suggested that free gadolinium (Gd-chelates are not 100% stable) may cause changes in fibroblast characteristics. Since the first reports of NSF, clinical guidelines have been adapted and the occurrence has been minimized³⁷.

Lipid-based contrast agents such as micelles and liposomes also pose several challenges, such as instability of the carrier *in vivo*, eventual release of their content including Gd-DTPA, and rapid blood clearance by the reticulo-endothelial system (RES), mostly liver and spleen³⁴. To improve the stability and prevent opsonization by the liver, the surfaces of liposomes and micelles have been coated with hydrophilic and inert polymers, mostly PEG. In turn such non-biodegradable contrast agent components may accumulate in certain organs, mostly in the RES, and may cause potential harm including immune-mediated toxicity, teratogenicity and potentially even carcinogenicity³⁸.

Finally, iron-oxide containing particles are known to accumulate in phagocytic cells and may accumulate in the body for weeks. Iron oxides themselves are considered to be safe, as free iron enters the body's iron storage. The main toxicological concern lies in the molecules that are used to improve the stability and prevent opsonization. Their toxicological profiles need to be assessed in depth before clinical translation is possible.

Clinical impact

Nevertheless, the opportunity to identify noninvasively the vulnerable patients and the vulnerable plaques is of tremendous clinical interest and from available pathophysiological and clinical studies of potential applications of molecular imaging may be foreseen.

Firstly, evaluation of asymptomatic patients classified at intermediate risk by current risk stratification algorithms may be useful to reclassify those with elevated coronary inflammatory activity in whom treatment is desired. Prognostic value and cost-effectiveness need to be compared to other currently applied techniques. Secondly, molecular imaging of atherosclerotic plaques allows a type of personalized medicine, with potential to tailor therapy to the presence/absence of specific targets in individual patients, as is already done in some cancer studies. Molecular imaging may also allow monitoring of the therapeutic efficiency of these drugs or changes in lifestyle. Thirdly, the nanoparticle approach that is central to most molecular imaging developments also allows delivery of drugs, leading to a theragnostic approach of atherosclerosis management.

The key point to understand is that the clinical translation of MRI contrast agents for the diagnosis of atherosclerosis requires a complete understanding of the relationship between the human

body and particle size, composition, formulation, supramolecular structure, chemical reactivity, and biomechanical strength and stability. To advance this knowledge correct histological validation of accumulation patterns is of utmost importance in the pre-clinical stages. Although a full comprehension of the fate of contrast agents *in vivo* is very complex, we do foresee clinical approval of targeted MRI contrast agents albeit in the medium- to long-term future.

CONCLUSION

To successfully implement molecular MRI as a clinical screening tool, it is of utmost importance for the *ex vivo* validation methods to be as efficient and transparent as possible. In this paper we have described various approaches for histological validation of molecular MRI contrast agents. We have also demonstrated several pitfalls that may give confounding or false-positive results, and provided strategies to circumvent these pitfalls. Thus, this paper provides a reference framework for future validation of molecular MRI contrast agents.

Acknowledgements

This work was supported by the European Network of Excellence Diagnostic Molecular Imaging (DIMI, LSHB-CT-2005-512146) to BdA, SB, GS, REP and BtB, the Integrated European Union Project Targeted Delivery of Nanomedicine (MEDITRANS, FP6-2004-NMP-NI-4/IP 026668-2) to BtB, the Netherlands Heart Foundation Grant (NHF, 2006T106 and 2003B249) to BdA and REP, NWO Athena (700.58.80) to LvdW, from NWO VIDI (700.58.42) to GS, from ICIN NELU (074.01) to SB and GP

REFERENCES

- 1 Libby P, Ridker PM, Hansson GK. Inflammation in atherosclerosis: from pathophysiology to practice. *J Am Coll Cardiol* 2009 Dec 1;54(23):2129-38.
- 2 Davies MJ. Stability and instability: two faces of coronary atherosclerosis. The Paul Dudley White Lecture 1995. *Circulation* 1996 Oct 15;94(8):2013-20.
- 3 Libby P, Ridker PM, Maseri A. Inflammation and atherosclerosis. *Circulation* 2002 Mar 5;105(9):1135-43.
- 4 Sary HC, Chandler AB, Dinsmore RE, Fuster V, Glagov S, Insull W, Jr., et al. A definition of advanced types of atherosclerotic lesions and a histological classification of atherosclerosis. A report from the Committee on Vascular Lesions of the Council on Arteriosclerosis, American Heart Association. *Circulation* 1995 Sep 1;92(5):1355-74.
- 5 Corti R, Fuster V, Badimon JJ, Hutter R, Fayad ZA. New understanding of atherosclerosis (clinically and experimentally) with evolving MRI technology in vivo. *Ann N Y Acad Sci* 2001 Dec;947:181-95.
- 6 Matter CM, Stuber M, Nahrendorf M. Imaging of the unstable plaque: how far have we got? *Eur Heart J* 2009 Nov;30(21):2566-74.
- 7 Saraste A, Nekolla SG, Schwaiger M. Cardiovascular molecular imaging: an overview. *Cardiovasc Res* 2009 Sep 1;83(4):643-52.
- 8 Choudhury RP, Aguinaldo JG, Rong JX, Kulak JL, Kulak AR, Reis ED, et al. Atherosclerotic lesions in genetically modified mice quantified in vivo by non-invasive high-resolution magnetic resonance microscopy. *Atherosclerosis* 2002 Jun;162(2):315-21.
- 9 Te Boekhorst BC, Cramer MJ, Pasterkamp G, van Echteld CJ, Doevendans PA. Recent developments and new perspectives on imaging of atherosclerotic plaque: role of anatomical, cellular and molecular MRI Part I and II. *Int J Cardiovasc Imaging* 2010 Apr;26(4):433-45.
- 10 Elster AD, Jackels SC, Allen NS, Marrache RC, Dyke Award. Europium-DTPA: a gadolinium analogue traceable by fluorescence microscopy. *AJNR Am J Neuroradiol* 1989 Nov;10(6):1137-44.
- 11 Zhang S, Zhu X, Chen Z, Cai C, Lin T, Zhong J. Improvement in the contrast of CEST MRI via intermolecular double quantum coherences. *Phys Med Biol* 2008 Jul 21;53(14):N287-N296.
- 12 Frame EM, Uzgiris EE. Gadolinium determination in tissue samples by inductively coupled plasma mass spectrometry and inductively coupled plasma atomic emission spectrometry in evaluation of the action of magnetic resonance imaging contrast agents. *Analyst* 1998 Apr;123(4):675-9.
- 13 van Bochove GS, Paulis LE, Segers D, Mulder WJ, Krams R, Nicolay K, et al. Contrast enhancement by differently sized paramagnetic MRI contrast agents in mice with two phenotypes of atherosclerotic plaque. *Contrast Media Mol Imaging* 2011 Jan;6(1):35-45.
- 14 Mulder WJ, Strijkers GJ, van Tilborg GA, Griffioen AW, Nicolay K. Lipid-based nanoparticles for contrast-enhanced MRI and molecular imaging. *NMR Biomed* 2006 Feb;19(1):142-64.
- 15 van Bochove GS, Paulis LE, Segers D, Mulder WJ, Krams R, Nicolay K, et al. Contrast enhancement by differently sized paramagnetic MRI contrast agents in mice with two phenotypes of atherosclerotic plaque. *Contrast Media Mol Imaging* 2011 Jan;6(1):35-45.
- 16 Kuhlencordt PJ, Gyurko R, Han F, Scherrer-Crosbie M, Aretz TH, Hajjar R, et al. Accelerated atherosclerosis, aortic aneurysm formation, and ischemic heart disease in apolipoprotein E/endothelial nitric oxide synthase double-knockout mice. *Circulation* 2001 Jul 24;104(4):448-54.
- 17 Te Boekhorst BC, Bovens SM, Hellingens WE, van der Kraak PH, van de Kolk KW, Vink A, et al. Molecular MRI of murine atherosclerotic plaque targeting NGAL: a protein associated with unstable human plaque characteristics. *Cardiovasc Res* 2011 Feb 15;89(3):680-8.
- 18 van Tilborg GA, Mulder WJ, van der Schaft DW, Reutelingsperger CP, Griffioen AW, Strijkers GJ, et al. Improved magnetic resonance molecular imaging of tumor angiogenesis by avidin-induced clearance of nonbound bimodal liposomes. *Neoplasia* 2008 Dec;10(12):1459-69.
- 19 Blackwell ML, Farrar CT, Fischl B, Rosen BR. Target-specific contrast agents for magnetic resonance microscopy. *Neuroimage* 2009 Jun;46(2):382-93.
- 20 Higuchi M, Iwata N, Matsuba Y, Sato K, Sasamoto K, Saïdo TC. 19F and 1H MRI detection of amyloid beta plaques in vivo. *Nat Neurosci* 2005 Apr;8(4):527-33.
- 21 Schmitz SA. [Iron-oxide-enhanced MR imaging of inflammatory atherosclerotic lesions: overview of experimental and initial clinical results]. *Rofo* 2003 Apr;175(4):469-76.
- 22 Jaffer FA, Libby P, Weissleder R. Molecular imaging of cardiovascular disease. *Circulation* 2007 Aug 28;116(9):1052-61.
- 23 Gilad AA, Winnard PT, Jr., van Zijl PC, Bulte JW. Developing MR reporter genes: promises and pitfalls. *NMR Biomed* 2007 May;20(3):275-90.
- 24 Hadjantonakis AK, Dickinson ME, Fraser SE, Papaioannou VE. Technicolour transgenics: imaging tools for functional genomics in the mouse. *Nat Rev Genet* 2003 Aug;4(8):613-25.
- 25 Kodibagkar VD, Yu J, Liu L, Hetherington HP, Mason RP. Imaging beta-galactosidase activity using 19F chemical shift imaging of LacZ gene-reporter molecule 2-fluoro-4-nitrophenol-beta-D-galactopyranoside. *Magn Reson Imaging* 2006 Sep;24(7):959-62.
- 26 Louie AY, Huber MM, Ahrens ET, Rothbacher U, Moats R, Jacobs RE, et al. In vivo visualization of gene expression using magnetic resonance imaging. *Nat Biotechnol* 2000 Mar;18(3):321-5.
- 27 Li Z, Qiao H, Lebherz C, Choi SR, Zhou X, Gao G, et al. Creatine kinase, a magnetic resonance-detectable marker gene for quantification of liver-directed gene transfer. *Hum Gene Ther* 2005 Dec;16(12):1429-38.

- 28 Walter G, Barton ER, Sweeney HL. Noninvasive measurement of gene expression in skeletal muscle. *Proc Natl Acad Sci U S A* 2000 May 9;97(10):5151-5.
- 29 Moore A, Basilion JP, Chiocca EA, Weissleder R. Measuring transferrin receptor gene expression by NMR imaging. *Biochim Biophys Acta* 1998 Apr 24;1402(3):239-49.
- 30 Moore A, Josephson L, Bhorade RM, Basilion JP, Weissleder R. Human transferrin receptor gene as a marker gene for MR imaging. *Radiology* 2001 Oct;221(1):244-50.
- 31 Weissleder R, Simonova M, Bogdanova A, Bredow S, Enochs WS, Bogdanov A, Jr. MR imaging and scintigraphy of gene expression through melanin induction. *Radiology* 1997 Aug;204(2):425-9.
- 32 Cohen B, Dafni H, Meir G, Harmelin A, Neeman M. Ferritin as an endogenous MRI reporter for noninvasive imaging of gene expression in C6 glioma tumors. *Neoplasia* 2005 Feb;7(2):109-17.
- 33 Cohen B, Ziv K, Plaks V, Harmelin A, Neeman M. Ferritin nanoparticles as magnetic resonance reporter gene. *Wiley Interdiscip Rev Nanomed Nanobiotechnol* 2009 Mar;1(2):181-8.
- 34 Choi HS, Frangioni JV. Nanoparticles for biomedical imaging: fundamentals of clinical translation. *Mol Imaging* 2010 Dec;9(6):291-310.
- 35 Pedersen M. Safety update on the possible causal relationship between gadolinium-containing MRI agents and nephrogenic systemic fibrosis. *J Magn Reson Imaging* 2007 May;25(5):881-3.
- 36 Bongartz G. Imaging in the time of NFD/NSF: do we have to change our routines concerning renal insufficiency? *MAGMA* 2007 Apr;20(2):57-62.
- 37 Maurer M, Heine O, Wolf M, Durmus T, Wagner M, Hamm B. Tolerability and diagnostic value of gadoteric acid in the general population and in patients with risk factors: results in more than 84,000 patients. *Eur J Radiol* 2012 May;81(5):885-90.
- 38 Nanotechnology: small matter, many unknowns. *Swiss Re* 2004.

MOUSE APPE READING REMAIN VALIDATION
VULNERABILITY PROCESSES PHENOTYPE MICRO
MACROPHAGES TREATMENT EVALUATION
PLAQUE MODEL
VULNERABILITY
ATHEROSCLEROTIC WALL THICKENING EARLY ATHEROSCLEROSIS
CARDIOVASCULAR
THERAPEUTIC AGENTS DEVELOPMENT
DISEASE LOAD RISK MODEL
INFLAMMATORY
MRI USE
ENDOTHELIAL LESION PHENOTYPIC
ACTIVATION INTEREST PASSIVE CELL
TARGETS VESSEL WALL

Cardiovascular disease (CVD) is the number one cause of death globally and is expected to remain so according to numbers of the World Health Organization¹. CVD imposes a significant healthcare burden, particularly in the industrialized countries. The single most important contributor to the growing burden of CVD is atherosclerosis, a progressive inflammatory disease characterized by the accumulation of lipids and fibrous elements in the large and medium-sized arteries^{2, 3}. Atherosclerosis is considered to be a multifactorial disease in which lipids and inflammation play major roles. Noninvasive screening for subclinical atherosclerosis as well as detection of high-risk atherosclerotic plaques in an established population of cardiovascular patients is important for patient management. This thesis presented and discussed the validation of a variety of pre-clinical MRI contrast agents that can be used for the early detection and differentiation of atherosclerotic plaque in murine models of atherosclerosis.

Molecular imaging

As recently as the mid-1990s, a new field in medical imaging was emerging. The term molecular imaging was adopted to describe the noninvasive characterization of biological processes at the molecular (and cellular) level. The progress of this field was driven by contemporary developments in multiple disciplines, including genomics, proteomics, molecular biology, imaging and nanotechnology. The promise of molecular imaging incorporates both early as well as "at risk" disease detection. Molecular imaging has gained increasing interest in the research field of cardiovascular diseases the last couple of years, mainly because atherosclerotic plaque composition turned out to be important as a predictor for clinical events, even more so than the degree of stenosis⁴.

Molecular MRI offers the potential to image events at the cellular and subcellular level which has, depending on the target of choice, added value over traditional contrast agents⁵⁻⁷. The introduction of targeted MR contrast agents has enabled the imaging of relatively sparsely expressed biological targets *in vivo*. During the development of atherosclerotic plaques, many potential biomarkers, such as adhesion molecules [vascular cell adhesion molecules (VCAMs), intercellular adhesion molecules (ICAMs), selectins], macrophages and their scavenger receptors, matrix metalloproteinases (MMPs), oxidized low-density lipoprotein (oxLDL), $\alpha_v\beta_3$ integrin, extracellular matrix, and fibrin, are up-regulated⁴. In *chapter 2* the current development status of vulnerable atherosclerotic plaque detection with MRI contrast agents is discussed. The review deals with the interplay between the complex vascular biology involved in plaque vulnerability and the potential use of MR contrast agents. The identification of suitable target-ligand combinations specific for a vulnerable plaque (or other pathology) is complex. At this point multiple MRI contrast agents have been developed that allow the detection of different markers and stages in atherosclerosis.

In this thesis, we investigated three main targeting approaches: passive accumulation in macrophages (*chapter 3, 4, 7 and 8*), active targeting towards a macrophage marker such as the scavenger receptor AI (*chapter 5*) or VCAM-1 (*chapter 6*), and endothelial targeting using markers for endothelial activation, namely VCAM-1 (*Chapter 6*) and E-selectin (*Chapter 7*).

Imaging of endothelial activation

Dysfunctional endothelium is one of the first and crucial pathophysiological factors in atherosclerosis, causing increased permeation of macromolecules such as lipoproteins, increased expression of chemotactic molecules (for example, monocyte chemotactic protein 1) and adhesion molecules (for example, intercellular adhesion molecule 1 (ICAM-1) and vascular cell adhesion molecule 1 (VCAM-1), as well as E-selectin and P-selectin), and enhanced recruitment

and accumulation of monocytes⁸. Markers of endothelial activation are present on the atherosclerotic vessel wall and therefore easily reached by contrast agents. Some adhesion molecules are differentially expressed during atherosclerotic plaque development. In *chapter 7* E-selectin expression was shown to increase with atherosclerotic plaque progression and targeted USPIO allowed to visualize plaque progression. VCAM-1 on the other hand was in *chapter 6* shown to decrease with plaque progression. VCAM-1 USPIO imaging short after injection thus mainly allowed visualizing the early lesion.

Macrophage imaging

One of the main points of interest in the field of molecular imaging of atherosclerosis are rupture-prone atherosclerotic lesions. As inflammatory processes are involved in all stages of atherosclerotic lesion development and the inflammatory status of the plaque is closely associated with plaque vulnerability, inflammatory cells and their derivatives are the primary targets for vulnerable plaque imaging⁵. One of the most obvious cells to focus on is the plaque macrophage. Macrophages form the most abundantly present inflammatory cell in the atherosclerotic plaque. Moreover, the infiltration of monocytes and their differentiation into macrophages and functional phenotype (i.e. M1/M2) are considered crucial hallmarks in atherogenesis^{9,10}. In mouse models it has been shown that in the absence of monocyte and macrophage migration into the vessel wall, atherosclerosis development is delayed, even in the presence of severe hyperlipidemia¹¹. In man, high macrophage content in plaques is even associated with vulnerability to rupture^{12,13}. In *chapter 6 and 7* treatment with atorvastatin and fenofibrate led to a decrease in endothelial activation together with a reduction in plaque macrophage load. Treatment with fenofibrate also led to a decrease in endothelial activation, however did not result in a reduction of the macrophage load, a phenomenon observed by passive targeting the macrophage pool by late USPIO imaging.

Macrophages as markers for vulnerable plaque

Macrophage phenotypic polarization towards M1 or M2-type macrophages has recently become a major point of interest as the macrophage phenotype plays a role in the fate of an atherosclerotic lesion. Classically activated macrophages (or M1) and alternatively activated macrophages (or M2) are two extremes representing inflammatory and reparative macrophage phenotypes¹⁴. The phenotypic change of plaque macrophages might depend upon the type (innate or adaptive) of immune cells infiltrating a developing atherosclerotic lesion. The initial M2 macrophage phenotype present at the site of inflammation develops independently of the adaptive immune system whereas the maintenance of the M2 macrophage phenotype requires IL-4-producing T cells, in the absence of which M2 macrophages normally switch to the M1 phenotype¹⁴. Further extrapolation of this mechanism to atherosclerosis suggests that the pro-inflammatory T helper cell type 1 (Th1) phenotype might trigger the M2-M1 phenotypic switch in advanced atherosclerotic plaques⁹. In a therapeutic perspective, controlling the local milieu within atherosclerotic plaques *in vivo* will be difficult to achieve due to the myriad of factors implicated in the balance between M1 and M2 macrophages. However, several recent studies have suggested that pharmacological treatments may skew macrophage polarization toward the M2 phenotype, thereby stabilizing atherosclerotic lesions^{10,15}.

In the current thesis we applied different clinically approved therapies to validate the MRI contrast agents. One of the results in this thesis is the dual imaging of macrophage load and E-selectin expression on the endothelium described in *chapter 7*. Treatment of ApoE^{-/-} mice with atorvastatin or fenofibrate resulted in both cases in less advanced plaques; atorvastatin treated mice had smaller plaques with less E-selectin as well as macrophages. Fenofibrate-treated mice on the

other hand had plaques that had a lower E-selectin expression however practically unchanged macrophage load. Both drugs are known to exert their actions in apoE^{-/-} mice mainly through their pleiotrophic effects on the immune system, the lipid regulating effect does not occur in these mice. This characteristic of statins has also been used in *chapter 6* where we differentiate plaque stages based on endothelium and intraplaque VCAM-1 expression.

The exact mechanism behind this difference in treatment effect between statins and fibrates remains speculative yet it is tempting to think the drugs either reduce the pool of M1 macrophages or induce a phenotypic change. Once these mechanisms of action are known, imaging of macrophage load may have clinical potential to monitor treatment response.

Mouse models and techniques for vulnerable plaque imaging

Contrast agents are developed to target molecules or cells known from human studies to be involved in plaque rupture and vulnerability. For this purpose a mouse model, which develops rupture-prone plaques, would be desirable, but unfortunately mouse physiology does not allow for the development of real vulnerable plaques. There have been few descriptions of myocardial infarction or stroke in mice as a consequence of atherosclerotic lesion formation, despite the presence of extensive lesions that display characteristics similar to that of “vulnerable” lesions in humans. Several “surrogate” mouse models have been developed trying to mimic the development of a vulnerable plaque. In the current work we chose to use the most commonly applied mouse models of atherosclerosis, i.e. ApoE^{-/-} and LDLr^{-/-} based athero-prone animals, because of their reproducible atherosclerotic lesion development with expression patterns comparable to humans. For the development and validation of contrast agents to detect atherosclerotic lesions these models have proven their use.

Despite the lack of vulnerable mouse models, mice remain the preclinical model of choice because of the wide array of transgenic models available. The studies in this thesis required dedicated high-resolution MRI sequences to visualize the murine atherosclerotic vessel wall. The small size of mouse arteries and their close proximity to the heart cause unpredictable flow artifacts, motion of the thin artery wall and problems with flow suppression in the presence of a circulating contrast agent. In *chapter 3* we therefore validated the value of retrospective-gated cine MRI of the aortic arch for atherosclerotic plaque detection and assessment of wall stiffness after injection of both T1 and T2*contrast agents. The retrospective-gated cine MRI provides a robust and simple way to detect and quantify contrast enhancement in atherosclerotic plaques in the aortic wall of ApoE^{-/-} mice.

For validation purposes, it is crucial that nanoparticle accumulation in the plaque, cellular association and localization can be assessed by ex vivo immunohistochemistry or fluorescence microscopy of tissue sections. In *chapter 9* various methods are described that are available, including the pitfalls that may give confounding or false-positive results, for histological evaluation of MRI contrast agent accumulation such as lipid-based nanoparticles and iron oxide particles.

Theranostics

Particles that integrate diagnostic imaging and therapeutic components, or “theragnostic” agents, gained much recent interest as a valuable advance for drug delivery^{16,17}. Although this strategy is still in its infancy for CVD, it has numerous potential advantages, which are being extensively investigated in the field of cancer nanomedicine. Combining a diagnostic imaging moiety with a targeted therapeutic nanoparticle allows for precise, temporal and spatial monitoring of the therapeutic agent as well as treatment outcomes. Its advantages include — but are not limited to — improving drug pharmacokinetics and enabling the therapeutic use of drugs that exhibit certain

drawbacks, such as low water-solubility, poor bioavailability, fast metabolism, limited specificity or severe adverse effects^{18,19}. One of the first clinically approved nanomedicinal therapies was a liposomal formulation of doxorubicin, a cytotoxic drug used for cancer chemotherapy. This formulation, branded Doxil, was approved by the US Food and Drug Administration in 1995 for the treatment of Kaposi's sarcoma and later approved for other cancer types²⁰. Subsequently, several other nanomedicinal therapeutics have been approved. Although still in its infancy, nanomedicine is likely to have a substantial role in the management of CVD in general and atherosclerosis in particular²¹. In *chapter 8* we describe the *in vitro* and *in vivo* validation of Gd-loaded micelles incorporating rosiglitazone to allow passive delivery of the drug into atherosclerotic lesions. It was of particular interest to use rosiglitazone in a theragnostic context as the drug was recently withdrawn from the market owing to severe cardiac side effects in a small subset of patients. The drug is known to exert its anti-atherosclerotic action independent of its metabolic effects, which made us postulate that local delivery could be beneficial. Significant anti-atherosclerotic effects were observed upon treatment with rosiglitazone micelles, holding promise to apply the drug in the treatment of atherosclerosis.

Perspectives

One of the aims of molecular imaging of atherosclerosis is to provide a means for the determination of plaque vulnerability and subsequent risk for plaque rupture. Ongoing developments in molecular biology have resulted in the identification of numerous molecular targets that allow for the identification and staging of atherosclerosis. It is generally accepted that plaque rupture has a multi-factorial origin. In this respect, MRI may in the future become the imaging modality of choice since it can provide information on plaque morphology, hemodynamic conditions, as well as on molecular processes. MRI is already frequently applied in all fields of cardiovascular research and in clinical evaluation. The increasing use is mainly due to its non-invasive nature and ability to differentiate between all sorts of tissues. The main drawback is the relatively low sensitivity for contrast agents, which is decreasing even more at higher magnetic fields. However, atherosclerosis is one of few applications where targets are readily accessible from the blood stream, allowing the use of large nanoparticles with a high payload of contrast moieties to compensate for the lack of sensitivity, as was shown in this thesis.

Of all the suggested markers for vulnerability, three appear to give robust pre-clinical results that should translate to the clinic given their potential to recognize efficiently vulnerability markers, those are fibrin, integrins and VCAM-1, with a good toxicological and biodistribution profile²²⁻²⁶ and *chapter 6*. It is important to point out that these molecules are not unique to atherosclerosis or cardiovascular diseases, but they are present at increased levels under these disease conditions as compared to disease free conditions.

With the development of targeted contrast agents to visualize the vulnerable atherosclerotic plaque, MRI may become even more important in the future, when clinical decision making is based on atherosclerotic plaque composition and not only on the degree of stenosis. An added value could most definitely be found in combined imaging techniques, such as MRI/SPECT and MRI/PET, in which the anatomical detail of MRI and high sensitivity of PET and SPECT tracers can be combined. This field is currently developing very fast both regarding the imaging equipment as well as the development of nanoparticles.

Unfortunately, many of the exciting preclinical findings with nanoparticles in animal models of atherosclerosis have not progressed from the developmental phase, as is often the case in drug development. One of the reasons for this is the accelerated development of atherosclerosis in animal models, thereby creating atherosclerotic lesions with somewhat different characteristics

to those found in humans²⁷. Moreover the physiology and lipid metabolism are different to those in humans.

There is also a need to further work on the development of less toxic and immunogenic contrast agents. A major set-back for the molecular imaging field was the withdrawal of a number of iron oxide nanoparticles from the market around 2008-2009, mainly because of marketing reasons. As a result approval of targeted agents for clinical use also became more unlikely. These limitations are among the current reasons that have motivated several groups to issue recommendations for accelerating the translation of nanoparticles into the clinic^{28, 29}. Nevertheless, the use of nanoparticles in cardiovascular disease has nowadays already led to a better understanding of atherosclerosis, the role of imaging and the evaluation of pharmacotherapy, and will continue to do so in the near future.

CONCLUSION

In this thesis several contrast agents to detect and stage atherosclerotic lesions were validated. I envision that molecular imaging in 20 years from now is likely to play a pivotal role in the evaluation, risk stratification, and management of patients with cardiovascular disease. In patients in the chronic phase of the disease and in the prevention of plaque build-up, the injection of nanoparticles for prolonged periods of time is unrealistic and impractical as the disease may remain asymptomatic. Screening for asymptomatic atherosclerotic lesions to prevent future plaque rupture has not yet been proven to be beneficial in patients, but it is hoped that the accurate identification of patients with an impending risk of cardiovascular events can be achieved using molecular imaging techniques³⁰. Targeted molecular MRI in combination with more conventional physiological imaging will allow a more "personalized" approach to the management of cardiac disease. The use of molecular imaging for the evaluation of the early molecular and cellular events associated with cardiovascular disease will allow early detection of disease and potentially improve patient outcome. The non-invasive *in vivo* evaluation of molecular and cellular processes could potentially also serve as endpoints for all therapies whether they are pharmacological, surgical, or even molecular targeted therapeutics.

REFERENCES

1. Lopez AD, Mathers CD, Ezzati M, Jamison DT, Murray CJ. Global and regional burden of disease and risk factors, 2001: systematic analysis of population health data. *Lancet* 2006;367(9524):1747-1757.
2. Falk E. Pathogenesis of atherosclerosis. *J Am Coll Cardiol* 2006;47(8 Suppl):C7-12.
3. Virmani R, Burke AP, Farb A, Kolodgie FD. Pathology of the vulnerable plaque. *J Am Coll Cardiol* 2006;47(8 Suppl):C13-C18.
4. Choudhury RP, Fuster V, Fayad ZA. Molecular, cellular and functional imaging of atherothrombosis. *Nat Rev Drug Discov* 2004;3(11):913-925.
5. Briley-Saebo KC, Mulder WJ, Mani V, Hyafil F, Amirbekian V, Aguinaldo JG, Fisher EA, Fayad ZA. Magnetic resonance imaging of vulnerable atherosclerotic plaques: current imaging strategies and molecular imaging probes. *J Magn Reson Imaging* 2007;26(3):460-479.
6. Chen W, Cormode DP, Fayad ZA, Mulder WJ. Nanoparticles as magnetic resonance imaging contrast agents for vascular and cardiac diseases. *Wiley Interdiscip Rev Nanomed Nanobiotechnol* 2010.
7. Cormode DP, Skajaa T, Fayad ZA, Mulder WJ. Nanotechnology in medical imaging: probe design and applications. *Arterioscler Thromb Vasc Biol* 2009;29(7):992-1000.
8. Hansson GK. Inflammation, atherosclerosis, and coronary artery disease. *N Engl J Med* 2005;352(16):1685-1695.
9. Khallou-Laschet J, Varthaman A, Fornasa G, Compain C, Gaston AT, Clement M, Dussiot M, Levillain O, Graff-Dubois S, Nicoletti A, Caligiuri G. Macrophage plasticity in experimental atherosclerosis. *PLoS One* 2010;5(1):e8852.
10. Bouhlef MA, Derudas B, Rigamonti E, Dievart R, Brozek J, Haulon S, Zawadzki C, Jude B, Torpier G, Marx N, Staels B, Chinetti-Gbaguidi G. PPARgamma activation primes human monocytes into alternative M2 macrophages with anti-inflammatory properties. *Cell Metab* 2007;6(2):137-143.
11. Smith JD, Trogan E, Ginsberg M, Grigaux C, Tian J, Miyata M. Decreased atherosclerosis in mice deficient in both macrophage colony-stimulating factor (op) and apolipoprotein E. *Proc Natl Acad Sci U S A* 1995;92(18):8264-8268.
12. Kolodgie FD, Gold HK, Burke AP, Fowler DR, Kruth HS, Weber DK, Farb A, Guerrero LJ, Hayase M, Kutys R, Narula J, Finn AV, Virmani R. Intraplaque hemorrhage and progression of coronary atheroma. *N Engl J Med* 2003;349(24):2316-2325.
13. MacNeill BD, Jang IK, Bouma BE, Iftimia N, Takano M, Yabushita H, Shishkov M, Kauffman CR, Houser SL, Aretz HT, DeJoseph D, Halpern EF, Tearney GJ. Focal and multi-focal plaque macrophage distributions in patients with acute and stable presentations of coronary artery disease. *J Am Coll Cardiol* 2004;44(5):972-979.
14. Loke P, Gallagher I, Nair MG, Zang X, Brombacher F, Mohrs M, Allison JP, Allen JE. Alternative activation is an innate response to injury that requires CD4+ T cells to be sustained during chronic infection. *J Immunol* 2007;179(6):3926-3936.
15. Odegaard JI, Chavla A. Alternative macrophage activation and metabolism. *Annu Rev Pathol* 2011;6:275-297.
16. Godin B, Sakamoto JH, Serda RE, Grattoni A, Bouamrani A, Ferrari M. Emerging applications of nanomedicine for the diagnosis and treatment of cardiovascular diseases. *Trends Pharmacol Sci* 2010;31(5):199-205.
17. Sakamoto JH, van de Ven AL, Godin B, Blanco E, Serda RE, Grattoni A, Ziemys A, Bouamrani A, Hu T, Ranganathan SI, De RE, Martinez JO, Smid CA, Buchanan RM, Lee SY, Srinivasan S, Landry M, Meyn A, Tasciotti E, Liu X, Decuzzi P, Ferrari M. Enabling individualized therapy through nanotechnology. *Pharmacol Res* 2010;62(2):57-89.
18. Farokhzad OC, Langer R. Impact of nanotechnology on drug delivery. *ACS Nano* 2009;3(1):16-20.
19. Zhang L, Gu FX, Chan JM, Wang AZ, Langer RS, Farokhzad OC. Nanoparticles in medicine: therapeutic applications and developments. *Clin Pharmacol Ther* 2008;83(5):761-769.
20. Davis ME, Chen ZG, Shin DM. Nanoparticle therapeutics: an emerging treatment modality for cancer. *Nat Rev Drug Discov* 2008;7(9):771-782.
21. Cyrus T, Zhang H, Allen JS, Williams TA, Hu G, Caruthers SD, Wickline SA, Lanza GM. Intramural delivery of rapamycin with alphavbeta3-targeted paramagnetic nanoparticles inhibits stenosis after balloon injury. *Arterioscler Thromb Vasc Biol* 2008;28(5):820-826.
22. Nahrendorf M, Jaffer FA, Kelly KA, Sosnovik DE, Aikawa E, Libby P, Weissleder R. Noninvasive vascular cell adhesion molecule-1 imaging identifies inflammatory activation of cells in atherosclerosis. *Circulation* 2006;114(14):1504-1511.
23. Spuentrup E, Botnar RM, Wiethoff AJ, Ibrahim T, Kelle S, Katoh M, Ozgum N, Nagel E, Vymazal J, Graham PB, Gunther RW, Maintz D. MR imaging of thrombi using EP-2104R, a fibrin-specific contrast agent: initial results in patients. *Eur Radiol* 2008;18(9):1995-2005.
24. Winter PM, Caruthers SD, Kassner A, Harris TD, Chinen LK, Allen JS, Lacy EK, Zhang H, Robertson JD, Wickline SA, Lanza GM. Molecular imaging of angiogenesis in nascent Vx-2 rabbit tumors using a novel alpha(nu)beta3-targeted nanoparticle and 1.5 tesla magnetic resonance imaging. *Cancer Res* 2003;63(18):5838-5843.
25. Winter PM, Caruthers SD, Yu X, Song SK, Chen J, Miller B, Bulte JW, Robertson JD, Gaffney PJ, Wickline SA, Lanza GM. Improved molecular imaging contrast agent for detection of human thrombus. *Magn Reson Med* 2003;50(2):411-416.
26. Winter PM, Neubauer AM, Caruthers SD, Harris TD, Robertson JD, Williams TA, Schmieder AH, Hu G, Allen JS, Lacy EK, Zhang H, Wickline SA, Lanza GM. Endothelial alpha(v)beta3 integrin-targeted fumagillin nanoparticles inhibit angiogenesis in atherosclerosis. *Arterioscler Thromb Vasc Biol*

- 2006;26(9):2103-2109.
27. Bentzon JF, Falk E. Atherosclerotic lesions in mouse and man: is it the same disease? *Curr Opin Lipidol* 2010;21(5):434-440.
 28. Buxton DB, Antman M, Danthi N, Dilsizian V, Fayad ZA, Garcia MJ, Jaff MR, Klimas M, Libby P, Nahrendorf M, Sinusas AJ, Wickline SA, Wu JC, Bonow RO, Weissleder R. Report of the National Heart, Lung, and Blood Institute working group on the translation of cardiovascular molecular imaging. *Circulation* 2011;123(19):2157-2163.
 29. Choi HS, Frangioni JV. Nanoparticles for biomedical imaging: fundamentals of clinical translation. *Mol Imaging* 2010;9(6):291-310.
 30. Muntendam P, McCall C, Sanz J, Falk E, Fuster V. The BioImage Study: novel approaches to risk assessment in the primary prevention of atherosclerotic cardiovascular disease--study design and objectives. *Am Heart J* 2010;160(1):49-57.





Appendix

Summery

Samenvatting

Curriculum Vitae

Publications

Dankwoord

SUMMARY

Molecular imaging has gained increasing interest in the research of cardiovascular diseases the last couple of years, mainly since it became apparent that atherosclerotic plaque composition is an important predictor for clinical events, even more so than the degree of (luminal) stenosis. Molecular MRI holds great potential for detection of different stages of atherosclerosis and differentiation of vulnerable lesions. Its application potential will depend on comprehensive knowledge of the detection possibilities and behavior of targeted and untargeted contrast agents *in vivo*.

To begin to address this, in **chapter 2** the current development status of (vulnerable) atherosclerotic plaque detection with MRI contrast agents is discussed.

In this thesis, we investigated three main targeting approaches: 1) passive accumulation in macrophages (**chapter 3, 4, 7 and 8**), 2) active targeting towards the macrophage using scavenger receptor AI (**chapter 5**) and VCAM-1 (**chapter 6**) targeted USPIOs, and 3) endothelial targeting using markers for endothelial activation, namely VCAM-1 (**Chapter 6**) and E-selectin (**Chapter 7**).

In **chapter 3** we first validated the value of retrospective-gated CINE MRI of the aortic arch for atherosclerotic plaque detection and assessment of wall stiffness after injection of both T1 and T2*contrast agents. The retrospective-gated cine MRI provided a robust and simple way to detect and quantify contrast enhancement in atherosclerotic plaques in the aortic wall of ApoE^{-/-} mice.

When using (targeted) contrast agents it is important, for correct interpretation of the data, to know their pharmacokinetic and pharmacodynamic properties. In **chapter 4** the *in vivo* behavior of paramagnetic micelles and liposomes was assessed in atherosclerotic mice for several days. This time course illustrates that paramagnetic micelles and liposomes are able to accumulate in atherosclerotic plaques, yet have a complex kinetic behavior when followed for longer periods of time.

Scavenger receptor-AI (SR-AI) is highly expressed by lesional macrophages and linked to an effective internalization machinery. In **chapter 5** evidence is given that SR-AI targeted molecular imaging of USPIO holds great promise for *in situ* detection of inflammatory, potentially vulnerable, plaques in manifest atherosclerosis.

In **chapter 6** the targeting potential of VCAM-1 is explored using VCAM-1 targeted USPIOs. Early stage atherosclerotic plaques showed the largest contrast change at 1.5 hours after VCAM-1 USPIO injection. The reverse was true for advanced lesions: the largest contrast change was observed at 6 hours after injection of VCAM-1 USPIO. The ratio between early and late enhancement provides a reliable measure of plaque progression.

In **chapter 7** E-selectin expression was shown to increase with atherosclerotic plaque progression and targeted USPIO allowed to visualize stages of plaque progression.

In **chapter 8** we describe the preliminary results of the *in vitro* and *in vivo* validation of Gd-loaded

micelles incorporating rosiglitazone to allow passive delivery of the drug into atherosclerotic lesions. ApoE^{-/-} and ApoE^{-/-}-eNOS^{-/-} mice treated with rosiglitazone had significantly smaller atherosclerotic lesions without the occurrence of the classical cardiac side effects often observed upon rosiglitazone treatment.

In **chapter 9** the histological validation of several contrast agents (targeted and untargeted) in murine models of atherosclerosis is described. The evaluation of tissue accumulation of contrast agents is very important, however choosing the correct histological evaluation method might be of similar importance, to rule out false-positive or negative results.

In **Chapter 10** the results described in this thesis are discussed and I speculated on the future perspectives of molecular MRI to detect atherosclerotic lesions.

In conclusion, the availability and rapid development of several MRI contrast agents is now expected to accelerate atherosclerosis research and offers a clinically relevant research tool for human disease prediction.

SAMENVATTING

Bij atherosclerose, ook wel slagaderverkalking genoemd, veranderen de kenmerken van de vaatwand als gevolg van een ontstekingsproces. Er ontstaan verdikkingen, zogenaamde plaques, in de vaatwand met ophopingen aan vetstoffen en cellen van het immuunsysteem. Sommige plaques kunnen scheuren, de zogenaamde kwetsbare plaques, en daardoor voor klinische problemen zorgen. De grootte en dikte van plaques kan met verschillende beeldvormende technieken goed vastgesteld worden. Deze parameters zijn echter een slechte voorspeller voor plaque ruptuur. Moleculaire MRI is een veelbelovende techniek waarbij gebruik gemaakt wordt van moleculaire eigenschappen van plaques voor de detectie van verschillende stadia van atherosclerose en het opsporen van plaques die kunnen ruptureren. Om verschillende plaques te onderscheiden, zonder operatief ingrijpen, hebben wij contrastmiddelen ontwikkeld die in de bloedbaan geïnjecteerd kunnen worden en vervolgens hechten aan een molecuul dat kenmerkend is voor een bepaald plaque type.

In dit proefschrift beschrijf ik de preklinische ontwikkeling van verschillende contrastmiddelen waarbij 3 benaderingen gevolgd zijn om plaques te visualiseren in atherosclerotische muizen: 1) passieve ophoping van contrastmiddelen in macrofagen (**hoofdstuk 3, 4, 7 en 8**), 2) actieve binding van macrofagen door contrastmiddelen gericht tegen scavenger receptor AI (**hoofdstuk 5**), VCAM-1 (**hoofdstuk 6**) gerichte ijzeroxide deeltjes (USPIO), en 3) actieve beeldvorming van het endotheel aan de binnenkant van een bloedvat met VCAM-1 (**hoofdstuk 6**) en E-selectine (**hoofdstuk 7**). We onderscheiden hiermee vroege van meer gevorderde plaques zonder alleen naar de grootte en dikte van de plaque te kijken zoals tot op heden in de kliniek gedaan wordt.

In **hoofdstuk 2** wordt de huidige literatuur kennis besproken van de MRI contrastmiddelen die ontwikkeld zijn om plaques te detecteren.

Hoofdstuk 3 beschrijft de waarde van een MRI techniek waarbij opgenomen beelden achteraf toegekend worden aan een fase van de hartslag om zowel atherosclerotische plaques te detecteren na contrastmiddel injectie als de elasticiteit van de vaatwand te bestuderen.

Het gedrag van (gerichte) contrastmiddelen na injectie zoals de tijd waarin een middel in de bloedstroom aanwezig blijft, ophoping in organen, is erg belangrijk voor de juiste interpretatie van resultaten. In **hoofdstuk 4** is het gedrag van vetachtige contrastmiddelbolletjes van verschillende groottes (micellen en liposomen) gedurende een week bestudeerd. De tijdscurve illustreert dat dit soort contrastmiddelen ophopen in atherosclerotische plaques maar tevens een complex gedragspatroon hebben.

Scavenger receptor AI (SR-AI) is een eiwit dat hoog tot expressie komt op immuuncellen in de plaque, de macrofagen. Moleculaire beeldvorming met USPIO gericht tegen SR-AI in **hoofdstuk 5** toont aan dat deze geschikt zijn om plaques en potentieel kwetsbare plaques op te sporen.

In **hoofdstuk 6** wordt het gebruik van USPIO gericht tegen VCAM-1 beschreven. VCAM-1 komt op de vaatwand tot expressie in vroege plaques maar komt op in vergevorderde plaques ook tot expressie om macrofagen en gladde spiercellen binnenin de plaque. Door zowel relatief kort als laat na injectie van het contrastmiddel MRI beelden te maken van de aortaboog en halsslagader van atherosclerotische muizen kunnen vroege en meer gevorderde plaques van elkaar onderscheiden worden.

In **hoofdstuk 7** worden verschillende stadia van plaque progressie in beeld gebracht met E-selectine gerichte USPIO. De expressie van E-selectine neemt gradueel toe op de vaatwand van ontwikkelende plaques. Het contrastmiddel signaal van E-selectine gerichte USPIO vertoont dezelfde trend.

In **hoofdstuk 8** beschrijf ik de preliminaire resultaten van de validatie van Gd-micellen geladen met het medicijn rozigitazone voor de lokale behandeling van atherosclerose door de passieve ophoping van deze micellen in de plaque.

In **hoofdstuk 9** worden de verschillende histologische validatie technieken beschreven om contrastmiddelen toegepast in muizen met atherosclerose te detecteren. Het komt erg nauw de juiste techniek te kiezen afhankelijk van het soort contrastmiddel en het soort weefsel om zowel vals-positieve als vals-negatieve resultaten te voorkomen.

Tot slot, in **hoofdstuk 10** bediscussieer ik de resultaten die in dit proefschrift beschreven zijn en speculeer ik over de toekomst van moleculaire MRI om atherosclerotische plaques te detecteren.

CURRICULUM VITAE

Brigit den Adel was born on 14 July 1981 in Rotterdam, the Netherlands. She grew up in Rotterdam and Schiedam. In 1999 she graduated (gymnasium) from the Scholengemeenschap Spieringshoek in Schiedam and went for a year to a high school in France where she graduated from lycée Beaussier in La Seyne sur Mer. In 2000, she started her study Biomedical Sciences at the University of Leiden.

During her studies she performed first an internship in the department of tumor immunology of the Leiden University Medical Center under supervision of Dr. G. van Mierlo and prof. Dr. C. Melief. During her master she became interested in cardiovascular disease. Her final research project was performed at the department of Cardiology of the Leiden University Medical Center under the supervision of Prof. Dr. A. van der Laarse and Drs. M. Hessel. Brigit graduated in April 2006.

From March 2006 till September 2007 she worked at the department for Molecular and Cellular Medicine at Leuven University in Belgium as a research associate. In Leuven she studied oxygen signaling in the cardiovascular system, under the supervision of Prof. Dr. P. Carmeliet.

In October 2007 she joined the group of Prof. Dr. Rob Poelmann and started her PhD project at the department of Anatomy and Embryology on a Dutch Heart Foundation project "Molecular MRI of vulnerable plaques". During her PhD she studied the characteristics of several MRI contrast agents and their potential to detect atherosclerotic lesions. The results of these studies are presented in this thesis.

In November 2012, Brigit started working as a post-doc in the department of Pathology of the Amsterdam Medical Center. Brigit is continuing her research on molecular imaging of atherosclerotic lesions in the group of Prof. Dr. Mat Daemen.



PUBLICATIONS

den Adel B, van der Graaf LM, Que I, Strijkers GJ, Löwik CW, Poelmann RE, van der Weerd L. Contrast enhancement by lipid-based MRI contrast agents in mouse atherosclerotic plaques; a longitudinal study.

Contrast Media Mol Imaging. 2013 Jan;8(1):63-71.

den Adel B, van der Graaf LM, Strijkers GJ, Lamb HJ, Poelmann RE, van der Weerd L. Self-gated CINE MRI for combined contrast-enhanced imaging and wall-stiffness measurements of murine aortic atherosclerotic lesions.

PLoS One. 2013 in press

den Adel B, Daemen MJ, Poelmann RE and van der Weerd L.

Molecular MRI for the possible detection of vulnerable plaques – where do we stand?

ATVB 2013, in press

den Adel B*, Bovens SM*, Boekhorst BT, Strijkers GJ, Poelmann RE, van der Weerd L, Pasterkamp G. Histological validation of iron-oxide and gadolinium based MRI contrast agents in experimental atherosclerosis: The do's and don't's.

Atherosclerosis. 2012 Dec; 225(2):274-80.

Segers ME, **den Adel B**, van der Graaf LM, Gonzalez W, Raynal I, de Winther M, Poelmann RE, van Berkel TJC, van der Weerd L and Biessen E.

Scavenger receptor A1 targeted contrast agents show improved T2-weighted Magnetic Resonance Imaging signal in atherosclerotic lesions.

ATVB, under revision.

Verhaart I, van Duijn RJ, **den Adel B**, Roest AA, Verschuren JG, Aartsma-Rus A, van der Weerd L.

Assessment of cardiac function in three Mouse dystrophinopathies by Magnetic Resonance Imaging.

Neuromuscular Dis. 2011 May;22(5):418-26.

Speelman L, Akyildiz AC, **den Adel B**, Wentzel JJ, van der Steen AF, Virmani R, van der Weerd L, Jukema JW, Poelmann RE, van Brummelen EH, Gijsen FJ.

Initial stress in biomechanical models of atherosclerotic plaques.

J. Biomech. 2011 Sept 2;44(13):2376-82.

Hessel M, Steendijk P, **den Adel B**, Schutte C, van der Laarse A.

Pressure overload-induced right ventricular failure is associated with re-expression of myocardial tenascin-C and elevated plasma tenascin-C levels.

Cell Physiol. Biochem. 2009; 24(3-4):201-10.

Umar S, Bax JJ, Klok M, van Bommel RJ, Hessel MH, **den Adel B**, Bleeker GB, Henneman MM, Atsma DE, van der Wall EE, Schalij MJ, van der Laarse A.

Myocardial collagen metabolism in failing hearts before and during cardiac resynchronization therapy.

Eur. J. Heart Fail. 2008 Sept; 10(9):878-83.

Hessel MH, Bleeker GB, Bax JJ, Henneman MM, **den Adel B**, Klok M, Schalij MJ, Atsma DE, van der Laarse A.

Reverse ventricular remodelling after cardiac resynchronization therapy is associated with a reduction in serum tenascin-C and plasma matrix metalloproteinase-9 levels.

Eur J Heart Fail. 2007 Oct;9(10):1058-63.

Hessel MH, Steendijk P, **den Adel B**, Schutte CI, van der Laarse A.

Characterization of right ventricular function after monocrotaline-induced pulmonary hypertension in the intact rat.

Am J Physiol Heart Circ Physiol. 2006 Nov;291(5):H2424-30.

Hoefler IE, **den Adel B**, Daemen MJAP.

Biomechanical factors as triggers of vascular growth.

Invited review *Cardiovasc Res* submitted

den Adel B, Suidgeest E, Burtea C, van der Heiden K, Stammes MA, Laurent S, van Gaalen K, Gijsen F, Muller RN, Poelmann RE and van der Weerd L.

Vascular cell adhesion molecule-1 targeted nanoparticles discriminate between atherosclerotic plaque stages in disease progression and therapy.

Submitted.

van Eldik WL*, Beqqali A*, **den Adel B**, Monshouwer-Kloots J, Salvatori D, Maas S, Boontje N, van der Velde J, Steendijk P, Mummery CL and Passier PC.

Overexpression of the Z-disk protein CHAPb leads to cardiac hypertrophy and diastolic dysfunction.

Submitted.

den Adel B, Suidgeest E, Burtea C, Stammes MA, van der Heiden K, Laurent S, Poelmann RE, Muller and van der Weerd L.

E-selectin targeted MRI visualizes progression of atherosclerotic plaques.

Submitted.

DANKWOORD

Na ruim vier en half jaar werken is het moment eindelijk daar; het schrijven van dit dankwoord is een van de laatste en meest persoonlijke dingen die ik doe voor het afronden van mijn proefschrift. Zonder de hulp en inzet van heel veel mensen, had ik dit proefschrift niet kunnen schrijven.

Allereerst, Rob en Louise, jullie steun en sturing in de afgelopen jaren was zeer waardevol en ik heb veel van jullie geleerd. Bedankt voor de interessant gedachtewisselingen en discussies. Rob ik wens je alle goeds toe, je hebt je laatste eigen aio nu "afgeleverd". Louise, voor ons houdt de rit hier niet op, hopelijk brengt de toekomst ons een mooie Leids-Amsterdamse samenwerking.

Christine, ik heb veel geleerd van jou en je groep. Bedankt voor het feit dat ik zoveel wetenschappelijke vrijheid heb gekregen binnen de groep.

Mijn dank gaat uit naar al mijn collega's van de Anatomie & Embryologie en Radiologie. In het bijzonder wil ik hierbij Linda, Bianca en Ernst bedanken, jullie hebben me in verschillende fasen van mijn promotie geholpen met praktische ondersteuning en vele uren gezelschap bij de MRI scanner. Zonder jullie hulp had ik veel minder werk kunnen verzetten!

Mijn kamergenoten over de jaren, Bianca, Kim, Fanneke, Pauline, Linda, Richard, Leon, Anastasia, Beerend, Milena, Simone en Stefan: jullie waren er altijd voor een wetenschappelijke discussie en een kop koffie. Mede dankzij jullie was mijn promotie een mooie tijd!

De MI-club: Louise, Mick, Maarten, Dana, Rob, Maaïke, Mascha, het was prettig met jullie te werken en heel leerzaam mede door onze diverse achtergronden. Ik kijk uit naar onze verdere samenwerkingen.

Many thanks to my colleagues from Mons, Belgium. It was a great pleasure to get introduced into "your chemical world", visit your lab, work and collaborate with you.

Fons, Kees, Karthick, Liesbeth en alle anderen van het LIC. Bedankt voor jullie technische hulp bij de MRI als er weer eens iets misging, maar ook dank voor de kopjes koffie en gezelligheid op mijn Gorlaeus scandagen.

Roel en Sandra, mijn mede-aio's op het hartstichtingsproject. Het was heel inspirerend om met jullie samen aan een groot project te werken ook al zaten we verspreid door het land. Sandra, jou wil ik in het bijzonder bedanken voor de fijne samenwerking. Klaas, Gustav, Glenda, Gerard, Marcel, Bernard, Cees, bedankt voor jullie bijdrage aan het project. Erik Biessen, Filip Segers, Theo van Berkel, Johan Kuiper, Jose van der Hoorn, Ilze Bot, bedankt voor de vruchtbare samenwerkingen.

Frank, Ton, Jolanda, Kim, Kim en Lambert, de "Rotterdamers", het was prettig samenwerking met jullie. Ik heb veel geleerd, maar waarschijnlijk nog veel meer niet begrepen, van de veelal theoretische en wiskundige besprekingen met jullie groep.

Ik kijk met veel plezier terug op mijn afstudeerstage bij Prof. Dr. van der Laarse en Dr. Hessel, Arnoud en Marleen, jullie hebben een belangrijke bijdrage geleverd aan mijn basisinzichten van

hart- en vaatziekten en jullie enthousiasme herinner ik me na al die jaren nog levendig.

Anne-Marie, Wies en Atie, bedankt voor de secretariële ondersteuning!

Mat, Diewertje, Nerissa, Katje en andere AMC'ers, bedankt voor jullie introductie in Amsterdam, ik kijk uit naar onze verdere samenwerking. Hierbij wil ik ook Marie-Jose Goumans bedanken; jij bent erg belangrijk geweest in mijn keuze voor Amsterdam.

Mijn vriendinnetjes: Lara, Noortje, Kim, Linda, Leontine, het was en is altijd heel fijn om met jullie op stap te gaan en "het leven" te kunnen delen.

Noortje en Simone, wat fijn dat jullie bij mijn promotie aan mijn zijde staan!

Noortje, we kennen elkaar inmiddels bijna 10 jaar. Ik ben je heel dankbaar voor je vriendschap. Ik mis de tijd dat we zowel collega's als vriendinnen hebben kunnen zijn. Het is fijn om nu de rollen om te draaien en jou als paranimf te hebben.

Simone, we hebben een vakantie samen, een vulkaan uitbarsting met als gevolg geen vliegverkeer en een meer dan 24-urige terugreis in een bus met 3 kinderen uit Portugal overleeft! Bedankt voor je vriendschap, het is een eer om je als paranimf te hebben.

Tonny, Gerard, Marlies, Jort en Sara, bedankt voor jullie warme welkom in de familie Braam en belangstelling voor de afronding van mijn proefschrift. Jort, bedankt voor je hulp met de layout.

Pap, mam, bedankt voor jullie geduld en steun. Ik weet dat het soms moeilijk is uit te leggen wat voor werk ik nu doe maar dit boekwerk is het resultaat van al die jaren "proefjes" doen.

Martin, jij bent de grootste wetenschapper in huis, elke dag een nieuwe ontdekking! Het is ontzettend fijn je moeder te zijn. Jij maakt elke dag weer verrassend.

Stefan, ik ben blij dat we kamergenoten werden. Jouw enthousiasme en passie voor wetenschap in de breedste zin van het woord zijn heel stimulerend geweest. Bedankt voor al je steun, begrip en liefde. Ik heb zin in de toekomst samen met jou!